Molecular Signposts of the Physics and Chemistry of Planet Formation

by

Lauren Ilsedore Cleeves

A dissertation submitted in partial fulfillment
of the requirements for the degree of
Doctor of Philosophy
(Astronomy and Astrophysics)
in the University of Michigan
2015

Doctoral Committee:

Professor Edwin Anthony Bergin, Chair
Professor Fred C. Adams
Professor Nuria Pilar Calvet
Professor Ewine Fleur van Dishoeck
Professor Lee William Hartmann

"There is nothing like looking, if you want to find something. You certainly usually find something, if you look, but it is not always quite the something you were after."

– J. R. R. Tolkien, *The Hobbit*

For my family.

ACKNOWLEDGMENTS

I am immeasurably grateful to the people that have encouraged and enabled me during my graduate studies at the University of Michigan. Nobody has said obtaining a PhD is easy, and it would be nearly impossible without a community of support from collaborators, friends, staff, and family. I have been so fortunate to have great folks cheering me on. Thank you.

Before I began graduate school – and even after visiting Michigan – I would have never believed that the word "chemistry" would be applied to my field of expertise. Fortunately my advisor, Ted Bergin, convinced first-year Ilse that this field of "astrochemistry" was both a) real and b) extremely interesting. I openly maintain that coming to Michigan to work with Ted was one of the best decisions I have made in my life, a point to which Ed Cackett cheekily told me, "you clearly haven't made very many good decisions." Regardless of the factuality of this statement, I am so grateful for the mentorship Ted has provided, helping me navigate the scientific landscape as well as the finer politics of academia (where the latter can often be more complicated than the former). And while Ted has generously provided the necessary resources (computing, travel funding, etc.) for a graduate student's success, one of the most valuable resources (and one of characteristics I hope to further develop) is Ted's limitless creativity. Observing proposal brainstorming sessions with the "Nerd Club[1]" were always a particularly fun and engaging time in the group – thinking up exciting and/or wacky new experiments to try with new observing facilities (*Herschel*, ALMA). I am also grateful

[1]Ted's eldest daughter's name for our research group.

for Ted's emphasis on moving towards better work/life balance in academia, something we could all try to do more of. Thank you, Ted.

I have truly been fortunate to have great mentorship (and encouragement to study astronomy) through college and even as far back as grade school. Attending Rice University (one of the other "best decisions" in my questionable list of "bests") and conducting a thesis project with Pat Hartigan and doing research with Chris Johns-Krull solidified my interest in galactic star-formation and was integral to me applying to and attending UM in the first place. Rice's personalized attention from a relatively small department and emphasis on undergraduate research early-on is how I first realized academia is where I want to be. And yet before that, I would have never attended Rice had I not had terrific math and science teachers at Rome High School. It is dizzying to look backwards and realize how one ended up on a given path, and I cannot imagine a more fortunate one. I am so thankful for all of my early mentors.

I am especially grateful to my dissertation committee: Fred Adams, Nuria Calvet, Ewine van Dishoeck and Lee Hartmann. I have been coached by those among the founders of modern star-formation and astrochemistry and have had the privilege of not only advisory roles but also collaborative roles with them, through writing papers, observing proposals, or both. Fred Adams, thank you for your advisement and being such a helpful co-author, not only helping me improve my writing skills, but also making sure that I fully earn the "theorist" badge stamped forever on my transcript. Thanks to Nuria for instilling confidence in me and a sense of fierce Michigan camaraderie and pride. Ewine, thank you for always bringing a new perspective to our scientific discussions and for generously hosting me at your institution, Leiden, in the Summer of 2014; it was an exciting week for me with the myriad of productive group meetings covering a diversity of topics. Thanks to Lee for providing the critical (and vast) contextual knowledge and always adding a touch of humor to every scenario. Furthermore, though not in an official capacity, I am grateful for the mentorship provided to me by Karin Öberg, who has always been a terrific scientific advisor

and friend, further encouraging me to pursue my goals and accepting (if not embracing) my idiosyncrasies.

I am also thankful to the department staff: especially Brian Cox, Jan Malaikal, and Anne Thomson, who made the behind-the-scenes part of running a department go smoothly, and always went above and beyond the call to support the graduate students. The department at large has also been a remarkable support network; the amount of career and/or technical advice I have received from non-committee faculty is incalculable, especially from Jon Miller and Emily Rauscher. Furthermore, I am grateful for the terrific female representation in our department, which demonstrates UM Astronomy's commitment to moving toward a better representative scientific population, and whose effects are reflected in the gender-balance of the incoming graduate classes year-after-year.

I have also been fortunate to have such a wonderful graduate cohort: Colin Slater, Anne Jaskot, Ashley King and Jeb Bailey, who together have been so helpful and motivating. Friendships fostered during graduate school are so important for the health and well-being of students – and our year was no exception. I owe so much to Colin for endless help debugging code, daily scientific discussions, and rescuing my stuffed-animal monkey from the roof of "Little Dennison" after it fell eight stories. I also had the best officemate a student could ask for, Anne Jaskot, who was simultaneously both the best listener and impossible to distract, especially when I would do little celebratory dances at my desk when a seemingly intractable problem got sorted out. Anne was always game to go get coffee at Espresso Royale or for a round of office Scrabble (keeping impeccable statistics on our scores), which forever will be some of my favorite graduate school memories. Outside of the department, I am grateful in particular to my dear friends Anna Wagner, Carrie Ott-Holland, and Noah Wolfson for providing balance and color in my otherwise largely astronomy-centric life, thank you!

Finally, my family has been one of my biggest and most important influences. I am immensely grateful for the love, support, and emphasis on education (of all kinds: art, math, etc.) that my parents provided. When I started becoming interested in astronomy

in fifth grade, their support never wavered, later gifting me a telescope that I would tote out into our neighborhood to one of the few intersections without a street light to look out at the stars. Thank you Mom and Dad for believing in me (and in my sometimes crazy dreams). On a similar note, I am infinitely appreciative of the patience and encouragement from my fiancé, Dustin Smith. Almost instantaneously upon meeting Dustin in 2012, I told him "that I am an astronomer, which means I will be moving often to unknown places," which apparently (miraculously) did not scare him off. I am so grateful for his love and care especially during the crunch-times, which we have come to refer to as "crewing," an homage to Dustin's passion for trail marathon running where crews are fundamental to the livelihood of the runners. Thank you for looking out for my physical and mental well-being, and for becoming so intimately familiar with my research that he is often able to describe it even better than me. In sum, this thesis is truly a testament to the collective support of all of the terrific people in my life. Thank you all.

TABLE OF CONTENTS

DEDICATION ii

ACKNOWLEDGMENTS iii

LIST OF FIGURES xii

LIST OF TABLES xvii

LIST OF APPENDICES xix

LIST OF ABBREVIATIONS xx

ABSTRACT xxi

CHAPTER

I. Introduction 1

1.1 Protoplanetary Disks, a Historical Perspective 2
1.2 Disk Formation 6
1.3 Physical Properties and Disk Structure 10
1.3.1 Disk Thermal Structure 10
1.3.2 High Energy Processes and Ionization 12
1.3.3 Gas Kinematics 14
1.3.4 The Dusty Disk 15
1.4 Disk Volatile Composition and Chemistry 16
1.5 Observational Characterization of the Gas Reservoir 21
1.6 Overview of the Dissertation 24

II. Transition disk chemistry and future prospects with ALMA 28

2.1 Preface 28
2.2 Abstract 28
2.3 Introduction 29
2.4 Chemical Modeling 30

2.4.1 Disk Framework . . . 30
2.4.2 Radiation Field . . . 31
2.4.3 Reaction Network . . . 35
2.5 Results . . . 36
2.5.1 Disk Chemistry . . . 36
2.5.2 Observables . . . 36
2.6 Further Considerations . . . 39
2.6.1 Accretion Heating . . . 39
2.6.2 Dust Settling and Grain Coagulation . . . 40
2.6.3 Dust in the Inner Gap . . . 40
2.6.4 Gas in the Inner Gap . . . 41
2.7 Conclusions . . . 41
2.8 Acknowledgements . . . 42

III. Indirect Detection of Forming Protoplanets via Chemical Asymmetries in Disks . . . 43

3.1 Preface . . . 43
3.2 Abstract . . . 43
3.3 Introduction . . . 44
3.4 Physical Model . . . 46
3.4.1 Axisymmetric Structure . . . 46
3.4.2 3D Thermal Structure . . . 48
3.4.3 Chemical Model . . . 50
3.5 Results . . . 52
3.5.1 Chemical Abundance Results . . . 52
3.5.2 Line Emission . . . 59
3.6 Discussion & Conclusions . . . 67
3.7 Acknowledgements . . . 70

IV. Exclusion of Cosmic Rays in Protoplanetary Disks: Stellar and Magnetic Effects . . . 71

4.1 Preface . . . 71
4.2 Abstract . . . 71
4.3 Introduction . . . 72
4.4 The Model . . . 75
4.4.1 Physical Parameters . . . 75
4.4.2 Disk Ionization Processes . . . 80
4.5 Exclusion of Cosmic Rays by Stellar Winds . . . 89
4.5.1 Modulation By the Solar Wind . . . 89
4.5.2 The Cosmic Ray Spectrum in a T-Tauriosphere . . . 92
4.5.3 Extent of the T-Tauriosphere . . . 97
4.5.4 Cosmic Ray Attenuation . . . 100
4.6 Exclusion of Cosmic Rays by Large Scale Magnetic Fields . . . 104

4.6.1 Environmental Magnetic Fields . . . 104
4.6.2 Stellar Magnetic Fields . . . 106
4.6.3 Cosmic Ray Exclusion by Magnetic Mirroring . . . 106
4.7 Cosmic Ray Exclusion and Dead Zones . . . 109
4.7.1 Ionization: Active Disk Criteria . . . 110
4.7.2 T-Tauriospheric Dead Zones . . . 112
4.7.3 Dead Zone Dependence on the Stellar X-ray Luminosity . . . 115
4.8 Further Considerations . . . 116
4.8.1 Radionuclide Ionization in the Midplane . . . 116
4.9 Conclusions . . . 119
4.10 Acknowledgments . . . 123

V. Radionuclide Ionization in Protoplanetary Disks: Calculations of Decay Product Radiative Transfer . . . 124

5.1 Preface . . . 124
5.2 Abstract . . . 124
5.3 Introduction . . . 125
5.4 Transfer of Short-Lived Radionuclide Decay Products . . . 127
5.4.1 Plane-Parallel Approximation . . . 129
5.4.2 Dust Settling . . . 134
5.4.3 Time Dependence . . . 138
5.5 Discussion . . . 140
5.6 Conclusion . . . 141
5.7 Acknowledgments . . . 142

VI. Exclusion of Cosmic Rays in Protoplanetary Disks. II. Chemical Gradients and Observational Signatures . . . 143

6.1 Preface . . . 143
6.2 Abstract . . . 143
6.3 Introduction . . . 144
6.4 The Physical Model . . . 147
6.5 Ionization Sources . . . 148
6.5.1 Stellar Photoionization . . . 149
6.5.2 Short-Lived Radionuclide Ionization . . . 152
6.5.3 Cosmic Ray Ionization . . . 153
6.6 The Chemical Network . . . 155
6.6.1 Chemical Model . . . 156
6.6.2 Chemical Abundance Results . . . 160
6.7 Line Emission Modeling . . . 165
6.7.1 Line Radiative Transfer . . . 166
6.7.2 Simulated ALMA Observations . . . 168
6.8 Further Considerations . . . 176
6.8.1 Higher X-ray Luminosity . . . 176

6.8.2 Short-Lived Radionuclide Time Decay . . . 177
6.8.3 Dependence on Disk Mass . . . 179
6.8.4 Dependence on Stellar Spectral Type . . . 181
6.8.5 Disk Magnetic "Opacity" to Cosmic Ray Ionization . . . 184
6.9 Discussion and Conclusions . . . 186
6.10 Acknowledgements . . . 189

VII. Constraining the X-ray and Cosmic Ray Ionization Chemistry of the TW Hya Protoplanetary Disk: Evidence for a Sub-interstellar Cosmic Ray Rate . . . 200

7.1 Preface . . . 200
7.2 Abstract . . . 200
7.3 Introduction . . . 201
7.4 Observations . . . 204
7.4.1 Submillimeter Array Data . . . 204
7.4.2 Archival Data . . . 208
7.5 Modeling . . . 209
7.5.1 Physical Structure . . . 210
7.5.2 Disk Chemistry . . . 210
7.5.3 Ionization . . . 214
7.5.4 Line Radiative Transfer and Synthetic Observations . . . 218
7.6 Results . . . 221
7.6.1 HCO^+ Spatial Distribution . . . 221
7.6.2 Model Grid Results . . . 222
7.6.3 Constraints on Ionizing Agents . . . 223
7.7 Discussion . . . 226
7.7.1 The Ionization Environment of TW Hya . . . 226
7.7.2 Dead-zones, Dust Growth and Accretion . . . 228
7.7.3 HCO^+ Asymmetry . . . 230
7.8 Conclusions . . . 231
7.9 Acknowledgements . . . 232

VIII. The ancient heritage of water ice in the solar system . . . 237

8.1 Preface . . . 237
8.2 Abstract . . . 237
8.3 Introduction . . . 238
8.4 Acknowledgements . . . 246

IX. In Conclusion . . . 247

9.1 Summary of Findings . . . 249
9.1.1 Chemistry in the Presence of Planetary Sculpting . . . 249
9.1.2 Ionization Processes in Planet-Forming Disks . . . 249

9.1.3 Ionization in the TW Hya Disk: Tentative First Detection an Extrasolar Heliosphere? . . . 250
9.1.4 Water in Protoplanetary Disks . . . 251
9.2 Future Directions . . . 252

APPENDICES . . . 254
D.1 Dust Model . . . 262
D.2 Gas Model . . . 264
E.1 Neutral Gas Constraints: CO . . . 268
E.2 Neutral Gas Constraints: HCN . . . 270
G.1 Physical Model . . . 275
G.2 Non-Stellar Ionization Processes . . . 277
G.3 Chemical Reaction Network . . . 279
G.4 Binding Energies . . . 281
G.5 Chemical Model Tests . . . 285
G.6 Further Considerations . . . 286

BIBLIOGRAPHY . . . 291

LIST OF FIGURES

Figure

1.1 The solar system's formation as depicted in Emanuel Swedenborg's *Opera Philosophica et Mineralia* (1736) 5

1.2 The cycle of star-formation 7

1.3 Schematic of important disk physical processes. 11

1.4 Left: Stratification of the chemical structure for species other than H_2 and helium. Right: Phases of water and the primary physical cause of phase changes locally. A similar plot can be made for all species, where the relative locations shift based upon the properties of the molecule in question. . . . 18

2.1 Generic transition disk physical model. 32

2.2 Lyα schematic illustration. 34

2.3 Transition disk chemical modeling results for CO, HCO^+, H_2CO, H_2O, N_2H^+ and HCN. 37

2.4 Simulated ALMA observations for the transition disk chemical models. . . 38

3.1 Large scale circumstellar disk properties, away from the embedded planet. . 47

3.2 Thermal structure in the region near the disk-embedded planets. 51

3.3 Vertically integrated column densities of select molecular species near the planet and opposite the planet for the planet at 5 AU. 53

3.4 Vertically integrated column densities of select molecular species near the planet and opposite the planet for the planet at 10 AU. 53

3.5 Vertically integrated column densities of select molecular species near the planet and opposite the planet for the planet at 20 AU. 54

3.6 Vertically integrated column densities of select molecular species near the planet and opposite the planet for the planet at 30 AU. 54

3.7 Three-dimensional chemical abundance structure for the 5 AU planet. . . . 58

3.8 Three-dimensional chemical abundance structure for the 10 AU planet. . . 59

3.9 Three-dimensional chemical abundance structure for the 20 AU planet. . . 60

3.10 Three-dimensional chemical abundance structure for the 30 AU planet. . . 61

3.11 HCN and $H^{13}CN$ emission for the planet at $d_p = 10$ AU. 64

3.12 HCN and $H^{13}CN$ emission for the planet at $d_p = 20$ AU. 65

3.13 HCN and $H^{13}CN$ emission for the planet at $d_p = 30$ AU. 66

4.1 Generic protoplanetary disk model, including density, temperature and radiation field. 76

4.2 Template UV and X-ray spectra at the stellar surface. 82

4.3 Relative contribution of stellar UV, X-rays, and cosmic rays to the total H_2 ionization rate. 84

4.4 Ionization rate due to UV from the central star and the interstellar radiation field. 87

4.5 Interstellar cosmic ray spectra, including the most recent *Voyager 1* data. . 90

4.6 Time variation of cosmic ray modulation strength compared to other observed solar properties. 95

4.7 Dependence of the energy spectrum of cosmic rays on the strength of stellar wind modulation/exclusion. 98

4.8 Cosmic ray spectra at increasing H_2 column densities. 102

4.9 Cosmic ray ionization rates as a function of column density for the different cosmic ray models. 103

4.10 Illustration of cosmic ray exclusion by magnetic mirroring. 107

4.11 Cosmic ray exclusion by magnetic fields for different field geometries. . . . 109

4.12 Molecular hydrogen ionization rate as a function of position in the disk, and the corresponding size of the turbulence-free "dead-zone," for different cosmic ray models. 113

4.13 Plots of the X-ray only ionization rate. 117

4.14 Molecular hydrogen ionization rate as a function of position in the disk including short-lived radionuclide decay. 118

5.1 Short-lived radionuclide ionization rate as a function of height from the midplane. 130

5.2 Short-lived radionuclide ionization rate including decay product escape. . . 133

5.3 Time dependence of short-lived radionuclide ionization. 138

5.4 Simple fits to the midplane ionization rate by radionuclides. 139

6.1 Generic disk model used for the chemical calculations. 147

6.2 Sources of H_2 ionization present in the midplane as a function of disk radius. 151

6.3 Disk chemical abundances under different ionization conditions. 162

6.4 Molecular column densities for different ionization models. 190

6.5 Molecular line opacity for different molecular ionization tracers. 191

6.6 Schematic illustrating the calculation of simulated Atacama Large Millimeter Array observations. 192

6.7 ALMA simulations for the observable transitions of HCO^+ and isotopologues. 193

6.8 ALMA simulations for the observable transitions of N_2H^+, N_2D^+, and H_2D^+. 194

6.9 ALMA simulations of the low CR ionization rate models with and without a constant SLR ionization rate. 195

6.10 Chemical models for different X-ray luminosities. 196

6.11 Column density dependence on radionuclide ionization including time dependence. 197

6.12 Column-derived abundances of the indicated molecular ions, normalized to CO column. 198

6.13 Vertical column densities of select ionization tracers as a function of stellar spectral type. 199

7.1 Submillimeter Array observations of TW Hya's HCO^+ $3-2$ emission. . . . 206

7.2 Disk integrated spectra of HCO^+ $(3-2)$ and $H^{13}CO^+$ $(3-2)$ in TW Hya. 207

7.3 TW Hya physical model. 211

7.4 Simulated TW Hya X-ray models. 217

7.5 Midplane ionization rates from different ionizing sources, X-rays, cosmic rays, and short-lived radionuclides. 219

7.6 Chemical model grid results for different ionization models for TW Hya. . . 224

7.7 Comparisons between observed line intensities and models. 233

7.8 Comparisons between the ion emission spatial profile of HCO^+ $(3-2)$ and models. 234

7.9 Comparisons between the ion emission spatial profile of N_2H^+ $(4-3)$ and models. 235

7.10 Estimates of TW Hya's dead-zone size as determined from the chemical calculations. 236

8.1 Atomic D/H ratios in solar system and interstellar water. 242

8.2 Schematic of energetic disk ionization sources. 243

8.3 Chemical abundances and column densities for the drivers of the deuterium enrichment, the ions; and the corresponding products, the ices. 245

9.1 Band 6 (1.3 mm) image of HL Tau as taken with ALMA during the long baseline commissioning campaign. One potential interpretation of the rings' origin is sculpting/shepherding by newly formed planets. 248

C.1 Short-lived radionuclide H_2 ionization rate in the disk midplane as a function of gas surface density and time. 261

D.1 Dust opacities for the two dust populations used in our SED model of TW Hya. 263

D.2 Our best fit model spectral energy distribution of TW Hya. 264

E.1 Comparison between the simulated $C^{18}O$ (2-1) and ^{13}CO (2-1) line intensities and the observed values. 270

E.2 The dependence on different initial nitrogen conditions of the HCN abundance after 1 Myr of chemical evolution. 271

F.1 Chemical model comparison between the disk model assumed in this work and the results for a different underlying disk model of TW Hya. 274

G.1 Generic protoplanetary disk model. 277

G.2 Temperature programmed desorption spectra of pure CO, CO desorbing off a CO_2 ice, and CO desorbing of an amorphous H_2O ice. 284

G.3 Abundances and deuterium-fractionation results for water with a standard ISM GCR rate. 287

G.4 Deuterium fractionation results for an atomic oxygen start. 288

LIST OF TABLES

Table

1.1 Critical densities for lines of interest at $T = 50$ K. 22

4.1 Stellar and disk model parameters. 79

4.2 $\zeta_{\rm CR}$ fitting parameters for different incident spectra shown in Figure 4.7, see Eq. (4.5). 97

4.3 Hourglass Magnetic Field Parameters. 105

4.4 Mass contained in dead zones for the different cosmic ray models without radionuclide ionization, see Fig. 4.12. 114

5.1 Selected SLR Data. 128

6.1 Stellar and disk model parameters. 148

6.2 CR model ionization rates for $N(\mathrm{H_2}) \leq 10^{25}$ cm^{-2}. 155

6.3 Initial chemical abundances, χ. 161

6.4 CASA Simulation Parameters. 169

7.1 Spectrally integrated TW Hya line fluxes used to constrain the physical model. Reported uncertainties on the molecular ions include statistical errors and a 15% systematic uncertainty in the absolute flux scale. 209

7.2 Incident CR model ionization rates, $\zeta_{\rm CR}$. 215

B.1 Reduced sulfur network adapted from the OSU gas-phase chemical network (March 2008; *Smith et al.*, 2004). 257

E.1 Chemical model initial abundances relative to total number of H-atoms. . 272

G.1 Log of the initial chemical abundances, χ, per total number of hydrogen atoms. 280

G.2 Physical parameters for the chemical model comparison points in the mid-plane at the specified radii. 285

G.3 Independent chemical model comparison results. Table values given with respect to D/H in H_2, i.e. $f[\mathrm{R}] = \mathrm{R}/4\times10^{-5}$. A = chemical model presented in the main text; B = complex gas-grain deuterium chemical model (*Du*, 2012, PhD). 286

G.4 D/H values and references from Figure 8.3. 290

LIST OF APPENDICES

Appendix

A. Approximation for the Interstellar Radiation Field 255

B. Sulfur Chemistry 256

C. Updated Short-Lived Radionuclide Rates 260

D. Physical Structure 262

E. Neutral Gas Constraints 268

F. Model Comparison 273

G. Physical Model and Supplementary Data 275

LIST OF ABBREVIATIONS

ALMA Atacama Large Millimeter/Submillimeters Array

AU Astronomical unit

CR Cosmic ray

FUV Far Ultraviolet

IR Infrared

ISM interstellar medium

LTE Local thermodynamic equilibrium

MHD Magnetohydrodynamic

pc Parsec

PdBI Plateau de Bure interferometer

RN Radionuclide

RT Radiative transfer

SED Spectral energy distribution

SLR Short-lived radionuclide

SMA Submillimeter Array

SSM Solar System Minimum

SSX Solar System Maximum

TT T Tauri

TTM T Tauri Minimum

TTX T Tauri Maximum

XR X-ray

ABSTRACT

Observations of molecules in planet-forming circumstellar disks are powerful diagnostic tools, enabling characterization of both gas composition and underlying physical conditions using molecular excitation. My thesis has primarily focused on the role of disk structure and ionization for the chemistry of disks and the corresponding submillimeter emission. Changes in the overall morphology of disks, including inner holes or gaps, significantly alters the stellar irradiation of the disk, which will affect the disk heating, especially at the walls of an inner hole (Chapter 2). I have modeled the 3D chemistry of gapped disks, carved out by planets, including for the first time heating by a luminous protoplanet. The planet sublimates ices beyond expected disk "snow-lines" leading to observable signatures detectable with ALMA (Chapter 3). Regarding ionization, I have studied disk ionization by cosmic rays (Chapter 4), short-lived radionuclides (Chapter 5), and X-rays from the central star (Chapter 6). In Chapter 6, I investigated the molecular dependence on each of these processes and made testable predictions for sensitive submillimeter observations to map out disk ionization, which I applied to the TW Hya disk, finding a substantially lower than interstellar cosmic ray rate (Chapter 7). One of the major implications of this work is related to the formation chemistry of water, which requires ionization to proceed. In the absence of water-formation in the solar nebula protoplanetary disk, this work demonstrates that there must be a substantial inheritance of water from earlier evolutionary stages, pre-dating the Sun's formation (Chapter 8). Together, these projects have also enabled the development of a comprehensive 2D and 3D disk modeling framework, useful for parameter space studies and source-targeted modeling.

CHAPTER I

Introduction

Protoplanetary disks around newly formed Sun-like stars are an agglomeration of dust, ice and gas. These materials have a number of potential fates: falling onto the star, ejection as winds or jets, dispersal outward as the disk spreads, or growing/accumulating into planetesimal bodies. Disks are the subject of this thesis, specifically illuminating the chemical composition of protoplanetary disks and how the composition is affected by disks' physical nature. Furthermore, we explore how these factors affect the resulting planetary systems and identify ways to detect signatures of recently formed planets in situ.

In the present body of work, I focus on protoplanetary disks around low-to-intermediate mass stars with masses typically ranging from a few tenths of a solar mass up to ~ 2 solar-mass stars, i.e., potential mirror systems of our own Solar System's formation. Such systems are commonly termed "T Tauri" disks after the prototypical star and disk system T Tau[1] (*Rydgren et al.*, 1976). To place our solar system's formation into context, we use detailed theoretical models of the disk environment, astronomical data from both ground and space-based observatories of young, currently star-forming regions, and data from our own Solar System's record to piece together aspects of our own history. This work aims to shed light on the conditions that arose to form planets – along with at least one habitable planet – and

[1]Though later reclassification as a stellar triple system of a primary star and an embedded binary seemingly makes T Tau not very prototypical at all (e.g., *Dyck et al.*, 1982; *Koresko*, 2000; *Duchêne et al.*, 2006).

to reveal how common such a phenomenon is throughout the local universe.

1.1 Protoplanetary Disks, a Historical Perspective

Humankind has contemplated its origins for millennia. The pursuit spans nearly all disciplines, philosophy, religion, physics, biology, geology, planetary science, and, of course, astronomy. Understanding our Solar System's origins, though somewhat younger conceptually, also has a rich history spanning back over two centuries.

The foundations of the modernly accepted formation scenario, i.e., formation from a nebular disk, are most commonly attributed to the original "nebular hypothesis" envisioned independently by Immanuel Kant and Pierre-Simon Laplace. Immanuel Kant's perspective, as described in the *Universal Natural History and Theory of the Heavens* (1755), begins with the initial gravitational collapse of some type of interstellar medium, or as he calls it "elementary basic material at the beginning of all things, [that] occupied the entire space of the universe. ... Nature as it bordered directly on creation, was as raw, as unformed as possible" (I-263). It should be noted that this supposition predates both the direct observation and confirmation of the diffuse interstellar medium, which would follow more than one hundred and fifty years later (*Hartmann*, 1904), and the detection of the emissive molecular interstellar medium by more than two centuries (*Penzias et al.*, 1971, 1972). This picture was instead inspired by observations of nebular astronomical objects whose filamentary structure had been recorded for nearly a century prior.

Upon the initial collapse of the nebula, Kant goes on to describe that once the central body has become massive enough, "it attracts the particles from great distances, is bent sideways by the weak degrees of repulsion by which the particles hinder each other, and changes into sideways motions that are capable of encompassing the central body in a circle through centrifugal force" (Section I-265). This is the stage in which Kant invokes the formation of a disk-like geometry. Kant argues that the motions of the "floating elements" naturally head towards a state of minimal hindrance, one where the particles move in the

same direction, and particles with vertical motions are drawn to the center of mass, i.e., the disk. Particles that are not coaxed into regular orbits "bring about their ultimate fall to the Sun by bumping into the elements floating around," i.e., are accreted onto their parent star. Once this ideal configuration has been achieved, Kant explains that the floating elements "would always remain in that state, if the attraction of these particles of the basic material among each other did not begin to have its effect and bring about new formations which are the seeds of planets that are to come into being."

Eventually though, the planetary bodies must form from this initial nebular disk, which he explains must occur through the growth of massive "lumps" in the disk. However, in a rather forward-thinking footnote he elaborates that Newtonian gravity alone will not work, and that "the first formation would occur through the flowing together of some elements which unite according to the ordinary laws of combination" – a realization not dissimilar to (relatively) modern theories of the coagulation and assembly of planetesimals (*Safronov and Zvjagina*, 1969; *Goldreich and Ward*, 1973).

Independently, Pierre-Simon Laplace developed his own version of the nebular hypothesis, explained in detail in *Exposition du systeme du monde* (1796). Essentially, Laplace proposed that the solar system formed from a unified solar atmosphere where, in its earliest phases, "must have embraced [the planets] all within the sphere of its action; and considering the immense distance which intervenes between them, nothing could have effected this but a fluid of almost indefinite extent." He continues, "from a consideration of the planetary motions, we are therefore brought to the conclusion, that in consequence of an excessive heat, the solar atmosphere originally extended beyond the orbits of all the planets, and that it has successively contracted itself within its present limits." By this time, the Messier catalogue along with William Herschel's observations of the Orion Nebula Cluster were more widely known, and Laplace goes on to draw direct parallels between the primitive young sun's nebulous-state and that of the known nebulae.

Laplace puzzles intensely over the formation and survival of the planets and, in particular,

what sets their orbital motions and locations. He proposes that "the planets were formed at its successive limits, by the condensation of zones of vapours, which it must, while it was cooling, have abandoned in the plane of its equator." Conceptually, this proposition draws interesting parallels with modern theories of planet formation and their potential association with condensation fronts, i.e., "snow lines" (*Stevenson and Lunine*, 1988; *Lecar et al.*, 2006), which are discussed further below (Section 1.4).

However, predating both theories, one lesser-known Emmanuel Swedenborg had sketched out his own vision for the Solar System's formation two decades prior to Kant in his 1734 *Opera Philosophica et Mineralia*. Swedenborg's theory focused on the concept of vortices arising within an initially spherical circumstellar nebula. Furthermore, Swedenborg included illustrative figures with his theories, something neither Kant nor Laplace ventured to incorporate. Figure 1.1 shows just a sample of Swedenborg's sketches, illustrating his picture of the planetary formation process. Swedenborg begins with a crustal sphere encompassing the star (top-left), that expands forth radially from the surface of the star. As this material expands, Swedenborg explains that it "can no longer contiguously cohere but bursts in some part or other." He elaborates that this expansion "incessantly acts upon the walls and barriers of its prison that the crustaceous expanse or volume which is perpetually circumfluent tends by its centrifugal force to a farther distance..." (The Principia, vol. ii. p. 261), see Figure 1.1 top-right. Once the crustal sphere has burst, the volume "collapses upon itself; and this toward the zodiacal circle of the vortex, or conformably to the situation and motion of the elementary particles; so that it surrounds the sun like a belt or broad circle..." He proposes that the belt self-similarly bursts to form "larger and smaller globes; that is to say forms planets and satellites of various dimensions, but of a spherical figure."

These theories collectively explain the remarkably planar configuration of our own solar system and the similar direction of the orbits, and that which is now being observed in numerous other exoplanetary systems. However, all three philosophers struggled with comets. Their highly eccentric orbits proved challenging to fit into the original nebular hypotheses.

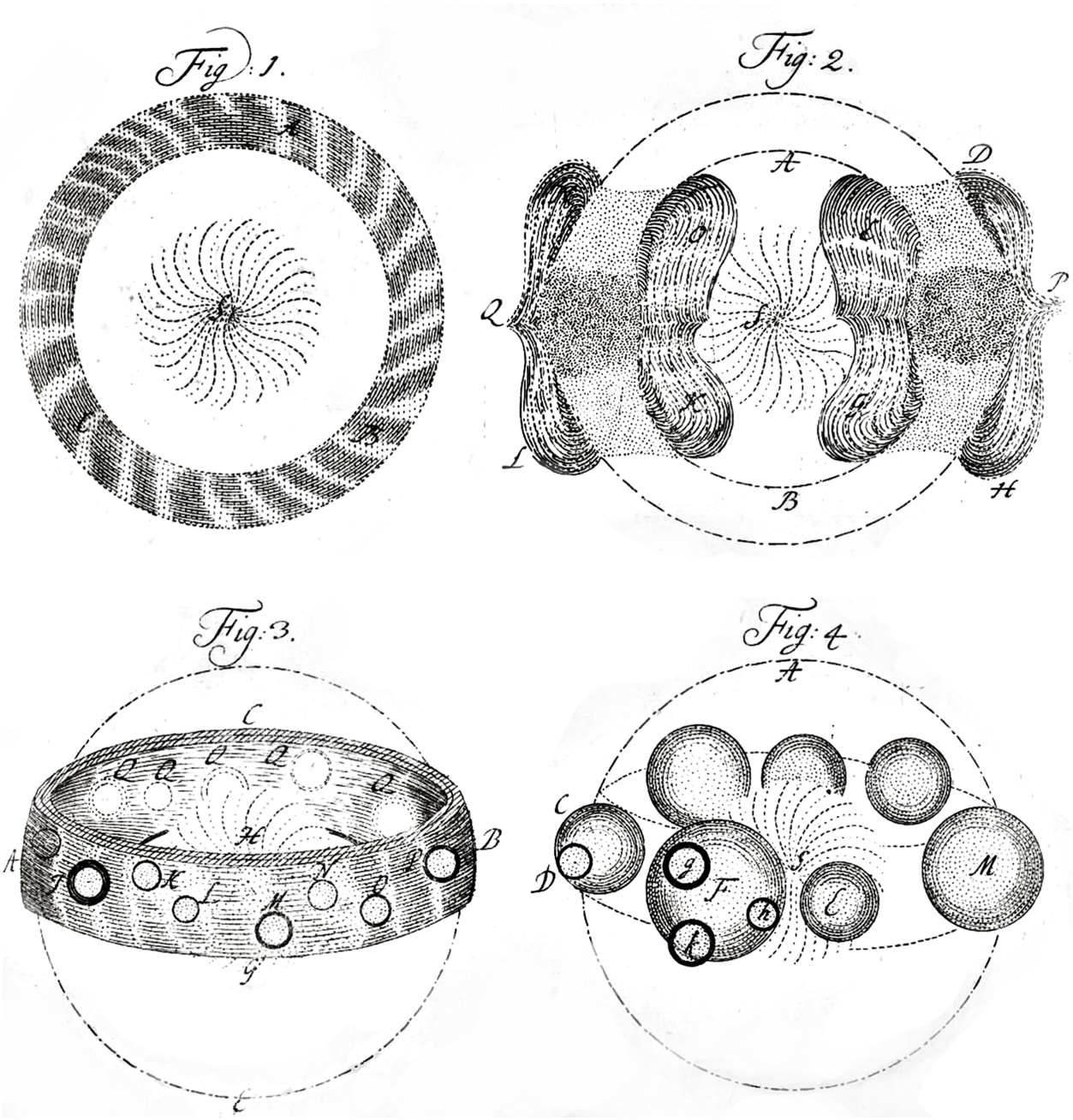

Figure 1.1 The solar system's formation as depicted in Emanuel Swedenborg's *Opera Philosophica et Mineralia* (1736)

Kant was unable to reconcile what he called the "lawless freedom of the comets," while Laplace went as far as to suggest that the comets represented independent condensations from the nebular medium independent of the Sun and solar system's formation, "wandering from one solar system to another."

Many other theories came and went over the centuries (including a particularly interesting theory by Georges-Louis Leclerc De Buffon invoking stellar or cometary fly-bys tearing away stellar material to form the planets also in the 1700's), but the original nebular theory remained the dominant hypothesis until it was updated in Victor Safronov's 1969 seminal work, where our generally accepted picture of the "solar nebula" was born.

Beyond the original concept of planet formation via a nebular disk, most of our knowledge of bulk disk properties has come about relatively recently. Advances in observations include identification of excess dust emission over the stellar photosphere at infrared wavelengths and beyond, suggesting a warm, dusty disk (*Mendoza V.*, 1966, 1968; *Hartmann and Kenyon*, 1985; *Rucinski*, 1985); images of distributed haloes of dusty-scattered light (*Beckwith et al.*, 1984); large-scale millimeter and submillimeter (*Weintraub et al.*, 1989a; *Beckwith et al.*, 1990) wavelength observations of glowing large grains, corresponding molecular emission from the cool gas disk (*Weintraub et al.*, 1987, 1989b; *Koerner and Sargent*, 1995); and finally, as made possible with the *Hubble Space Telescope*, direct imaging of dark dusty lanes occulting the central star in optical light (*McCaughrean and O'Dell*, 1996). Observations such as these, combined with advances in theory, have helped clarify the structure and composition of protoplanetary disks (Protostars & Planets VI provides a number of insightful reviews of the subject; *Beuther et al.*, 2014). We are now at the precipice of detecting and quantifying young planetary systems embedded in their parent disks, moving us closer to a complete picture of planet-formation nearly three centuries after Emmanuel Swedenborg's original vision.

1.2 Disk Formation

The modern picture of the star formation process is not too dissimilar from that of the initial stages of either Immanuel Kant or Pierre Laplace's theories. It is now well established that such molecular "nebulae" or as they are now termed, clouds, are the primary sites of star formation (see Figure 1.2, top-left). Giant molecular cloud (GMC) complexes contain

$\sim 10^5 - 10^6$ solar masses of material, and can span many tens of parsecs, with typical temperatures of 10 K and densities of $\sim 10^2$ cm^{-3} (e.g., *Blitz*, 1993). These structures

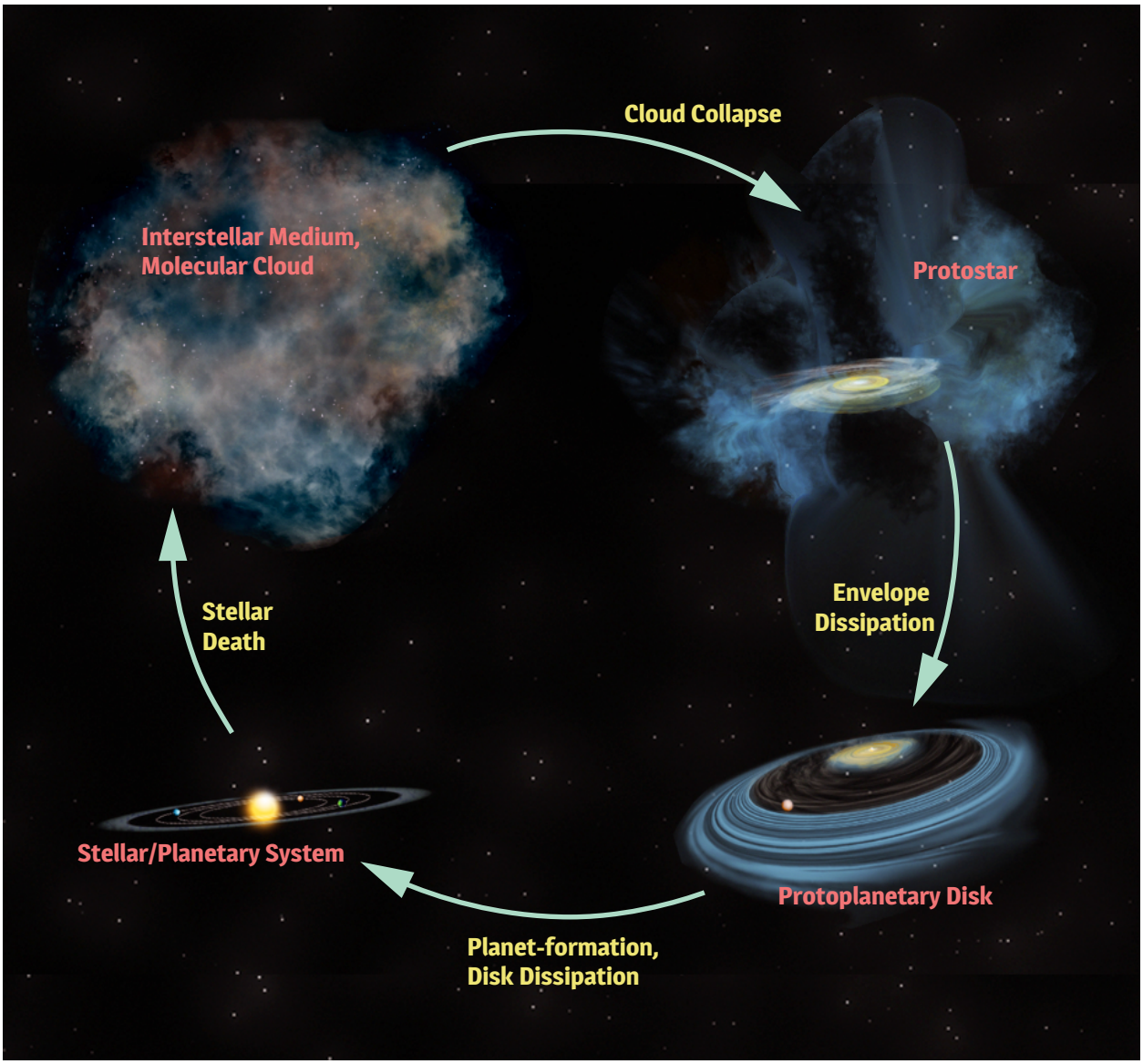

Figure 1.2 Illustration of the cycle of star-formation. The dense molecular interstellar medium (top-left) collapses to form a young protostar, embedded in its envelope (top-right), which dissipates to leave a star/disk system (bottom-right), from which the planets form (bottom-left). The cycle continues with each generation of stars, which replenishes the interstellar medium with heavy elements, the future building blocks of planets.

are self-gravitating and are thought to be partially supported by internal magnetic pressure and/or turbulence. These lower density molecular cloud complexes were known to contain

denser substructure, with subunits termed "clumps" ($n_{\rm H_2} \sim 10^2 - 10^4$ cm^{-3}) and at even smaller scales, "cores" ($n_{\rm H_2} \sim 10^4 - 10^6$ cm^{-3}; see review of *Williams et al.*, 2000). However, relatively recent results from *Herschel* has revealed an even more complex structure, where it appears that molecular clouds ubiquitously are broken up into intricate filamentary structure (e.g., *Ward-Thompson et al.*, 2010). Filaments have long been recognized; i.e., the "integral shaped" filament of Orion, among others (*Barnard*, 1907; *Schneider and Elmegreen*, 1979; *Myers*, 2009); yet *Herschel* revealed filaments to be a common feature of the star formation process (see also *André et al.*, 2014, for a discussion of filament properties). Embedded within filaments are dense cores with typical densities of 10^5 cm^{-3} and lifetimes of $\sim 10^5 - 10^6$ years (*Lee and Myers*, 1999; *Jessop and Ward-Thompson*, 2000). Eventually these dense structures, "pre-stellar cores," with typical size scales of $0.01 - 0.1$ pc, will collapse, signaling the onset of future star (or multiple star) formation.

Prior to the collapse process, the core carries some degree of initial rotation. This rotation, in concert with the need to conserve angular momentum, causes the collapsing system to naturally form a disk. Material infalling along the rotation axis lands more-or-less directly onto the center of the system, i.e., the stellar position, while material with more angular momentum ends up at larger disk radii. During the earliest phases, the system contains a central protostar of mass 0.1-1 $M_\odot$ that typically drives a high-powered jet, a natal disk/toroidal structure with 0.01-0.1 $M_\odot$ whose motions are simultaneously driven by rotation and infall, and a large scale envelope, approximately 0.1 pc in size. The envelope continues to fall on the disk, fueling intermittent rapid accretion of gas onto the central protostar ($\dot{M} = 10^{-4} - 10^{-6}$ $M_\odot$ year^{-1}; *Zhu et al.*, 2010; *Kratter et al.*, 2010), leveling to $\dot{M} \sim 10^{-7}$ $M_\odot$ year^{-1} at "quiescence." The protostellar phase (Figure 1.2, top-right) is expected to last between 10^5 to 10^6 years (see review of *Dunham et al.*, 2014, and references therein), at which point the envelope is dissipated and a young star (or stars) and a circumstellar disk remain.

By this point, the star has built up its mass in near entirety, and the remaining proto-

planetary disk (Figure 1.2, bottom-right) contains between 1-10% of the mass of the parent star. For a solar mass star, the disk thus contains enough material to form up to 10-100 Jupiters, in competition with various disk mass loss processes such as accretion or photo-evaporative flows/winds. The median inner disk lifetime as traced by infrared dust measurements typically spans a few Myr (*Skrutskie et al.*, 1990; *Cieza et al.*, 2007; *Hernández et al.*, 2007), while the cold molecular outer disk may have lifetimes of 1-10 Myr (*Mamajek*, 2009). The discrepancy has been referred to as the two-time-scale problem and may indicate that the disk clears out from the inside-out, e.g., by stellar photoevaporation (see discussion of *Williams and Cieza*, 2011a). Nonetheless, these timescales set the clock for giant planet formation, whether via bottom-up channels such as the core accretion scenario (*Goldreich and Ward*, 1973), or top-down through gravitational collapse of an unstable protoplanetary disk (*Cameron*, 1978; *Boss*, 1997). The end of the isolated protoplanetary disk phase is marked by the cessation of accretion onto the star and the dispersal of the molecular gas. It should be noted that terrestrial planet formation likely continues on even after the dispersal of the gas disk, where terrestrial planets continue to "feed" from the planetesimal disk for many tens of Myr post dispersal (see discussion in *Morbidelli et al.*, 2012).

Then begins the onset of the main sequence phase, the longest stretch of a solar-mass star's lifetime (Figure 1.2, bottom-left). At the end of the main sequence, depending on the stellar mass and its companionship (multiplicity), the dying star will replenish the ISM by shedding its envelope, thus enriching the next generation of star formation. For more massive stars with shorter evolution times less than the lifetime of the GMC complex, the lifecycle of such stars may even fundamentally trigger the onset of another generation of star-formation through interactions with the cloud (*Blaauw*, 1964; *Elmegreen and Lada*, 1977; *Blaauw*, 1991).

1.3 Physical Properties and Disk Structure

The physical environment of protoplanetary disks is highly complex and in-homogenous (see the reviews of *Bergin et al.*, 2007; *Calvet and D'Alessio*, 2011; *Dutrey et al.*, 2014). Typical densities span between 10^{15} cm^{-3} at the inner disk midplane (the geometrical center of the disk in the orbital plane) to 10^{5} cm^{-3} in the outer disk surface layers, ten orders of magnitude in variation. Temperatures range from 10 K in the outer disk midplane to thousands of Kelvin at the super-heated tenuous disk surface or at the inner edge of the disk itself itself where even dust is sublimated (*D'Alessio et al.*, 1998). In addition to the optical heating irradiation, the central star emits high energy photons at both ultraviolet (*Yang et al.*, 2012, and references therein) and X-ray wavelengths (e.g., *Ku and Chanan*, 1979; *Feigelson and Decampli*, 1981a; *Montmerle et al.*, 1983), which induce strong ionization gradients from the surface down to the shielded midplane (e.g., *Glassgold et al.*, 1997; *Igea and Glassgold*, 1999). These factors and others directly influence the formation process and final properties of young planets, and combined advances in both theory and observations have significantly improved our characterization of this dynamic environment. In the present section we summarize recent results on disk structure. Figure 1.3 illustrates the important physical processes discussed in more detail below.

1.3.1 Disk Thermal Structure

Disks have thermal gradients in both the radial and vertical direction, which are broadly determined by stellar properties, dust properties and chemical structure. The star directly heats the upper layers of the circumstellar dust, which re-radiate in the infrared and indirectly heat the otherwise optically-shielded dust disk deeper in (*Calvet et al.*, 1991; *D'Alessio et al.*, 1998). Near the midplane, the gas thermal properties are fully coupled with that of the dust where densities are high enough for efficient collisional transfer of energy. In terms of visual extinction, these regions typically have extremely high dust attenuation, $A_V \geq 10$ (*Gorti and Hollenbach*, 2008). Moving upward, closer to the disk surface, between $A_V = 1 - 10$,

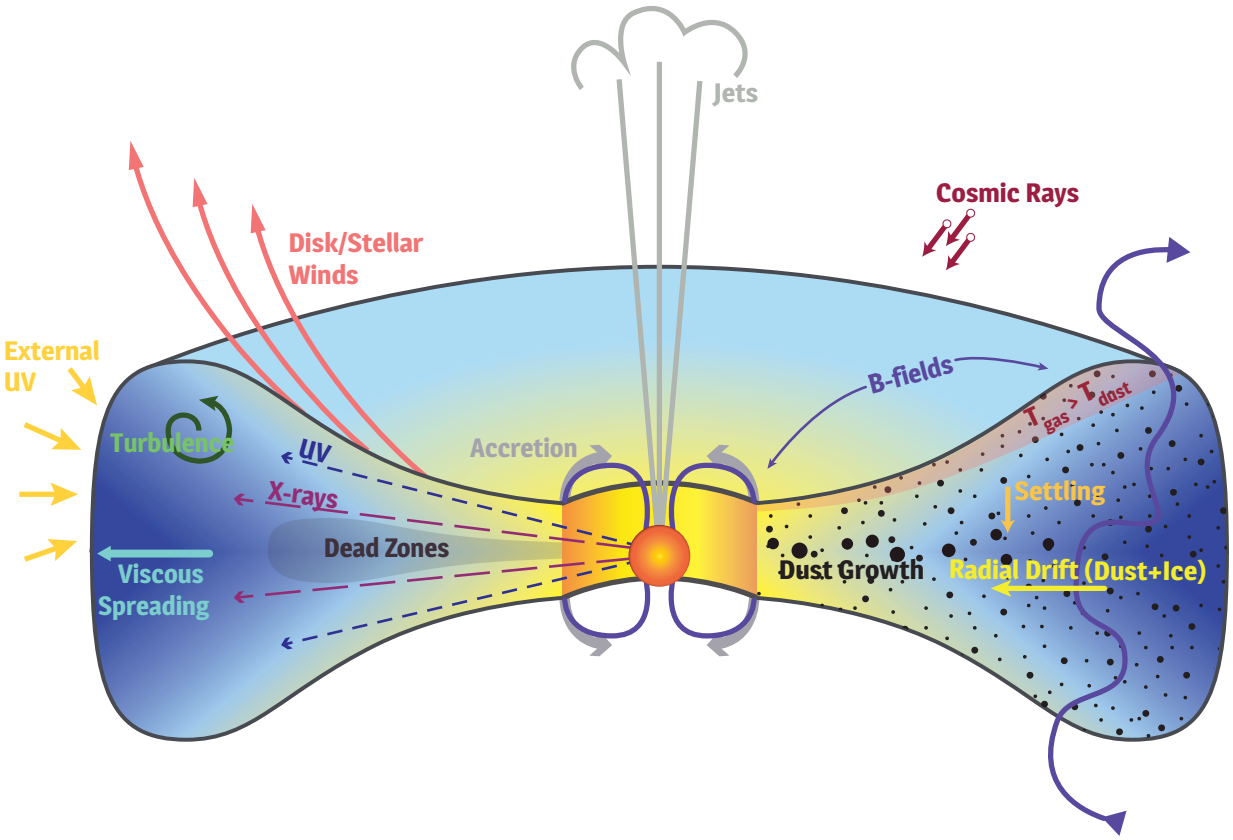

Figure 1.3 Schematic of important disk physical processes. The left half emphasizes stellar radiation processes including stellar UV and X-rays and kinematic processes, including accretion and winds/jets. Regions shielded from X-ray irradiation have low ion-fractions and may sustain a turbulence-free "dead zone." External UV from the interstellar radiation field is important, especially in star clusters. On the right, dust processes are emphasized, including dust growth via coagulation, the inward radial drift due to gas drag, and the depletion of dust grains from the surface due to settling. Magnetic fields play a role in the inner disk, funneling accretion onto the star and in the outer disk as primordial fields frozen in from the initial formation of the disk, twisted due to bulk gas disk motions. The upper layers of the disk are super heated over local dust temperatures due to high radiation levels from the star. High energy galactic protons, or cosmic rays may also bombard the disk, enhancing ionization, though their distribution is strongly influenced by magnetic fields and winds.

high energy stellar UV and X-ray photons penetrate the disk, providing additional heating through energetic electrons produced by the photoelectric effect, resulting in elevated gas temperatures (e.g., *Glassgold et al.*, 2004; *Woitke et al.*, 2009; *Bruderer et al.*, 2012). The magnitude of this effect corresponds to a $\sim$ 25% increase in gas temperature over dust

temperature at an $A_V \sim 1$ based on the comprehensive thermochemical models of *Gorti and Hollenbach* (2008). According to the same models, above $A_V > 1$, in the low density upper layers of the disk, gas and dust collisions are increasingly less frequent and the dominant gas coolant is instead emission from lines, primarily [O I] and CO, at which point the gas temperatures exceed the dust temperatures by an order of magnitude or more and are fully decoupled.

Another important source of heating at the inner disk is accretion. At radii $R < 1$ AU, the mechanical transfer of material inward through accretion provides an additional source of energy that goes into heating the disk, increasing the midplane temperature by a factor of ~ 5 depending upon dust properties for typical accretion rates of $\dot{M} = 10^{-8}$ $M_\odot$ year^{-1} (e.g., *D'Alessio et al.*, 1998; *Espaillat*, 2009, PhD Thesis). In this instance the midplane temperature in the inner disk can be greater than that of the directly stellar-irradiated surface for accretion rates exceeding $\dot{M} \geq 10^{-8}$ $M_\odot$ year^{-1}.

1.3.2 High Energy Processes and Ionization

High energy stellar photons also play an important role in both the disk physical and chemical structure. T Tauri stars exhibit a strong far-UV (FUV) excess arising from the accretion shock on the stellar surface where material is being funneled from the disk onto the star along magnetic field lines (e.g., *Uchida and Shibata*, 1985; *Shu et al.*, 1994; *Calvet et al.*, 2004). The FUV radiation field sets the ionization structure in the upper layers of the disk, where species such as atomic carbon and sulfur, with their low ionization potential, are readily ionized. An important feature of the stellar FUV spectrum in T Tauri stars is strong, broad Lyman-α emission, which accounts for 80-90% of the total FUV luminosity (*Herczeg et al.*, 2002, 2004). Lyman-α has unique scattering properties, mainly that it undergoes resonant scattering off atomic hydrogen atoms in the surface layers of the disk, which redistributes the radiation isotropically, sending some fraction of photons directly into the disk (*Bethell and Bergin*, 2011a), greatly increasing their penetration power.

In addition to the central star, the interstellar radiation field (ISRF) provides an important isotropic UV source incident on the disk, where the typical strength of the ISRF as measured in G_0 is 1 to 1.7 Habing which is equal to 1.2×10^{-4} erg cm^{-2} s^{-1} sr^{-1}. For comparison, the stellar UV at the disk surface at a distance of 100 AU is typically a few hundred Habing (*Bergin et al.*, 2004), and thus the ISRF is expected to be mainly important well beyond these radii for isolated systems. However, in cluster environments, especially massive star-forming regions where the ISRF can be elevated to hundreds or thousands of Habing (*Fatuzzo and Adams*, 2008), the ISRF plays a much larger role.

While UV photons are a powerful source of ionization, they are extremely well attenuated by small dust grains and are largely restricted to the disk surface. As a result, the dense gas ionization is dominated primarily by stellar X-rays, cosmic rays (CRs) and the decay of short-lived radionuclides (SLRs). Stellar X-ray radiation provides a central ionizing source that, while powerful, is obstructed by the high density inner disk, with relatively modest attenuation depths corresponding to gas column densities of $\Sigma_{\rm XR} \sim 0.01$ g cm^{-2} for a mixture of gas and dust of 100:1 (*Bethell and Bergin*, 2011b). For comparison, CRs permeate the galaxy mostly isotropically, giving them an advantageous incidence angle for outer disk ionization. CRs additionally have a considerably larger stopping distance than X-rays, where $\Sigma_{\rm CR} \sim 100$ g cm^{-2} (*Umebayashi and Nakano*, 1981). However, they are efficiently stopped by stellar winds and/or background magnetic fields. As a result, circumstellar CR particle fluxes may be reduced by $> 1-5$ orders of magnitude below the interstellar rate (see Chapter 3 of this thesis). SLRs, known to be over-abundant in the young Solar System, may contribute to ionization by radiating from the midplane outward; however, their exact nature is highly uncertain, with unknown "typical" abundances and inherent time evolution. In addition to age and abundance, a large fraction of ionizing SLR decay-products are expected to escape from the tenuous outer disk prior to depositing all of their energy (see Chapter 4 of this thesis). Consequently there is significant ionization structure throughout the disk, which has important consequences for the chemistry of the bulk molecular disk (see Section 1.4

and Chapter 6 of this thesis).

1.3.3 Gas Kinematics

The disk gas has simultaneously a very complex and a very simple velocity structure. The bulk disk motion is simple, where the gas follows roughly Keplerian orbits around the star. Observations of spectrally resolved molecular emission lines feature this simple velocity field through typical "double-horned" profiles or butterfly patterns when the emission is spatially resolved on the sky (e.g., *Beckwith and Sargent*, 1993). However, beyond this simple bulk motion the velocity field becomes more complicated. First, the gas velocities are not exactly Keplerian. The gas in the disk is partially pressure supported, and, as a result, the disk is expected to orbit at slightly sub-Keplerian speeds. Future observations at extremely high spectral resolution with ALMA will be able to measure these effects directly (*Rosenfeld et al.*, 2013). Disk accretion physically transports material from the outer disk inward, where the typical mass flow rate is $\dot{M} \sim 10^{-9}$–10^{-8} $M_\odot$ year^{-1} (*Gullbring et al.*, 1998; *Hartmann et al.*, 1998; *Ingleby et al.*, 2013). Simultaneously, to conserve angular momentum, the inward accretion-driven transport must be compensated by outward motions, either by viscous spreading (*Hartmann et al.*, 1998; *Hughes et al.*, 2008), ejecting winds from the surface of the disk, or launching a jet (e.g., *Hartigan et al.*, 1995). Compounded on the bulk orbital motion and inward/outward motions, there will also be some degree of disk turbulence mixing the material on small scales. It is unclear what role mixing plays at present. Sensitive, high spectral resolution observations with the SMA of the face-on TW Hya disk indicate that turbulent motions in the vertical direction are small, $v_{\rm turb} < 50$ m s^{-1} (*Hughes et al.*, 2008). Increasingly sensitive observations with ALMA with tracers of multiple vertical layers will shed additional light on this puzzle. However, some amount of small grains undoubtedly are maintained at high disk latitudes as evidenced by the presence of 10μm and 20μm silicate features in emission, and, with a relatively short settling times ($\sim 10^4$ years for 0.1 μm-sized grains to fall below $\tau = 1$; *Dullemond and Dominik*, 2004), the presence of these grains

will require some type of turbulent stirring (*Dullemond and Dominik*, 2004; *Dullemond and Dominik*, 2005) or buoyant magnetic forces (*Turner et al.*, 2014a) to maintain their present vertical distribution.

1.3.4 The Dusty Disk

While dust constitutes just 1% of the overall disk mass, it forms the foundation of the terrestrial planets and gas giant cores. Initially the dust that fills GMCs are typically small, sub-micron sized grains, primarily silicate and carbonaceous in composition, which is the starting condition of the dusty component of the disk beyond $\sim$ 1 AU. The high densities present in disks facilitate rapid dust growth, growing from micron to millimeter-sized dust grains. These dust grains are no longer easily lofted by turbulent motions in the disk as compared to the smaller particles, and so they naturally settle-out to the midplane (*Weidenschilling and Cuzzi*, 1993; *D'Alessio et al.*, 2006). The observation of disks with depleted dust in the surface layers naturally bear out this expectation (*Furlan et al.*, 2006). The settled grains continue to grow at the midplane; however, they experience significant barriers on their way to building planets. One such barrier is the fragmentation barrier, where centimeter sized bodies and larger are theoretically expected to fragment upon collision (*Brauer et al.*, 2008). In addition, meter-sized bodies experience strong headwinds against the gas, which moves at slightly sub-Keplerian speeds (with smaller bodies affected at larger radial distances). The latter process results in a phenomenon known as radial drift, where dust moves inward, and if unimpeded, will fall onto the central star itself (*Weidenschilling*, 1977; *Nakagawa et al.*, 1986). This process is rapid, and thus provides a timing challenge for the formation of planets if it is not physically overcome by, e.g., pressure bumps halting inward migration (see also the review by *Testi et al.*, 2014). With high spatial resolutions afforded by interferometers such as the Submillimeter Array (SMA), Plateau de Burre Interferometer (PdBI) and most recently the Atacama Large Millimeter/Submillimeter Array (ALMA), the hallmarks of radial drift are now being directly observed as strong inner concentrations of

large millimeter-sized grains relative to the small micron-sized grains and gas. For the case of our nearest disk neighbor, TW Hya, the gas and small grains trace over 200 AU radial scales, while the large mm-grains only extend to a 60 AU radius (*Andrews et al.*, 2012).

1.4 Disk Volatile Composition and Chemistry

The composition of disks is 99% gas by mass, primarily in the form of H_2 and helium. At typical disk densities (pressures), H_2 and helium do not freeze-out onto cold dust grains until temperatures of $\sim$ 7 K (*Allamandola et al.*, 1993) and $\sim$ 3 K (*Tielens and Hagen*, 1982), respectively, and thus are both in the gas phase throughout many hundreds of AU. Of the more trace constituents, oxygen is mainly in H_2O ice, with some in CO. Nitrogen is likely primarily in N_2, however like H_2, this molecule lacks a permanent dipole moment and is correspondingly not directly observable for the bulk disk reservoir, and thus the nitrogen reservoir is less well constrained. Carbon is expected to be mainly in CO – at least in the very early stages of disk evolution – though it is quickly chemically converted into other species over the disk lifetime, including CO_2, H_2CO, CH_3OH and organics (*Aikawa et al.*, 1996; *Garrod and Pauly*, 2011; *Bergin et al.*, 2014). Further evidence of such processing exists in at least one system where there is measured substantial CO depletion in warm gas (*Favre et al.*, 2013, Chapter 7) supported by an independent gas mass measurement (*Bergin et al.*, 2013). Regarding sulfur and even rarer species, the total volatile abundances are unknown, where volatile sulfur in particular is known to be already depleted in the dense ISM, perhaps converted into a "sulfur-rich residuum" (*Grim and Greenberg*, 1987; *Wakelam et al.*, 2004; *Chen et al.*, 2015). Detailed observations of increasingly rarified species with ALMA in the coming years will provide a necessary more complete census of disk chemistry.

Figure 1.4 highlights major features of the overall chemical structure of disks. The left-hand side of the figure outlines the typical distribution of the major "heavy" volatile reservoirs (excluding H_2 and helium). The structure is much like a wedge-shaped photon-dissociated region, or PDR, where the extinction of radiation sets the layered composition of

the disk (see *Bergin et al.*, 2007, for a review). The surface layers are dominated by atomic ions, mainly C^+ given its low ionization potential, though other ions exist via subsequent charge exchange. As A_V approaches $\sim$ 1 the chemistry quickly transitions to primarily neutrals and molecules, where ion recombination becomes more efficient and molecules are shielded from the photodissociating stellar radiation. The layer where CO is present, the so-called "warm molecular layer" (*Aikawa et al.*, 2002) is also coincident with other abundant, observable molecular species including HCN, CS, H_2CO and HCO^+. CO, N_2 and H_2 have much thicker "molecular layers" owing to fact that these species are dissociated via line processes rather than continuum photons. As a result these molecules "self-shield" and are able to substantially reduce the photodissociation rate with sufficient protective column density of itself (e.g., *van Dishoeck and Black*, 1988; *Lee et al.*, 1996; *Li et al.*, 2013). Deeper in the disk, well below the UV photodissociation layer, the overall temperatures steadily drop and eventually the chemistry of the disk becomes dominated by the adsorption of volatiles onto dust grains as ices.

On the right hand side of Figure 1.4 we highlight the expected distribution of the phases of water in disks. Water, with its relatively high binding energy, is in the ice-phase for the majority of the disk where temperatures are well below its desorption temperature of $\sim$ 100 K. Only inside of $\sim$ 1 AU is water able to sublimate and become present as vapor in abundance, confirmed by bright water line observations with *Spitzer* (e.g. *Carr and Najita*, 2008). Water vapor is also observed well beyond 1 AU, and its presence is attributed to the UV photodesorption of icy dust grains near the surface of the cold outer disk (*Hogerheijde et al.*, 2011). UV photodesorption is only one type of non-thermal desorption, however. X-ray photons and cosmic rays can induce spot heating of dust grains (*Leger et al.*, 1985; *Najita et al.*, 2001), locally sublimating ices in regions deeper in the disk than UV penetrates, especially for species with desorption temperatures below 70 K (*Bringa and Johnson*, 2004). All of these non-thermal desorption mechanisms are able to sustain a low level of gas-phase molecules even in the regime where freeze-out is expected to dominate, thus providing a

glimpse into the composition of ices.

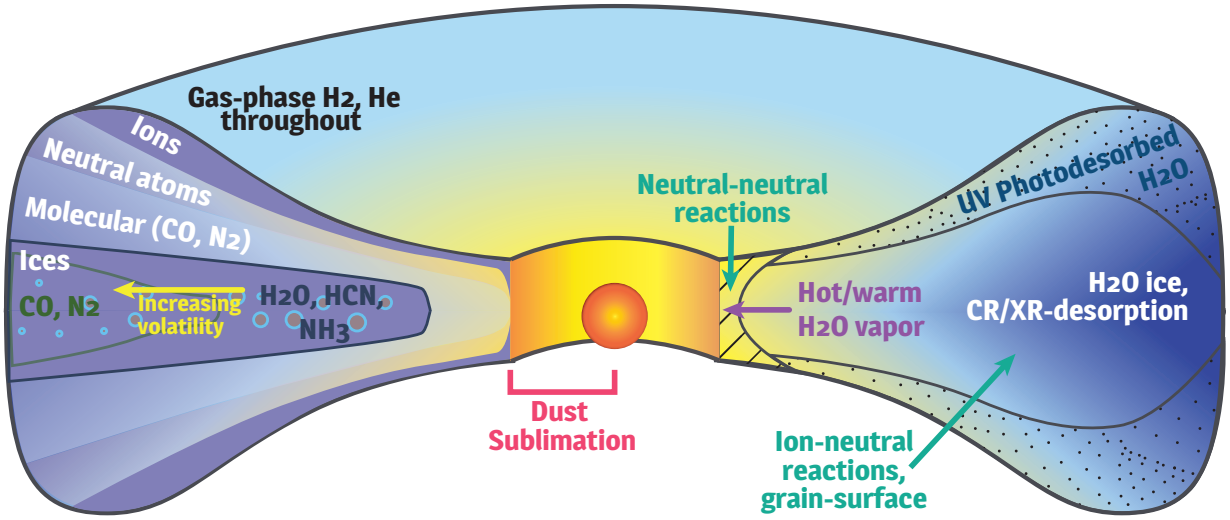

Figure 1.4 Left: Stratification of the chemical structure for species other than H_2 and helium. Right: Phases of water and the primary physical cause of phase changes locally. A similar plot can be made for all species, where the relative locations shift based upon the properties of the molecule in question.

Even in the presence of non-thermal desorption mechanisms, thermal desorption/adsorption by-and-large dominates the disk chemical structure, especially in the midplane. Due to disks' decreasing temperature with radius, at certain radial locations the dust temperature crosses the condensation temperature of different molecular species, such as H_2O, CO, and CH_4. At these locations, the molecule under goes a transition from being primarily gas to primarily ice, and thus these points are termed "snow lines" or "frost lines." In reality, the combination of the radial temperature gradient (decreasing with radius) and vertical temperature gradient (decreasing with depth) result in a "snow surface," which was recently directly imaged by *Rosenfeld et al.* (2013) using extremely high spectral and spatial ALMA science verification data of the HD163296 system. Snow lines are of particular interest in the context of planet formation as these locations naturally cause a dramatic increase in

the solid-mass surface density through the addition of ices, especially at the H_2O and CO snow lines. The enhanced surface density of solids is thought to facilitate more efficient giant planet formation (*Stevenson and Lunine*, 1988; *Lecar et al.*, 2006).

In addition to the overall phase changes between solids and gas and photo-destruction and shielding, the disk also undergoes chemical reactions that lead to the formation (and destruction) of more complex species. *Henning and Semenov* (2013) provide a comprehensive overview of relevant chemical reactions in protoplanetary disks, and I will only outline the most important aspects. The chemistry of the disk can be generalized into inner disk chemistry, where the temperatures exceed hundreds of Kelvin, and outer disk chemistry, where temperatures are below 100 K. The inner disk is characterized by high densities and high temperatures, which together enable two-body (and perhaps three-body) neutral-neutral reactions to form more complex species, even if they are exceptionally endothermic. One such example is the direct formation of H_2O in the gas from $H_2 + OH \rightarrow H_2O + H$. At low temperatures as are present in the outer disk ($R > 1$ AU), this reaction is entirely inefficient, but in the inner disk it proceeds rapidly. The outer disk chemistry is markedly different. The most efficient reactive channels are ion-neutral reactions, which are rapid at low temperatures. Water, by comparison, forms in the gas starting with H_3^+, which reacts with oxygen or oxygen bearing species to form H_3O^+ that, upon recombination with electrons or negatively charged grains, forms water. The second important type of reaction for the outer disk are grain surface reactions. Simple species freeze-out onto the surface of cold dust grains, but are still somewhat mobile, and are able to hop across the surface (*Tielens and Hagen*, 1982; *Hasegawa et al.*, 1992a). When these simple species find a suitable reaction partner, they will bond to form a more complex species, with the excess energy of formation most frequently absorbed into the grain lattice, but for some small fraction of the time, 1-10%, desorbs the product itself, though these values are highly uncertain (*Garrod et al.*, 2007). Water will form as an ice by the sequential hydrogenation of oxygen atoms on dust grains in this way. Similarly NH_3, CH_4 and CH_3OH can be formed by hydrogenation of N, C and CO. These

processes are only efficient at low temperatures, however ($T < 50$ K), when the intermediate products are able to spend a sufficient amount of time on grains to be fully hydrogenated.

Isotopes are also an important facet of disk chemistry. The self-shielding effects described above for CO and N_2 manifest themselves in the isotopes through selective self-shielding, where the less abundant isotopologues are unable to self-shield until deeper into the disk, and as a consequence the upper layers of the disk can have abundant CO with very low amounts of ^{13}CO (70× less abundant) and C^{18}O (500× less abundant) due to these effects (*van Dishoeck and Black*, 1988; *Visser et al.*, 2009a). As described in *Lyons and Young* (2005), selective destruction of the isotope-bearing molecules releases these into the gas to participate in the chemistry, thereby elevating the ^{18}O/^{16}O ratios in other species (see also *Heays et al.*, 2014, for the case of N_2). The alteration of isotope ratios, or fractionation, can also occur chemically. The difference in mass between the isotopes can lead to mass-dependent fractionation effects as the lighter isotope moves faster and forms weaker bonds. The changes are more substantial for isotopes with larger mass differences. For the case of deuterium, i.e., hydrogen with an additional neutron, the mass difference is the largest, a factor of two. Molecules formed with a deuterium atom substituted for hydrogen, such as HDO, are more energetically favorable (i.e., have a lower zero point energy) than the lighter isotope. Thus at low temperatures, where the energy difference between the lighter and heavier isotope is comparable or greater than that of the environment, reactions will tend to over produce deuterated isotopes. The same will happen for isotopes of oxygen and carbon but to a far lesser extent given the small mass difference. The application to deuterium fractionation in water is discussed in more detail in Chapter 8.

One of the biggest questions in our understanding of disk chemistry is the question of primordial inheritance versus disk chemical processing. As outlined in Section 1.2, the star-disk system forms from dense concentrations within a giant, cold molecular cloud. The molecular core is already quite chemically rich as determined from observations of the local environment of young protostars, where the star provides a background candle revealing

an environment rich in water, organics, and many simple molecular species in absorption (e.g., *Boogert et al.*, 2000; *Boogert et al.*, 2002). Observationally, it is unknown how much of this chemically rich material survives the formation of a star and disk. Theoretical models presented in *Visser et al.* (2009b) demonstrate that during the initial collapse of the rotating cloud, parcels of infalling material that come to rest at beyond an orbital radius of 20 AU (their standard model) stay below temperatures of 100 K for their entire trajectory, implying that their water ice remains adsorbed on grains beyond this radius. CO ice, on the other hand, with its far lower binding energy, sublimates at least once during its trajectory inward at all radii inside of $R < 2000$ AU. These findings imply that species with relatively high freeze-out temperatures, higher than $\gtrsim$ 60 K, were delivered in a pristine state beyond $R > 50$ AU. Within this range, potential inherited species include SO_2, CH_3OH, CH_3CN and potentially NH_3. More volatile ices like CO can be delivered as well, however they would need to be trapped within the water ice matrix (*Sandford and Allamandola*, 1990, 1993; *Ayotte et al.*, 2001; *Horimoto et al.*, 2002; *Collings et al.*, 2003, 2004). How primordial ices survive beyond this stage, however, will fundamentally depend upon mixing and accretion, and the rate of chemical reprocessing in the disk.

1.5 Observational Characterization of the Gas Reservoir

Beyond molecular accounting and measuring abundances, molecular emission is a powerful tool in determining physical conditions in the disk. It was recognized early on that symmetric rotors provide interstellar "thermometers" (*Solomon et al.*, 1973; *Ho and Townes*, 1983). Multiple lines within the same K-ladder of symmetric rotors such as CH_3CN, NH_3 and CH_3CCH are readily observable simultaneously, and by using Boltzmann plots, the temperature is determined from the slope of the log of the upper state column density versus upper state energy. In high density environments such as disks, other molecular species can be used as temperature probes by measuring multiple lines of the same species with large upper state energy differences. The density requirement is set by the critical density of a par-

ticular line, which corresponds to the ratio of the spontaneous de-excitation versus collisional de-excitation. For environments with densities exceeding the critical density of a particular line, the rotational level population will be set by the Boltzmann distribution (and is said to be in local-thermodynamic equilibrium, or LTE) and thus is set by the local temperature. By measuring multiple rotational lines of optically thin tracers, such as $C^{18}O$ in the $J = 6-5$ and $J = 3 - 2$ lines, the line ratio should encode temperature information. However, this technique is somewhat less efficient than using symmetric rotors given that these lines must be observed individually due to the large frequency spacing between them and optical depth effects. Table 1.1 provides critical densities for commonly observed lines in disks as well as important water lines. HCN, CO, N_2H^+ and many other simple molecules have low critical densities compared to typical disk densities, which typically exceed 10^8 cm^{-3}. Water lines, on the other hand, have relatively high critical densities, and will only be in LTE in the inner dense disk, or the outer disk if the photodesorbed layer originates from deeper in than the surface. Given the wide range of critical densities across observable lines, local density information will also be folded into the disk emission signatures. By studying multiple lines with very different critical densities, one can also potentially constrain the local density of the emitting medium.

Molecule	Line	Frequency	Critical Density
CO	$3-2$	345.796 GHz	1.1×10^4 cm^{-3}
N_2H^+	$4-3$	372.673 GHz	2.2×10^6 cm^{-3}
HCO^+	$3-2$	267.558 GHz	1.1×10^6 cm^{-3}
o-H_2CO	$5_{15}-4_{14}$	351.769 GHz	2.2×10^6 cm^{-3}
HCN	$4-3$	354.505 GHz	1.1×10^7 cm^{-3}
o-H_2O	$1_{10}-1_{01}$	556.936 GHz	7.3×10^7 cm^{-3}
p-H_2O	$1_{11}-0_{00}$	1113.343 GHz	3.2×10^8 cm^{-3}
o-H_2O	$3_{12}-2_{21}$	1153.127 GHz	2.8×10^8 cm^{-3}
o-H_2O	$3_{12}-3_{03}$	1097.365 GHz	5.0×10^9 cm^{-3}

Table 1.1 Critical densities for lines of interest at $T = 50$ K.

Beyond density and temperature, molecular emission carries substantial information about other physical parameters of the system. High spectral and spatial resolution will

provide kinematic information in the disk, which has been used to but limits on disk turbulence (*Hughes et al.*, 2011) and dynamical information, including discovering a warp in the inner disk of TW Hya (*Rosenfeld et al.*, 2012). The relative abundances of ions compared to neutrals provides critical information about the high energy ionizing radiation incident on the disk (see Chapter 5). High spatial resolution observations can furthermore isolate the location of various "snow lines" in the disk, providing information simultaneously about temperature and molecular properties, including binding energies (with independent determinations of the dust temperature) and information about the ice-substrate (*Collings et al.*, 2004). Molecules with hyperfine structure, such as N_2H^+, can directly elucidate opacity information for the species of interest given the wide range of line intensities across the hyperfine components. Thus molecular emission is a powerful tool to understand a wide range of aspects regarding the physical nature of the major mass reservoir in protoplanetary disks.

One of the strongest observational limitations in determining chemical abundances from molecular emission is the general lack of a direct mass tracer. Submillimeter and millimeter dust emission is often used to measure mass, assuming a dust-to-gas mass conversion factor of 1:100 (e.g., *Adams et al.*, 1990). Regarding gas tracers, CO is the second most abundant molecule after H_2, and correspondingly is a commonly used tracer of warm gas mass – i.e., without dust (e.g., *van Zadelhoff et al.*, 2001; *Thi et al.*, 2001). By assuming an abundance conversion from CO to H_2, typically $1{:}10^4$ in gas above 17 K (the freeze-out temperature of CO; *Öberg et al.*, 2005), one can obtain a gas mass. However, CO unlike H_2 undergoes rapid freeze-out at temperatures below 17 K, and thus will inherently miss cold mass in the outer disk (see discussion of *van Zadelhoff et al.*, 2001). In addition to freeze-out related depletion, CO's active role in the chemistry can cause it to become similarly chemically depleted as well, especially in regions above 17 K (*Aikawa et al.*, 1996; *Bergin et al.*, 2014). Thus the CO-derived mass provides mainly a lower limit, and indeed, CO-derived masses are typically far smaller than those derived from submillimeter dust measurements (e.g., *Thi et al.*, 2001; *Bergin et al.*, 2013, and Chapter 7 of this thesis). For at least one disk

system, the *Herschel Space Observatory* detected the HD isotopologue of H_2. HD indicated a far larger mass in TW Hya's gas disk than derived from CO, and one more in line with that derived by the dust (*Bergin et al.*, 2013), not inconsistent with an interstellar gas-to-dust mass ratio of 100. Based upon this important constraint, TW Hya is the only disk where we can measure the CO abundance, where *Favre et al.* (2013) found it was $1-2$ orders of magnitude lower in the warm gas than expected. However, it should be noted that CO selective self-shielding discussed above can reduce the apparent abundance of CO and needs to be considered via multi-isotopologue observations when measuring CO abundances (*Miotello et al.*, 2014). These considerations emphasize the importance of HD as a mass tracer. Furthermore, it stresses the importance of relative abundance measurements rather than absolute values when studying these actively chemically evolving systems.

1.6 Overview of the Dissertation

In this thesis I present a theoretical and observational approach to characterize aspects of planet detection in disks and physical/chemical properties of the disk itself. The thesis has two general parts described in more detail below. The first half (Chapters 2 and 3) is concerned with identifying signatures of planet formation, first through a theoretical chemical study of disks with large inner holes cleared out by a nascent planetary system and second via local sublimation of ices near a singular warm embedded planet. The second part of this thesis (Chapters 4-8) is concerned with characterizing the contribution of different disk ionizing sources, how these are observationally distinguished, and how they impact the chemistry at large.

In Chapter 2, we explore models of protoplanetary disks which contain a large inner cavity approximately the size of Pluto's orbit. Observations of similar cavities have been attributed to either inner disk photoevaporation or clearing by a multiple planet system. We examine how the removal of the inner disk and the presence of the gap changes the disk's thermal structure and as a result, the chemical structure of the outer disk. The addition of

direct stellar heating at the midplane provides a unique opportunity to study an otherwise hidden reservoir of ices, freshly sublimated by direct stellar irradiation.

In Chapter 3, we move toward the more localized phenomenon of planet formation, where young, self-luminous gas giants embedded in the cold molecular disk are predicted to produce observable signatures that will be detectable with ALMA. The heating due to the planet will locally sublimate ices in the midplane that are otherwise fully frozen-out onto dust grains, creating a unique gas phase signature. Due to the rapid timescales for freeze-out and desorption, the gas-phase enhancement near the planet will follow the planet closely, which offers the possibility of repeat measurements to confirm orbital motion.

In Chapter 4, we transition to topics relating to the high energy radiation field incident on disks. Given the importance of ion-neutral chemistry outlined above, it has long been assumed that the active chemistry of the cold outer disk is powered by cosmic ray ionization of H_2. However, in the context of our own solar system, it has long been recognized that cosmic rays are efficiently deflected by winds and/or magnetic fields. The possibility of a cosmic ray starved environment has been considered in previous work (*Gammie*, 1996; *Turner and Drake*, 2009), however we build upon this and examine varying degrees of modulated CR flux as would be expected if CRs are driven out by winds or fields. We include self-consistent energy propagation and calculate the ionization rate as a function of depth. We estimate disk ionization fractions, and based upon this calculation, estimate the size of the region in the disk where the ionization fraction is low enough that it becomes decoupled from any type of magnetic turbulence. These regions, termed dead zones (*Gammie*, 1996), are posited as favorable for planet growth (e.g., *Matsumura and Pudritz*, 2006). We find that the size of the dead zone is extremely sensitive to the assumed cosmic ray flux and its distribution.

In Chapter 5, motivated by our work on CR ionization, we study the next most important ionizing source for the midplane, the decay of short lived radionuclides. The most important contributors are ^{26}Al, ^{60}Fe and ^{36}Cl. Each of these species has different daughter products, each of which has different propagation depths. Previous work had taken into account the

differing energy range of daughter products produced (e.g., *Umebayashi and Nakano*, 1981; *Finocchi and Gail*, 1997; *Umebayashi and Nakano*, 2009; *Umebayashi et al.*, 2013), however no previous work had included the energy losses by the escape of decay products, including β particles and γ-rays. Losses substantially reduce the energy available for disk ionization, and are an important factor when considering the overall ionization state of the disk.

In Chapter 6, we combine our knowledge of CR and SLR ionization with an expanded treatment of X-ray ionization, and examine how the chemical abundances in disks are (or are not) sensitive to various ionizing agents. The motivating factor of this work is to determine how sensitive ALMA observations will be in the future to changes in the ionization rate. We find that HCO^+ isotopologue emission is mainly sensitive to stellar X-rays, while N_2H^+ traces both cosmic ray and X-ray ionization. Furthermore, by taking into account time-decay in the short-lived radionuclide ionization rate, we find that the SLR rate becomes negligible at a few millions years, and thus the disks we observe today will have mainly X-ray and also cosmic ray driven ionization structures when the latter are present.

In Chapter 7, we apply the results of the theoretical study presented in Chapter 6 to the case of the nearest protoplanetary disk, TW Hya. Combining new observations taken with the SMA as part of my PhD with archival observations and ALMA science verification observations, we put constraints on the disk ionization rate in addition to the CO abundance and nitrogen abundances. We find that in TW Hya, the maximum ionization rate in the midplane is $< 10^{-19}$ s^{-1} per H_2, two orders of magnitude below the expected rate due to CRs alone. Thus this is the first empirical determination of a low CR ionization rate in disks. The low rate can be due to one of two factors, a jumbled magnetic field in the local environment or within the disk itself (*Dolginov and Stepinski*, 1994), or repulsion by a stellar and/or disk wind. If the exclusion is wind-related, this would be the first direct evidence of an extra-solar heliosphere analogue, i.e., an "astrosphere" forming a bubble of reduced galactic CR flux around the disk. Whether disk magnetic fields are able to provide similar levels of exclusion remains to be tested. Taking our best fit model, we compute the size of

the dead zone in TW Hya and find that it coincides with a region of large grain concentration inside of 60 AU. In the light of previous theories which suggest dead zones promote grain growth, we may be seeing this process in action in the TW Hya disk.

Finally, in Chapter 8, we explore the chemical consequences of a lower than average cosmic ray rate. In a wide range of solar system bodies the measured D/H ratio in water is substantially elevated over the atomic D/H level, including in Earth's oceans. This feature is a signature of chemistry occurring in cold environments, as discussion in Section 1.4. The two possible environments where this may have occurred are in the interstellar molecular cloud core, prior to the Sun's formation, or in the outer disk. For the relevant reactions to proceed in the disk, a source of ionization is necessary. We explored models of the formation of water in the absence of CR ionization and discovered that the formation of excess HDO relative to H_2O is inhibited in the outer disk due to the inefficiency of both gas phase and grain surface reaction pathways. The direct implications of this work were that the disk is not a viable source for water in the solar system, and that a substantial fraction of ices must have been inherited from an earlier stage, prior to the Sun's birth. The results of this work have important broader implications for the chemistry of all planet-forming disks around Sun-like and low-mass stars, i.e., that a chemistry rich in the ingredients necessary for life is widely available to all protoplanetary disks.

CHAPTER II

Transition disk chemistry and future prospects with ALMA

2.1 Preface

The following work appears in the Astrophysical Journal Letters, Volume 743, L2, 6 pp. (2011). The work is co-authored by Edwin A. Bergin,[1] Thomas J. Bethell,[1] Nuria Calvet,[1] Jeffrey K. J. Fogel,[1] Jürgen Sauter,[2] and Sebastian Wolf.[2] The paper is copyright 2011, the American Astronomical Society, reproduced here under the non-exclusive right of republication granted by the AAS to the author(s) of the paper.

2.2 Abstract

We explore the chemical structure of a disk that contains a large central gap of R $\sim$ 45 AU, as is commonly seen in transitional disk systems. In our chemical model of a disk with a cleared inner void, the midplane becomes revealed to the central star so that it is directly irradiated. The midplane material at the truncation radius is exposed to reprocessed optical heating radiation, but opaque to the photo-dissociating ultraviolet, creating an environment

[1]Department of Astronomy, University of Michigan, 825 Dennison Building, 500 Church St, Ann Arbor, MI 48109

[2]Christian-Albrechts-Universität zu Kiel, Institut für Theoretische Physik und Astrophysik, Leibnizstr.

abundant in gas-phase molecules. Thus the disk midplane, which would otherwise for a full disk be dominated by near complete heavy element freeze-out, should become observable in molecular emission. If this prediction is correct this has exciting prospects for observations with the Atacama Large Millimeter/Submillimeter Array (ALMA), as the inner transition region should thus be readily detected and resolved, especially using high-J rotational transitions excited in the high density midplane gas. Therefore such observations will potentially provide us with a direct probe of the physics and chemistry at this actively evolving interface.

2.3 Introduction

Over the last thirty years, our knowledge of pre-main sequence evolution has undergone significant advances. Observations of the full spectral energy distribution (SED) from disks around young stars have shown that not all are alike, with the striking discovery of a subset of disks with optically thin inner "holes" devoid of small grains, surrounded by optically thick outer disks (e.g. *Strom et al.*, 1989; *Calvet et al.*, 2005; *Cieza et al.*, 2010; *Espaillat et al.*, 2010). This inner void was later confirmed by resolved sub-mm interferometry (e.g. *Piétu et al.*, 2006; *Brown et al.*, 2008; *Hughes et al.*, 2009; *Andrews et al.*, 2009, 2011) and was interpreted as an intermediate stage between primordial and debris disks, coined "transition disks" (*Strom et al.*, 1989).

In this work we adopt the physical definition of "transition disk" as an optically thick disk truncated within some inner radius within which there has either been substantial grain growth or removal. Such objects are of particular interest, as the presence of a gap has been attributed to clearing by young protoplanets (e.g. *Skrutskie et al.*, 1990; *Bryden et al.*, 1999; *Rice et al.*, 2003) or tidal interactions with young stellar companions (e.g. *Dutrey et al.*, 1994).

Dullemond et al. (2001) investigated the physical structure of Herbig Ae/Be disks that

15, 24098 Kiel, Germany

possess large inner radii similar to those seen in low mass transition disks. In this work it was found that at the inner rim, the normal incidence angle of the stellar irradiation causes the disk rim to be much hotter than it would otherwise be for a classical flared disk, where the radiation arrives at a glancing angle. Further observational evidence for the directly irradiated wall was later seen both in studies of the SED (e.g., *Espaillat et al.*, 2007) as well as through scattered light imaging (*Brown et al.*, 2008).

ALMA will readily resolve such inner gaps and voids in the dust disk (e.g., *Wolf et al.*, 2002; *Wolf and D'Angelo*, 2005); however, here we seek to make predictions regarding the significant gas reservoir in transition disks. In particular, one interesting aspect of disk chemistry that has yet to be explored is the potential that this warm UV irradiated inner rim should have unique chemical properties. This has important implications since it is possible that the physical and chemical conditions of the previously hidden, but now exposed, midplane will be revealed and potentially detectable with high spatial resolution observations, such as those anticipated by ALMA. Here we present a chemical model of a protoplanetary disk with a large inner gap similar to those seen in classical transition disks (e.g. *Hughes et al.*, 2009; *Espaillat et al.*, 2010) as a prospective study of observability with ALMA.

2.4 Chemical Modeling

2.4.1 Disk Framework

For our model we adopt the comprehensive disk structure from *Sauter et al.* (2009), originally purposed for CB26 and constrained by a large set of observations: the SED from nanometer to millimeter wavelengths, near-infrared scattered light images, and resolved millimeter images. For the central star, the model of *Sauter et al.* (2009) assumes standard T Tauri values of $M = 0.5\ M_\odot$ and $L = 0.9\ L_\odot$. The disk density profile is given by:

$$\rho = \rho_0 \left(\frac{r}{r_0}\right)^{-\alpha} \exp\left(-\frac{1}{2}\left(\frac{z}{h}\right)^2\right) \tag{2.1}$$

$$h = h_0 \left(\frac{r}{r_0} \right)^{\beta} \tag{2.2}$$

Using this model and temperatures derived with MC3D (*Wolf et al.*, 1999), *Sauter et al.* (2009) successfully reproduced the full set of observations with the following best-fit model parameters: $r_0 = 100$ AU, $h_0 = 10$ AU, $\alpha = 2.2$, $\beta = 1.4$, $R_{\rm outer} = 200$ AU and $R_{\rm inner} = 45$ AU. The measured size of the hole is typical of that seen in resolved millimeter observations and SED modeling of transition disks, which range from a few AU to upwards of 70 AU (*Andrews et al.*, 2011; *Espaillat et al.*, 2007). The inner disk irradiation substantially increases the disk temperature at the wall, reaching ~ 50 K, as compared to a typical midplane temperature of ~ 15 K as seen at larger radii. We note that this model is taken as a "snapshot" and any subsequent disk physical evolution is beyond the scope of this work.

For the gas density we assume a standard ISM gas-to-dust mass ratio of $f_{\rm g} = 100$ and that the dust and gas are co-spatial. The gas temperature is taken to be equal to $\rm T_{dust}$, which holds true near the dense midplane (*Jonkheid et al.*, 2004). We furthermore note $\rm T_{dust}$ was originally derived assuming passive heating by the central star, with accretion heating treated as negligible (*Sauter et al.*, 2009). The effects of inclusion of accretion heating are discussed in Section 2.6.1. The model physical structure is shown in Fig. 2.1.

For the opacities we adopt *Weingartner and Draine* (2001) for a blend of astronomical silicates and carbonaceous grains with $\rm R_V = 5.5$. We also assume an unsettled disk and uniform dust composition for simplicity. Deviations from these assumptions, such as the affect of vertical settling of small grains and grain-growth, are discussed in Section 2.6.2.

2.4.2 Radiation Field

Both the ultraviolet and X-ray radiation field are believed to be dominant factors driving the chemistry in disks (*Glassgold et al.*, 1997, 2004; *van Zadelhoff et al.*, 2003). While low mass young stars peak in the optical regime with negligible chromospheric contribution to the FUV, the accretion shock at the central star provides a significant source of both FUV

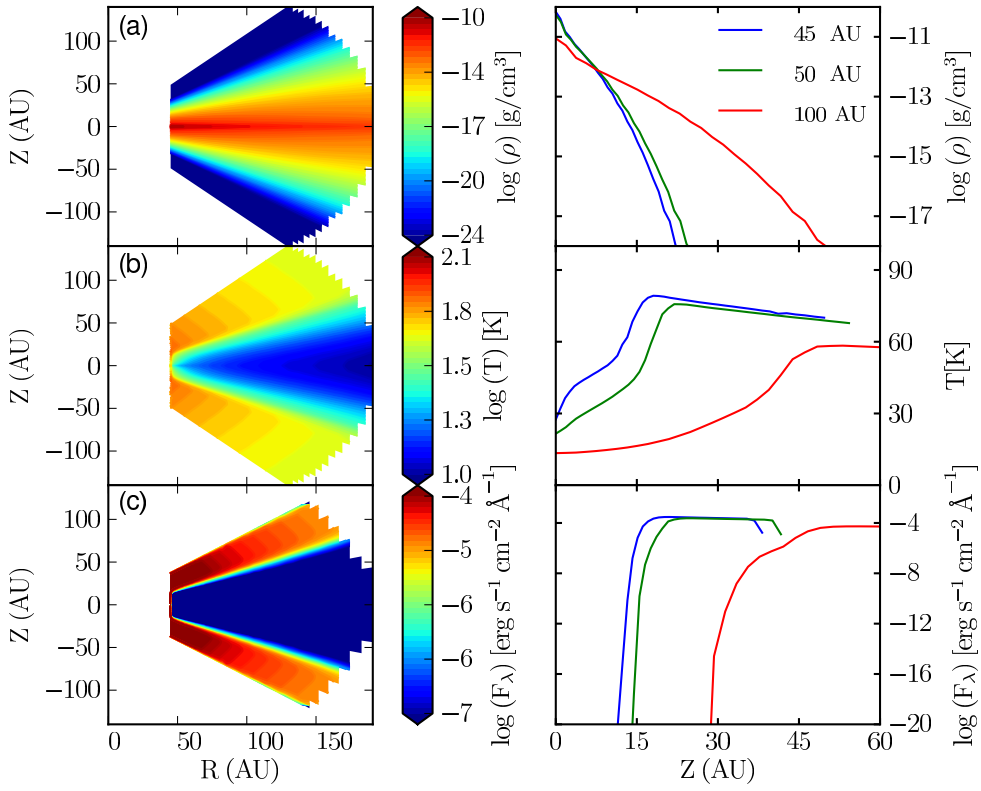

Figure 2.1 Left: Plot of the transition disk model with the central star at the origin. Panels: a) gas density b) temperature c) FUV radiation field at 1600 Å. Right: Vertical cuts of the same quantities taken at R = 45, 50 and 100 AU.

and soft X-ray flux (e.g., *Günther et al.*, 2007). We neglect external contribution from the ISRF since the stellar FUV will dominate external sources by orders of magnitude in the inner disk (*Bergin et al.*, 2003), though its import may lie in understanding the outer disk chemistry (*Öberg et al.*, 2010). Due to the geometry of the star-disk system it is then necessary to properly treat the radiative transfer into the disk (*Willacy and Langer*, 2000; *van Zadelhoff et al.*, 2003; *Fogel et al.*, 2011). This is especially true in transition disks, where voids and gaps can allow photons to propagate more freely into the outer disk material. Possible implications of the presence of a small amount of undetected dust within the gap are discussed in Section 2.6.3.

2.4.2.1 Continuum Radiative Transfer

We assume the FUV continuum opacity is dominated by the dust, and consequently the UV field is dependent on settling of small grains, opacities assumed, and disk geometry. Using the measured FUV spectrum of TW Hydra (*Herczeg et al.*, 2002, 2004) binned down to nine discrete wavelengths between 950-2000 Å, we calculate the continuum radiative transfer into the disk using the method of *Bethell and Bergin* (2011a), implementing the opacities described in Section 2.4.1. The choice of nine wavelengths was motivated by the need to sufficiently capture the shape of the FUV continuum, to be insensitive to individual weak emission lines, and to also remain computationally efficient.

2.4.2.2 Lyman-α Radiative Transfer

While many individual lines in the observed TW Hydra spectrum are weak, the Lyman-α line alone carries $\sim 85\%$ of the total FUV flux (*Herczeg et al.*, 2004; *Bergin et al.*, 2003). This line is furthermore expected to play a significant chemical role as a number of molecular species have photodissociation cross sections near 1216Å (*Fogel et al.*, 2011). In addition to dust scattering, Lyman-α undergoes isotropic scattering off hydrogen atoms (*Bethell and Bergin*, 2011a), which in principle requires an iterative and computationally expensive calculation between the radiation field and the chemistry.

In this work, we incorporate the effects of Lyman-α using an approximate treatment motivated by *Bethell and Bergin* (2011a). The procedure is illustrated in Fig. 2.2. If one assumes a priori that there is an optically thick layer of atomic hydrogen on the disk surface located at $\tau_{\rm FUV} = 1$ as defined by the dust (Fig. 2.2: Region II), the Lyman-α photons will first encounter this isotropic H-scattering layer. A fraction of the radiation will be lost to space ($\lesssim 50\%$, Region I: wavy arrows), with the surviving Lyman-α photons diffusively propagating through the H-layer. Below the atomic layer, the hydrogen is predominantly H_2 and the Lyman-α photons proceed as continuum photons scattering off only the dust grains (Fig. 2.2: Region III). Thus, at the base of the hydrogen scattering layer (II$\rightarrow$III), the

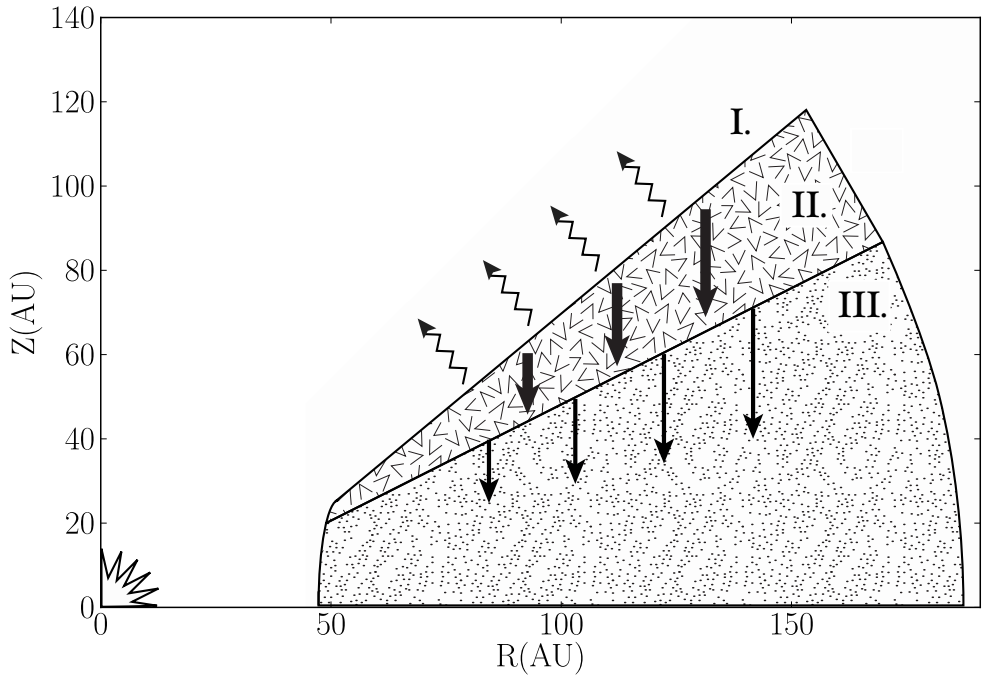

Figure 2.2 Lyα schematic illustration. (I.) "Free-streaming" region above $\tau_{\rm radial} \sim 1$ surface; half of the Lyα radiation escapes the disk. (II.) H-scattering layer with a vertical depth of $\tau_{\rm vertical} \sim 1$. Remaining photons diffuse downward until they escape the atomic region. (III.) Region where H is predominantly H_2. Dust now becomes the dominant source of opacity to Lyα photons, and the Lyα radiation now behaves as vertically attenuated continuum photons, which significantly enhances its penetrating power. The (I.) $\rightarrow$ (II.) interface illustrates the $\tau \sim 1$ surface for continuum photons, whereas the (II.) $\rightarrow$ (III.) interface is effectively the $\tau \sim 1$ surface for Lyα photons.

photons effectively form a layer of isotropically emitting point sources, which together create a planar source of radiation that shines at a nearly normal angle to the midplane. Therefore even though a significant fraction of Lyman-α photons are lost to space, the remaining photons will have greater vertical penetration power into the disk and can propagate many AU deeper than the UV continuum radiation. On the front edge of the disk, at the dense inner rim, Lyman-α is similarly "stopped" as was seen for the continuum photons. (cf. Fig. 2.1 (c)). We discuss the implications of an inner void that is not empty of gas on Lyman-α transfer in Section 2.6.4.

2.4.3 Reaction Network

Combining the model detailed in Section 2.4.1 and the radiation field in Section 2.4.2, the resultant chemistry is calculated using *Fogel et al.* (2011)'s comprehensive disk chemical model, based on the Ohio State University Astrophysical Chemistry Group's gas-phase network (*Smith et al.*, 2004). The reaction types include photo-desorption, photo-dissociation, freeze-out, grain surface reactions, ion and electron reactions, cosmic-ray and stellar X-ray ionization, and radiative reactions. In total, the network encompasses 5910 reactions and 639 reacting species, including some time-dependent reactions, encompassing the main species of astrochemical importance, and described in detail in *Fogel et al.* (2011).

The model initially assumes uniform molecular cloud chemical abundances *Aikawa and Herbst* (1999a) and follows the chemical evolution for 3 Myr. In this work we take the abundances at 1 Myr, which is long enough such that the chemistry has "relaxed" but not so long that the disk would likely have *physically* evolved away from this state.

Furthermore, we assume a typical integrated T Tauri star X-ray luminosity of 10^{30} erg s^{-1} and a thermal X-ray spectrum between 1-10 keV (*Glassgold et al.*, 1997, and references therein). The model of *Fogel et al.* (2011) incorporates the method of *Aikawa et al.* (2001) for X-ray propagation. For cosmic rays we adopt a typical cosmic ray ionization rate of 1.3×10^{-17} s^{-1} per H, with an attenuation column of 96 g cm^{-2} (*Umebayashi and Nakano*, 1981).

2.5 Results

2.5.1 Disk Chemistry

The resultant chemical abundances (relative to $n_{\rm H} = n_{\rm HI} + 2n_{\rm H_2}$) for six observed gas-phase species are shown in Fig. 2.3. Molecules such as CO, H_2CO, and N_2H^+ show an enhanced gas-phase abundance at the wall. For comparison, in an untruncated disk model, all neutral species plotted in Fig. 2.3 would be otherwise frozen onto grains at the midplane at $R_{\rm wall} = 45$ AU. The two ions shown, N_2H^+ and HCO^+, would also not be present in an untruncated disk, as their chemical precursors, N_2 and CO, would be frozen out, inhibiting the formation of these two species. Consequently the gas-phase enhancement at the truncation radius shown for all species plotted here, besides H_2O, would not exist if it were not for the large inner gap.

Water, with a freeze-out temperature of ~ 100 K, is frozen onto grains at the ~ 50 K transition region. One could however envision a disk with a wall closer to the central star and thus warmer, such that water would sublimate from grains and be observable. Thus the specific species present are not necessarily the most important result, but that the star can efficiently heat the wall, warming it above the sublimation temperature of a variety of species, potentially allowing us to observationally probe disk physics as well as evolutionary state. Therefore the existence of a cleared inner gap should produce unique chemical features in the outer disk not present in full classical disks.

2.5.2 Observables

If such an enhancement is present it is of interest to determine observability. While previous observations reveal a diverse chemistry (e.g., *Dutrey et al.*, 1997; *Öberg et al.*, 2010), the sensitivity and resolving power of ALMA is required to fully understand the detailed structure of these systems.

We adopt a disk inclination of 60° and calculate the resulting emission for rotational

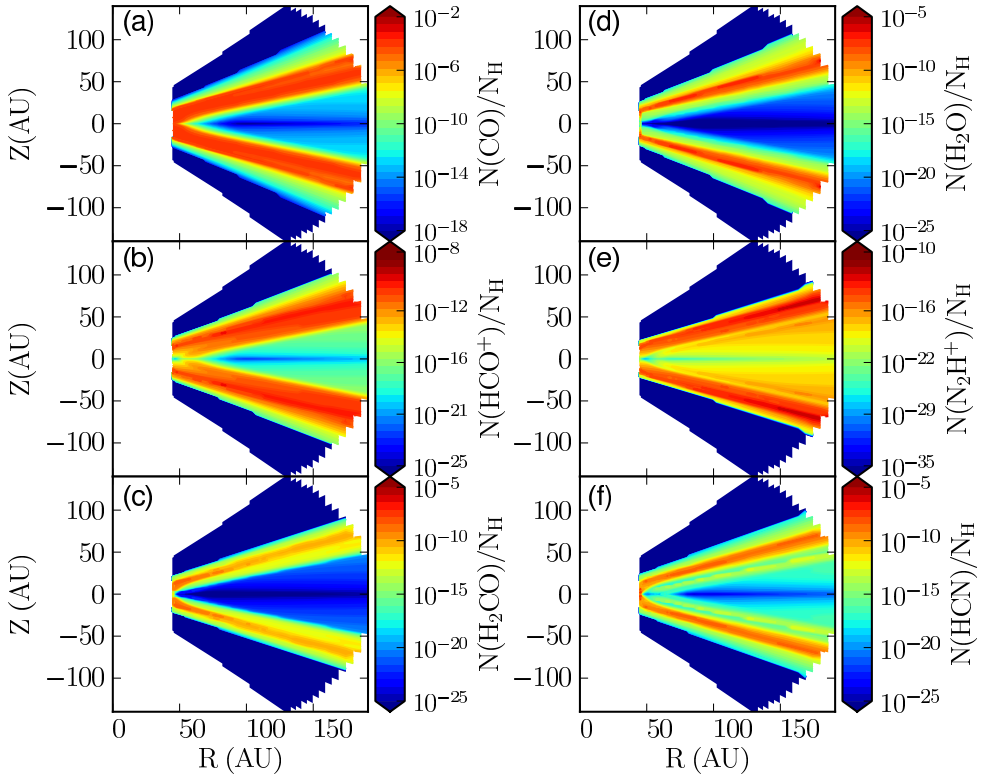

Figure 2.3 Chemical model results, plotted as abundance relative to the total number of hydrogen atoms. Shown are common species of astrophysical interest: (a) CO, (b) HCO^+, (c) H_2CO, (d) H_2O, (e) N_2H^+, (f) HCN.

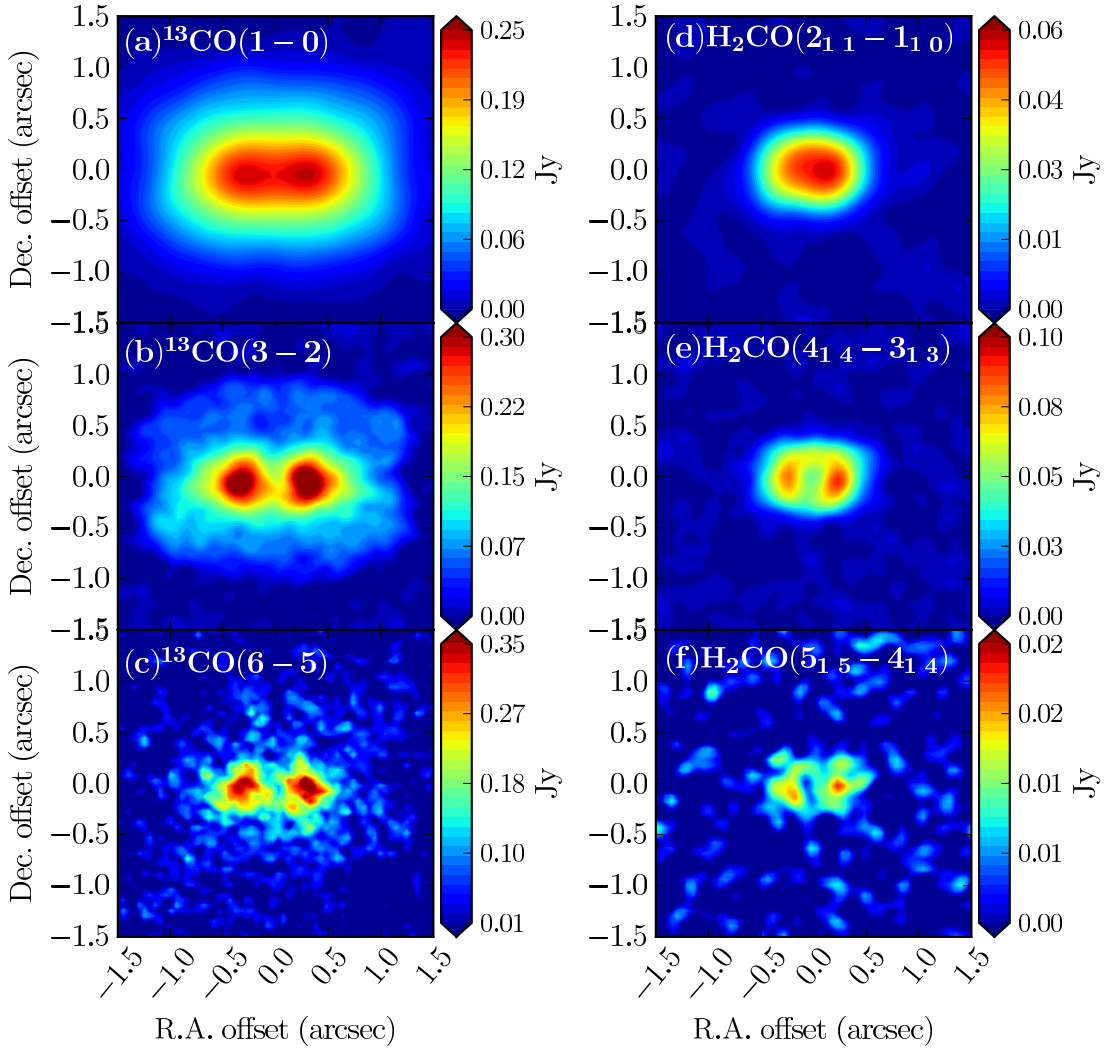

Figure 2.4 Simulated ALMA observations (computed with one hour integration time) of ^{13}CO and H_2CO for a disk at 140 pc, at different rotational transitions with increasing J. This demonstrates the increasing contrast between the inner transition region and outer disk emission for higher J, along with ALMA's future capabilities at these frequencies.

transitions of ^{13}CO and o-H_2CO as would be seen at a distance of 140 pc using the non-LTE line radiation transfer code, LIME (*Brinch and Hogerheijde*, 2010). These species have been chosen as both are commonly observed towards disks around low mass T Tauri stars (e.g., *Öberg et al.*, 2010, 2011c). The densities reached at the frontally illuminated midplane preferentially excite high-J rotational transitions, and therefore transition disks should uniquely exhibit high-J bright molecular rings at the wall when resolved by sub-mm observations with ALMA. Using this calculated line emission, we then use the *SIMDATA* package in CASA to calculate the ALMA visibilities and reconstruct the image from the UV coverage of the full ALMA array. Fig. 2.4 shows the simulated observations for these lines as seen by ALMA for an antenna configuration with $\sim 0.1''$ resolution at 672 GHz, chosen to provide adequate resolution and sensitivity assuming typical thermal noise.

2.6 Further Considerations

In this work we propose the presence of gas-phase molecules at the inner edge of transition disks. This effect could however be erased if either the dust at the inner edge is not sufficiently heated or if the wall becomes permissive to molecule destroying UV radiation. In the following we discuss potential caveats of the model and how these would alter the results presented here.

2.6.1 Accretion Heating

The original model was computed assuming passive heating by the central star and heating due to disk accretion was treated as negligible. Accretion heating, however, predominantly increases the midplane temperature (*D'Alessio et al.*, 1998), and, if significant, will increase the thermal desorption of molecules from grains, enhancing the predicted effect. Details of the dynamical transport of gas and dust and their effects on the chemistry, however, are beyond the scope of this Letter.

2.6.2 Dust Settling and Grain Coagulation

For this model we have assumed an unsettled outer disk with grains of ISM abundance. In our analysis we have also explored a model that includes mixed grain growth of dust particles of up to 1 mm in size, without vertical settling. This lowers the UV opacity (cm^2 g^{-1}) by ~ 2 orders of magnitude, which is a direct consequence of the fact that large grains contribute significantly to the mass but little to the UV opacity. The high model densities at the inner edge ($\rho_{\rm dust} \sim 10^{-14}$g cm^3), however, are still of sufficient magnitude such that the wall remains optically thick to UV radiation for a model with mixed grain growth alone.

Strong settling or removal of small grains can also make the disk more permeable to the UV radiation. We can ask how much dust would need to be removed/settled to allow the UV photons to penetrate and photodissociate the enhanced abundance of molecules present at the wall. To approximate this, the unsettled wall density is $\rho_{\rm dust} \sim 10^{-14}$ g cm^3 and the UV dust opacity is $\sim 5 \times 10^4$ cm^2 g^{-1} at 1000 Å (*Weingartner and Draine*, 2001). Based on the thermal model, the thickness of the "warm" inner edge is ~ 5 AU at R = 45 AU. For the UV to penetrate the inner 5 AU, the disk would need contain $< 0.1\%$ of the original amount of dust present to erase the effect seen here. We note however that settling will also increase the depth of the heating, which will in principle thicken the extent of the wall further.

2.6.3 Dust in the Inner Gap

An underlying feature of the disk model is the presence of a large inner "void" which allows the outer disk to be heated directly by the star. One possible explanation for such a void is grain growth into rocky planetesimals (e.g. *Skrutskie et al.*, 1990). Thus one could postulate the existence of a small amount of undetected dust inside the gap. Indeed some models infer the presence of some moderate mass of silicates in the inner disk (e.g. *Calvet et al.*, 2002, 2005; *Espaillat et al.*, 2007). This material has the ability to shadow the outer disk from being directly heated by the star, thus inhibiting the presence of the warm molecular interface presented here.

First, one can ask how much dust would be required to cause the gap to become opaque ($\tau \sim 10$) to optical radiation peaking at $\lambda = 0.7$ μm as is the case for a $T = 4000$ K star. If we assume that the inner disk follows the outer disk profile (Section 2.4.1), a total mass in dust of $M_{dust} = 10^{-3}$ M_{Moon} inside 45 AU would be sufficient for the midplane to become optically thick to the optical heating radiation. While this is an extremely small amount of dust, one must also consider the scale height of the material: $h \sim 3.3$ AU at R = 45 AU. Therefore, this cross-section is very small, and would not strongly shadow the outer disk and would not significantly alter the heating and UV irradiation except at the very central midplane region. Furthermore, because the original model from *Sauter et al.* (2009) included scattered light images, the presence of small grains at or above the disk scale height would significantly contribute to the amount of scattered light and not match observations for the model presented here.

2.6.4 Gas in the Inner Gap

By assuming gas and dust are co-spatial we intrinsically assume the gap is empty of gas. Gas within the gap would not alter the original optical heating calculation of the outer disk or the propagation of UV continuum photons, both of which have dust-dominated opacities. However, the presence of gas would strongly affect the propagation of Lyman-α as gas within the gap would likely be predominantly atomic. The presence of hydrogen within the gap would cause a net reduction in the Lyman-α flux reaching the outer disk. This would either not change or marginally enhance the abundance of gas phase molecules at the truncation radius since the amount of photo-dissociating radiation is reduced.

2.7 Conclusions

We have investigated the chemistry of a transition disk employing the model structure of *Sauter et al.* (2009) and have shown that a disk with a 45 AU inner void depleted of dust and gas should have unique chemical properties. At the truncation radius, the midplane is both

heated by optical photons and irradiated by the stellar UV and X-rays. The net effect is that the previously hidden midplane is revealed as a region rich in gas-phase molecules, that should be readily observable by ALMA. For comparison, in a full untruncated disk model, the midplane is normally cold and shielded from the central star, resulting in substantial freeze-out of gas onto grains, preventing direct observation. While this analysis focuses on a specific disk model, these first results provide insight into our ability to directly probe the unique chemistry of transition disks. The rich chemistry at the transition region will allow us to probe the physical conditions, such as density, temperature and kinematics. It is important to note that this model provides one possibility, which can be readily tested with ALMA. We will be exploring a suite of disk models with a variety of geometric frameworks both in dust and gas content in future work, to further explore the full parameter space of transition disks, with the aim of pioneering future observational campaigns with ALMA to explore these exciting objects.

2.8 Acknowledgements

The authors thank the anonymous referee for their helpful comments. This work was partially supported by NSF grant AST-1008800. J.S. acknowledges support by the DFG through the research group 759 "The formation of planets: The critical first growth phase."

CHAPTER III

Indirect Detection of Forming Protoplanets via Chemical Asymmetries in Disks

3.1 Preface

The following work has been submitted to the Astrophysical Journal (January 2015). The work is co-authored by Edwin A. Bergin[1] and Tim Harries[2].

3.2 Abstract

We examine changes in the molecular abundances resulting from increased heating due to a self-luminous planetary companion embedded within a narrow circumstellar disk gap. Using 3D models that include stellar and planetary irradiation, we find that luminous young planets locally heat up the parent circumstellar disk by many tens of Kelvin, resulting in efficient thermal desorption of molecular species that are otherwise locally frozen out. Furthermore, the heating is deposited over large regions of the disk, ± 5 AU radially and spanning $\lesssim 60^\circ$ azimuthally. From the 3D chemical models, we compute rotational line emission models and full ALMA simulations, and find that the chemical signatures of the

[1]Department of Astronomy, University of Michigan, 1085 South University Avenue, Ann Arbor, MI 48109
[2]School of Physics, University of Exeter, Stocker Road, Exeter EX4 4QL

young planet are detectable as chemical asymmetries in $\sim 10h$ observations. HCN and its isotopologues are particularly clear tracers of planetary heating for the models considered here, and emission from multiple transitions of the same species is detectable, which encodes temperature information in addition to possible velocity information from the spectra itself. We find submillimeter molecular emission will be a useful tool to study gas giant planet formation in situ, especially beyond $R \gtrsim 10$ AU.

3.3 Introduction

Planetary systems form from the accretion disks encircling young stars. The composition of ice, gas and dust within the disk sets the initial chemical conditions of the planets and also regulates the physical conditions under which planets form. The properties of the pre-planetary materials can then be compared to the composition of the present day solar system (e.g. *Öberg et al.*, 2011b) and even that of extrasolar planetary atmospheres (*Madhusudhan*, 2012; *Teske et al.*, 2013). Nonetheless, there is a missing link between these two stages, separated in time by billions of years. It is essential to observationally capture a forming young planet in situ to put together a complete chemical (and physical) history of planet formation.

The upcoming capabilities of the Atacama Large Millimeter Array (ALMA) will provide extremely high sensitivity and spatially resolved observations of disks (up to $0.007''$ at 650 GHz, or 0.7 AU at distances of $d = 100$ pc). At these scales, detailed disk structure will be readily revealed, and observations of the local environment near forming protoplanets should be accessible. Young proto-Jupiters are expected to be intrinsically hot as they accrete matter through their circumplanetary disk and liberate gravitational potential energy, thereby generating substantial accretion luminosity, $L_{\rm acc}$. Theoretical models of early-stage circumplanetary disks find typical "quiescent" accretion levels between $\dot{M} = 10^{-10}$ $M_\odot$ year^{-1} and 10^{-8} $M_\odot$ year^{-1} (*Ayliffe and Bate*, 2009; *Lubow and Martin*, 2012). Periodically, the circumplanetary disk is theorized to undergo accretion outbursts similar to those seen in FU

Ori objects (*Hartmann and Kenyon*, 1985; *Zhu et al.*, 2009), where the planet's accretion rate jumps to $\dot{M} = (1 - 10) \times 10^{-5}$ $M_\odot$ year^{-1}. Accretion rates can be translated into accretion luminosities,

$$L_{\rm acc} = \frac{GM_p\dot{M}_p}{2R_{\rm in}} \tag{3.1}$$

(*Pringle*, 1981), where M_p and $\dot{M}_p$ are the planet's mass and accretion rate, and $R_{\rm in}$ is the inner radius of the circumplanetary disk, which is something like the radius of the planet. Assuming a Jupiter-mass planet and $R_{\rm in} = 3$ $R_{\rm Jup}$, the quiescent accretion levels translate to $L_{\rm acc} = (3 - 300) \times 10^{-5}$ $L_\odot$. During an accretion burst, however, the planet can outshine even the star in bolometric luminosity, where the accretion luminosity due to the planet can be as high as $L_{\rm acc} \sim 15$ $L_\odot$ but for less than 0.1% of the planet's formation time (*Lubow and Martin*, 2012). *Kraus and Ireland* (2012) reported the detection of a possible embedded protoplanet companion in LkCa 15 for which they estimated a substantial accretion luminosity of $L_{\rm acc}= 10^{-3}$ $L_\odot$. Planets with similar accretion luminosities will heat the nearby circumstellar dust disk and may give rise to detectable signatures with sensitive submillimeter continuum observations, though detecting the circumplanetary disk itself will be challenging (*Wolf and D'Angelo*, 2005).

In addition to the thermal effects on the dust, the planetary accretion heating will have a substantial impact on the chemical structure in the vicinity of the young planet. In the present work, we explore local heating due to a single massive protoplanet (a gas giant precursor) on the three-dimensional chemistry of the surrounding circumstellar disk. We do not calculate the chemistry of the hot, young circumplanetary disk, but focus instead on the larger scale effects on the cold, molecular disk within which the planet is entrenched. We vary the planet's orbital location from the star for a fixed accretion rate of $\dot{M} = 10^{-8}$ $M_\odot$ year^{-1}, where the physical and thermal structure are described in §3.4. On this model, we calculate the time-dependent chemistry in 2D slices over the 3D model, focusing the calculations on the region near the planet and opposite the planet (§3.5.1). For species that are particularly sensitive to the presence of the planet and have strong submillimeter transitions, we identify

submillimeter emission line tracers and compute the emission based on the three-dimensional structure to determine detectability (§3.5.2). Finally, in §3.5, we summarize our findings and discuss their implications.

3.4 Physical Model

3.4.1 Axisymmetric Structure

3.4.1.1 Density Model

The background disk density is described by a simple power law in surface density, $\Sigma_g \propto R^{-1}$ and vertically gaussian with a scale height of $h \propto 12.5\,(r/100\text{ AU})^{\beta}$ AU, $\beta = 1.1$. The gas and dust are uniformly mixed with a gas-to-dust mass ratio of 100, and the disk gas mass contains $M_g = 0.01$ $M_\odot$. The dust is a simple MRN distribution in grain size ($a_{\rm gr} \propto r_{\rm gr}^{-3.5}$; *Mathis et al.*, 1977) with minimum size of 0.005 μm and maximum size of 1 μm. The dust composition is assumed to be Draine and Lee astrosilicates (*Draine and Lee*, 1984). We fix the central star to have a mass of $M_* = 0.5$ $M_\odot$, an effective temperature of $T_{\rm eff} = 4000$ K and $R_* = 2.0$ $R_\odot$, characteristic of low mass T Tauri stars. We consider four planet locations, $d_p = 5$ AU, 10 AU, 20 AU, and 30 AU. For each location, we simply "cut out" a vertical gap in the disk corresponding to the Hill radius of a $M_p = 1$ $M_{\rm Jup}$ planet as consistent with theoretical models, which find massive planets open gaps comparable to the size of their Hill sphere (e.g., *Lin and Papaloizou*, 1986, 1993; *Bryden et al.*, 1999; *Lubow et al.*, 1999). The gap radii (half the gap-width) for the planet models at $d_p = 5$ AU, 10 AU, 20 AU, and 30 AU are 0.4 AU, 0.9 AU, 1.7 AU, and 2.6 AU, respectively. The density of the gap is taken to be a factor of 10^6 lower than the density of the disk, and is – for the purposes of the heating calculations – optically thin at infrared wavelengths. We emphasize that these models are designed to understand and isolate the local effects of planetary heating, and that we do not include variations in the 3D density structure near the planet, either excess flaring near the edges of the gap (e.g., *Jang-Condell*, 2009), or accretion streams, both of which

will alter the vertical and radial disk structure and should be examined in future work. The density structure of the bulk disk is shown in Figure 3.1a.

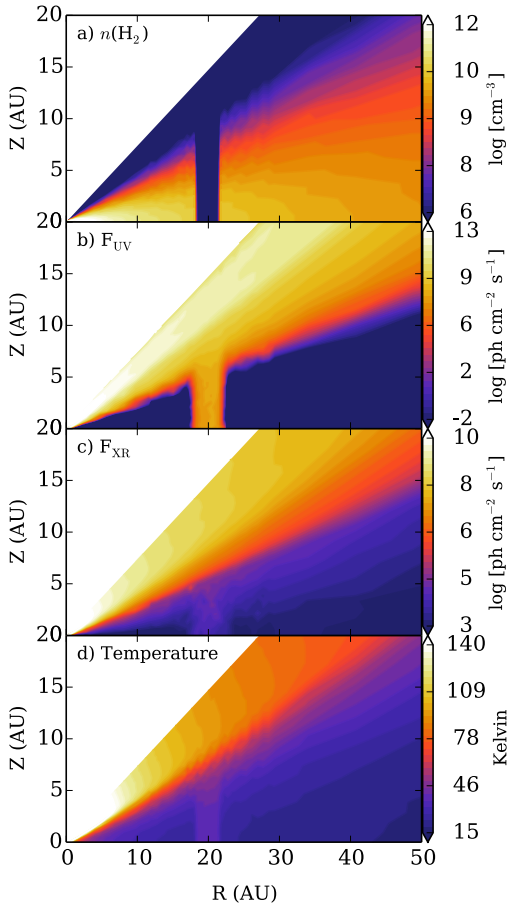

Figure 3.1 Circumstellar disk properties shown for the planet at $d_p = 20$ AU. Disk properties away from the gap are similar for the $d_p = 5$ AU and $d_p = 10$ AU. The central star is located at R=0 and Z=0 and the plot is made for an azimuthal angle of $\phi = 270°$ (opposite the location of planet).

3.4.1.2 High-energy Stellar Irradiation Field

We calculate the UV and X-ray radiation field from the central star for each of the four planet locations, d_p, from a single 2D slice and assume the high energy stellar radiation field is otherwise azimuthally symmetric. The procedure for calculating the 2D X-ray and FUV field are the same as described in Chapters 4 and 6, using the Monte Carlo radiative transfer code of *Bethell and Bergin* (2011a). The FUV radiation is used to estimate the gas temperatures

(S. Bruderer, in private communication), which are coupled to the dust temperatures in the region where the planet's impact is the greatest, and as such, our results do not depend on the gas temperature in the upper layers where the gas and dust temperatures are decoupled. The disk is quite opaque to the FUV stellar photons (wavelengths between $930 - 2000$ Å, including that of Lyman-α) due to our use of an unsettled disk model. A substantial amount of FUV continuum and line (Lyman-α) radiation is down-scattered into the gap, aided by the UV-exposed, optically thick outer gap edge, which tends to deflect photons both into the gap and away from the disk. However, the scattered continuum and line photons within the gap do not penetrate far into the gap edges and do not have a substantial impact on the chemistry beyond the illuminated wall. The integrated FUV field between $\lambda = 930 - 2000$ Å is shown in Figure 3.1b.

The X-ray radiation field is computed using the same transfer code as the UV with the combined gas and dust X-ray absorption cross sections of *Bethell and Bergin* (2011b) and Thompson scattering. Because the X-ray photons are stopped at larger column densities much further into the disk, the presence of the gap does not have as significant of an effect as it does for the FUV (Figure 3.1c). The gap exposes more of the disk to X-ray photons, but the overall X-ray field is much more sensitive to distribution of disk mass rather than the specific gap location; these Hill radius-sized gaps are relatively narrow compared to the path length of an X-ray photon at ~ 5 keV. For cosmic ray ionization, we use the model presented in Chapter 4 for the cosmic ray ionization rate at solar maximum for the present day Sun ($\zeta_{\rm CR} \sim 2 \times 10^{-19}$ s^{-1} per H_2) as an upper limit to the contribution from cosmic rays, consistent with the upper limit determined from observations of the TW Hya disk (Chapter 7).

3.4.2 3D Thermal Structure

We calculate the thermal structure of the disk assuming two passive radiation sources: the self-luminous central star the protoplanet shining due to its accretion luminosity. We assume

a circumplanetary accretion rate of $\dot{M} = 10^{-8}$ $M_\odot$ year^{-1} on an $M_p = 1$ $M_{\rm Jup}$ and $R_p = 3$ $R_{\rm Jup}$ planet, corresponding to an accretion luminosity of $L_{\rm acc} = 5 \times 10^{-4}$ $L_\odot$. In this simple picture, the planet is treated as a spherical, 1500 K blackbody that heats its self-carved gap from the inside. The dust temperatures are calculated using the code TORUS (*Harries*, 2000; *Harries et al.*, 2004; *Kurosawa et al.*, 2004; *Pinte et al.*, 2009) assuming radiative equilibrium with the Lucy method (*Lucy*, 1999). We note that we do not include the differential rotation of the circumstellar disk in the dust temperature calculation because radiative equilibrium at ~ 50 K is quickly attained within minutes to hours (*Woitke*, 1999). For a planet at 10 AU, this timespan is negligible compared to the $\sim$ 30 year period of the planet's orbit, thus planetary heating of the disk is expected to remain a local phenomena and will not become highly sheared out by differential rotation. The thermal structure for the bulk circumstellar disk (away from the planet) is shown in Figure 3.1d for the planet at $d_p = 20$ AU. The large-scale physical properties are largely similar for all four planet locations in our models (i.e., the presence of the gap does not significantly change the thermal/irradiation structure away from the gap). All four models have an outer disk radius of 50 AU and an inner disk radius of 0.2 AU.

The additional heating by the planetary companion primarily results in an azimuthally extended ($\Delta\phi \sim \pm 30°$) but somewhat thin ($R \lesssim 5$ AU) swath of material along the gap edges, centered on the planet itself. The temperature structures in the midplane and for a vertical slice centered on the planet's location are shown in Figure 3.2. The contours highlight the change in temperature due to the presence of the planet. The planet increases the temperature by greater than 10% within about $\Delta R \sim 1.1$ AU, 1.6 AU, 2.7 AU, and 4 AU from the edge of the gap for the 5, 10, 20, and 30 AU orbital radius, respectively. The absolute change in temperature at the gap edges closest to the planet ($\lesssim 0.5$ AU from the wall) due to the additional heating corresponds to an increase from 42 K to 60 K ($d_p = 5$ AU), 35 K to 47 K ($d_p = 10$ AU), 27 K to 34 K ($d_p = 20$ AU), and 24 K to 31 K ($d_p = 30$ AU) for both gas and dust temperatures. These substantial $\sim 10 - 20$ K changes in cold, dense

molecular gas will substantially alter the local chemistry close to the planet.

3.4.3 Chemical Model

From the physical structure outlined above, we can estimate molecular abundances as a function of 3D position throughout the disk. The disk chemical code used for the calculations is presented in *Fogel et al.* (2011) and further expanded in Chapter 6. The chemical code itself is inherently 1+1D, and so to address this limitation we extract 2D azimuthal cuts from full 3D model to compute the abundances, and reconstruct the full disk profile from the individual 2D calculations. We consider ten 2D slices at 3° intervals in azimuth ranging from the planet's location to 30° away from the planet, and assume that the planet is symmetric upon reflection. For the rest of the disk beyond 30°, we calculate the chemistry based upon one 2D slice on the opposite side of the disk from the planet, i.e. the "anti-planet" side. Differential rotation is not included in the present models but will be explored in future work (see further discussion below). The 1+1D *Fogel et al.* (2011) code calculates the time-dependent abundances relative to hydrogen as a function of radius and height from the midplane based on a fixed grid of temperature, density, and radiation field conditions. The chemical reaction network is based on the OSU gas-phase chemical network (*Smith et al.*, 2004), expanded to include grain-surface chemistry in the method of *Hasegawa et al.* (1992b), where the grain-surface reactants "sweep-out" the surface at a rate related to the binding energy and mass of the reactant. We treat the hydrogen binding energy in the method in Chapter 8, where we assume that the binding energy for desorption processes is the chemisorbed value such that H_2 can form even at high temperatures, while the binding energy adopted for the rate of hydrogenation reactions on the surfaces of cold dust grains is assumed to be the lower, physisorbed value, or $E_b(\mathrm{H}) = 450$ K, such that the H-atoms are highly mobile across the ice mantle. The reaction network has a total of 6292 reactions, including both chemical reactions and physical processes (i.e., ionization, desorption, etc.) and 697 species. All chemical calculations are examined after 1 Myr of chemical evolution.

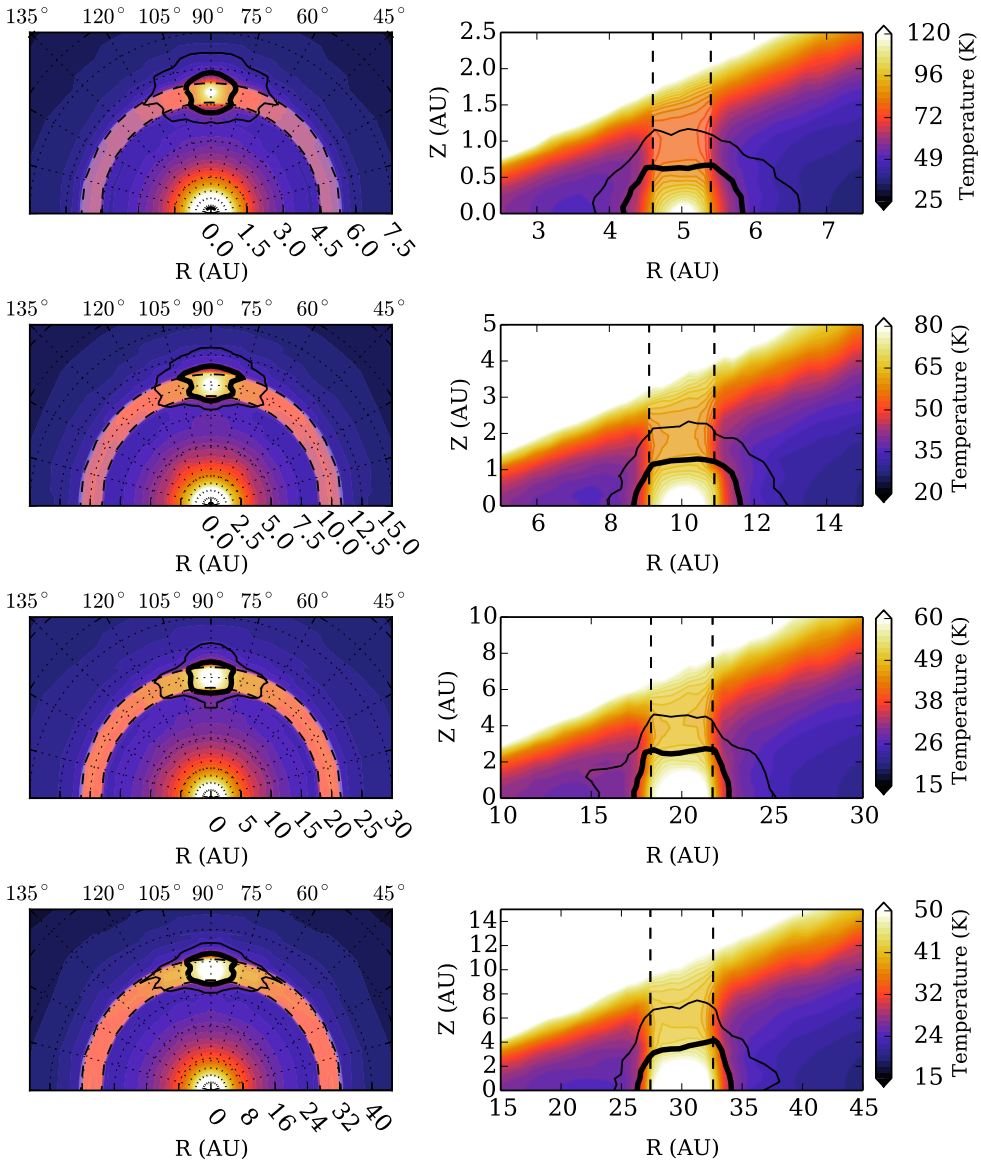

Figure 3.2 Thermal structure in the region near the planet. Left column shows the midplane temperature over radius and azimuth (planet is located at 90° in all cases). Right column shows the vertical temperature structure centered on the planet. The thin (thick) contour line highlights the region of the disk where the planet increases the local temperature by $> 10\%$ ($> 30\%$). Top, middle and bottom rows are models for planets at 5 AU, 10 AU, 20 AU and 30 AU, respectively.

3.5 Results

In the following section, we present chemical abundance signatures due to the additional heating from a planetary companion as calculated over the disk. We then simulate the emergent line emission for the fully 3D physical and chemical model. Based upon these emission models we generate ALMA simulations of planets embedded in disks.

3.5.1 Chemical Abundance Results

The most important chemical effect from the planet is the thermal desorption of molecular species that are otherwise frozen out as ices in the midplane at the orbital distance of the planet, which we term "primary tracers." As discussed in Section 3.4.2, the dust temperature rapidly equilibrates to the local irradiation conditions. To assess whether the simplification of neglecting differential rotation is important for the chemical structure, we must compare the chemical timescales for adsorption/sublimation to the orbital time. If the chemical timescales are longer than the orbital time, the chemical effects of the planetary heating within the gap will become sheared out over azimuth. In contrast, short chemical timescales relative to the planet's orbital time indicate the relevant chemistry is able to adjust quickly, and thus "follow" the planet.

In our model, the midplane at $d = 10$ AU has a density of approximately $n_{\rm H_2} \sim 10^{10}$ cm^{-3} and a temperature of $\sim 50 - 60$ K near the planet. The timescale for freeze-out of a molecule is related to the surface area of grains per unit volume, or $n(\sigma_{\rm gr})$ cm^2 cm^{-3}, as well as the thermal speed of the molecule in the gas phase, $v_{\rm X}$, such that molecule X freezes out in a characteristic time $t_{\rm fo}({\rm X}) = (n(\sigma_{\rm gr})v_{\rm X})^{-1}$. At gas densities of $n_{\rm H} = 10^{10}$ cm^{-3}, a typical grain surface area density is $n(\sigma_{\rm gr}) \sim 10^{-11}$ cm^2 cm^{-3} (i.e., 0.1 μm-sized grains at an abundance relative to H-atoms of 6×10^{-12}), an H_2CO molecule (for example) with mass of 30 amu, will collide with a grain on average every ~ 0.3 years, which is roughly the time for circumstellar disk chemistry to reset when not directly heated by the planet. The corresponding timescale for thermal evaporation of an H_2CO molecule (assuming a

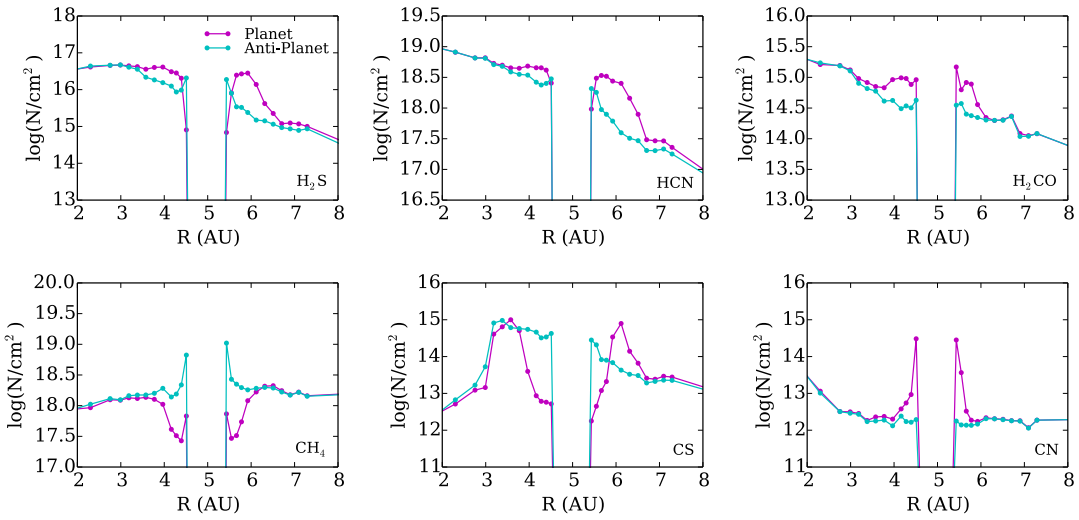

Figure 3.3 Vertically integrated column densities of select molecular species (labeled in the lower right corner) after 1 Myr of chemical evolution for the planet at $d_p = 5$ AU with an accretion luminosity of $L_{\rm acc} = 5 \times 10^{-4}$ L$_\odot$. The column density at the disk azimuthal angle centered on the planet (90° in Figure 3.2) is shown in magenta, where the points correspond to the specific radii calculated in the chemical models. The chemistry of the disk near the gap in the absence of the planet is shown in cyan, i.e., at the 'anti-planet' side of the disk.

desorption temperature of $T_d \sim 2050$ K; *Garrod and Herbst*, 2006) on a 50 K dust grain based on the Polyani-Wigner relation (see *Fogel et al.*, 2011) is 0.02 years (the timescale for molecules to evaporate when exposed to the planet's heating). Both of these timescales are sufficiently rapid compared to the orbital time around a 1 M$_\odot$ star for the planets considered here (about 11, 32, and 89 years) and therefore we expect the chemistry of the primary tracers to follow the planet and not experience strong azimuthal shear. It is important to note that the relevant timescales will increase with height; however, in all cases, the chemical effect of

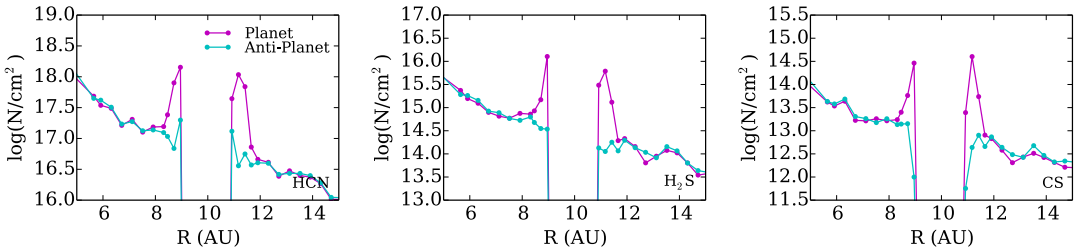

Figure 3.4 Vertically integrated column density of select species for the planet at $d_p = 10$ AU. Figure as described in Figure 3.3.

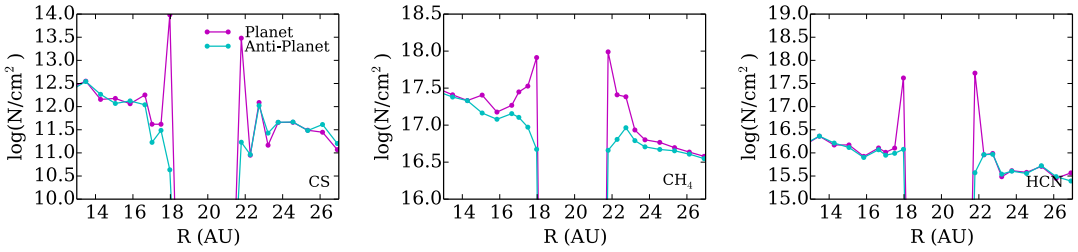

Figure 3.5 Vertically integrated column density of select species for the planet at $d_p = 20$ AU. Figure as described in Figure 3.3.

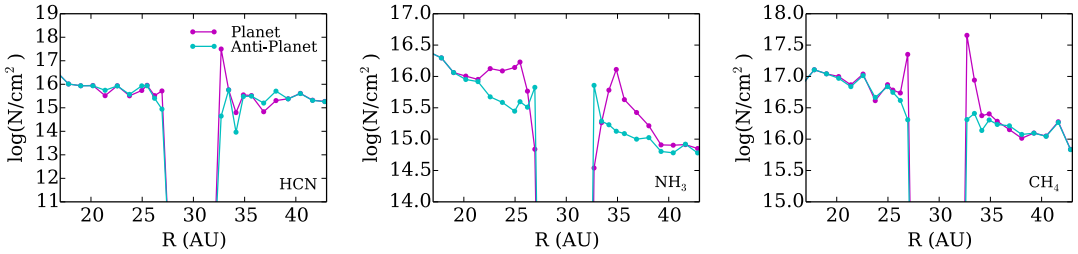

Figure 3.6 Vertically integrated column density of select species for the planet at $d_p = 30$ AU. Figure as described in Figure 3.3.

the planet is limited to a narrow vertical region close to the midplane where $z/r < 0.1$, over which the density only decreases by $\sim 30\%$.

Molecules that form via gas-phase or grain-surface chemistry as a direct result of primary species desorption are "second-order" chemical effects – i.e., secondary tracers. The timescales for secondary species formed from primaries to return to the low-temperature state will depend on the particular formation pathways for the secondary species and the availability of He^+ ions to break up newly formed molecules that would otherwise not be present without the planet (e.g., *Bergin et al.*, 2014; *Furuya and Aikawa*, 2014). In this case, the distribution of secondary species formed due to the planet are more likely to be affected by shear (see discussion below).

Given the size of the chemical network, we took an unbiased approach to search for promising chemical tracers of planetary heating, both primary and secondary. We calculate the vertical column density of every species in the network versus radius, and filter out species with low column density near the planet, $N_X \leq 10^{10}$ cm^{-2}, since these will be the

most difficult to detect. We then calculate the fractional difference between the column densities, $\Delta N_X(R)$, at the azimuthal location of the planet and the anti-planet side, and integrate this quantity over radius to get an estimate for the total fractional change due to the planet. We then sort by the fractional change to identify which species are most affected by the additional heating. The results of this "blind search" for gas-phase tracers are shown in Figures 3.3 ($d_p = 5$ AU), 3.4 ($d_p = 10$ AU), 3.5 ($d_p = 20$ AU), and 3.6 ($d_p = 30$ AU).

For certain species, the additional heating changes the vertical column density at the edges of the gap by many orders of magnitude. For most "signpost" molecules, the heating from the planet lifts the local dust temperature at the midplane from below the particular species desorption temperature to above, causing a large enhancement in the column density at the edges of the gap. Two species stand out from this trend for the planet at 5 AU, where CS and CH_4 instead exhibit large deficits. The assumed binding energies of CS and CH_4 are $E_b = 2000$ K and $E_b = 1330$ K, respectively. In the case of CS, the 5 AU planet causes an initial, fast desorption of CS (and higher column density), but the heating simultaneously increases the abundance of gas-phase oxygen bearing molecules. Over ~ 2000 year timescales, the chemical network converts the CS to OCS ice, resulting in the net chemical deficit plotted in Figure 3.3. The orbital time at 5 AU is clearly much shorter than the chemical timescale for this process to occur, and so in this case, the conversion from CS to OCS (and the corresponding CS-deficit) is over-predicted in our simplified models. To properly model the planet's effects on the CS chemistry in the inner disk requires models that include differential velocity shear to address these second-order time-dependent effects. However, for planets located further out in the disk, CS shows simple net desorption behavior without further chemical processing for the more distant, 10 and 20 AU planets. The change in chemical behavior arises because the chemistry leading to OCS is not as efficient radially further out where the gas-phase oxygen is depleted. As a result, CS becomes a "primary" planet tracer for the planets located further out. Thus using thermal desorption as a search tool for planets is more reliable in the more chemically inactive outer disk.

For CH_4, this species' low binding energy ($T_d \sim 27$ K) allows for it to be in the gas phase regardless of the planet's location. The deficit in CH_4 is purely a second-order effect, where the CH_4 at 5 AU primarily forms via gas-phase channels originating from CH_5^+. The presence of additional, sublimated gas-phase species that are also able to react with CH_5^+ will form other molecules besides CH_4. These additional pathways stymy the formation efficiency of CH_4 and leads to the CH_4 deficit in Fig. 3.3 of about a factor of three in column density. This process likewise occurs over much longer timescales than the planets' orbital times and should be studied in further detail including disk differential rotation to fully characterize the CH_4 chemistry in the presence of the planet.

There is some variation of the radial extent of the region affected by the planet as seen in the column density plots. For example, as seen in Figures 3.5 and 3.6, the 20 AU and 30 AU planets exhibit enhanced HCN confined to a narrow region close the gap edges ($\lesssim 0.6$ AU), while CH_4 is enhanced over a much wider region, $\lesssim 1.5$ AU. The main factors that determine the chemically affected region are the gap size (i.e., a larger gap reduces the amount of heating at the wall's interface; Chapter 2) and the binding energy of the species in question. CH_4 is more weakly bound to the grain surface, $E_B \sim 1360$ K, compared to HCN, $E_B \sim 1760$ K (*Hasegawa and Herbst*, 1993), and so the region near the planet is only sufficiently hot to evaporate HCN close to the gap walls.

In addition to HCN and CH_4, NH_3 is also enhanced in the presence of the 30 AU planet (see Fig. 3.6). This behavior is a feature of the relatively low NH_3 binding energy used in the present models, $E_b = 1100$ K (*Hasegawa and Herbst*, 1993), corresponding to a desorption temperature of $T_d \sim 28$ K. Alternatively, NH_3 deposited on a H_2O ice surface has a much higher binding energy, E_b 3200 K (*Collings et al.*, 2004), or $T_d \sim 90$ K. Thus if the higher desorption temperature applies, NH_3 evaporation may be a more useful tracer of planets in the inner few AU of a cool protoplanetary disk, or further out for warmer disks like those around Herbig Ae/Be stars. In summary, the ideal chemical tracer for identifying planets is fundamentally a balance of the appropriate chemical binding energies and the disk thermal

structure.

From the 2D chemical model slices we reconstruct the 3D abundance profiles. We plot the abundance structure for particularly promising species for the four planet locations in Figures 3.7, 3.8, 3.9, and 3.10. From these plots, it is clear that the chemical effects extend over a larger azimuthal range than radial range for most cases. The abundance enhancement furthermore spans the full wall height until the abundance profile merges into that set by the surface chemistry, as driven by the central star. However, the vertical density structure is such that the densities are highest closest to the midplane and most tenuous near the surface. Thus the midplane heating by the planet can have a large effect on the total, integrated column density, similar to the direct midplane illumination of transition disks by the central star(see Chapter 1).

Of all the species considered here, HCN is a particularly robust tracer with a simple midplane chemistry, such that the thermal effects from the planet are primarily its desorption. The binding energy of HCN in our models is set to 1,760 K (*Hasegawa and Herbst*, 1993), i.e, a characteristic desorption temperature of $\sim$ 44 K . For the planets beyond 10 AU, HCN should otherwise be frozen-out in the midplane for the majority of the disk. Even at 5 AU (midplane temperature of $\sim$ 40 K), HCN is just beginning to freeze-out in the absence of the planet. Thus HCN should be an excellent tracer of planets at orbital distance of $d_p > 5$ AU from the central star. Even if the particular HCN binding energy is revised, the location HCN as a planet-tracer will scale accordingly based upon the midplane temperature profile of the disk and the molecules' binding energy to the grain. Furthermore, if the HCN binding energy varies with the properties of the substrate (e.g., *Collings et al.*, 2004), the azimuthal region away from the planet can be used as a baseline against which the HCN enhancement can be compared independent of the specific binding energy assumed. For all four models, the enhancement in HCN is typically an order of magnitude in column density due to the planetary heating. In the absence of the planet's effects, the baseline HCN column density on the opposite side of the disk is $N_{\rm HCN} \sim 10^{16}$ cm^{-2} for the planet at 30 AU and

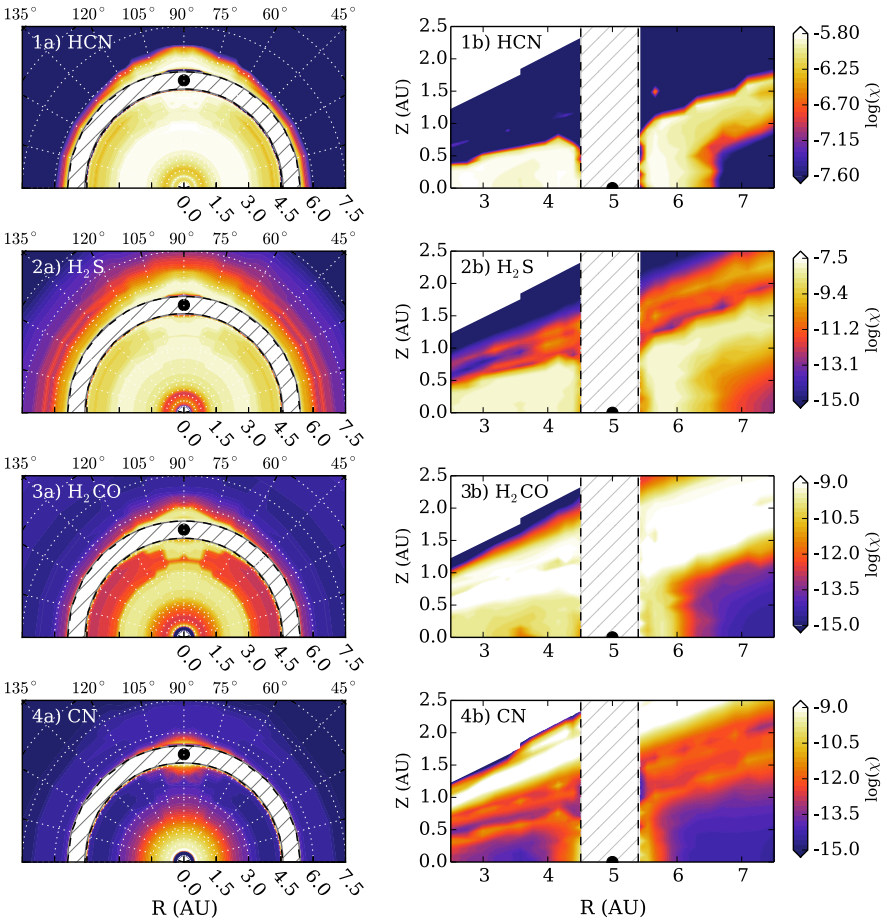

Figure 3.7 Chemical abundances for species that are sensitive to the planet's additional heating. The left column shows the abundances in the disk midplane, while the right column shows the vertical abundances centered on the planet. Chemical models are shown for the planet at $d_p = 5$ AU.

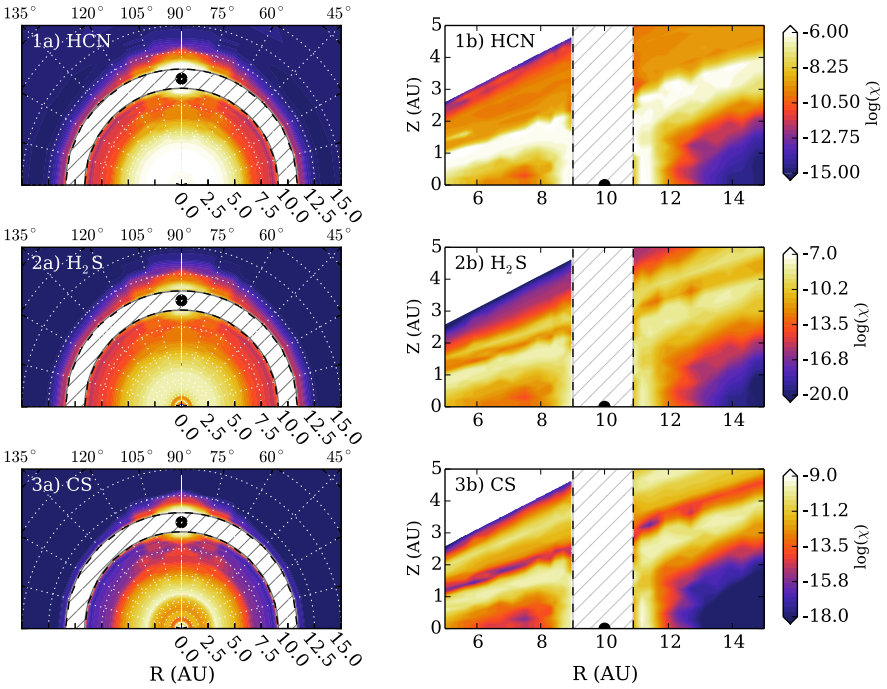

Figure 3.8 Chemical models for the planet at $d_p = 10$ AU. Panels are the same as for Figure 3.7.

$N_{\rm HCN} \sim 10^{18}$ cm^{-2} for the planet at 5 AU. The column of HCN in the absence of the planet arises almost entirely from the HCN present at the warm disk surface.

3.5.2 Line Emission

Many of these "signpost" molecular species have strong rotational transitions that can be used to observationally identify and characterize the local physical conditions near the planet. Because of its simple interpretation and large column density, we focus on HCN emission as a tracer in the present Chapter, but emphasize that other, perhaps stronger tracers may exist, and the particular tracer will depend on the luminosity of the central star, which will set the thermal structure of the midplane at the disk radii probed by ALMA.

We use the flexible line modeling code LIME (*Brinch and Hogerheijde*, 2010) to simulate the emergent line emission from the full disk, oriented face-on at a distance of $d = 100$ pc. We assume the bulk motion of the protoplanetary disk gas is Keplerian about the central star and add a thermal broadening component of 100 m s^{-1} on top of the Keplerian velocity

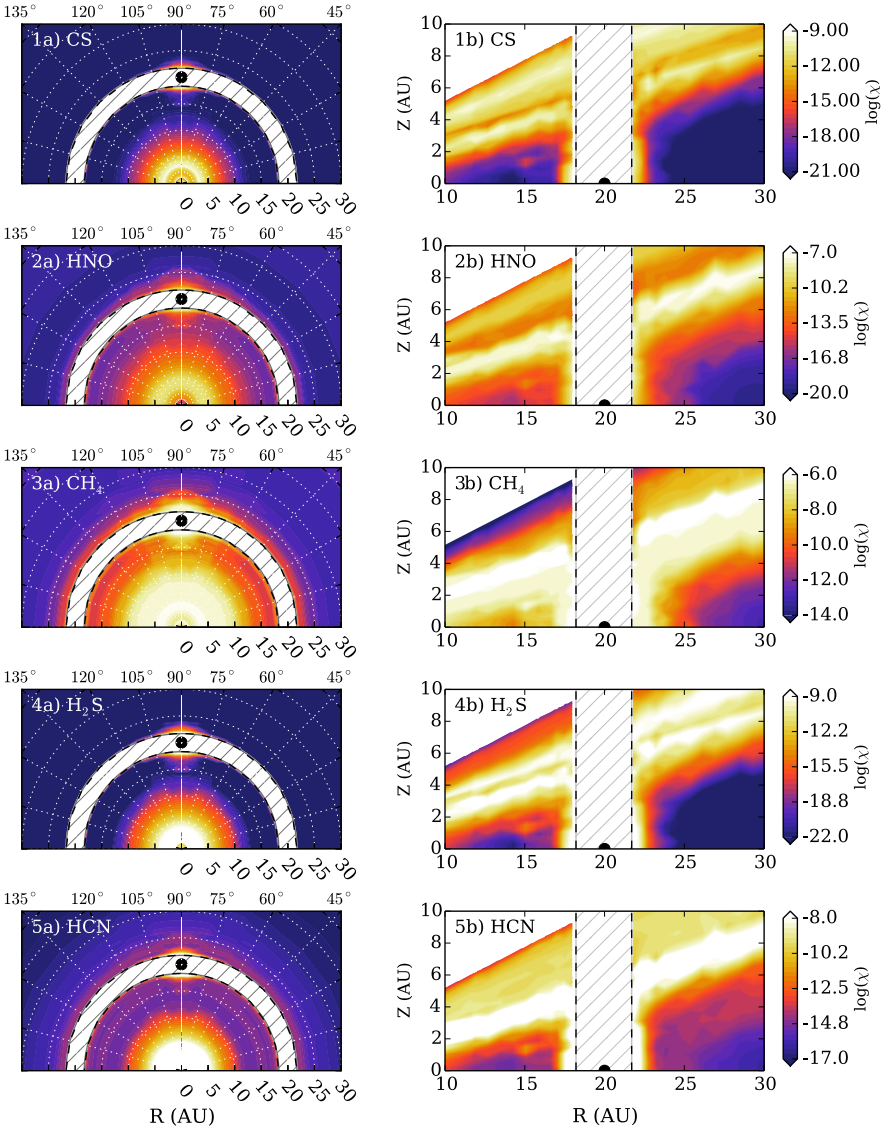

Figure 3.9 Chemical models for the planet at $d_p = 20$ AU. Panels are the same as for Figure 3.7.

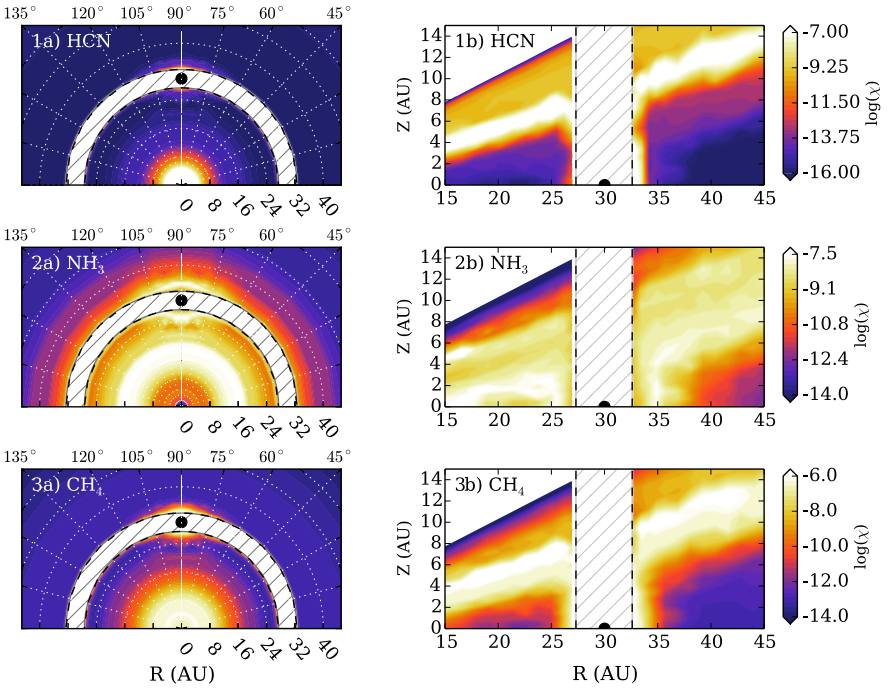

Figure 3.10 Chemical models for the planet at $d_p = 30$ AU. Panels are the same as for Figure 3.7.

for simplicity. We present HCN emission results for the planets at $d_p = 10$ AU, 20 AU and 30 AU as the HCN signature for the 5 AU planet was not detectable or distinguishable from the background disk in any of the models considered. Because LIME samples the model's native grid by selecting random points and accepting/rejecting them based upon particular criteria (in our case, normalized density and HCN abundance), the code can potentially not adequately sample relatively small scale local features in the disk when considering the full 3D volume of the disk. Arbitrarily increasing the point number, however, will add more points into the inner, high density regions of the disk that are already well-sampled. To address this issue, we cast two grids of points, a large grid over the full disk range (including the planet), and a refined spherical grid centered on the planet that contains 5% of the total number points (∼300,000) used to sample the model. This insures that a sufficient number of points encompass both the disk and the region near the planet. We furthermore tested this technique for a model without any planet (but still with the refined local grid) to confirm that the refined grid does not introduce emission signatures. Such sub-grids will be useful

in modeling all types of substructure with LIME.

Because HCN is fairly optically thick at the surface, we model both the HCN and $H^{13}CN$ isotopologue assuming an isotope ratio of $^{12}C/^{13}C = 60$. We emphasize that at the high densities where the planet is depositing its heating that selective photodissociation effects on N_2 relating to HCN chemistry (*Heays et al.*, 2014) are not expected to play a major role. For the emission calculations, we consider the $J = 4 - 3$ and $J = 8 - 7$ rotational transitions for both species, which we identify as likely strong transitions accessible with ALMA using preliminary RADEX[3] models (RADEX is a statistical equilibrium solver under the assumption of the large velocity gradient approximation; *van der Tak et al.*, 2007). Using LIME, we calculate the line optical depth for the four transitions considered. For both HCN lines, the disk is optically thick ($\tau > 100$) at all positions at the line center. However, in the line wings at velocities $\delta v > 0.3$ km s $^{-1}$, the circumstellar disk is optically thin for both transitions, while the emission near the planet is thick. Thus these lines will be useful for constraining the temperature of the emitting circumplanetary medium. The $H^{13}CN$ $J = 4-3$ line is also thick at line center across the disk (τ $15 - 50$), but becomes thin and the lines, and has an optical depth of $\tau \sim 1$ near the planet. $H^{13}CN$ $J = 8 - 7$ is marginally optically thick at line center ($\tau \sim 10$), and thin at all locations in the wings.

The LIME models represent "perfect" images of the emission lines without any thermal noise or beam-convolution (besides the inherent limitations of the pixel size, which is $0\farcs0025$ per pixel or 0.25 AU in our models). To create more realistic emission models, we take the LIME output and, using the simulation capabilities of CASA[4] we compute simulated ALMA observations in the same method in Chapter 6. The alma.out13 antenna configuration is used for the $d_p = 10$ AU simulation of both $J = 4 - 3$ lines and the alma.out10 antenna configuration was used for the $J = 7 - 6$. For the planet at $d_p = 20$ AU (30 AU), alma.out16 (alma.out14) was used for $J = 4 - 3$ and alma.out.11 (alma.out09) for $J = 7 - 6$.

[3]http://home.strw.leidenuniv.nl/ moldata/radex.html
[4]http://casa.nrao.edu/

Configurations were chosen to provide optimal sensitivity and signal-to-noise to detect the planet. We add realistic thermal noise with 0.25 mm precipitable water vapor, and then reconstruct the image using CLEAN applied with natural weighting. The synthesized beam of the simulated observations is typically between 0.″1 and 0.″2. The results of the simulated line observations (with noise) are shown in Figure 3.11 for the $d_p = 10$ AU planet, Figure 3.12 for the $d_p = 20$ AU planet, and Figure 3.13 for the $d_p = 30$ AU planet.

In most cases, the emission from the planet is difficult to disentangle from the emission originating from the disk. However, the planet's sublimation effects are confined to a $\pm 30°$ azimuthal extent, which leaves the remaining $\sim 300°$ as a counterpoint against which we can compare. To better isolate the signature of the planet (without making use of a priori knowledge of the planet's location), we average the emission from the entire disk in annuli to estimate the radial line emission profile of the circumstellar disk (Figure 3.11, 3.12, and 3.13, middle row). Then, using the average disk profile, we subtract off the smooth background component from the simulated observation and examine the residual features. This technique will only work if the asymmetric feature is small and/or weak relative to the disk's emission, otherwise a median or averaging azimuthally restricted annuli (to mask out the feature) should be used instead. Though this system is face-on, the technique would similarly work for systems that are not face-on if the inclination is known, i.e., by taking a projected annular average.

The bottom row of Figures 3.11, 3.12, and 3.13 shows the residual emission, where the planets location is circled in all of the panels. Without the additional knowledge of the planet's location, the signature in the $J = 4 - 3$ is not strong enough to identify emission from the noise for the planet, primarily because of the high opacity of this line, which partially hides the deep emission from the midplane. The lower opacity for $J = 8 - 7$ for both isotopologues, however, makes for a substantially stronger signal from the planet, even though the noise is substantially higher at these frequencies. The main limitation is the extremely high sensitivity required to measure the small fractional change in the emission

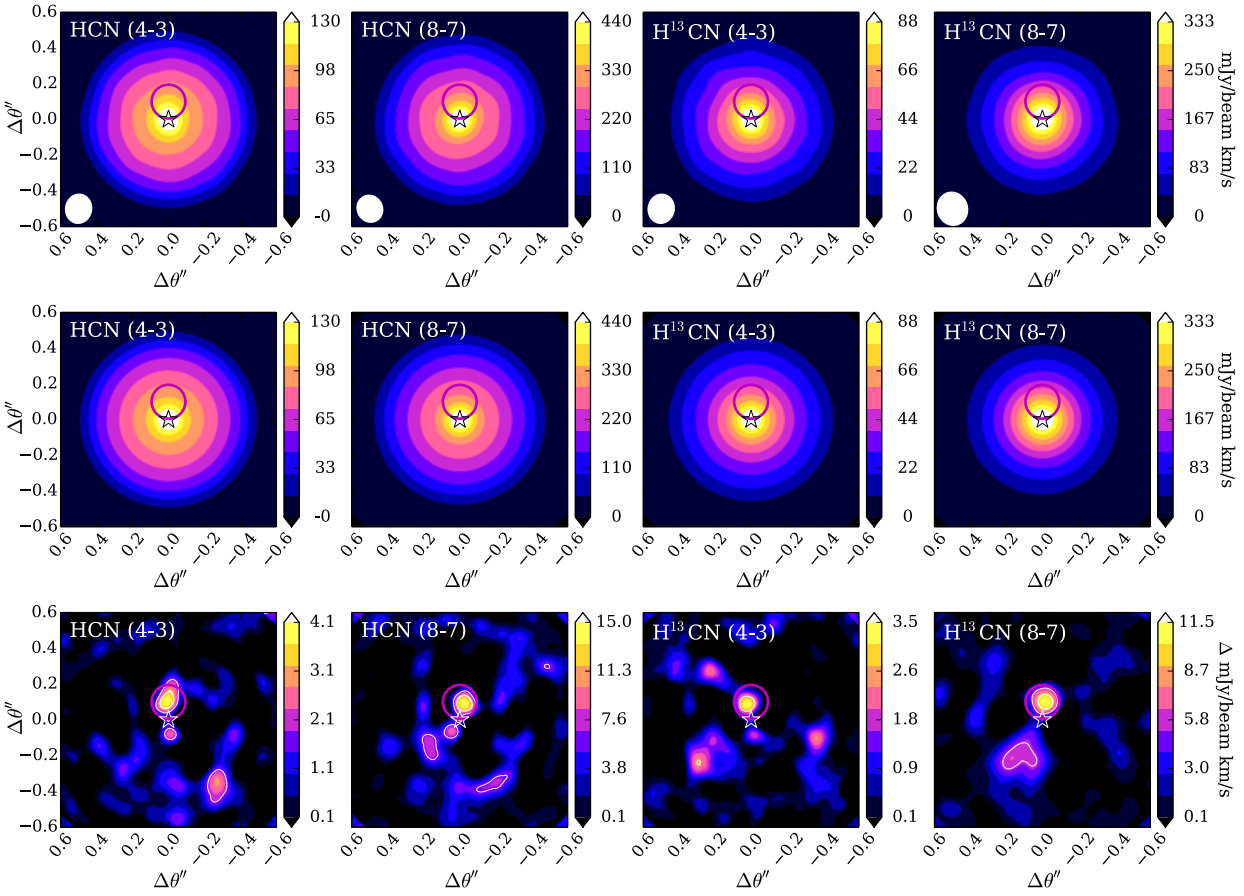

Figure 3.11 Select emission lines for the planet at $d_p = 10$ AU. The top row shows $10h$ simulated observations of the indicated species as velocity integrated line emission. The middle row plots the annular averaged emission profile, that is representative of the background disk. The bottom row shows the residual between the full disk simulation (top) and the averaged profile (middle), highlighting the asymmetric emission. Contours for the residual plots are 3σ and 5σ (where applicable). The magenta circle highlights the location of the planet.

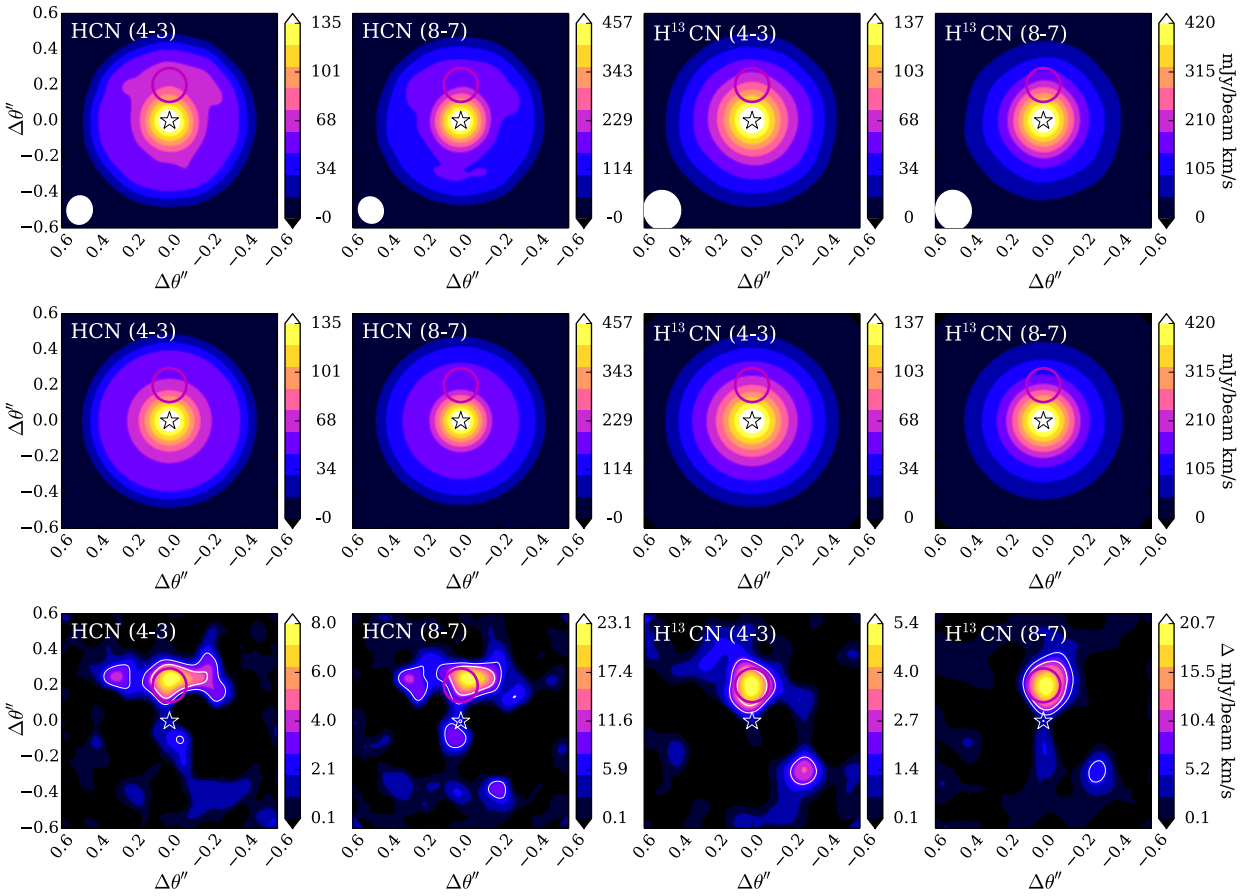

Figure 3.12 Select emission lines for the planet at $d_p = 20$ AU. Panels are the same as for Figure 3.11.

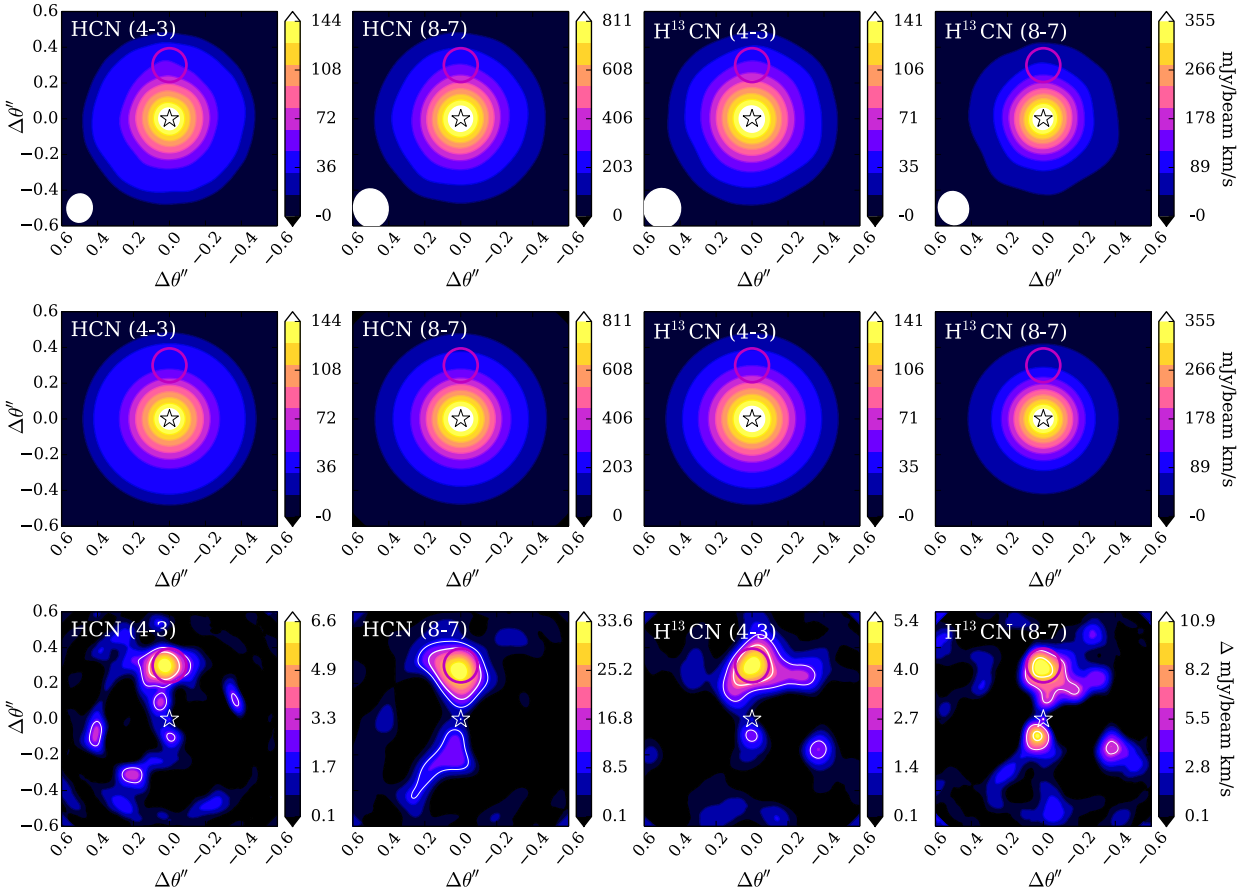

Figure 3.13 Select emission lines for the planet at $d_p = 30$ AU. Panels are the same as for Figure 3.11.

signature from the bright circumstellar disk emission.

Because in our models the HCN abundance is highest along the walls of the gap near the planet, the face-on inclination provides the largest column density due to the planet. However, if a more inclined viewing geometry may allow direct imaging of the gap wall depending on the overall scale height of the disk. We examined emission simulations of a disk oriented at 60° with the planet at 90° from the projected rotation axis (in the gap corner), and were unable to recover any emission from the planet. If the planet is on the far-edge of the disk such that the outer gap wall is more directly viewable, and the emission signature may be observable but only for a fraction of the orbit. Thus low inclination (face-on) disks are favorable for planet searches with chemistry.

3.6 Discussion & Conclusions

We have examined the chemical structure of simple toy models of a protoplanetary disk heated by two sources, the central star and an embedded, luminous young proto-Jupiter accreting at $\dot{M} = 10^{-8}$ $M_\odot$ year^{-1}. Chemical species with intermediate freeze-out temperatures, around $\sim$ 40 K, will be particularly useful tracers of the additional planetary heating, as the midplane will be colder than 40 K outside of $R \gtrsim 5$ AU. A planet in a Hill-radius sized gap will heat the gap edges by $\sim 10 - 20$ K, which will sublimate certain species and greatly enhance the column density of these species locally. These changes in column density will translate to observable signatures in the circumstellar disk emission, which will appear as emission line asymmetries. Such asymmetries can be highlighted by subtracting off the azimuthally averaged line brightness profile of the circumstellar disk. We found that HCN isotopologues are a particularly robust tracer of the heating effects of the planet. Additionally, multiple lines of HCN should be detectable, which will provide additional physical information (temperature) about the planet's local environment. In addition to the excitation information afforded by molecular line observations, the use of gas tracers (as opposed to continuum) will also provide spectral information that can be used to look

for velocity substructure near the planet. This technique is most useful for planets between $R \sim 10-30$ AU, where the inner disk is innately too warm to provide sufficient temperature contrast, and planets in the outer disk are expected to carve larger gaps (have larger $R_{\rm Hill}$), and as a direct consequence the planet's heating of the disk is more diluted at larger radii.

The assumed accretion rate is on the high end of the range for quiescent planetary accretion as predicted by models, $\dot{M} = 10^{-10}-10^{-8}$ $M_\odot$ year^{-1}. The corresponding accretion luminosity, $L_{\rm acc} = 5 \times 10^{-4}$ $L_\odot$, however, is similar to that observed for the tentative LkCa 15 planet. Furthermore, if young planets undergo frequent accretion outbursts (increasing the planet's luminosity by many orders of magnitude, see *Lubow and Martin*, 2012) and the cadence of such outbursts is competitive with the chemical timescales, the region affected by the planet might be much larger and more easily detectable.

One simplification in the present models is the use of a constant gas-to-dust mass ratio of 100. Disks are observed to have a deficit of small dust grains in their upper layers, attributed to the settling of grains from the surface into the midplane (*Furlan et al.*, 2006). One of the overall effects of settling is to create a warmer disk, where stellar radiation penetrates deeper. If the disk becomes too warm, ice sublimation due to the planet may be less effective and one would have to i) observe gas-phase tracers with relatively higher binding energies to achieve the same contrast between the planet and the background disk or ii) look for planets at larger radii where the circumstellar disk is cooler. The addition of dust mass (in particular dust grain surface area) in the midplane will also increase the rate of absorption onto grains (i.e., decrease the freeze-out time) and as a consequence, this may help reduce the effects of shear by disk rotation. On the other hand, if small grains are quickly converted to large grains with low surface area to mass ratios, then the freeze-out time will increase, and there may be a lag in the removal of planet-desorbed molecules from the gas phase thus spreading out the thermal effect of the planet over a larger area (see below).

We have also used a simplified density model in the present calculations. Massive planets will gravitationally interact with the circumstellar disk, generating density waves that can

form spiral arms, changing the disk's radial and azimuthal density structure (see the review of *Kley and Nelson*, 2012). Planets can also excite vortices, creating large azimuthal pressure traps, observationally seen as asymmetries in the dust distribution (as seen in IRS 48; *van der Marel et al.*, 2013). Furthermore, the presence of the gap exposes the top of the outer gap edge to direct stellar irradiation, which enhances heating near the gap at the disk surface (*Jang-Condell and Turner*, 2012). While the latter effect is azimuthally symmetric, the heating can be locally exacerbated by the presence of a massive planet perturbing the vertical disk structure, creating local hot/cold spots near the stellar-irradiated surface at the planet's location (*Jang-Condell*, 2009). We emphasize that all of these planet induced structures/physical effects can happen in concert with planet-heating and ice-desorption in the midplane. The presence of spiral arms can be potentially confirmed as planetary in origin if associated with a warm accreting source. Furthermore, the gap-edge heating occurs primarily at the surface of the disk, away from the planet's primary effects near the midplane, for which the use of spectral lines with high critical densities can help mitigate. Finally, the concentration of dust in pressure bumps can alter the chemical timescales such as the freeze-out time, though it should be noted that the small grains (which dominate the freeze-out given their high surface area to mass ratio) are still azimuthally distributed in IRS 48, providing a substrate for freeze-out. Thus ideally one would find evidence of planets through multiple signatures, both chemical and physical.

Finally, we have assumed very simple adsorption/desorption physics, with a single HCN binding energy. However, in reality, the HCN ice is expected to be mixed with less volatile ices, such as H_2O or CH_3OH. Trapping can thus increase the desorption temperature to that of the strongly bound ice, $\sim$ 5000 K (e.g., *Sandford and Allamandola*, 1990; *Collings et al.*, 2004), reducing the effects predicted in this Chapter. How trapping mediates the effect will essentially depend on how ices were initially deposited on the grain surface substrate, whether simultaneously or sequentially.

Finally, the primary (sublimated) species can trigger additional chemical processing, cre-

ating so-called "secondary" planet tracers. These secondary products may be even brighter than the primary products; however, to fully characterize them we must take into account the differential rotation of the disk, which is beyond the scope of the present Chapter. If the timescales for secondary product formation are a substantial fraction of the orbital time, the local effects may be sheared out over a large azimuthal range, i.e., as an "arc." If the relevant chemical timescales are much longer than the orbital time, the emission signature of the planet will become a ring (or double ring) at the gap edges. However, in the simple case of rapid sublimation/condensation, the chemical signature is predicted to "follow" the planet, implying that we will be able to re-observe and confirm that the emission is associated with the planet as it traverses its orbit. Furthermore, we can look for additional signatures of the presence of the young planet, including continuum emission from the circumplanetary disk itself (*Zhu*, 2015).

3.7 Acknowledgements

The authors are grateful for comments from an anonymous referee, which have improved this manuscript. We also thank Bruce Macintosh and Neal Turner for useful discussions. LIC and EAB acknowledge the support of NSF grant AST-1008800 and the Rackham Predoctoral Fellowship. TJH acknowledges funding from STFC grant ST/J001627/1. Some calculations for this chapter were performed on the University of Exeter Supercomputer, a DiRAC Facility jointly funded by STFC, the Large Facilities Capital Fund of BIS, and the University of Exeter.

CHAPTER IV

Exclusion of Cosmic Rays in Protoplanetary Disks: Stellar and Magnetic Effects

4.1 Preface

The following work appears in the Astrophysical Journal, Volume 772, 5, 20 pp. (2013). The work is co-authored by Fred C. Adams[1] and Edwin A. Bergin[2]. The paper is copyright 2013, the American Astronomical Society, reproduced here under the non-exclusive right of republication granted by the AAS to the author(s) of the paper.

4.2 Abstract

Cosmic rays (CRs) are thought to provide an important source of ionization in the outermost and densest regions of protoplanetary disks; however, it is unknown to what degree they are physically present. As is observed in the Solar System, stellar winds can inhibit the propagation of cosmic rays within the circumstellar environment and subsequently into the disk. In this work, we explore the hitherto neglected effects of cosmic ray modulation by both stellar winds and magnetic field structures and study how these processes act to reduce disk

[1]Department of Physics, University of Michigan, 450 Church St, Ann Arbor, MI 48109
[2]Department of Astronomy, University of Michigan, 500 Church St, Ann Arbor, MI 48109

ionization rates. We construct a two-dimensional protoplanetary disk model of a T-Tauri star system, focusing on ionization from stellar and interstellar FUV, stellar X-ray photons, and cosmic rays. We show that stellar winds can power a Heliosphere-like analogue, i.e., a "T-Tauriosphere," diminishing cosmic ray ionization rates by several orders of magnitude at low to moderate CR energies ($E_{\rm CR} \leq 1$ GeV). We explore models of both the observed solar wind cosmic ray modulation and a highly simplified estimate for "elevated" cosmic ray modulation as would be expected from a young T-Tauri star. In the former (solar analogue) case, we estimate the ionization rate from galactic cosmic rays to be $\zeta_{\rm CR} \sim (0.23-1.4)\times10^{-18}$ s^{-1}. This range of values, which we consider to be the maximum CR ionization rate for the disk, is more than an order of magnitude lower than what is generally assumed in current models for disk chemistry and physics. In the latter elevated case, i.e., for a "T-Tauriosphere," the ionization rate by cosmic rays is $\zeta_{\rm CR} \lesssim 10^{-20}$ s^{-1}, which is 1000 times smaller than the interstellar value. We discuss the implications of a diminished cosmic ray ionization rate on the gas physics by estimating the size of the resulting MRI dead zones. Indeed, if winds are as efficient at cosmic ray modulation as predicted here, short-lived radionuclides (now extinct) would have provided the major source of ionization ($\zeta_{\rm RN} \sim 7.3 \times 10^{-19}$ s^{-1}) in the planet-forming zone of the young Solar Nebula.

4.3 Introduction

Ionization is one of the most fundamental processes that drives the physics and chemistry of young protoplanetary disks. From the physical perspective, processes such as accretion and planet formation depend crucially on the ability of the disk to transport angular momentum. The primary mechanisms posited for transport are gravitational instability (*Cameron*, 1978; *Boss*, 1997) and the magnetorotational instability (MRI; *Velikhov*, 1959; *Chandrasekhar*, 1960; *Balbus and Hawley*, 1991). For disks with masses similar to that of the minimum mass Solar Nebula ($M_d \lesssim 0.05\ M_\odot$; *Weidenschilling*, 1977) gravitational instability is not expected to be efficient and thus MRI is thought to drive angular momentum transfer. However,

for MRI to operate, the predominantly neutral disk must be sufficiently coupled to the magnetic fields through frequent ion–neutral collisions. Therefore ions are essential in setting the kinematic and turbulent properties of the disk, in turn impacting important physical processes such as accretion onto the star and planet formation. Indeed, it has been suggested that low-ionization MRI-inactive regions of the disk, a.k.a. "dead zones" (*Gammie*, 1996; *Matsumura and Pudritz*, 2003), provide a favorable safe haven for planetesimal formation from dust coagulation (*Gressel et al.*, 2012).

Futhermore, ionization plays an important role in the heating of circumstellar gas. Models of ionization by cosmic rays and X-rays have shown that the primary and secondary electrons generated in these processes can be a significant source of heating through inelastic collisions with gas molecules (*Glassgold and Najita*, 2001; *Glassgold et al.*, 2004; *Nomura et al.*, 2007; *Glassgold et al.*, 2012). This additional heating source can significantly raise gas temperatures in the innermost radii and the tenuous surface layers of the disk, thereby influencing the strength and opacity of the observed emission lines.

Finally, ions are critical for powering gas-phase chemistry, which proceeds predominantly through ion-neutral reactions – the main chemical pathways in the interstellar medium. At low temperatures ($T < 50$ K), ion–neutral reactions typically have reaction rates orders of magnitude faster than neutral–neutral reactions (*Watson*, 1976), and therefore are the dominant drivers towards gas-phase complexity and enhancing deuteration, e.g., though reactions with H_2D^+.

The circumstellar molecular reservoir of the disk will eventually provide the material that will feed young proto-Jupiters, thereby setting the initial chemical composition of the gas-giants. The turbulent properties of the disk also affects the efficiency with which the disk forms rocky planets and gas-giant cores (e.g., *Gressel et al.*, 2012), impacting the formation of smaller, Earth-like planets. As a result, ions, through dynamical, thermal, and chemical mechanisms, influence all aspects of planet formation.

The primary sources of ionization present in the disk environment include stellar and

interstellar UV radiation, stellar X-rays, decay of short-lived radionuclides, cosmic rays (CR), and thermal ionization. In the surface layers and close to the star ($R \lesssim 0.5$ AU), stellar UV and X-ray photons are the dominant ionizing agents. At large radii ($R \gtrsim 100$ AU) and in the dense disk midplane where the optical depth to stellar and interstellar radiation is extremely large, it is often assumed that cosmic rays permeate material with column densities $\Sigma_g \lesssim 100$ g cm^{-2} (*Umebayashi and Nakano*, 1981), providing a base level of ionization and permitting MRI driven turbulence in the outer disk (e.g., *Gammie*, 1996; *Perez-Becker and Chiang*, 2011a).

The need for CR ionization presents an interesting question. First, it is seen that within the Solar System the solar wind modulates CR protons with energies below ~ 1 GeV (*Gleeson and Axford*, 1967, 1968; *Webber and Lezniak*, 1974) within a region called the Heliosphere (*Davis*, 1955; *Axford et al.*, 1963). Results from the Voyager spacecraft show the Heliosphere extends out to distances of at least 121 AU (*Krimigis et al.*, 2011; *Decker et al.*, 2012), with the true boundary yet to be crossed. Young stellar objects are intrinsically magnetically active with significant mass-loss rates, and therefore it would be unsurprising for a young star to produce an analogous region of decreased CR flux, i.e., a "T–Tauriosphere." It is important to note that the background CR flux in massive star-forming regions can have an elevated CR flux, amplified by supernova interactions with nearby molecular clouds (*Fatuzzo et al.*, 2006).

Second, the star formation process is seen to reshape the magnetic environment (e.g., *Girart et al.*, 2006), and as a result the presence of magnetic structure can also modify cosmic ray propagation (*Padovani and Galli*, 2011; *Rimmer et al.*, 2012). Therefore it is not clear that cosmic rays are indeed present at rates predicted for the diffuse ISM ($\zeta_{\rm CR} \sim 10^{-16}$ s^{-1}; *McCall et al.*, 2003; *Indriolo et al.*, 2007; *Neufeld et al.*, 2010) or even at the levels predicted for dense molecular clouds (e.g., $\zeta_{\rm CR} \sim 3 - 7 \times 10^{-17}$ s^{-1}; *Black et al.*, 1990). It is the latter rate that is typically adopted in simulations of MRI turbulence and circumstellar chemistry.

For the first time, this work explores the potential for stellar winds and magnetic fields to exclude CRs from the protoplanetary disk environment. Although this effect is extraordinarily well-studied within our own Heliosphere, it is typically neglected in modeling of circumstellar disks. *Turner and Drake* (2009) were the first to attempt to account for this reduction by integrating the ISM cosmic ray spectrum above $E_{\rm CR} \geq 100$ MeV. As this current Chapter shows, however, the exclusion of cosmic rays should be significantly more efficient and will reduce cosmic ray fluxes at all energies $E_{\rm CR}$. Here we examine how both wind and magnetic processes modify the ionization rate in the deep planet-forming layers of the disk and show how this shielding, in turn, can affect the size of dead zones. This Chapter is only the first step toward a full understanding of these processes. In Chapter 6, we examine the effects of cosmic ray exclusion on molecular ion chemistry and make predictions for observable tests by the Atacama Large Millimeter/Submillimeter Array (ALMA).

The current Chapter is laid out as follows. In Section 4.4, we motivate the physical model and discuss the sources of ionizing radiation present in the disk. In Sections 4.5 and 4.6, we discuss the impact of stellar winds and magnetic fields on the cosmic ray ionization rate, respectively. In Section 4.7, we examine the effects of low ionization rates in the context of dead zones. In Section 4.8, we discuss the possibility of additional ionization from the decay of radionuclides. Finally, in Section 4.9, we summarize our results.

4.4 The Model

4.4.1 Physical Parameters

Physical models of the dust and gas in protoplanetary disks have become increasingly complex (e.g., *D'Alessio et al.*, 1998; *Woitke et al.*, 2009; *Fogel et al.*, 2011). However, in this work we aim to isolate and demonstrate the effects of modifications to the cosmic ray flux and energy spectrum. To do this, we have created a generic model of a T-Tauri disk and have altered the incident cosmic ray flux. While the structure will depend in detail

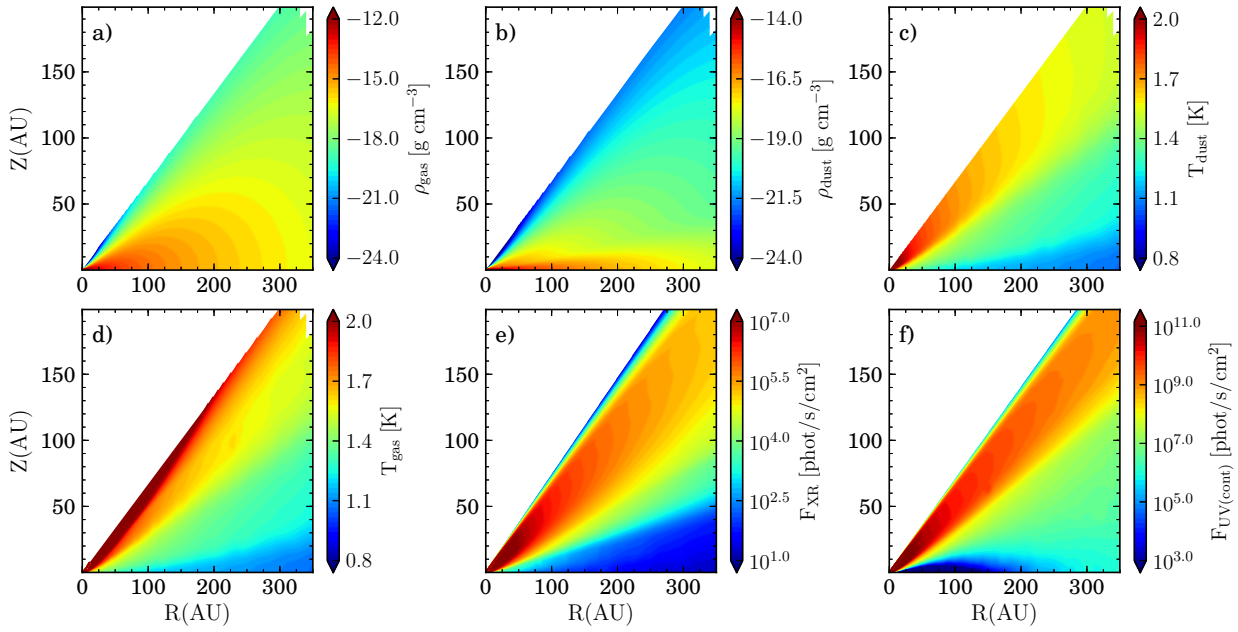

Figure 4.1 Model a) gas density, b) dust density, c) dust temperature, d) gas temperature, and e) integrated X-ray- and f) UV-radiation fields. The UV flux is integrated between 930 – 2000 Å and has a spectral shape of TW Hydra (*Herczeg et al.*, 2002, 2004). The model X-ray flux has a total luminosity of $L_{\rm XR} = 10^{29.5}$ erg s^{-1} between 0.1 – 10 keV.

on the assumptions made for this incident flux (e.g., additional gas heating produced from secondary electrons), we have set out to understand the scope and intensity of cosmic rays throughout the disk in the context of ionization.

With that established, we have created a 2D azimuthally symmetric model of a disk with the radiation transfer capabilities of the TORUS code (*Harries*, 2000; *Harries et al.*, 2004; *Kurosawa et al.*, 2004; *Pinte et al.*, 2009). The 2D model structure and dust composition is fixed and then passively irradiated by the central star as described in detail below. For our fixed density structure we have implemented a simple disk model of the form presented in *Andrews et al.* (2011):

$$\Sigma_g(R) = \Sigma_c \left(\frac{R}{R_c}\right)^{-1} \exp\left[-\left(\frac{R}{R_c}\right)\right], \tag{4.1}$$

$$h(R) = h_c \left(\frac{R}{R_c}\right)^{\psi}, \tag{4.2}$$

$$\rho_s(R,Z) = \frac{(1-f)\Sigma}{\sqrt{2\pi}Rh} \exp\left[-\frac{1}{2}\left(\frac{Z}{h}\right)^2\right], \tag{4.3}$$

and

$$\rho_l(R,Z) = \frac{f\Sigma}{\sqrt{2\pi}R\chi h} \exp\left[-\frac{1}{2}\left(\frac{Z}{\chi h}\right)^2\right]. \tag{4.4}$$

The first equation describes the radial surface density, a power-law with an exponential taper, where Σ_c and R_c are the characteristic surface density and radius of the profile, respectively. In this simple model, we mandate that both the gas and dust follow the same radial surface density profile, with the critical dust surface density equal to $\Sigma_d = \Sigma_g/100$ as per the standard ISM ratio. The values for the parameters used are outlined in Table 4.1 and are fixed unless otherwise noted.

Motivated by the *Spitzer* inference that small grains are not present in the upper layers of protoplanetary disks, i.e., are settled (*Furlan et al.*, 2006), we have incorporated the UV and X-ray optical effects of dust settling into our model. Following the prescription described in

Andrews et al. (2011), we have used an approximation to include vertical size segregation of dust grains by defining two distinct grain populations: one distribution corresponding to large, settled millimeter-sized grains and a second corresponding to a small micron-sized grain population, e.g., the "atmosphere." Both the micron-sized grains and gas are distributed with a Gaussian profile of scale height $h(R)$ given by Equation (4.2) where h_c is the characteristic scale height of the model and ψ is the power law dependence of the scale height versus radial distance. The large grains are distributed over a smaller scale height χh. The value of $\chi < 1$ is fixed to 0.2, or, equivalently, large grains are distributed over 20% of the scale height of small grains. While the vertically integrated gas mass to dust mass ratio is set to be 100, the gas to dust mass ratio is much larger in the surface layers and much smaller in the midplane. This geometry is expected due to grains preferentially settling out from the surface and increasing the mass of dust in the midplane, while simultaneously depleting the surface of dust.

For the dust chemical composition, we implement a blend of 80% astronomical silicates (*Draine and Lee*, 1984) and 20% graphite; the mix is not varied between different size populations. Both dust populations (atmosphere and midplane) are described by an MRN distribution (*Mathis et al.*, 1977), e.g., $n(a) \propto a^{-p}$ where $p = 3.5$, and have a characteristic minimum and maximum size $a_{\rm min}$ and $a_{\rm max}$. The minimum size is furthermore fixed to be $a_{\rm min} = 0.005$ μm across all populations. The small grains are broken up into two subsets, one with $a_{\rm max} = 1$ μm corresponding to 15% small grains by mass and a second with $a_{\rm max} = 10$ μm accounting for 85% of the mass in small grains. The large grains are a single population with $a_{\rm max} = 1$ mm. We have mandated that the mass in large grains, f, is 85% of the total dust mass, see Equations (4.3) and (4.4).

On this fixed model, TORUS solves for the dust thermal radiative equilibrium using the Lucy method (Lucy 1999). For the central star, we adopt the following parameters: $M = 1.06$ $M_\odot$, $R = 1.83$ $R_\odot$, and $T_{\rm eff} = 4300$ K. Furthermore, the dust temperatures computed by TORUS are assumed to be equal to the gas temperatures. We find that this

Table 4.1. Stellar and disk model parameters.

Stellar Model	
Stellar Mass	1.06 $M_\odot$
Stellar Radius	1.83 $R_\odot$
Stellar $T_{\rm eff}$	4300 K
$L_{\rm UV}$	2.9 $\times 10^{31}$ erg s^{-1} [a]
$L_{\rm XR}$	$10^{29.5}$ erg s^{-1}
Disk Model	
$R_{\rm inner}$	0.1 AU
$R_{\rm outer}$	400 AU
$M_{\rm dust}$	3.9 $\times 10^{-4}$ $M_\odot$
$M_{\rm gas}$	0.039 $M_\odot$
$a_{\rm max}$ [atm.]	1μm (15%)
	10μm (85%)
$a_{\rm max}$ [midplane]	1 mm
$a_{\rm min}$	0.005 μm
f	0.85
χ	0.2
ψ	0.3
Σ_c	3.1 g cm^{-2}
R_c	135 AU
h_c	12 AU

[a] As computed from the observed FUV spectrum of TW Hya integrated between 930 and 2000 Å (*Herczeg et al.*, 2002, 2004).

assumption is acceptable as the bulk mass of the disk beyond $R = 0.5$ AU is well below the temperature threshold for thermal ionization ($T >$1000 K; *Fromang et al.*, 2002). To check this assumption, we have computed a simple equilibrium gas temperature by balancing heating from stellar X-rays against grain–gas collisional cooling (*Glassgold and Najita*, 2001; *Glassgold et al.*, 2004; *Qi et al.*, 2006) and find that the majority of the disk is below the thermal ionization threshold. For completeness, we show the calculated gas temperature in Figure 4.1d., but emphasize that only the dust temperatures are used in the following calculations as this work focuses on ionization in the densest material where the dust and gas are thermally coupled. The density and thermal structure of the disk model are plotted in Figure 4.1.

4.4.2 Disk Ionization Processes

4.4.2.1 Stellar Ionization

It is well known that young T-Tauri stars are bright X-ray and UV emitters (*Feigelson and Montmerle*, 1999). This emission irradiates the circumstellar environment and drives chemical, ionizing, and thermal physics. The radiation from the star reaches the flared disk surface at a predominantly glancing angle and is scattered and absorbed by the circumstellar dust and gas. While the tenuous disk atmosphere is bathed completely by stellar UV and X-ray radiation, the large line-of-sight optical depths to the midplane hinder ionizing photons reaching the very densest outer regions (Figure 4.1). It is thus important to model the propagation of radiation in the disk as accurately as possible to determine the volume of disk gas that is exposed to the stellar ionizing photons (e.g., *Glassgold et al.*, 1997; *Igea and Glassgold*, 1999). In this section we quantitatively show the relative contribution from each of the dominant sources of ionization for our prototypical disk model.

To determine the position dependent UV and X-ray fields, we employ a Monte Carlo radiative transfer code as described in *Bethell and Bergin* (2011a,b). For the input stellar UV field, we adopt the observed spectrum of TW Hya (Figure 4.2; *Herczeg et al.*, 2002,

2004). The continuum opacity is set by the position dependent dust model and is computed via the Monte Carlo code at eight discrete wavelengths and interpolated between the range 930-2000 Å. In addition to these continuum points, we include the Monte Carlo radiative transfer of Lyman-α photons as described in *Bethell and Bergin* (2011a). In addition to dust scattering, Lyman-α photons undergo resonant isotropic scattering off hydrogen atoms, and therefore to determine the location of this hydrogen scattering layer the equilibrium H and H_2 abundances are computed using the method of *Spaans and Neufeld* (1997) and H_2 self-shielding functions of *Tielens and Hollenbach* (1985).

The methodology of the X-ray radiative transfer is similar to that of the UV and incorporates both absorption and scattering of the X-ray photons. We have used the updated X-ray cross sections of *Bethell and Bergin* (2011b) that incorporate the recently updated solar abundances of *Asplund et al.* (2009). *Bethell and Bergin* (2011b) found that even in the case of a fully dust-settled disk there exists an X-ray opacity "floor" from the gas. Therefore, while settling does decrease the X-ray opacity, it is reduced by at most a factor of two at $\sim$ 1 keV.

The input X-ray spectra were generated using the MEKAL model (*Liedahl et al.*, 1995) included in *XSPEC* (*Arnaud*, 1996) and correspond to a two-temperature optically thin thermal plasma. In Figure 4.2, the black line corresponds to a "characteristic" T-Tauri X-ray spectrum as measured at the stellar surface with temperature components corresponding to $T = 9$ MK and 30 MK respectively (*Getman et al.*, 2005; *Preibisch et al.*, 2005). On the same plot, the light grey line corresponds to the spectral shape typical of a T-Tauri in a X-ray high-flaring state (*Getman et al.*, 2008), normalized to the same luminosity as the quiescent spectrum with temperature components of $T = 12$ MK and 100 MK respectively.

The second spectrum is characteristic of T-Tauri stars with high X-ray luminosities ($L_{\rm XR} \gtrsim 10^{31}$ erg s^{-1}) and is thought to be the result of high stellar X-ray flare activity. Observations of X-ray flaring sources show that during this period the X-ray spectrum furthermore becomes characteristically harder (*Getman et al.*, 2008). In the following calcula-

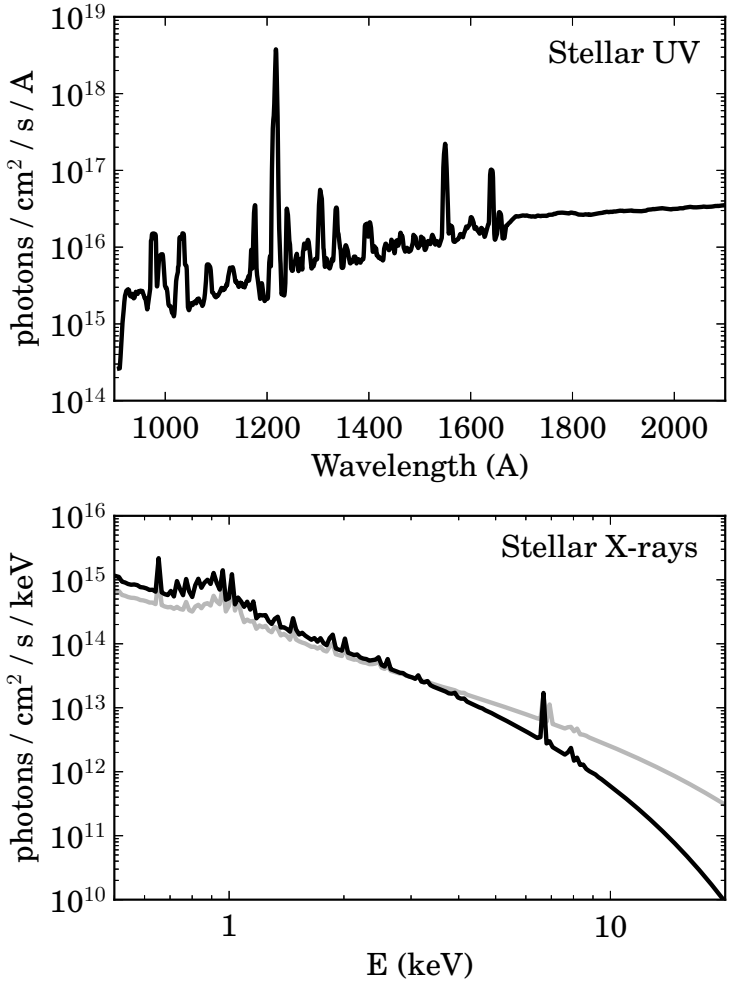

Figure 4.2 Model UV and X-ray spectra from the central star taken at the stellar surface. *Top:* Observed FUV spectrum of TW Hya (*Herczeg et al.*, 2002, 2004); note the strong Ly-α emission at 1216 Å. *Bottom:* Model X-ray spectra as described in Section 4.4.2.1. The black line shows a "characteristic" T-Tauri X-ray spectrum and the grey line corresponds to a highly flaring T-Tauri star. Both spectra are normalized to $L_{\rm XR} = 10^{29.5}$ erg s^{-1}. We note that both models rise below $E \sim 1$ keV because we do not a include foreground absorption component in the model, typically required to reproduce observed foreground-extincted X-ray spectra.

tions we consider the "characteristic" (Fig. 4.2, black line) X-ray spectrum in our benchmark model, but in Section 4.7.3 we consider the implications for an enhanced $L_{\rm XR}$ and harder X-ray spectrum.

The photon propagation is treated using the Monte Carlo code of *Bethell and Bergin* (2011b), where X-ray photons originate from the central star and then scatter/absorb as they propagate through the disk. The radiative transfer is computed at energies ranging $E = 1$ – 20 keV in 1 keV intervals. We note that some previous papers have adopted the assumption that X-rays are generated in accretion streams originating high above the stellar surface and therefore are able to "shine down" onto the disk. For example, *Igea and Glassgold* (1999) assume X-rays originate at a height of $z \approx 10\ R_\odot$ above the midplane. However, even if this is the case, beyond 1 AU the difference in incidence angle between photons coming from the stellar surface and from an accretion stream would be $\lesssim 3°$; thus, the approximation of a point source origin is satisfactory beyond 1 AU. The results of the UV and X-ray transfer are shown in Figure 4.1 (e and f).

Ultraviolet ionization (with rate $\zeta_{\rm UV}$) acts largely on carbon in the upper atmosphere of the disk. As an upper limit we assume all carbon is in C or CO with $\chi_{\rm C} = 1.4 \times 10^{-4}$ and approximate the C–CO transition layer by balancing CO photodissociation with CO formation (*Nelson and Langer*, 1997). The UV volumetric ionization rate ($\zeta_{\rm UV}$ multiplied by the number density of carbon atoms), in units of $\rm s^{-1}\ cm^{-3}$, is shown in Figure 4.3 (a). The volumetric ionization rate is a rough proxy for the electron production rate per unit volume (as opposed to comparing the less intuitive ionization rate per C against X-rays or cosmic rays per H_2).

X-ray photons have a higher penetration column compared to UV and can ionize denser regions, acting primarily on H_2 and He. We note that while gas and metals in the dust provide an important source of X-ray photon extinction, the ionization of H_2 produces the bulk of the electron/ion abundance, along with He to a lesser extent. In Figure 4.3 (b) we plot the volumetric ionization rate due to X-ray ionization of H_2 using the X-ray ionization

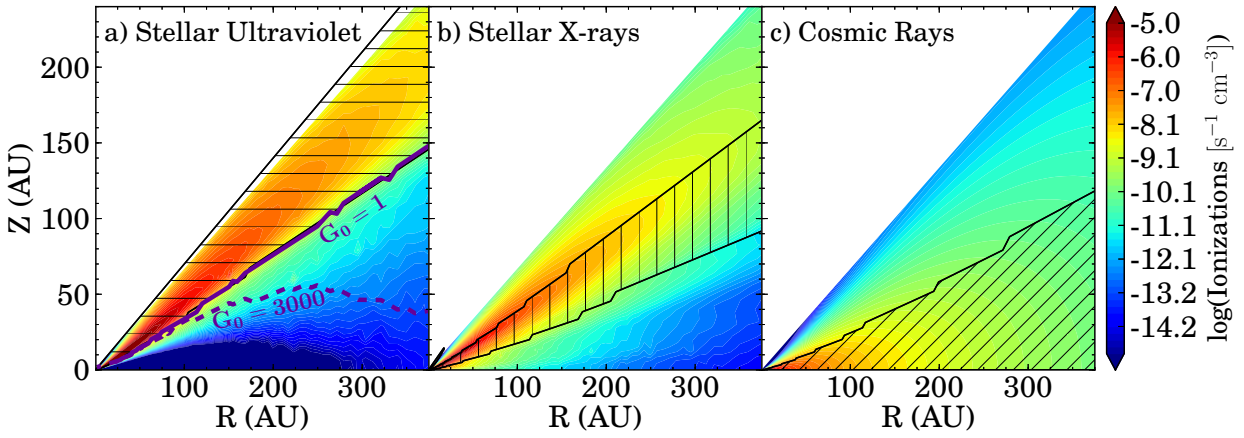

Figure 4.3 Relative contribution of stellar UV, X-rays, and cosmic rays to the total ionization rate. Colored contours show the volumetric ionization rate due to each source on the same scale. Hatched region delineates region of the disk where each respective source of ionization provides $> 30\%$ of the total ionizations per unit time per unit volume. The filled contours are a) FUV ionization of C, $n_{\rm C}\zeta_{\rm UV}$; b) X-ray ionization of H_2, $n_{\rm H_2}\zeta_{\rm XR}$; c) cosmic ray ionization of H_2, $n_{\rm H_2}\zeta_{\rm CR}$, for a standard ISM cosmic ray ionization rate $\zeta_{\rm CR} = 5 \times 10^{-17} \exp\left[-\Sigma/(96 \text{ g cm}^{-2})\right]$. See Fig. 4.4 for details of the G_0 contours (thick purple lines).

cross sections of *Igea and Glassgold* (1999) for the case of a settled (segregated) disk and assume an energy $\delta\epsilon = 37$ eV is necessary to produce an ion pair (*Shull and van Steenberg*, 1985; *Voit*, 1991; *Igea and Glassgold*, 1999), as a result, a 1 keV X-ray photon produces $\sim$ 27 ion pairs.

Taking the TW Hydra FUV field, $L_{\rm XR} = 10^{29.5}$ erg s^{-1}, $\zeta_{\rm CR} = 5 \times 10^{-17}$ s^{-1} H^{-1} and $\Sigma_{\rm CR} = 96$ g/cm^2 (see Section 4.4.2.3 regarding CR parameters), we plot the volumetric ionization rate from each major ionization source on the same scale (Figure 4.3). The surface is clearly dominated by UV ionization of carbon (left panel), while at a deeper intermediate layer X-rays dominate (center panel). The black hatched regions indicate where each source provides at least 30% of the total ionizations respectively.

4.4.2.2 Interstellar Ultraviolet Ionization

In addition to ultraviolet irradiation from the central star, the interstellar radiation field (ISRF) provides an external source of UV ionization. For an isolated disk or low mass star forming region the interstellar field provides an omnidirectional incident UV flux $\int F_\nu d\nu = 1.6 \times 10^{-3}$ erg cm^{-2} s^{-1} between 912 – 2000 Å, corresponding to $G_0 = 1$ (*Habing*, 1968). For comparison, the integrated flux from the star at a distance of 100 AU has typical values of $G_0 = 240$ – 1500 (*Bergin et al.*, 2004), dropping off as $\propto r^{-2}$. However, for a disk in a stellar cluster G_0 can be much higher, with values ranging from 300 – 30,000, with a typical value of 3000 (*Fatuzzo and Adams*, 2008). As a result, the interstellar field in a cluster can rival the stellar FUV radiation in the outermost regions of the disk. This complication will certainly have important chemical implications but in this section we focus on the implications for outer disk ionization.

To address this problem we took a subsample of points throughout the disk and computed a weighted optical depth evenly spaced over 4π steradians. The details of this approach are discussed in Appendix A. Unlike the case of stellar FUV ionization, it is not carbon, but rather sulfur that feels the interstellar UV ionization in the outer disk edge. This difference arises because in the outer disk, CO self-shielding severely limits the thickness of the CII ionization front. Sulfur self-shields as well, but at a much less efficient rate (*Perez-Becker and Chiang*, 2011b), and therefore the thickness of the SII front is set instead by dust attenuation. Combining the stellar and interstellar UV fields, we compute a simple equilibrium sulfur chemistry (see Appendix B) to determine the volumetric ionization rate arising from the ISRF.

We re-plot the combined fractional contribution from stellar FUV and interstellar FUV in Figure 4.4 (see also Figure 4.3 (a), purple lines). We consider both an interstellar average case $G_0 = 1$ and an enhanced external field, $G_0 = 3000$. The $G_0 = 1$ case is very similar to the star alone, while the $G_0 = 3000$ case shows that for an elevated interstellar flux the ionization from the FUV can become significant. We note the exact location of the

ISRF boundary depends on one's assumptions, namely the sulfur chemistry, which we have significantly simplified. Nonetheless, the interstellar radiation field, especially in the cluster environment, can create a thin ionized layer on the disk exterior and enhance the surface ionization (Figure 4.4, bottom panel) and can even become the dominant source of ionization in the absence of cosmic rays.

4.4.2.3 Cosmic Ray Ionization

Galactic cosmic rays are high energy atomic nuclei, largely protons (87%) with 12% alpha particles and the remaining $\sim 1\%$ as heavier atoms. In our Solar System, galactic CRs are strongly modulated by the solar wind making direct measurements of CR spectrum difficult, especially at low energies (see also *Nath et al.*, 2012). The extrasolar ISM CR ionization rate $\zeta_{\rm CR}$ has been studied using various observational and theoretical techniques (e.g., using molecular ion emission such as HCO^+ and H_3^+, see discussion and references in *Indriolo and McCall*, 2012) as well as towards sources spanning vastly different physical environments. Values as high as $\zeta_{\rm CR} \sim 10^{-15}$ s^{-1} have been measured for diffuse cloud sources (*McCall et al.*, 2003; *Shaw et al.*, 2008) while values as low as $\zeta_{\rm CR} \sim 1 \times 10^{-17}$ s^{-1} have been derived for dense cores (e.g., *Caselli et al.*, 1998). In Figure 4.3, we use typical values $\zeta_{\rm CR} = 5 \times 10^{-17}$ s^{-1} H^{-1} and $\Sigma_{\rm CR} = 96$ g/cm^2 (*Umebayashi and Nakano*, 1981). It is important to point out that this attenuation column is significantly higher than both FUV photons (10^{-3} g cm^{-2}) and 1 keV X-rays (0.5 g cm^{-2}), allowing only cosmic rays to penetrate the densest gas. Furthermore, the disk is isotropically bombarded by cosmic ray particles, causing a greater volume of gas to be more readily ionized by cosmic rays (see Figure 4.3). We note that recent measurements and models have revised both the value of the CR ionization rate and functional form of $\zeta_{\rm CR}(N_{\rm H_2})$ (discussed below), but for the purposes of illustration in Figure 4.3 we adopt the standard *Umebayashi and Nakano* (1981) values.

One explanation for the range in measured cosmic ray ionization rates is variations in the local supernova frequency and proximity, as well as magnetically controlled propagation

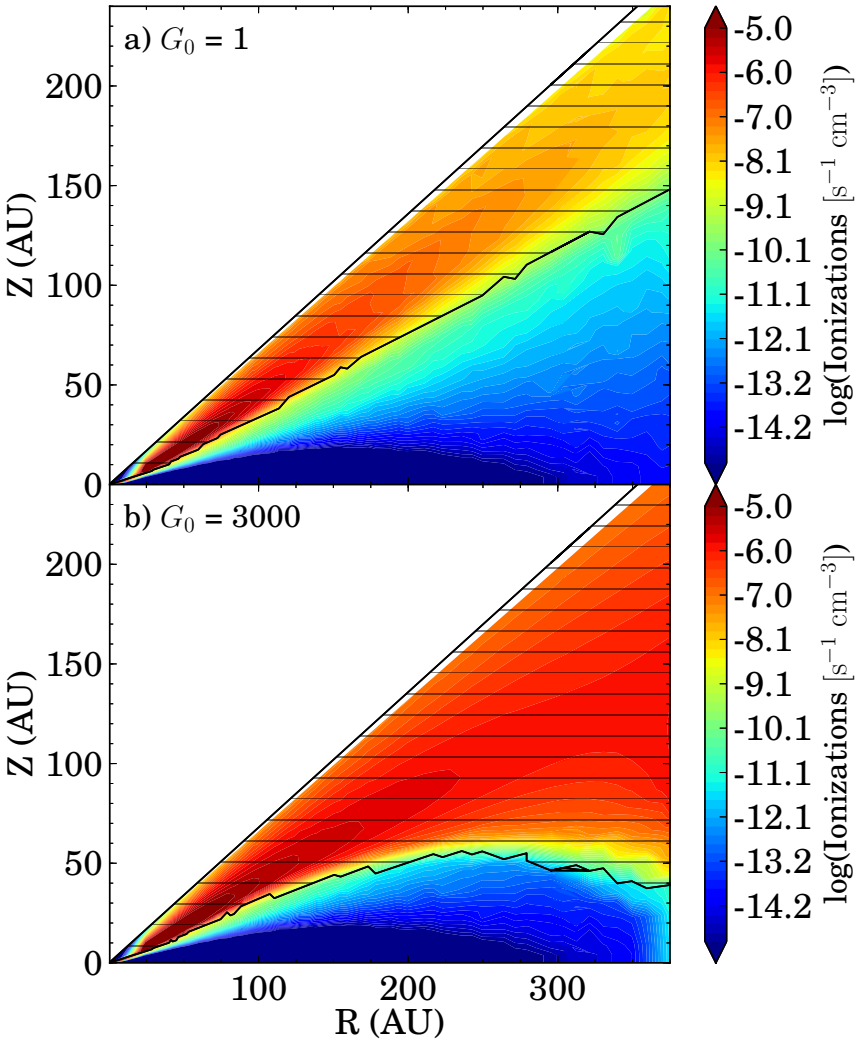

Figure 4.4 Volumetric ionization rate (filled color contours) from stellar FUV and interstellar FUV combined for the cases of: a) a typical external field, $G_0 = 1$, and b) an elevated cluster-like field, $G_0 = 3000$. The black hatched lines denote the region where the total (stellar plus external) FUV flux provides $> 30\%$ of the ionizing radiation. The $G_0 = 1$ case is similar to the star-only, while the cluster scenario provides a significant source of ionization both at the surface and outer edge of the disk.

within molecular clouds (*Fatuzzo et al.*, 2006). *Padovani et al.* (2009) proposed that the range in measured rates across different types of sources can be reconciled by accounting for the low energy cosmic rays ($E_{\rm CR} < 100$ MeV) and their attenuation with column density. At high densities, *Umebayashi and Nakano* (1981) find that cosmic rays attenuate exponentially with a critical mass column of 96 g cm^{-2}. To reproduce observations in both low density (diffuse clouds) and high density regimes (cores), *Padovani et al.* (2009) found a better fit to their numerical calculations by using combined power law and exponential terms with relative contributions depending upon choice of incident spectrum, $\rm J_{CR,0}(\mathit{E})$. The full functional form of this expression is given by :

$$\zeta_{\rm CR} = \frac{\zeta_{\rm pow,0} \times \zeta_{\rm exp,0}}{\zeta_{\rm exp,0} \left(\frac{N({\rm H_2})}{10^{20}{\rm cm^{-2}}}\right)^{\alpha} + \zeta_{\rm pow,0} \left[\exp\left(\frac{\Sigma}{\Sigma_0}\right) - 1\right]}, \tag{4.5}$$

which reproduces the power law behavior at low densities and exponential behavior at high densities (*Padovani et al.*, 2013). The relation between surface and column density is given by $\Sigma = \mu m_{\rm p} N({\rm H_2})$ where $m_{\rm p}$ is the proton mass and $\mu = 2.36$.

There are four parameters in this fitting function: $\zeta_{\rm pow,0}$, $\zeta_{\rm exp,0}$, α and Σ_0. For a given incident CR spectrum, these parameters describe the shape of the integrated CR ionization rate $\zeta(N_{\rm H_2}) = \int 4\pi\sigma_{\rm ion} J(E) dE$. Because the cosmic ray energy spectrum is only marginally constrained at low energies, *Padovani et al.* (2009) consider two possible extremes for the local interstellar cosmic ray spectra (LIS) shown in Figure 4.5. The first of these is the LIS spectrum determined by *Webber* (1998) [W98] derived from extrapolated *Voyager* and *Pioneer* measurements up to 60 AU – generally considered to be the absolute minimum case. The second spectrum is from *Moskalenko et al.* (2002) [M02], which reproduces a large span of supplementary data including the proton, antiproton, and alpha particle spectra as well as the diffuse γ-ray background. We note that both spectra have been extrapolated at low energies, $E_{\rm CR} \lesssim 10$ MeV, by *Padovani et al.* (2009) from the original published calculations in the spirit of providing benchmark values for the incident cosmic ray spectra on a molecular

cloud.

For each of these LIS spectra (solid and dot-dash magenta lines, Fig. 4.5) *Padovani et al.* (2009) then numerically compute and fit $\zeta_{\rm CR}(N_{H_2})$ using the function provided in Equation (4.5). Table 4.2 lists the fitting coefficients for each LIS spectrum (see also Figure 4.5). We note that these values have been updated and refit from the original *Padovani et al.* (2009) values (see *Padovani et al.*, 2013).

The ISM value of $\zeta_{\rm CR}$ is, however, likely not appropriate for the circumstellar disk environment. Winds from young stars will be able to shield the disk from cosmic rays at magnitudes that will likely far exceed that of the solar wind due to rapid stellar rotation and strong stellar magnetic fields (*Svensmark*, 2006; *Cohen et al.*, 2012). In the following section we apply the results of *Padovani et al.* (2009) to compute $\zeta_{\rm CR}(N_{H_2})$ incident on the circumstellar disk for various degrees of wind-modulation efficiency, both at solar and more extreme levels.

4.5 Exclusion of Cosmic Rays by Stellar Winds

4.5.1 Modulation By the Solar Wind

As described in Section 4.4.2.3, our solar wind drives out low energy ($E \lesssim 1$ GeV) cosmic rays within a region called the Heliosphere, the very CRs responsible for the bulk ionization of H_2 in the ISM. Furthermore, the degree of modulation by the solar wind varies over the solar magnetic activity cycle by an order of magnitude at energies below $E_{\rm CR} < 100$ MeV (Figure 4.5). Understanding the detailed physics of cosmic ray modulation is still an open question (see review by *Florinski et al.*, 2011). To leading order, the dense slow solar wind originates from the hot ($\sim 1 - 2$ MK) solar corona and travels at the Sun's escape velocity, carrying with it magnetized plasma frozen-in from the surface of the Sun. The density of the wind and magnetic field strength decrease with distance from the Sun until the point at which pressure from the ISM overcomes that of the expanding solar wind. It is here

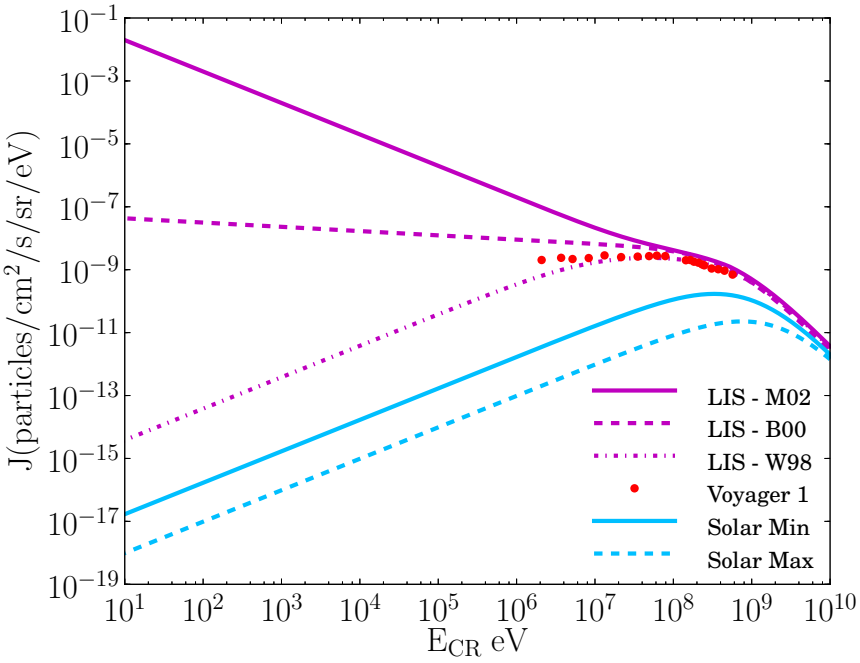

Figure 4.5 Local interstellar (LIS) cosmic ray spectra models (magenta) from top to bottom, solid: *Moskalenko et al.* (2002), dashed: *Burger et al.* (2000), dot-dash: *Webber* (1998). The red points are the most recent 2013 results from the Voyager 1 spacecraft (*Webber and McDonald*, 2013). Spectra at $R = 1$ AU (blue) for solar minimum ($\phi = 500$ MeV, solid) and solar maximum ($\phi = 1350$ MeV, dashed). *Moskalenko et al.* (2002) and *Webber* (1998) are the extrapolations of *Padovani et al.* (2009) below $E_{\rm CR} \lesssim 10$ MeV.

the solar wind is compressed resulting in a magnetic "pile-up," forming a barrier which prevents low energy CRs from freely streaming through the Solar System (*Weymann*, 1960; *Burlaga et al.*, 2005; *Opher et al.*, 2011). Young, magnetically active rotating T-Tauri stars are likewise expected to have stellar winds (*Guenther and Emerson*, 1997; *Vidotto et al.*, 2009) in addition to disk winds (*Hollenbach et al.*, 2000) or X-winds (*Shu et al.*, 1994), and therefore it would be unsurprising for T-Tauri stars to similarly drive out low energy cosmic rays within an analogue "T-Tauriosphere." Previous papers have examined reductions in the cosmic ray flux for the early Sun in context of the young, $\lesssim$ 2 Gyr-old Earth (*Svensmark*, 2006; *Cohen et al.*, 2012) and find that even at this relatively late stage their models predict substantial reduction in cosmic ray flux.

It is important to note that even though the mechanism by which the magnetic field is generated on the surface of a T-Tauri star is different from a main sequence dwarf like our Sun, the ability to drive and the properties of a stellar wind simply depends on the presence of a corona, the mass of the star, stellar rotation, and the general magnetic topology on the surface. Bright X-ray emission from T-Tauri stars is thought to arise from both the stellar corona as well as an accretion shock (*Kastner et al.*, 2002; *Brickhouse et al.*, 2010). From X-ray measurements, typical temperatures for T-Tauri star's coronas can exceed 10 MK (*Feigelson and Kriss*, 1981; *Preibisch et al.*, 2005; *Flaccomio et al.*, 2012) compared to the relatively cooler 1-2 MK solar corona. Such hot coronae are thought to be "enhanced" versions of the Sun's corona (*Feigelson and Kriss*, 1981; *Feigelson and Montmerle*, 1999; *Favata and Micela*, 2003). A detailed discussion of the physics behind the link between the solar corona and generation of the solar wind can be found in *Gombosi* (2004); but in brief, the single most predictive factor of the efficiency of cosmic ray modulation by the solar wind is the magnitude of the magnetic activity at the solar surface. Between solar minimum and maximum, the cosmic ray flux observed at Earth varies by over an order of magnitude (see Figure 4.5). Additional parameters, like the solar wind speed, the degree of spiral wrapping in the wind, and mass loss rate ($\dot{M}$), are, to leading order, set by the escape velocity of the

star, the stellar rotation rate and surface magnetic topology (e.g., *Cohen*, 2011).

By using our knowledge of how cosmic ray modulation by winds operates in our only measured example, the Solar System, we can begin to learn something about how stellar wind modulation may operate and impact the circumstellar environment in other systems. In the following section we use the results of *Usoskin et al.* (2005) to make simple predictions for scaled-up degrees of cosmic ray modulation. To determine $\zeta_{\rm CR}(N_{H_2})$ in the extreme case of a T-Tauri star, we compare solar cosmic ray modulation against various cyclical solar parameters relating to the solar magnetic activity. We then extrapolate these results to obtain a starting point estimate for the degree to wind modulation of cosmic rays operates in the environment of a T-Tauri star. Such approximations will help illuminate our understanding and interpretation of ionization measurements in disks, which with existing limits on H_2D^+ towards disks already point to ionization rates lower than ISM (*Chapillon et al.*, 2011).

4.5.2 The Cosmic Ray Spectrum in a T-Tauriosphere

While the details of the mechanisms of cosmic ray exclusion are still an active area of research, there is fortunately abundant time-resolved data of the Sun. Sunspots have been monitored since the time of Galileo, and the Wilcox Solar Observatory has conducted daily observations of the Sun's global magnetic field since 1975[3]. Space weather is monitored on the timescale of minutes and cosmic ray rates have been monitored hourly (or more frequently) since 1964[4]. Such a wealth of time sequence data is useful because properties of the solar wind – the excluder – are set largely by the Sun. The winding of the field is determined by solar rotation; the magnetic field is for the most part frozen in from the Sun's surface. The magnetic activity cycles on the Sun are imprinted on the solar wind, and in turn directly impact the CR-modulating ability of the wind.

To empirically relate solar activity and the strength of cosmic ray modulation by stellar

[3]http://wso.stanford.edu/
[4]http://cosmicrays.oulu.fi

winds we use a parametric form of the differential energy spectrum of cosmic rays $J_{\rm CR}(E)$ at 1 AU. The expression below is commonly known as the "force-field" approximation, and it provides a very useful way to describe the observed shape of the cosmic ray spectrum throughout the solar cycle using a single parameter, the modulation potential ϕ (*Usoskin et al.*, 2005) with good astrophysical agreement at heliocentric distances, D, near $D = 1$ AU (e.g. *Caballero-Lopez and Moraal*, 2004; *Usoskin et al.*, 2005). Caveats of this approximation are discussed later in this section. The modulated cosmic ray proton spectrum $J_{\rm CR}(E)$ in units of cm^{-2} s^{-1} sr^{-1} eV/nucleon^{-1} is:

$$J_{\rm CR}(E,\phi) = J_{\rm LIS,CR}(E+\phi)\frac{E(E+2E_r)}{(E+\phi)(E+\phi+2E_r)}, \tag{4.6}$$

where

$$J_{\rm LIS,CR}(E) = \frac{1.9\times10^{-9}\ P(E)^{-2.78}}{1+0.4866\ P(E)^{-2.51}}, \tag{4.7}$$

with $P(E) = \sqrt{E(E+2E_r)}$ and the proton rest mass energy $E_r = 0.938$ GeV. In Equations (4.6) and (4.7), E is in GeV per nucleon and the modulation potential ϕ is in GeV. We note that values of the modulation potential ϕ in the literature and in this work are most frequently given in MeV, but in the commonly used functional form reproduced in Equation (4.7) energy must be provided in GeV. The LIS spectrum assumed by *Burger et al.* (2000) [B00], given in Equation (4.7), is typically used and is shown in Figure 4.5. Since this function is used to fit cosmic ray data, we stress that the specific assumption for $J_{\rm LIS}$ does not matter so long as the fit is accurate and it is not changed (it acts as a normalizing factor). Indeed, according to *Usoskin et al.* (2005) different definitions for ϕ have led to confusion in the literature, and in that work the authors attempt to reconcile this confusion and reconstruct a large time baseline of ϕ values, looking at the longterm variations in ϕ over roughly five solar cycles (see Fig. 7 of that work).

In addition to variations over the solar cycle, the modulation efficiency of the wind varies with heliocentric distance. For example, the cosmic ray flux at $E_{\rm CR} = 300$ MeV varies

from $D = 1$ AU to $D = 80$ AU by a factor of ~ 6 (*Caballero-Lopez and Moraal*, 2004). We emphasize that the force field approximation is indeed a simple approximation, which tends to *over predict* the cosmic ray flux at low energies at large heliocentric distances. For example, at $D = 60$ AU, the force field approximation over predicts the 20 MeV CR proton flux by a factor of $\sim 4.2\times$ as compared to a full numerical model of the one-dimensional cosmic ray transport equation (see Fig. 2 of *Caballero-Lopez and Moraal*, 2004). For energies above $E_{\rm CR} \gtrsim 80$ MeV, however, the approximation improves significantly and the predicted differential cosmic ray fluxes are in agreement with the full numerical model to better than 20% accuracy. For our simple models we assume a constant modulated spectrum incident on the disk as computed at $D = 1$ AU without radial variation; however, in Section 4.7.2, we consider the effect of a positive cosmic ray flux gradient on disk ionization.

To attempt to extrapolate the magnitude of modulation from solar values to the case of a more magnetically active T-Tauri star, we have correlated the time aggregated values of the modulation potential $\phi(t)$ (*Usoskin et al.*, 2005) against other time-resolved measured solar quantities, including mean magnetic field strength on the Sun from the Wilcox Solar Observatory data, number of sunspots from the *SPIDR*[5] database (*O'Loughlin*, 1997), and fractional area coverage of sunspots (*Balmaceda et al.*, 2009) shown in Figure 4.6. Because the mass loss rate in the solar wind is related to the coverage of open magnetic field line regions (*Cohen*, 2011), tracing the correlation between ϕ and the magnitude of the open $|B|$-field component via solar coronal hole measurements would prove the most useful. Coronal holes reveal regions where plasma can freely escape along open field lines, in contrast to X-ray bright regions where the hot plasma is trapped. The time coverage of coronal hole observations, however, cover just over one solar cycle (*Insley et al.*, 1997), and therefore the correlation cannot be accurately determined without a longer baseline of data. In Figure 4.6 we plot the solar mean magnetic field amplitude, the number of spots and the area of spot

[5]http://spidr.ngdc.noaa.gov/spidr/

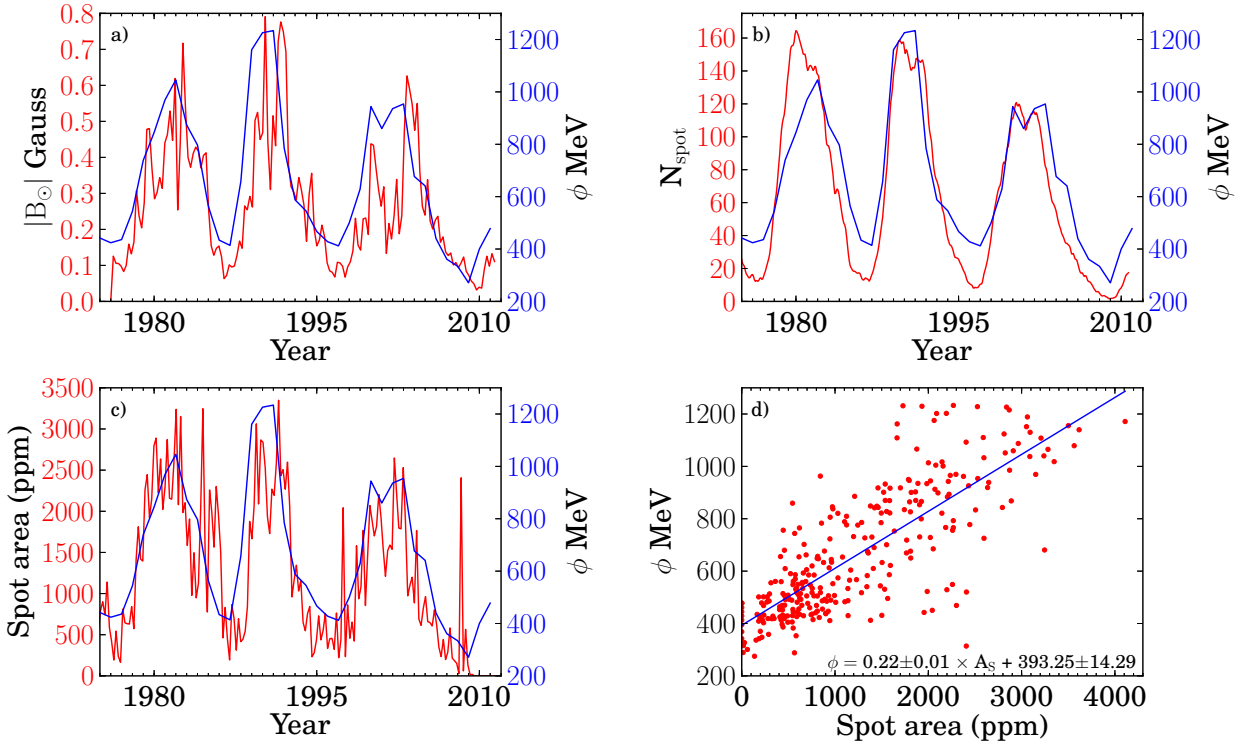

Figure 4.6 Time correlation of the cosmic ray modulation parameter ϕ (*Usoskin et al.*, 2005) with other solar quantities: a) solar mean magnetic field from the Wilcox Solar Observatory, b) number of sunspots (*SPIDR*; *O'Loughlin*, 1997), c) fractional area covered by sunspots in millionths of the solar surface area (*Balmaceda et al.*, 2009), and d) the correlation between spot area and modulation parameter with a linear fit. Fit parameters listed at the bottom right.

coverage alongside ϕ (blue curve in panels a, b, and c) as a function of time. By linking the state of the solar magnetic activity with the modulation parameter, ϕ, we can extrapolate ϕ to make a simple prediction for the degree of cosmic ray modulation for a more magnetically active young star.

These quantities are convenient as they can be measured for other stars, specifically magnetic field strength and spot coverage. Number of spots is less meaningful as T-Tauri stars are suggested to have single spots covering large areas (*Donati et al.*, 2007, 2011a,b, 2012). The magnetic field strengths on T-Tauri stars are complex, multicomponent and span a large range in magnitude (see the overview in *Johns-Krull*, 2007). Recent work to map photospheric magnetic topology on a handful of objects using spectropolarimetry (e.g., *Donati*, 2003; *Donati et al.*, 2007) may allow us in the future to link coronal hole coverage to radial field components on T-Tauri stars. For the time being, we are left with spot coverage area as the proxy for magnetic activity and cosmic ray exclusion.

Fractional coverage by spots ranges from 3% to 17% and is time variable (*Bouvier and Bertout*, 1989). Extrapolating the results in Figure 4.6 (d) yields cosmic ray modulation parameter values of ϕ = 4800 MeV, 9200 MeV, and 18,000 MeV for 2%, 4% and 8% spot coverage respectively. Under the force-field approximation, these modulation parameters, ϕ, fully describe the shape of the differential cosmic ray energy spectrum, $J_{\rm CR}(E, \phi)$, given in Equation (4.6). For spot coverage $\geq$ 10% and a stellar X-ray luminosity $L_{\rm XR} \geq 10^{29}$ erg s^{-1}, the cosmic ray flux falls below the ionizing X-ray flux from the star and can be neglected throughout the disk (see also Figure 4.3). Figure 4.7 shows the incident differential cosmic ray spectra $J_{\rm CR}(E, \phi)$ from Equation (4.6) with the caveats outlined in Section 4.5.2 for modulation at solar minimum, solar maximum, T-Tauri minimum (2%), and T-Tauri maximum (8%).

Using this simple empirical estimate, we find similar magnitudes of CR exclusion as the theoretical models of *Cohen et al.* (2012) [C12] and *Svensmark* (2006) [S06], which predict reduced cosmic ray fluxes at Earth under the conditions present for the young Sun (Y.S.), at

Table 4.2. $\zeta_{\rm CR}$ fitting parameters for different incident spectra shown in Figure 4.7, see Eq. (4.5).

Model	$\zeta_{\rm pow,0}$ [s^{-1}]	α	$\zeta_{\rm exp,0}$ [s^{-1}]	Σ_0 [g cm^{-2}]
ISM M02	6.8×10^{-16}	0.423	3.7×10^{-18}	210
ISM W98	2.0×10^{-17}	0.021	9.4×10^{-19}	260
Solar Min	1.3×10^{-18}	0.00	3×10^{-18}	190
Solar Max	2×10^{-19}	-0.01	8×10^{-19}	230
T-Tauri Min	1×10^{-20}	-0.03	2×10^{-19}	270
T-Tauri Max	3×10^{-22}	-0.03	2×10^{-19}	270

age $t = 0.8$ Gyr. We fit and extrapolate their results using Equation (4.6) and show these fits in Figure 4.7 (Y.S., dark pink lines) for comparison. While the specific flux of cosmic rays entering a T-Tauriosphere depends on either simplifying assumptions, i.e., our "scaled-up" Heliosphere approach, or the specifics of the detailed models, it is clear that cosmic rays are likely excluded at a substantial degree, at least ~ 3 orders of magnitude below solar levels for 1 MeV cosmic rays, and equivalently $\gtrsim 6$ orders of magnitude below the inferred ISM CR flux.

4.5.3 Extent of the T-Tauriosphere

How large do we expect the T-Tauriosphere, i.e., the circumstellar region of reduced cosmic ray flux, to be? The Sun's Heliosphere, for example, extends out to at least $R \sim 120$ AU. The boundary of the Heliosphere, called the Heliopause, is set roughly by the balance of the outward magnetic and ram pressure from the solar wind and the external pressure from the surrounding ISM. If the T-Tauriosphere only encompasses the inner regions of the disk, the outer disk would be left fully exposed to galactic cosmic rays.

The external pressure from the ISM in the solar neighborhood is approximately $P_{\rm ISM} \sim B_{\rm ISM}^2/8\pi$, where $B_{\rm ISM} \sim 3$ – 10 μG. To estimate the outward pressure from a T-Tauri star's stellar wind we must make a few assumptions. For the internal magnetic and ram pressure $P_{\rm mag}$ and $P_{\rm ram}$ we must assume a wind flow velocity v, mass-loss rate $\dot{M}$, and magnetic field

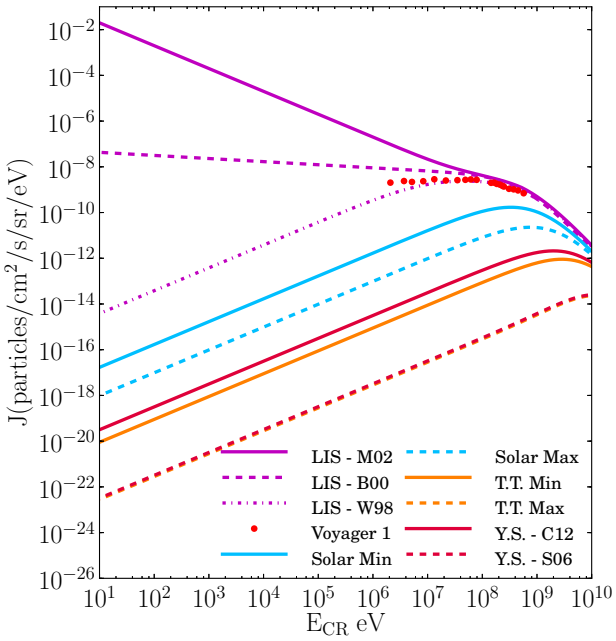

Figure 4.7 Modulated cosmic ray spectra with unmodulated ISM rates shown for comparison (magenta), as well as red points from recent Voyager 1 measurements, same as Figure 4.5. Blue lines – Solar: minimum $\phi = 500$ MeV and maximum $\phi = 1350$ MeV. Orange lines – T-Tauri extrapolation models: 2% spot coverage ($\phi = 4800$ MeV) orange dashed line and 8% spot coverage ($\phi = 18{,}000$ MeV). Solid dark pink line shows a fit by Eq. (4.6) to the results of *Cohen et al.* (2012) ($\phi = 3500$ MeV) and *Svensmark* (2006) ($\phi = 17{,}500$ MeV) both for the 800 Myr-old Sun.

dependence $B_{\rm w}$. The flow velocity is typically of order the star's escape velocity, and the wind's magnetic pressure is typically negligible at all radii compared to the ram pressure (see below). The mass-loss rate is a bit more complicated and depends on whether the wind is a stellar or disk wind. How a disk wind would interact with the T-Tauriosphere would require a full MHD treatment and is thus beyond the scope of this Chapter. However, this interaction could be important and could lead to more confined regions of CR exclusion or potentially enhance the ability of winds (star and disk-driven) to modulate the CR flux.

The outward pressure can be written as $P_{\rm wind} = P_{\rm mag} + P_{\rm ram} = B_{\rm w}(R)^2/8\pi + \dot{M}v/4\pi R^2$. The radial dependence of the magnetic field term depends on how tightly wound the wind is; for example, a perfectly radially outward flowing wind would drop as $B \sim R^{-2}$, but more circumferentially wrapped wind would drop as only R^{-1}, causing $P_{\rm mag}$ to drop as R^{-4} and R^{-2} respectively. Moreover, such a highly wrapped wind would exclude galactic cosmic rays even more efficiently, therefore leading to even more severe modulation not considered here. *Sterenborg et al.* (2011) created a grid of solar wind models to study the physical properties of the stellar wind when the Sun was $\sim$ 1 Gyr-old. That work found that the stellar wind was typically slower, had higher mass-loss rates and was stronger magnetically than at the present day, with typical values of $v = 266$ km/s, $B = 0.25$ mG, and $\dot{M} = 1.42 \times 10^{-12}$ $M_\odot$ yr^{-1} taken at $\sim$ 1 AU respectively. At 1 AU the contribution from each pressure component is $P_{\rm mag} = 2.3 \times 10^{-9}$ dyne cm^{-2} and $P_{\rm ram} = 8.4 \times 10^{-7}$ dyne cm^{-2}; as a result, for either radial or tightly would wind magnetic fields, $P_{\rm ram}$ always exceeds $P_{\rm mag}$ outside of $\gtrsim 0.1$ AU.

Therefore, using the simple equality $P_{\rm ISM} = P_{\rm wind} \rightarrow B_{\rm ISM}^2/8\pi = \dot{M}v/4\pi R^2$, we can solve for the radius at which the external ISM pressure and outward wind pressure balance. Given the wind values above, the boundary occurs at 1540 AU and 460 AU for $B_{\rm ISM} = 3$ μG and 10 μG respectively. The values of the parameters discussed above are applicable for a very young Sun, but are old compared to the age of a T-Tauri star, 1-10 Myr. Youthful T-Tauri stars are even more magnetically active and likely have elevated coronal activity, resulting in much higher stellar-wind mass loss. Furthermore, rapid rotation characteristic of the first $\sim$

30 - 50 Myr will strongly enhance the stellar wind's ability to modulate the cosmic ray flux (see Fig. 2 of *Cohen et al.*, 2012). This can operate in tandem with mass loss from a disk wind, creating substantially higher mass loss rates $\dot{M}$. Based upon observed T-Tauri X-ray fluxes, *Decampli* (1981) predict that a T-Tauri star's hot coronal gas has sufficient pressure to power mass loss rates via a stellar wind of up to $\dot{M} \sim 10^{-9} M_{\odot}$ yr^{-1}. With all other parameters held constant, this would correspond to an $R \sim$ 12,000 AU-sized T-Tauriosphere for a $B_{\rm ISM} = 10$ μG background magnetic field, much larger than typical disk sizes of a few hundred AU. At this point the outer boundary could instead be set by intervening remnants of the parent molecular cloud.

How the disk and environment would interact with the solar wind "fluid" however is beyond the scope of this Chapter, e.g., is the T-Tauriosphere doubly-lobed or does it flow over the disk producing wind eddies and vortices? How do the magnetic fields contained in the stellar winds and disk winds connect with external magnetic fields at an analog "T-Tauriopause?" Nonetheless, as we have demonstrated, the region of cosmic ray exclusion likely extends over a large region and it would not be unreasonable for it to fully enclose the disk, even for massive disks hundreds of astronomical units in radius, and therefore for the remainder of this Chapter we consider the incident cosmic ray spectra to be uniformly modulated over the entire disk.

4.5.4 Cosmic Ray Attenuation

From these cosmic ray spectra $J_{\rm CR}(E)$ described in Section 4.5.2 we can now determine the integrated ionization rate as a function of H_2 column density. The study of cosmic ray penetration clouds and circumstellar disks has an extensive history (e.g. *Hayakawa et al.*, 1961; *Cesarsky and Volk*, 1978; *Umebayashi and Nakano*, 1981; *Padovani et al.*, 2009) The interaction and attenuation of a cosmic ray in molecular matter critically depends on its initial energy. As a result the shape and energy range of the incident CR intensity spectrum directly determines the integrated ionization rate $\zeta = \int 4\pi\sigma_{ion}(E) J_0(E) dE$, where $J_0(E)$ is

the differential cosmic ray spectrum (from now on simply spectrum) at the disk surface (see Fig. 4.7) and $\sigma_{ion}(E)$ is the energy dependent ionization cross section of H_2.

Here we compute the ionization rate $\zeta_{\rm CR}$ as a function of depth, given a "heliospheric" incident CR proton spectrum on a disk. In general, the decay of cosmic ray flux with column density can be thought of as an energy reprocessing of CR particles with column density. To compute the density evolution of the cosmic ray flux, we follow the "continuous slowing down approximation" method of *Padovani et al.* (2009) (hereafter P09). Ionization processes included are ionizations of H_2 and He by protons and electrons, electron capture, dissociative ionization, double-ionization, and a correction for ionization by secondary particles. We consistently solve for the particle travel range, Equation (21) of that work, the energy loss incurred, and subsequent particle energy reprocessing, see Equation (25) of P09. Furthermore, we include a correction for secondary ionizations following *Glassgold and Langer* (1973) with a logarithmic extrapolation at high energies as was done in P09. In Figure 4.8 we show the resulting spectra for the case of solar maximum wind modulation ($\phi = 1350$ MeV) at the indicated log column densities. This can be directly compared with the column density evolution presented in Figures 9 and 10 of P09 for the M02 and W98 incident spectra. We note that from this point, we adopt the M02 spectra as our "true" interstellar spectrum and compare our modulated results to this.

Finally, each differential energy curve $J(E_{\rm CR})$ is then integrated between $E_{\rm CR} = {\rm I}(H_2)$ and 100 GeV to produce a total ionization rate per H_2: $\zeta(N_{H_2}) = \int 4\pi\sigma_{ion}(E)J(E)dE$ s^{-1}, where σ_{ion} is the CR ionization cross section provided by P09. These results are shown in Figure 4.9 (squares). These points are then fit (solid lines) using the function provided in Equation (4.5) and the corresponding coefficients are listed in Table 4.2. For the most severely modulated T-Tauri models there is a small rise in the ionization rate at high column density that results from particle conservation of the reprocessed high energy particles. This effect is otherwise hidden in the models that have more initial cosmic rays energies below $E_{\rm CR} < 100$ MeV. We do not fit the bump using the simple parameterization as it only

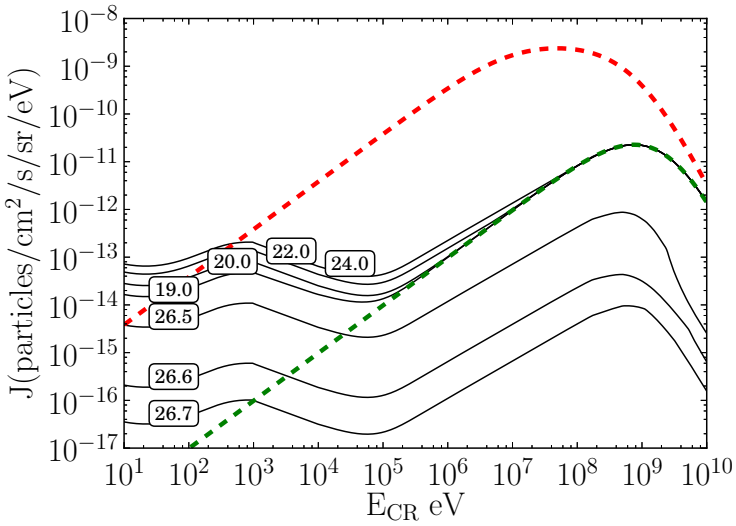

Figure 4.8 Cosmic ray spectra as a function of column density N_{H_2} cm^{-2} for the case of a solar maximum incident spectrum $\phi = 1350$ MeV. Note the initial rise at low energies due to the reprocessing of high energy cosmic rays. Box-labels denote $\log(N_{H_2}/\mathrm{cm}^{-2})$, the dashed green line is the incident spectrum, and the W98 spectrum is shown in red for comparison.

deviates from the otherwise good fit by less than a factor of ~ 2.

As can be seen, modulation of cosmic rays even by a solar-like wind has a significant effect on the integrated cosmic ray ionization rate, ζ_{CR}. While the LIS ionization rates vary between $\zeta_{CR} \sim 10^{-15} - 10^{-17}$ s^{-1}, the effect of solar minimum modulation on ζ_{CR} is more than an order of magnitude below the LIS values, and the *unattenuated* incident CR rates from our simple extrapolation model for the 2% and 8% spot-covered T-Tauri stars are just $\zeta_{CR} \sim 10^{-20}$ s^{-1} and $\sim 3 \times 10^{-22}$ s^{-1}, respectively. Below these values, scattered stellar X-ray ionization of H_2 begins to dominate the weak cosmic ray field. Indeed, the cosmic ray flux in these cases is so low that, if present, ionization by decay products of short-lived radionuclides ($\zeta_{RN} = 7.3 \times 10^{-19}$ s^{-1}) as inferred from the early Solar Nebula (*Umebayashi and Nakano*, 2009) can readily dominate the cosmic ray and X-ray ionizing flux in the disk midplane (dashed black line, Figure 4.9); see also Section 4.8.1 for further discussion.

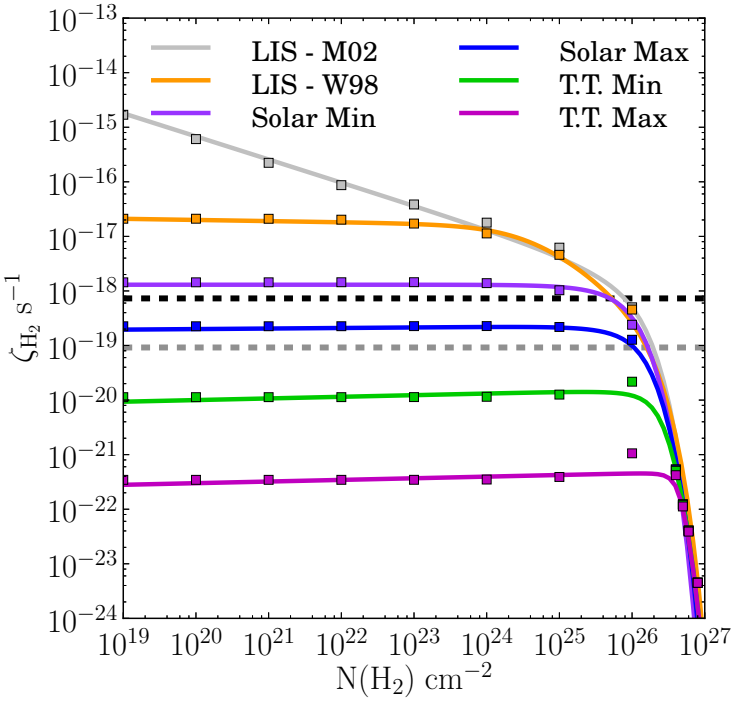

Figure 4.9 Integrated cosmic ray ionization rates as a function of column density for different incident CR spectra. Note: the solar values and extrapolated T-Tauri models are formally taken at $D = 1$ AU. Squares are the computed values while solid lines show the best fit to Eq. (4.5). Fitting parameters are given in Table 4.2, and labels are as described in Figures 4.5 and 4.7. For comparison, the black dashed line represents the inferred ionization rate due to radionuclide decay in the Solar Nebula while the gray dashed line is derived from the mean interstellar abundance of ^{26}Al (*Umebayashi and Nakano*, 2009).

4.6 Exclusion of Cosmic Rays by Large Scale Magnetic Fields

Cosmic rays are intrinsically high velocity ions and as such their trajectory will be shaped by the presence of a magnetic field. In the protoplanetary disk environment magnetic structure may originate from the central star and/or remain from earlier stages in protostellar development, i.e., from the collapse of the parent cloud. The CR's motion will be directed by the field lines so long as the gyroradius, r_g, of the ion is less than the relevant scales considered, where the smallest scale of interest is $\sim R_{\rm disk}$. For a cosmic ray proton of energy $E_p = 1$ TeV and a magnetic field strength $B = 10\mu$G, the gyroradius $r_g = \gamma m v_\perp c/(ZeB) \sim 0.02$ AU, much smaller than $R_{\rm disk} \sim 100$ – 1000 AU. Given that the field strength is expected to be generally higher than this value and the energy of cosmic rays lower, we are safely within the bounds of this criterion for all particles considered.

In the following sections we introduce the magnetic topologies considered, how mirroring and funneling modulate the propagation of galactic cosmic rays, and how this modulation impacts the disk ionization state.

4.6.1 Environmental Magnetic Fields

Dust polarimetric observations of young protostars in some instances exhibit large scale magnetic field structure in what has been described to resemble the shape of an hourglass (e.g., *Girart et al.*, 2006), thought to arise from the gravitational collapse of a magnetized molecular cloud (see review by *Crutcher*, 2012). The large scale magnetic structure surrounding a T-Tauri star is difficult to constrain, however. T-Tauri stars are known to be strongly magnetized (e.g., *Basri et al.*, 1992; *Johns-Krull et al.*, 1999; *Yang et al.*, 2005); how and if the stellar fields couple to a large scale background is unknown. However, by necessity the disk must be magnetized for MRI to initiate, and while deep within the disk the magnetic fields may be randomized by turbulent motions, at large scales the imprint of a protostellar field may still exist.

For the case of an hourglass-like background magnetic fields, we have solved the semi-

Table 4.3. Hourglass Magnetic Field Parameters.

H_0	λ	$B_{z,100\mathrm{AU}}$ [G]
2.50e-05	852.52	7.76e-06
1.25e-04	387.29	1.63e-05
2.50e-04	270.26	2.42e-05
1.25e-03	121.21	5.25e-05
6.25e-02	13.58	3.86e-04
5.00e-01	2.66	1.43e-03

Note. — Col. (1): Dimensionless parameter representing the degree of pinching at the waist of a magnetic flux tube. Col. (2): Tabulated mass to flux ratio contained in a flux tube Φ where $\lambda = M(\Phi)/\Phi$. See *Li and Shu* (1996) for further details regarding these parameters. Col. (4): Vertical magnetic field strength at $R = 100$ AU in the midplane.

analytical magnetized singular isothermal toroid models of *Li and Shu* (1996) for a range of mass to flux ratios (i.e., degrees of pinching at the waist of the hourglass), $\lambda = M/\Phi$. These types of models are representative of the magnetic field of a protostar, and thus provide a first approximation for the "fossil" background remnant field near a very young T-Tauri star. We treat the field as temporally static, with the waist of the magnetic field tied to the disk and at large stellar distances tied to the natal cloud.

Each model is formally characterized by a parameter H_0 (see *Li and Shu*, 1996), which in practice sets the enhanced magnetic field density in the midplane relative to the cloud. In Table 4.3 we provide H_0, mass to flux ratios, and the vertical magnetic field strength B_z in the disk midplane at $R = 100$ AU for each field model. We note that these mass to flux ratios are related to masses of natal core material over the magnetic flux contained in the core, and not disk masses.

4.6.2 Stellar Magnetic Fields

Zeeman broadening observations of young T-Tauri stars have revealed strong magnetic fields at the stellar surface with magnitudes of order 100 G - 1.6 kG (e.g., *Johns-Krull*, 2007). The magnetic topology as determined by sensitive spectro-polarimetric measurements is a complex superposition of octupolar, dipolar and split-monopolar magnetic fields (*Donati et al.*, 2011a,b, 2012). Higher order field components drop off rapidly at large distances from the star; for example, the dipolar field drops off as $B_{\rm dip} \propto r^{-3}$, and therefore its influence in determining the fate of CRs would only matter very close to the star. Some fraction of the field lines are opened up by the stellar wind to form a split-monopolar configuration, forming an approximately radial field component and hence dropping less steeply as $B_{\rm mono} \propto r^{-2}$. As a result, the stellar field component that matters most in magnetically directing cosmic ray motion is that contained within the split-monopole component.

For the stellar field we set the total magnetic field strength at the surface of the star to be $B_{\rm surf} = 3$ kG and assign a fraction γ to be in the radial component. We then vary the strength of the split-monopolar field as a fraction of the total field. In Equation (4.9) we can simply replace $B_{\rm disk}$ with $B(R) = \gamma B_{\rm tot}(R/R_{\rm star})^{-2}$ where γ is the fraction of the stellar magnetic field contained within the split-monopole.

4.6.3 Cosmic Ray Exclusion by Magnetic Mirroring

The shape of the environmental magnetic field can modulate the propagation of cosmic rays through a process known as magnetic mirroring. The basic principle of mirroring is described as follows (see also *Desch et al.*, 2004). Charged particles gyrating about magnetic field lines will conserve their total kinetic energy $\propto v_\parallel^2 + v_\perp^2$ and magnetic moment $\propto v_\perp^2/B$. As the particle enters an area of high magnetic field density it must increase its perpendicular velocity. As $v_\perp$ increases, $v_\parallel$ must decrease to keep the total kinetic energy constant. If the field is pinched to sufficiently high magnetic field strengths, the particle's parallel velocity can be halted ($v_\parallel = 0$) and reversed, thus driving the cosmic ray in the opposite direction

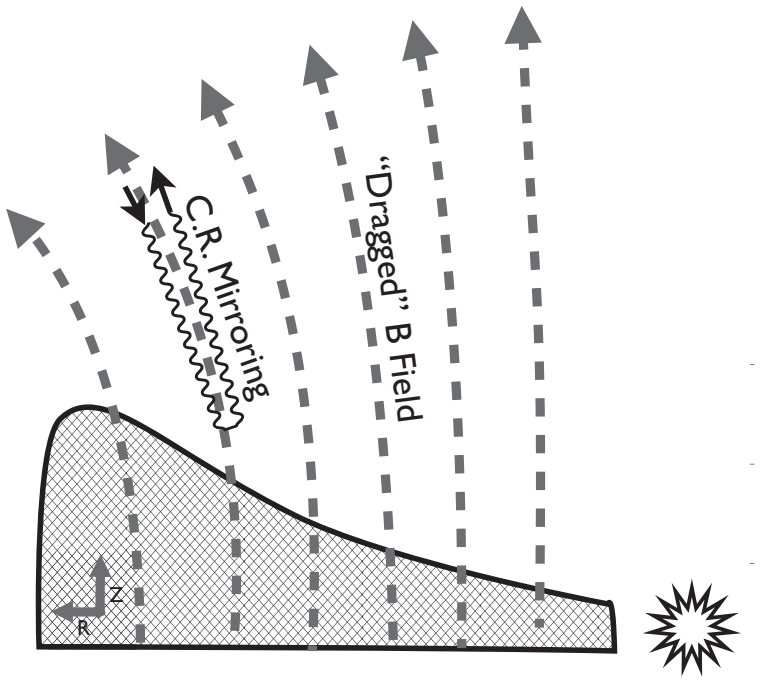

Figure 4.10 Illustration of cosmic ray exclusion by magnetic mirroring. Dashed lines denote background hourglass-shaped magnetic field and the hatched region indicates the disk, viewed edge on. Cosmic ray (zig-zag arrow) enters along the magnetic field line but is repelled before reaching the surface of the disk.

along the field line. The cosmic ray thus reflects off of the region of large magnetic field strength (hence the term mirroring).

If $\alpha_{\rm ISM}$ is the initial pitch angle between a CR's velocity vector and the magnetic field, cosmic rays with small $\alpha_{\rm ISM}$ will tend not to mirror (whereas cosmic rays with initial pitch angle $\alpha_{ISM} = 90$ degrees would gyrate around the field, although that case represents a set of measure zero). The pitch angle α of a cosmic ray starting with $B_{\rm ISM}$ and $\alpha_{\rm ISM}$ at any given point along the field line is given by

$$\frac{\sin^2 \alpha}{\sin^2 \alpha_{\rm ISM}} = \frac{B}{B_{\rm ISM}} = \chi. \tag{4.8}$$

For a disk threaded with a field of magnitude $B_{\rm disk}$, there is a critical initial pitch angle such that cosmic rays with $\alpha > \alpha_{\rm crit}$ will be repelled before reaching the disk surface; in other words, particles attain $\alpha = 90^\circ$ at $B = B_{\rm disk}$ and reverse course. For particles arriving on

one side of the disk, this condition corresponds to a fractional reduction of cosmic rays by mirroring $f_{\rm mirror} = \sqrt{1 - [B_{\rm ism}/B_{\rm disk}]^2}$.

However, simultaneously the open magnetic field lines tend to draw in a larger number of cosmic rays via funneling, enhancing the cosmic ray flux proportionally to the increase in field line density, or $f_{\rm funnel} = B_{\rm ISM}/B_{\rm disk}$. In general mirroring dominates over funneling (*Desch et al.*, 2004; *Padovani and Galli*, 2011), but the effects are of similar magnitude. The combined fractional removal of cosmic rays as given by *Desch et al.* (2004) is:

$$f_{\rm CR,net} = \left[\chi - \left(\chi^2 - \chi\right)^{1/2}\right], \tag{4.9}$$

where χ is given by Equation (4.8). In the limit that the magnetic field in $\rm B_{disk} \gg B_{ISM}$, then the net fraction of cosmic rays removed is $f_{\rm CR,net} = 0.5$.

For completeness we note that mirroring is only important when the change in pitch angle due to magnetic field variations is greater than that due to scattering. The T Tauri systems of interest here are expected to have large gradients in magnetic field strength, so that mirroring can be important. Nonetheless, scattering effects should be considered in future work.

In Figure 4.11, the results for the environmental hourglass model are shown in solid lines and the results for the stellar split-monopolar field are shown in dashed lines. Stellar magnetic effects are only able to modulate cosmic rays relatively near ($R < 100$ AU) the star. Examples of observed split-monopolar field strengths are 4–5 kG (GQ Lup; *Donati et al.*, 2012), 170 G (V4046 Sgr; *Donati et al.*, 2011b), and thus we expect stellar magnetic fields to modulate cosmic ray propagation within 96 AU and 20 AU respectively. Hourglass magnetic fields can, however, reduce incident cosmic ray fluxes on the scale of hundreds of AU. For fields that are only moderately pinched at $H_0 \geq 0.0625$ the entire cosmic ray rate would be reduced by a factor of two. Such a field configuration corresponds to $B_z = 0.9$ mG at 100 AU in the midplane (see Table 4.3).

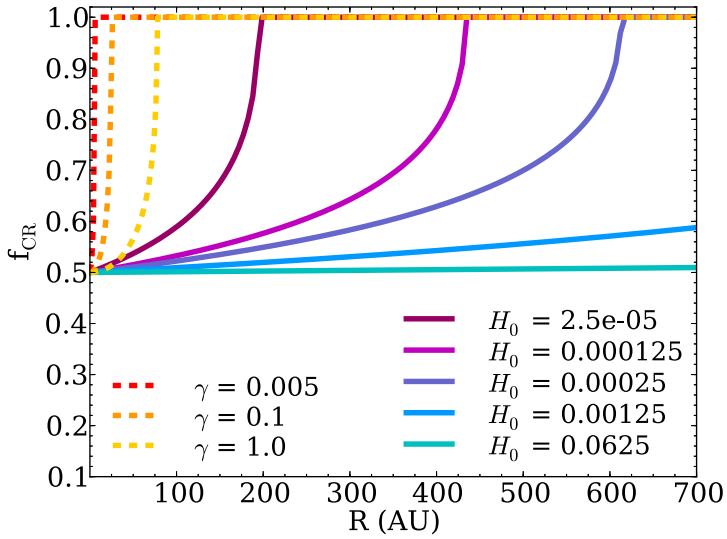

Figure 4.11 Fraction of cosmic rays removed versus disk radius for both the stellar split-monopole models (left, dashed lines) and hourglass models (right, solid lines).

While the magnitude of magnetic modulation is far smaller than the orders of magnitude achieved by a stellar wind, the effect of mirroring more importantly is that this fraction will *radially* vary from $f_{\rm CR,net} = 0.5$ in the inner disk to 1 in the outer disk. As described in Section 4.5.2 the cosmic ray fluxes will formally experience an energy dependent radial gradient in wind modulation efficiency that can vary by a factor of a few between distances of $D = 1$ AU to 80 AU (*Caballero-Lopez and Moraal*, 2004; *Langner and Potgieter*, 2005; *Manuel et al.*, 2011; *Manuel*, 2011), see also Section 4.7.2. Therefore looking for radial gradients in the disks of T-Tauri stars to learn about extrasolar Heliospheres may be confused observationally with magnetic effects from the star or environment, especially if they are of the same magnitude (i.e., a factor of two).

4.7 Cosmic Ray Exclusion and Dead Zones

The magnitude of cosmic ray exclusion by stellar winds and magnetic fields presented here will have significant implications for the ionization state in the disk. This in turn will have important implications for the size of the region in disks that is dead to MRI as well

as chemical implications to be discussed in Chapter 6. In this section we use criteria from simulations of MRI in the literature to compute the size of the active and turbulence-dead regions of the disk and explore how they depend on the cosmic ray ionization rate.

4.7.1 Ionization: Active Disk Criteria

From these ionization rates, ζ, we can determine the electron abundance, which is used to identify the turbulence dead versus active regions. To determine the electron abundance χ_e we use the steady state expression

$$\chi_e = \sqrt{\frac{\zeta_{\rm H_2}}{n\alpha}}, \tag{4.10}$$

where $\alpha = 2 \times 10^{-6}\ T^{-1/2}$ cm^3 s^{-1} is the rate coefficient for recombination with molecular ions (*Glassgold et al.*, 1997). This is of course a simple estimate for the ionization state in the gas and does not, for example, include the possibility of charged dust grains. A more detailed estimate of the ionization fraction including chemistry and charge exchange will be addressed in Chapter 6. For the disk to be MRI active, the ions must first be well-coupled to the neutral gas and must have a sufficiently high magnetic Reynolds number, Re, given by

$$Re \equiv \frac{c_s h}{D} \approx 1 \left(\frac{\chi_e}{10^{-13}}\right) \left(\frac{T}{100\rm K}\right)^{1/2} \left(\frac{a}{\rm AU}\right)^{3/2} \tag{4.11}$$

where c_s is the sound speed, h is the disk scale height, and D is the magnetic diffusivity (*Perez-Becker and Chiang*, 2011a). Recent models by *Flock et al.* (2012) indicate that values of $Re \sim 3300 - 5000$ are required for sustained turbulence, with a critical value $Re_{\rm crit} \sim 3000$. We adopt this critical value for the minimum $Re > Re_{\rm crit}$ required for the disk to be MRI active.

The second criterion for the disk to be unstable to MRI is that there must be frequent ion–neutral collisions for the ions to transfer turbulent motions to the largely neutral disk. This

condition is determined by the ion-neutral collision rate normalized to the orbital frequency,

$$\begin{aligned} Am &\equiv \frac{\chi_i n_{\rm H_2} \beta_{in}}{\Omega} \\ &\approx 1 \left(\frac{\chi_i}{10^{-8}}\right) \left(\frac{n_{\rm H_2}}{10^{10}{\rm cm}^{-3}}\right) \left(\frac{a}{\rm AU}\right)^{3/2}, \end{aligned} \tag{4.12}$$

(*Perez-Becker and Chiang*, 2011a). Simulations by *Hawley and Stone* (1998) find that $Am \sim 10^2$ is required for sufficient coupling. However, even in the case of our most strongly ionized models we reach values of at most $\lesssim 3$. Similarly, *Perez-Becker and Chiang* (2011a) found even in their most MRI favorable model they could only attain $Am \lesssim 10$ (see §4 of that work). In the weakly ionized limit, *Bai and Stone* (2011) show that a disk can become MRI unstable at *any* value of Am, as long as the disk is weakly magnetic. The maximum magnetic field strength such that Am is not a limiting factor is dependent on the ratio of the gas pressure to magnetic pressure, β. To be in this regime, β must be larger than $\beta_{\rm min}$ (see Eq. (26) of *Bai and Stone* (2011)). For our disk model this condition is equivalent to $|{\rm B_{max}}(50{\rm AU})| \sim 0.3$ mG – 5 mG for our most weakly and most strongly ionized models, respectively.

The magnetic field strength in disks is observationally unknown, however. Zeeman measurements of molecular clouds give us a "starting value" with line of sight estimates of 0.1-1 mG (*Crutcher et al.*, 2010; *Falgarone et al.*, 2008). The fields in disks may be further amplified by the collapse of the cloud during formation of a protostar, though diffusion and magnetic reconnection may likely reduce the role of magnetic fields. Therefore, the Am criterion may still be important due to the inferred relatively high magnetic field strengths. In this work we take $Am > 0.1$ as the critical value for sufficient ion–neutral collisional frequency (*Bai and Stone*, 2011). For completeness, however, in the dead zone plots presented, we indicate both the region that satisfies simultaneously Am and Re (white cross hatched = active) as well as the region that satisfies Re only (outside of orange contour = active); see, for example, Figure 4.12.

4.7.2 T-Tauriospheric Dead Zones

As can be seen in Figures 4.7 and 4.9 the presence of a T-Tauriosphere plays an important role in determining the ionization rate from cosmic rays. This ionization rate will in turn impact the steady state electron abundances (see Equation (4.10)) and thus the region of the disk that is dead to MRI turbulence. In Figure 4.12 we plot the results for our standard model, varying the cosmic ray flux for each spectrum considered. In these models we assume the cosmic rays come from both sides of the disk and therefore reduce the cosmic ray contribution per side by half. We integrate the column of material from the surface downward and bottom upward and sum the contributions from both sides of the disk.

The contour plot in the left column shows the total H_2 ionization rate from cosmic rays and X-rays combined. The second column shows contour plots of the critical magnetic field, which sets the relative importance of the Am parameter in determining the disk's dead region. The third column shows the net result, with the Am and Re active region hatched in white, while the region enclosed by the orange curve is dead according to the Re criterion alone. In the "TT Max" plot on the bottom, it can be seen that nearly the entire bulk mass of the disk is dead based upon Re and Am, while the Re-only dead region spans just the central ~ 100 AU. The Re-only region can thus be thought of as the minimum size of the dead region, depending upon the importance of Am. We compute the mass contained in the dead zone for each of these scenarios (see Table 4.4). Recall that the disk mass $M_d = 0.039 M_\odot$, so that the dead zone represents $\sim 1/8$ of the disk (for ISM and solar models) to $\sim 3/4$ of the disk (for the maximum TT model).

The size of the dead zone depends directly on the mass of the disk, which sets the vertical column density of gas normal to the plane of the disk. A denser (and thus more massive) disk of the same size would thus be less permeable to cosmic rays and have a larger (more massive) dead zone. Our disk within 400 AU contains 0.039 $M_\odot$ of gas and therefore is on the more massive end of the typical range of disk masses. If we reduce the disk mass by a factor of two, the dead zone shrinks radially by approximately 15% for the ISM through

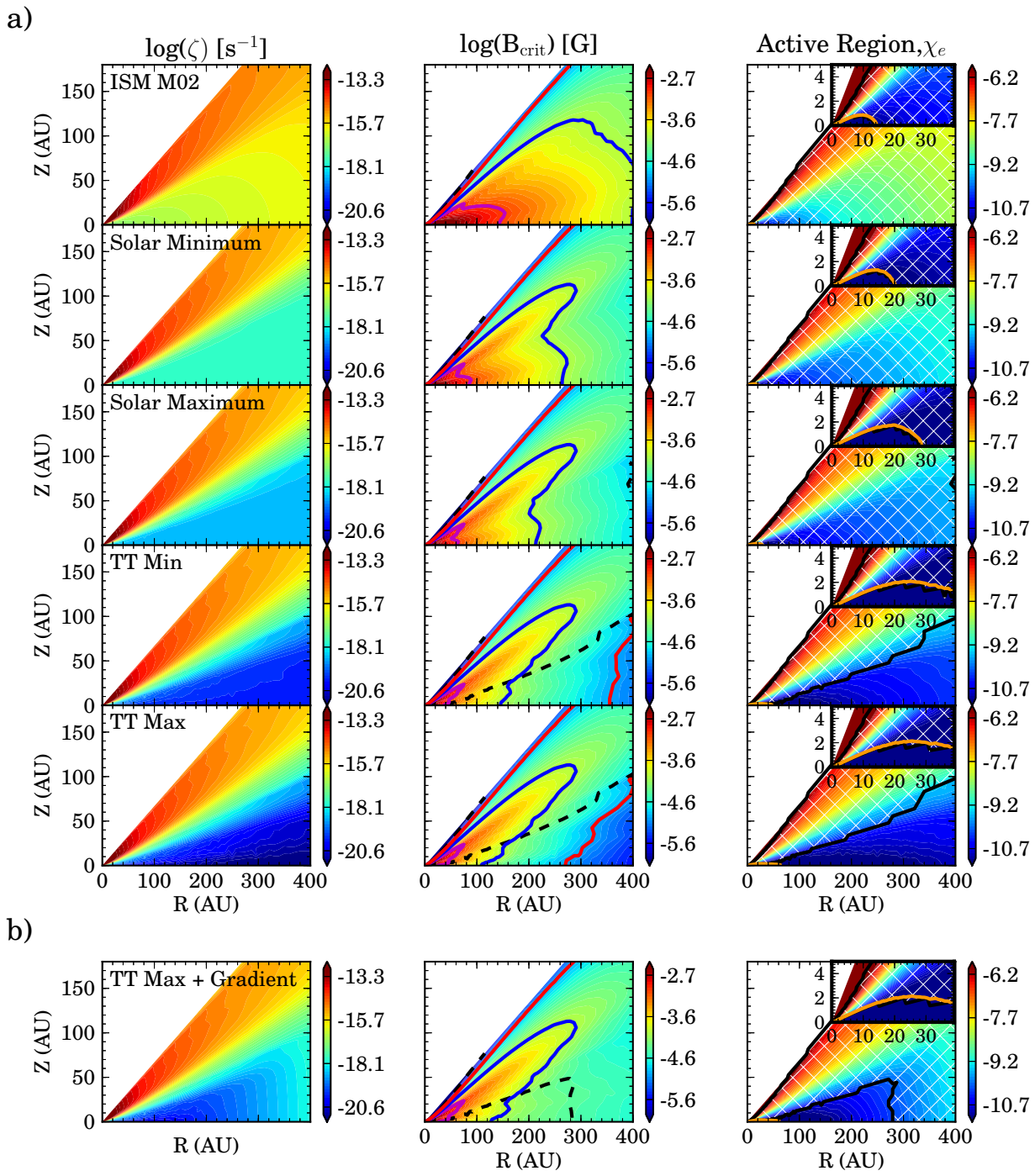

Figure 4.12 H_2 ionization $\zeta_{tot} = \zeta_{CR} + \zeta_{XR}$ s^{-1} and MRI-active regions. a) Uniformly reduced CRs. Left: total H_2 ionization rate from X-rays and CR for $L_{XR} = 10^{-29.5}$ erg s^{-1} and CR rate as labeled. Center: critical B-field for *Am* criterion. Magenta, blue and red lines denote 1 mG, 100 μG, and 10 μG. Right: MRI-active regions. Regions of the disk that satisfy both *Re* and *Am* criteria are indicated by the white crosshatching. The minimum region of the disk inactive to MRI, i.e., satisfies *Re* but not *Am*, is orange. b) Quantities same as above, now including a 2%/AU positive radial gradient in CR flux.

Table 4.4. Mass contained in dead zones for the different cosmic ray models without radionuclide ionization, see Fig. 4.12.

Model	$M_{\rm dead}$: *Re* & *Am* $[M_\odot]$	$M_{\rm dead}$: *Re*-only $[M_\odot]$
ISM M02	0.0038	0.0038
Solar Min	0.0051	0.0051
Solar Max	0.0065	0.0065
T-Tauri Min	0.0268	0.0085
T-Tauri Max	0.0279	0.0093

solar cosmic ray models, but has only a minuscule effect on the extensive dead regions in the T-Tauri models, flattening them in vertical extent by no more than a few AU at $R = 100$ AU.

In all of the models discussed above, the cosmic ray rate is uniformly reduced throughout the disk. As discussed in Section 4.5.2, however, there is an observed radial gradient in the cosmic ray flux, which is both strongly energy and distance dependent. For example, a $E_{\rm CR} \sim 20$ MeV cosmic ray at $R = 10$ AU varies by $\sim 0.8\%$/AU while the same cosmic ray at $R = 70$ AU has an intensity gradient of $\sim 9\%$/AU (*Caballero-Lopez and Moraal*, 2004). This is compared to a ~ 1 GeV CR proton, which has uniform gradient of $\sim 1\%$/AU throughout the Heliosphere. To approximate this in our current framework, we have taken the T-Tauri (max)imum extrapolation model and applied a uniformly increasing 2%/AU radial gradient in the cosmic ray ionization rate, shown in Figure 4.12b. The gradient is incorporated with the expression $\zeta_{\rm CR}(R_{\rm AU}) = \zeta_{\rm CR}(1\ {\rm AU}) \times (1+p)^{R_{\rm AU}-1}$, where $\zeta_{\rm CR}(1\ {\rm AU})$ is the wind-modulated cosmic ray ionization rate at $R = 1$ AU (see Section 4.5.4), p is the fractional cosmic ray increase per AU (thus $p = 0.02$ corresponds to 2%/AU) and $R_{\rm AU}$ is the distance from the central star in AU. Since the T-Tauri-modulated cosmic ray spectra peak at around $E_{\rm CR} \sim 1$ GeV where the gradient in the Solar System is closer to 1%/AU – 1.5%/AU, this may over estimate the magnitude of the gradient but nevertheless demonstrates that a modest gradient can allow the outer disk ($R > 250$ AU) to be sufficiently ionized for MRI turbulence

even with a strongly modulated cosmic ray intensity.

4.7.3 Dead Zone Dependence on the Stellar X-ray Luminosity

T-Tauri stars are both X-ray luminous and highly variable (*Feigelson and Decampli*, 1981b; *Feigelson et al.*, 1993; *Neuhaeuser et al.*, 1995; *Telleschi et al.*, 2007). Furthermore, it has been observed that objects with high stellar X-ray luminosity ($L_{\rm XR} \gtrsim 10^{31}$ erg s^{-1}) typically have harder X-ray spectra at energies exceeding 2 keV, characteristic of emission contribution from stellar flares (*Carkner et al.*, 1996; *Imanishi et al.*, 2001; *Wolk et al.*, 2005; *Preibisch et al.*, 2005). Figure 4.13 demonstrates the effect of an enhanced X-ray luminosity on the ionization rates and the resulting size of dead zones. The filled color contours show the ionization rates per H_2 for three purely X-ray models (no cosmic rays) with the following X-ray luminosities: $L_{\rm XR} = 10^{28}$, $10^{29.5}$, and 10^{31} erg s^{-1}. In this plot, the crosshatching follows the same convention as Figure 4.12.

For the stellar sources with $L_{\rm XR} = 10^{28}$ and $10^{29.5}$ erg s^{-1}, we adopt the "characteristic" spectral template shown in black in Figure 4.2, and for the $L_{\rm XR} = 10^{31}$ erg s^{-1} we adopt the "flaring" spectral template shown in the same figure in grey to simulate the X-ray hardening with increasing luminosity. Hard X-ray photons ($E > 2$ keV) are able to penetrate dense gas more readily than their soft X-ray counterparts, allowing flaring stars to ionize a larger fraction of the disk mass.

For our prototypical model, $L_{\rm XR} = 10^{29.5}$ erg s^{-1}, the disk midplane is largely dead to MRI without inclusion of cosmic ray ionization. Even in the highly X-ray irradiated case, there are two dead midplane regions, one extending out to $R \sim 25$ AU (see Fig. 4.13 c, inset) and one in the outer disk beyond $R \sim 200$ AU. This structure is a result of the *Am* criterion depending on both density and ionization; in the inner dense disk the ionizing radiation cannot penetrate and in the outer low density disk ion-neutral collisions are not frequent enough.

This large dead region is contrary to the results of *Igea and Glassgold* (1999) [IG99], who

found that incorporation of stellar X-ray scattering into the radiative transfer permitted the entire disk beyond 5 AU to support MRI even in the absence of cosmic rays. The difference between their results and ours is readily explained by different assumptions for an active disk. In IG99 the critical electron fraction depends on the viscous disk parameter as $x_{\rm cr} \propto \alpha^{-1/2}$, where α was originally taken to be unity (see Equations 22 and 23 of that work). Under the same assumptions with $L_{\rm XR} = 10^{29}$ erg s^{-1}, our model finds a similarly-sized dead zone, extending out to 5.5 AU in the midplane. A lower value of $\alpha \simeq 0.01$ causes MRI to be less efficient at viscously stirring the disk, and therefore the electron fraction required to be turbulent is subsequently higher, creating a substantially larger dead region.

We note that a more dust-settled disk would also change the size of the dead zone by reducing the X-ray opacity due to dust by up to a factor of two (*Bethell and Bergin*, 2011b). Reducing the X-ray opacity causes deeper layers in the disk to see X-ray photons having a similar effect to increasing the X-ray luminosity. This would vertically flatten the MRI inactive region but not reduce the radial extent of the dead zone in the midplane.

4.8 Further Considerations

4.8.1 Radionuclide Ionization in the Midplane

An important source of ionization we have neglected thus far is the decay of short-lived radionuclides (RNs). Species such as ^{26}Al and ^{60}Fe have relatively short half-lives, $\tau_{1/2} <$ 10 Myr, and therefore their presence in the early Solar System is inferred by measurements of the decay products in meteorites (*Gray*, 1974; *MacPherson et al.*, 1995, and others). While the net ionization rate from RN depends on assumptions regarding their distribution and abundances, typical values estimated for the Solar Nebula from ^{26}Al decay lie near $\zeta_{\rm RN} = (7.3 - 10) \times 10^{-19}$ s^{-1} (*Umebayashi and Nakano*, 2009). Thus $\zeta_{\rm RN}$ in the early Solar System likely rivals or even exceeds $\zeta_{\rm CR}$ by orders of magnitude for nearly all of the wind-modulation models considered here. Even the unattenuated solar maximum cosmic ray rate

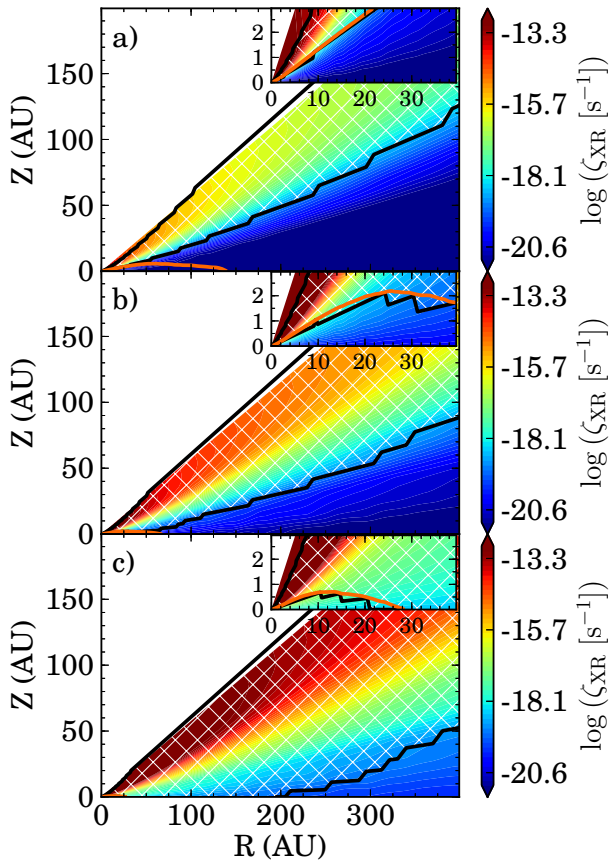

Figure 4.13 Plots of the X-ray only ionization rate throughout the disk per H_2, varying the stellar X-ray luminosity: L_{XR} = a) 10^{28} erg s^{-1} b) $10^{29.5}$ erg s^{-1} c) 10^{31} erg s^{-1}. Filled contours show the X-ray ionization rate, ζ_{XR} s^{-1}. Hatched region and contour lines are the same as for Figure 4.12. The right panel, $L_{XR} = 10^{31}$ erg s^{-1}, has a harder X-ray spectrum characteristic of flaring T-Tauri stars, see Sections 4.4.2.1 and 4.7.3.

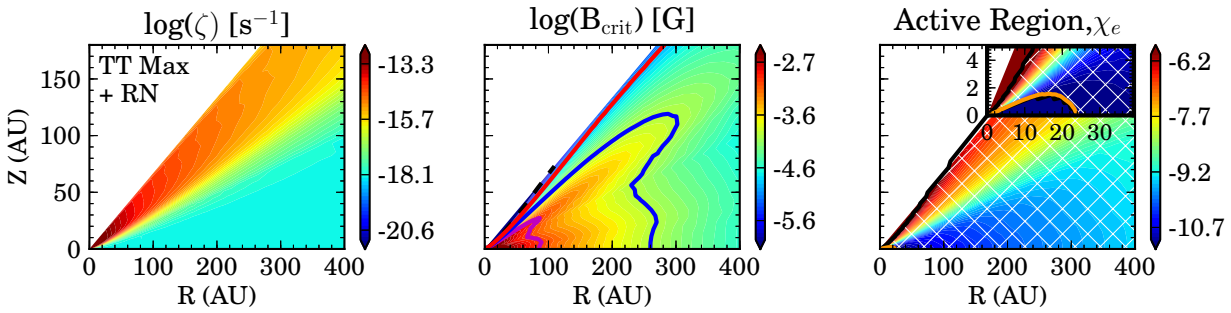

Figure 4.14 Quantities same as Fig. 4.12, now including uniform ionization from decay of short-lived radionuclides, $\zeta_{\rm RN} = 7.3 \times 10^{-19}$ s^{-1}. The total ionization rate of H_2 is given by $\zeta_{\rm tot} = \zeta_{\rm RN} + \zeta_{\rm CR} + \zeta_{\rm XR}$.

with a uniform 1.5%/AU CR gradient (Section 4.7.2) has $\zeta_{\rm CR}(R) \lesssim \zeta_{\rm RN}$ within $R \leq 100$ AU, assuming the Solar Nebula value of $\zeta_{\rm RN}$ (see Figure 4.9 dashed black line).

Consequently, short-lived radionuclides such as ^{26}Al may become the dominant source of ionization if they are indeed present in an isolated ($G_0 \sim 1$) protoplanetary disk. To demonstrate the effect of the addition of ionization by radionuclide decay at levels inferred in the early Solar System, we have recreated the bottom panel (TT Max) of Figure 4.12 to include contribution from decay of ^{26}Al by treating it as a uniformly well-mixed ionization source throughout the disk with a magnitude of $\zeta_{\rm RN} = 7.3 \times 10^{-19}$ s^{-1} (Figure 4.14). In this case the midplane ionization is clearly dominated by ionization as a result of the local radionuclide decay. For comparison, the presence of radionuclides has little effect on the size of dead zones for the ISM models and moderately restricts the extent of the dead zone to $R \sim 20$ – 30 AU for the Solar System-like cosmic ray models. For the TT Max case, the dead region encompasses the inner $R \lesssim 30$ AU and contains 0.015 $M_\odot$ of material in the dead zone.

Unfortunately, the ionization contribution from radionuclides in a "typical" disk however is entirely unknown. Indeed, there is evidence for an *enhanced* abundance of short-lived RN in the early Solar System. However, the source of this enhancement is exceedingly controversial, typically falling into two categories: stellar spallation (internal) (e.g., *Lee et al.*, 1998; *Shu*

et al., 2001) or enrichment of the parent molecular cloud from supernovae or Wolf-Rayet stars (external) (*Wasserburg et al.*, 2006; *Gounelle et al.*, 2009; *Gaidos et al.*, 2009; *Makide et al.*, 2011; *Gounelle and Meynet*, 2012). While ^{26}Al can be explained both by internal and external mechanisms, the presence of ^{60}Fe is solely a stellar nucleosythensis product and thus is external in origin. Indeed, an inferred enhanced abundance of ^{60}Fe found in chondrites was originally attributed to a nearby type II supernova during the formation of the Solar System (*Tachibana et al.*, 2006); however, this result has come under intense scrutiny with later works claiming no such enhancement (*Moynier et al.*, 2011; *Dauphas and Chaussidon*, 2011; *Tang and Dauphas*, 2012). In summary, the relative contribution from external versus internal processes is still unclear (for an extensive discussion see *Adams*, 2010, and references therein), but we know that the early Solar System was to some degree enriched by external sources. In Figure 4.9 we include the radionuclide ionization rate as is computed from the mean interstellar abundance of ^{26}Al derived from γ-ray observations of ^{26}Al decay in the Milky Way, (see discussion in *Umebayashi and Nakano*, 2009). This rate is a factor of ~ 8 below the Solar Nebula value, lending credence to the hypothesis that the Solar System formed in an enriched environment. Furthermore *Diehl et al.* (2006) find the ^{26}Al abundance to be anisotropic throughout the galaxy, concentrated near massive star-forming regions. Therefore this enhanced radionuclide abundance may be typical of protoplanetary disks formed in massive clusters.

4.9 Conclusions

In this work we have explored several mechanisms that act to reduce the cosmic ray flux incident on protoplanetary disk surfaces. The first mechanism, exclusion by a magnetized wind, actively operates within the Solar System and excludes cosmic rays at high efficiency, especially at low $E_{\rm CR}$. We have extrapolated the magnitude of cosmic ray exclusion using spot coverage as a tracer of solar magnetic activity to T-Tauri stars with spot coverages of 2% and 8%, and have examined the effects on the cosmic ray energy spectrum $J(E)$. For

our extrapolated modulation models we find good agreement with numerical and analytical models of *Svensmark* (2006) and *Cohen et al.* (2012) for their models of the young Sun (Y.S.), where we have extrapolated their results at energies < 10 MeV. If this reduction in the cosmic ray flux is real, the incident cosmic ray flux should be reduced by at least ten orders of magnitude for 1 MeV cosmic rays and five orders of magnitude at 1 GeV. In the analysis of *Turner and Drake* (2009), the authors attempt to account for cosmic ray modulation by considering only cosmic rays with energy above 100 MeV, where solar modulation is small. It can be seen, however, from our results as well as the young Sun models that cosmic ray modulation operates at all energies when wind exclusion is significant (see Fig. 4.7).

Using the results of the cosmic ray propagation models of *Padovani et al.* (2009) we reconstruct the ionization rate versus depth into a molecular slab (disk surface) for the wind-modulated cosmic ray spectra (Fig. 4.9). We provide numerical fits for the integrated cosmic ray ionization rate $\zeta_{\rm CR}(N_{\rm H_2})$ s^{-1} for a range of modulation strengths. At the low ionization rates inferred, cosmic rays do not contribute significantly to the ionization rate in the outer disk. Indeed, the calculated CR rates are many orders of magnitude lower than the ionization rates inferred from decay of short-radionuclides in the early Solar System, though to what degree radionuclides contribute to other systems is unknown. Regardless, in our simple prediction for wind modulation in a T-Tauri star system we find that the cosmic ray ionization rate is more than an order of magnitude below the interstellar averaged ^{26}Al ionization rate, $\zeta_{\rm RN} = 9.2 \times 10^{-20}$ s^{-1} (*Umebayashi and Nakano*, 2009). Therefore, it is this value that we recommend as a minimum H_2 ionization rate in disks, though there may be some variation with galactic location (e.g. *Diehl et al.*, 2006) and with disk evolution, i.e. enhancement via dust settling (*Umebayashi et al.*, 2013).

Furthermore, external radiation fields can contribute to the SII ion abundance in the outer disk, but its contribution is limited by dust extinction if some amount of small dust is present. Elevated external FUV fields present in stellar clusters, however, can dominate cosmic rays, X-rays and radionuclides at the outermost surface of the disk if the cosmic

ray rate is reduced (Fig. 4.4). In the absence of cosmic rays, a strong external field, and radionuclides, the scattered stellar X-rays dominate the H_2 ionization in the outer regions of the disk.

In summary, we draw the following conclusions from our models:

1. Modulation by stellar winds can reduce the cosmic ray flux in the circumstellar environment by many orders of magnitude, resulting in cosmic ray ionization rates substantially lower ($\zeta_{CR} \lesssim 10^{-20}$ s^{-1}) than typically assumed in models of MRI turbulence and circumstellar chemistry. At the low CR rates inferred, the dominant source of ionization at the midplane throughout the disk can become short-lived radionuclides, if present.

2. If a T-Tauri star drives a Heliosphere-like region of cosmic ray exclusion, the cosmic ray ionization rate should be no higher than $\zeta_{CR} \lesssim 1.4 \times 10^{-18}$ s^{-1}, the solar minimum modulation rate. This CR upper limit, however, is likely much too high given the more extreme wind and magnetic properties of T-Tauri stars compared to the Sun, thus we expect $\zeta_{CR} << 10^{-18}$ s^{-1}. At the lower end, however, decay by short-lived radioactive particles should provide a floor to the H_2 ionization rate set by ^{26}Al decay, $\zeta_{RN} \gtrsim 9.2 \times 10^{-20}$ s^{-1} at the mean interstellar ^{26}Al abundance (*Umebayashi and Nakano*, 2009). As a result, we recommend the inferred ^{26}Al radionuclide ionization rate in the Solar Nebula for the H_2 ionization rate throughout protoplanetary disks, $\zeta_{RN} = (7.3 - 10) \times 10^{-19}$ s^{-1} (*Umebayashi and Nakano*, 2009) within a T-Tauriosphere. This is of course in addition to X-ray ionization from the central star. Outside of the T-Tauriosphere the cosmic ray rate should be that of the ISM, and here we suggests ionization rates in the range of the W98 and M02 models (Sections 4.4.2.3 and 4.5.4).

3. These rates can and will be tested with spatially and spectrally resolved observations of molecular ions with ALMA, at which point more complex models of a T-Tauriospheric cosmic ray modulation will certainly be of interest. We defer predictions for chemical

effects until Chapter 6.

4. Based on our models we provide fits to the ionization rate $\zeta_{\rm CR}(N_{\rm H_2})$ predicted for T-Tauri stars assuming: 1. extrapolated interstellar CR fluxes (i.e., unmodulated), 2. solar wind modulated CR fluxes, and 3. T-Tauri-like wind modulated CR fluxes. The analytical fits are in the same form as provided by *Padovani et al.* (2009, 2013) and are made for ease in use in a variety of physical and chemical simulations.

5. Global magnetic fields can modulate the cosmic ray flux impacting the disk through the competing processes of mirroring and funneling. The effect is limited to a net 50% reduction in addition to any wind exclusion but will imprint a 50% radial gradient in the CR ionization rate. The possibility of such an effect will need to be considered when modeling "T-Tauriospheres" around other stars, as they too will imprint gradients in the cosmic ray flux.

6. Under these low cosmic ray conditions, large regions of the disk will be unable to sustain MRI turbulence. Radionuclides can "reactivate" MRI turbulence in the midplane outside of $\sim$ 25 AU if they are present at the enhanced rates inferred for the Solar Nebula. Furthermore, an enhanced external FUV radiation field can create an active "shell" of material on the disk's outermost surface.

This Chapter represents only the first step in assessing the exclusionary effects of winds and magnetic fields in T-Tauri systems. Our work to date utilizes simple, but physically motivated, models. More sophisticated theoretical work should thus be carried out as our understanding of the problem increases. Moreover, the effects explored in this Chapter will have clear chemical implications that can be readily observed in the near future. As one example, recent studies have sought to measure the degree of turbulence in protoplanetary disks by observing line broadening of strong gas emission lines (e.g., *Hughes et al.*, 2011; *Guilloteau et al.*, 2012). While we expect vertical stratification between the active surface and dead midplane, it would not be unexpected to find additional radial variations in, for

example, turbulent line broadening and coagulative dust growth. In general, protoplanetary disks will be affected by a diversity of ionization sources: stellar UV photons in the inner disk, X-rays in the molecular layer, external radiation ionizing the outer "skin" of the disk, and (potentially) both short-lived radionuclides and cosmic rays in the deep planet-forming midplane. Furthermore, all of these ionization sources are likely to vary — perhaps substantially — from system to system. As a result, the determination of the diverse ion chemistry of these disks, as well as the turbulent kinematic properties, will be fertile ground for future ALMA observations.

4.10 Acknowledgments

The authors are grateful to the referees for their useful suggestions and perspectives. The authors also wish to thank Mark Moldwin and Marco Fatuzzo for illuminating discussions on various aspects of the Chapter, M. Padovani for being extremely helpful in providing access to his numerical results, and T. Harries for kindly providing the TORUS radiative transfer code used to produce the disk model. LIC thanks Prof. Jon M. Miller for assisting with the *XSPEC* X-ray modeling. Wilcox Solar Observatory data used in this study was obtained via the web site http://wso.stanford.edu at 2012:11:06, 08:43:00 EST courtesy of J.T. Hoeksema. This work was supported by NSF grant AST-1008800. FCA is supported by NSF grant DMS-0806756 from the Division of Applied Mathematics and by NASA grant NNX11AK87G from the Origins of the Solar System Program.

CHAPTER V

Radionuclide Ionization in Protoplanetary Disks: Calculations of Decay Product Radiative Transfer

5.1 Preface

The following work appears in the Astrophysical Journal, Volume 777, 28, 6 pp. (2013). The work is co-authored by Fred C. Adams[1] and Edwin A. Bergin[2].

5.2 Abstract

We present simple analytic solutions for the ionization rate $\zeta_{\rm SLR}$ arising from the decay of short-lived radionuclides (SLRs) within protoplanetary disks. We solve the radiative transfer problem for the decay products within the disk, and thereby allow for the loss of radiation at low disk surface densities; energy loss becomes important outside $R \gtrsim 30$ AU for typical disk masses $M_g = 0.04$ $M_\odot$. Previous studies of chemistry/physics in these disks have neglected the impact of ionization by SLRs, and often consider only cosmic rays

[1]Department of Physics, University of Michigan, 450 Church St, Ann Arbor, MI 48109
[2]Department of Astronomy, University of Michigan, 500 Church St, Ann Arbor, MI 48109

(CRs), because of the high CR-rate present in the ISM. However, recent work suggests that the flux of CRs present in the circumstellar environment could be substantially reduced by relatively modest stellar winds, resulting in severely modulated CR ionization rates, $\zeta_{\rm CR}$, equal to or substantially below that of SLRs ($\zeta_{\rm SLR} \lesssim 10^{-18}$ s^{-1}). We compute the net ionizing particle fluxes and corresponding ionization rates as a function of position within the disk for a variety of disk models. The resulting expressions are especially simple for the case of vertically gaussian disks (frequently assumed in the literature). Finally, we provide a power-law fit to the ionization rate in the midplane as a function of gas disk surface density and time. Depending on location in the disk, the ionization rates by SLRs are typically in the range $\zeta_{\rm SLR} \sim (1-10) \times 10^{-19}$ s^{-1}.

5.3 Introduction

Ionization plays an important role in setting thermal, dynamical, and chemical properties of protoplanetary disks. The dominant ionization processes thought to be active in such disks include photoionization from stellar and interstellar UV and X-ray radiation, thermal ionization, ionization by the decay products of short-lived radionuclides (SLRs), and cosmic ray (CR) ionization (e.g., *Glassgold et al.*, 1997; *Finocchi and Gail*, 1997; *Glassgold and Najita*, 2001; *Walsh et al.*, 2012). Of these sources, only CR and SLR-decay are able to provide ionization in the densest and coldest layers of the disk where UV and X-ray photons are highly attenuated. However, the importance of CR ionization is highly uncertain, and position dependent, due to stellar-wind modulation from the central star (see Chapter 4). With the substantially reduced CR rates expected for these disk systems, SLR-decay is left as the dominant midplane ionization contributor at distances beyond the hard X-ray dominated region, $R \gtrsim 10$ AU from the central star.

Indeed, the Solar System's meteoritic record points to an early enhancement (~ 10 times the mean ISM abundance; *Umebayashi and Nakano*, 2009) of ^{26}Al, the most chemically significant of the SLRs, indicating an enrichment of massive star byproducts in the Solar

birth cluster (*Adams*, 2010). Furthermore, maps of 1.808 MeV γ-rays resulting from ^{26}Al decay confirm an enhancement of SLRs near major star-forming regions (*Diehl et al.*, 2006). While the ubiquitous presence of SLRs during star-formation and subsequent disk-formation is expected, the degree to which their energetic decay products contribute to the ionization rate remains uncertain. For example, there is inherent time evolution in both the total mass of SLRs (set by their respective half-lives where $t = 0$ corresponds to the time of formation of CAIs; *MacPherson et al.*, 1995) and the spatial distribution of dust particles that carry the SLRs, which tend to settle towards the midplane with time (*Umebayashi et al.*, 2013). Furthermore, the diversity of original sources of radioactive particles, including supernovae (*Cameron and Truran*, 1977), Wolf-Rayet winds (*Arnould et al.*, 1997; *Gaidos et al.*, 2009), and stellar spallation (*Lee et al.*, 1998; *Shang et al.*, 2000), adds further complexity to characterizing the initial abundances of SLRs present at the time of disk-formation (see also *Adams*, 2010). Nevertheless, the meteoritic record provides clues regarding which species were once present in one particular protoplanetary disk, our Solar Nebula, and the abundances therein (e.g., *Gounelle and Meynet*, 2012).

A number of studies have quantified the ionization of molecular gas by energetic particles resulting from SLR decay (e.g., *Umebayashi and Nakano*, 1981; *Finocchi and Gail*, 1997; *Umebayashi and Nakano*, 2009). For a disk with an incident CR flux at ISM levels, previous work predicts that ionization by CRs should exceed that of SLRs in regions where the gas surface density $\Sigma_g < 1000$ g cm^{-2} (*Umebayashi and Nakano*, 1981, 2009). However, under the influence of a wind-reduced CR flux (Chapter 4), even a modest "present-day" solar wind reduces the CR ionization rate to values rivaling or substantially below that of SLRs ($\zeta_{\rm CR} \lesssim 10^{-18}$ s^{-1}) *throughout the disk*. Careful treatment of ionization by SLRs is thus necessary for models of disk chemistry and physics. Furthermore, previous studies of disk ionization by SLRs did not take into account the escape of the decay products, which becomes important when the surface density drops below $\Sigma_g \lesssim 10$ g cm^{-2}.

In the present Chapter we develop easy-to-use approximations to implement position-

dependent SLR ionization rates in protoplanetary disks, $\zeta_{\rm SLR}(r,z)$, for use in chemical models and/or studies of the magnetorotational instability (*Balbus and Hawley*, 1991). Section 5.4.1 calculates the ionization rate using a plane-parallel approximation for the radiative transfer, which explicitly includes the escape of decay products from the disk. Although this Chapter focuses on the dominant ionizing source, ^{26}Al, we examine the effects of including other SLR species, ^{60}Fe and ^{36}Cl, on the estimated ionization rates. Section 5.4.2 generalizes the calculation to include the effects of dust settling on the ionization rates. Finally, Section 5.4.3 considers the time evolution of the ionization rates.

5.4 Transfer of Short-Lived Radionuclide Decay Products

For a given parent SLR, the decay process can result in the emission of $E \sim 1$ MeV photons, positrons, electrons and α-particles, whose energy goes into ionization, excitation, and heating of the surrounding gas via secondary electrons (see *Umebayashi and Nakano*, 1981; *Dalgarno et al.*, 1999; *Glassgold et al.*, 2012). Because the SLR mass reservoir in the disk is finite, the half-life $t_{\rm half}$, in addition to the mass/abundance of parent SLRs, is vital, as it sets both the total duration and occurrence rate of the decays. A short half-life results in frequent decays (high ionization rates), but lasts for a potentially negligible fraction of the disk lifetime. From the ionizing secondary electrons, the energy required to create a single ion-pair from H_2 gas is $W_{\rm H_2} = 36$ eV, where only $\sim$47% of the energy goes into ionization (*Dalgarno et al.*, 1999; *Glassgold et al.*, 2012). As the decay products propagate through the gas disk, the main source of opacity for $E \sim 1$ MeV photons is Compton scattering and for positrons/electrons is collisional ionization. As a result, the decay products have finite, energy-dependent ranges. The branching ratios, ranges and decay sequences of the SLR parents considered in this work are shown in Table 5.1. In the following section we compute H_2 ionization rates; however, these results can be extended to include helium ionization, where $\zeta_{\rm He} \approx 0.84\zeta_{\rm H_2}$ (*Umebayashi and Nakano*, 2009).

The problem of interest is essentially a classical radiative transfer problem where the

Table 5.1. Selected SLR Data.

Parent SLR $\log_{10}(n_\chi/n_{\mathrm{H_2}})$	t_{half} (Myr)	Decay Mode	Product (MeV)	κ ($\mathrm{cm^2/g}$)
^{26}Al (-9.378)	0.74	β^+ 82%	e^+ (0.473)	11.76
			γ (2×0.511)	0.148
			γ (1.808)	0.080
		E.C.[3] 18%	γ (1.808)	0.080
^{60}Fe (-10.270)	1.5	β^- [^{60}Co]	e^-(0.184)	52.63
			γ (0.0586)	0.282
		β^- [^{60}Ni][4]	e^-(0.315)	21.74
			γ (1.173)	0.101
			γ (1.332)	0.094
^{36}Cl (-10.367)	0.30	β^-[5]	e^-(0.7093)	7.541

distribution of emitters follows the refractory material (assuming that most of the radioactive metals are carried by dust grains). Furthermore, we assume that the decay products escape the dust grains from which they are emitted, which is appropriate for dust grains sizes $a \leq 10$ cm for $E \sim 1$ MeV photons and $a \leq 0.1$ cm for positrons (*Umebayashi et al.*, 2013). The absorption is due to energy losses in the gas, and the resulting equation for the frequency-averaged particle/photon intensity, I, has the general form

$$\hat{s} \cdot \nabla I = \rho_g \left(\frac{100}{f_g} \right) \frac{J}{4\pi} - \rho_g \kappa I, \tag{5.1}$$

where J is the emissivity from the production of photons/positrons/electrons due to radioactive decay, κ is the mass absorption coefficient, ρ_g is the gas density, and f_g is the gas-to-dust mass fraction ($f_g = 100$ for uniformly distributed gas and dust).

To start, we neglect energy/frequency evolution of the decay product cross sections (see Section 5.5). To specify J, we consider decay product (k) from a single radioactive species (p). If E_k is the energy of the decay product and $\omega_p = \log 2/t_{\mathrm{half}}$ is the decay rate, then $E_k \omega_p$ is the energy generated by k per second per parent SLR p. Let χ_p be the abundance of the parent species relative to H_2 and let $\langle m \rangle = \mu m_{\mathrm{H}}$ denote the mean molecular weight

of gas (where $\mu \approx 2.36$). We thus expect the emissivity J_k to have the form

$$J_k = \frac{E_k \omega_p \chi_p}{\langle m \rangle} \ \left[\mathrm{erg\,s^{-1}g^{-1}}\right]. \tag{5.2}$$

In the regime where all decay products are trapped, the ionization rate per H_2 is given by the usual expression $\zeta^k_{H_2} = E_k \omega_p \chi_p / W_{H_2}$ s^{-1} (e.g., *Umebayashi and Nakano*, 1981). This exercise can be extended over all parent SLRs p, and decay products k, within a decay series, thus obtaining:

$$\zeta^{\mathrm{tot}}_{H_2}(r,z) = \sum_p \sum_k \zeta^{p,k}_{H_2}(r,z)\,. \tag{5.3}$$

While the following section provides ionization prescriptions that apply to general disk models, the plots are calculated using our model from Chapter 4. The gas and dust densities are described by a power-law with an exponential taper at the outer-edge (*Andrews et al.*, 2011) with a total disk gas mass of $M = 0.04$ M$_\odot$. Formally, the vertical dust profile is described by two gaussians for millimeter- (midplane) and micron-sized (atmospheric) grains. For our well-mixed calculation in Section 5.4.1, we assume instead that the dust follows the gas with a uniform gas-to-dust mass ratio $f_g = 100$. For the settled disk discussed in Section 5.4.2, we compare different methods by which to approximate ζ_{SLR} with more sophisticated dust profiles.

5.4.1 Plane-Parallel Approximation

For disks where the radial variation in density is much slower than variations with height z, we can treat the disk as essentially an "infinite slab." We thus carry out a plane-parallel radiative transfer calculation where intensity I is a function of height z above the midplane, and one direction variable. The ray direction is determined by the angle θ with respect to the z-direction, or, equivalently, $\mu = \cos\theta$. The validity of this approximation requires that the disk scale height $H \ll r$.

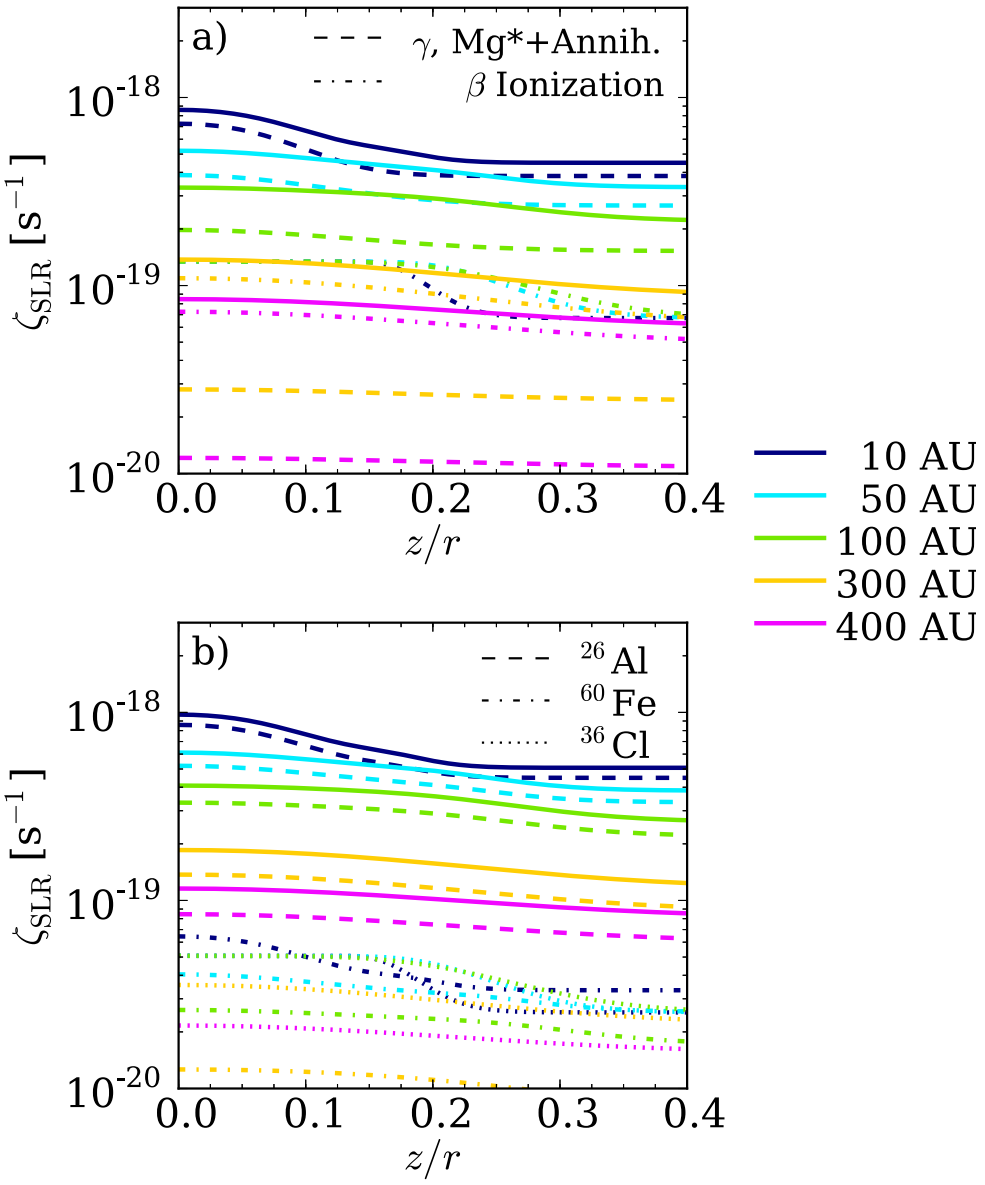

Figure 5.1 H_2 ionization rate as a function of normalized height (z/r) and at specified disk radii (indicated by line color). *Top panel:* ^{26}Al ionization broken into photon (dashed) and particle processes (dot-dash); solid line represents the total ionization rate. *Bottom panel:* Total ionization from ^{26}Al, ^{60}Fe, and ^{36}Cl; individual contributions indicated by dashed, dot-dash, and dotted lines, respectively.

In the well-mixed case, the radiative transfer equation (5.1) has the formal solution:

$$\begin{aligned} I(z,\mu) &= \frac{1}{4\pi}\int_0^{\infty} \rho J \exp[-\tau(z,\mu;s)]ds \\ &= \frac{1}{4\pi}\int_0^{\tau_\mu(z)} \frac{J}{\kappa}\exp[-\tau(z,\mu;s)]d\tau, \end{aligned} \tag{5.4}$$

where the optical depth along a ray in the μ-direction is

$$\tau(z,\mu;s) = \int_0^{s} \kappa\rho(s')ds'. \tag{5.5}$$

Equation (5.4) allows both the emissivity J and the opacity κ to vary with position. In many applications, however, these quantities are constant. In general, we want to evaluate the intensity I at a given height z and for a given ray direction specified by μ. Along the ray, the cylindrical height z' is given by

$$z' = z - \mu s\,. \tag{5.6}$$

Given the optical depth expression (5.5), and the substitution $dz' = -\mu ds$, we can write the optical depth $\tau_\mu(z)$ in the μ-direction in terms of the vertical optical depth $\tau_\pm$,

$$\tau_\mu(z) = -\frac{1}{\mu}\int_z^{\pm\infty} \kappa\rho(z')dz' \equiv \frac{1}{|\mu|}\tau_\pm(z)\,. \tag{5.7}$$

By separating out the angular dependence from the optical depth, we only need to calculate the $\tau_\pm$ integrals once for a given location. Accordingly, the specific intensity is given by

$$\begin{aligned} I(z,\mu) =& \frac{J}{4\pi\kappa}\left(1-\exp\left[-\tau_\mu(z)\right]\right) \\ =& \frac{J}{4\pi\kappa}\left(1-\exp\left[-\frac{1}{|\mu|}\tau_\pm(z)\right]\right)\,. \end{aligned} \tag{5.8}$$

We integrate (5.8) over solid angle to determine the total energy density in ionizing decay photons/particles $\mathcal{E}(z)$:

$$\begin{aligned} c\mathcal{E}(z) &= \int I(z,\mu) d\Omega = 2\pi \int_{-1}^{1} I(z,\mu) d\mu \\ &= 2\pi \int_{-1}^{1} \frac{J}{4\pi\kappa} \left(1 - \exp\left[-\frac{1}{\mu}\tau_{\pm}(z)\right]\right) d\mu. \end{aligned} \tag{5.9}$$

Substituting $t = 1/|\mu|$, we can evaluate this expression in terms of exponential integrals of order two (*Abramowitz and Stegun*, 1972),

$$\begin{aligned} c\mathcal{E}(z) =& \frac{J}{2\kappa} \left\{ 2 - \int_{1}^{\infty} \frac{1}{t^2} \exp\left[-t\tau_{+}(z)\right] dt \right. \\ & \left. - \int_{1}^{\infty} \frac{1}{t^2} \exp\left[-t\tau_{-}(z)\right] dt \right\} \\ =& \frac{J}{2\kappa} \left\{ 2 - E_2\left[\tau_{+}(z)\right] - E_2\left[\tau_{-}(z)\right] \right\}. \end{aligned} \tag{5.10}$$

The ionization rate is then given by

$$\zeta^{k}_{\mathrm{H_2}}(z) = \frac{c\mathcal{E}(z)\langle m \rangle \kappa}{W_{\mathrm{H_2}}} \tag{5.11}$$

$$= \frac{1}{2} \frac{E_k \omega_p}{W_{\mathrm{H_2}}} \left\{ 2 - E_2\left[\tau_{+}(z)\right] - E_2\left[\tau_{-}(z)\right] \right\} \tag{5.12}$$

Equation (5.12) provides the general solution for the ionization rate due to decay product k for a well-mixed disk. This expression can be readily evaluated with knowledge of the disk's opacity in the z-direction. Note that the functions $E_2(z)$ are standard (e.g., *Abramowitz and Stegun* 1972, or the Python library *SciPy*).

For a vertically gaussian disk of the form $\rho_g(z) = \rho_0 \exp\left[-1/2\ (z/H)^2\right]$, we can solve

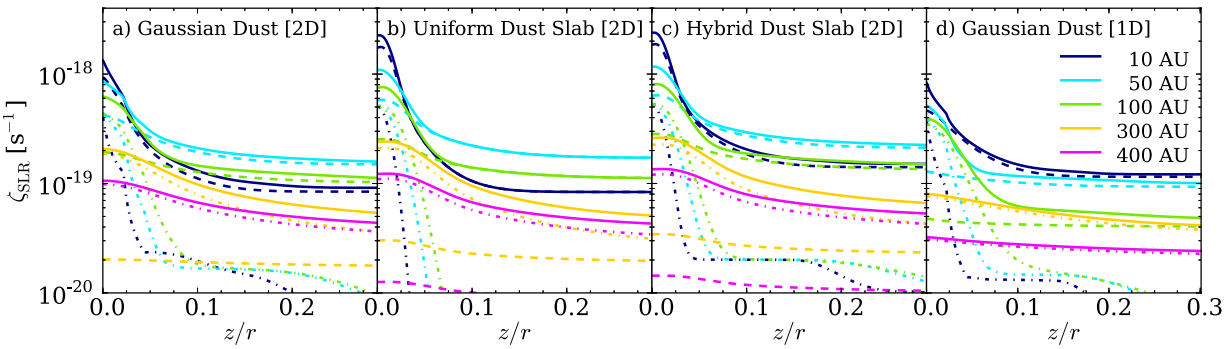

Figure 5.2 Line-styles as indicated in Figure 5.1 for ^{26}Al ionization only: a) infinite slab calculation for the original model dust profile; b) infinite slab calculation for a uniform density dust layer in the midplane; c) hybrid model of uniform dust layer combined with a small-grain gaussian distribution; and d) original density profile with decay product escape restricted to the z-direction.

exactly for $\tau_{\pm}$,

$$\tau_{\pm}(z) = \tau_0 \left\{ 1 \mp \mathrm{erf}\left[\frac{z}{\sqrt{2}H} \right] \right\}, \tag{5.13}$$

where we have defined

$$\tau_0 = \kappa \rho_0 H \sqrt{\frac{\pi}{2}} = \frac{\kappa \Sigma_g}{2}. \tag{5.14}$$

Note that $\tau_{\pm}$ must be computed for each type of decay product k where the decay ranges are provided in Table 5.1. Nonetheless, Equation (5.13) allows the ionization rate to be calculated – easily and exactly – from Equation (5.12) at any point (r, z) in the disk.

Figure 5.1 presents the results from Equations (5.12,5.13) for our standard disk model. Of the various SLR parent bodies, ^{26}Al dominates the ionization rate ζ_{SLR} at early times, as demonstrated in the bottom panel where we include ionization contributions from ^{26}Al, ^{60}Fe, and ^{36}Cl decay, which together increase ζ_{SLR} by $\sim 13\%$. Among the ^{26}Al decay products, within $R < 100$ AU the more energetic γ-rays play the largest role, while outside of this region the more readily stopped positrons carry the ionization (see Figure 5.1, dashed and dot-dash lines, respectively).

5.4.2 Dust Settling

As dust settles towards the midplane, the sources of emissivity (SLRs in the dust) and the absorbers (gas) are no longer well-mixed. In our settled disk model (Chapter 4), the large grains have a smaller scale-height h than the gas and small grains, H, where both dust reservoirs are described by a gaussian profile and where $h/H = 0.2$. This section provides two methods to approximate this more complicated radiative transfer problem.

The original integral for the energy density can be written in the form

$$c\mathcal{E}(z) = \frac{J}{2} \int_{-1}^{1} d\mu \int_{0}^{\infty} \rho_g(s) \frac{100}{f_g(s)} \exp\left[-\tau(s)\right] ds, \tag{5.15}$$

from which $\zeta_{\rm SLR}$ can be directly computed via Equation (5.11). Using the plane-parallel approximation in conjunction with $f_g(s) = \rho_g(s)/\rho_d(s)$, we can solve Equation (5.15), as was done for the well-mixed case (Section 5.4.1). In general, this integral must be carried out numerically and is moderately computationally expensive, but it provides an accurate treatment of the problem. We use this numerical result (see Figure 5.2a) to benchmark the approximations derived below.

5.4.2.1 Uniform Thin Dust Layer

Our first approximation considers the case where the radioactive elements have settled into a thin layer with scale height $h \ll H$. We can write the density distribution with the limiting form

$$\rho_d(z) = \Sigma_d \delta(z), \tag{5.16}$$

where $\delta(z)$ is the Dirac delta function and $\Sigma_d = \Sigma_g/100$ is the total dust surface density. With this substitution, the solution to the integral in Equation (5.4) for a gaussian disk is

$$I(z \gg h; \mu) = \frac{J\Sigma_g}{4\pi\mu} \exp\left[-\frac{\tau_0}{|\mu|} \operatorname{erf}\left(\frac{z}{\sqrt{2}H}\right)\right], \tag{5.17}$$

which is valid for $\mu \geq 0$. In the limit where all SLRs are concentrated at the midplane, $I = 0$ for $\mu < 0$, i.e., nothing is emitted from above. The term in brackets is the optical depth from the midplane to height z (divided by μ), and can be calculated for a general disk. The corresponding energy density has the form

$$c\mathcal{E}(z) = 2\pi \int_0^1 I(z,\mu) d\mu = \frac{J\Sigma_g}{2} E_1 \left[\tau_0 \, \mathrm{erf}\left(\frac{z}{\sqrt{2}H} \right) \right], \tag{5.18}$$

where $E_1(\tau)$ is the exponential integral of order one. In the limit $\tau \to 0$, $E_1(\tau) \to \infty$ as a natural consequence of the δ-function. To evaluate the ionization rate near the midplane, we now consider the density distribution to have finite thickness

$$\rho_d(z) = \frac{\Sigma_d}{2\sqrt{2}h} \qquad \text{for} \qquad |z| \leq \sqrt{2}h, \tag{5.19}$$

where $\rho_d(z) = 0$ for $|z| > \sqrt{2}h$. With this specification, the specific intensity has the form

$$I(z;\mu) = \frac{J}{4\pi} \frac{\Sigma_g}{2\sqrt{2}h} \int_0^\infty \Theta(z') \exp[-\tau(s)] ds, \tag{5.20}$$

where $\Theta(z') = 1$ for $-\sqrt{2}h \leq z' \leq \sqrt{2}h$ and is zero otherwise. If $z > \sqrt{2}h$, then only rays with $\mu > 0$ result in nonzero I. Next we define $t \equiv z'/\sqrt{2}H$ such that

$$\tau(t) = \frac{\tau_0}{|\mu|} \left| \mathrm{erf}\left(\frac{z}{\sqrt{2}H} \right) - \mathrm{erf}(t) \right|. \tag{5.21}$$

For $z < \sqrt{2}h$, the specific intensity becomes

$$I(z < h; \mu > 0) = \frac{J}{4\pi} \frac{\Sigma_g}{\mu} \frac{H}{2h} \int_{-h/H}^{z/H} \exp\left[-\tau(t)\right] dt, \tag{5.22}$$

$$I(z < h; \mu < 0) = \frac{J}{4\pi} \frac{\Sigma_g}{|\mu|} \frac{H}{2h} \int_{z/H}^{h/H} \exp\left[-\tau(t)\right] dt. \tag{5.23}$$

In the limit $z \to 0$, the specific intensity becomes

$$I(z \to 0, \mu) = \frac{J}{4\pi} \frac{\Sigma_g}{2h} \frac{H}{|\mu|} \int_0^{h/H} \exp\left[-\frac{\tau_0}{|\mu|} \mathrm{erf}(t)\right] dt, \tag{5.24}$$

where we have used Equation (5.21). Next we evaluate the specific intensity in the limit $h \ll H$ where we can approximate $\mathrm{erf}(t) \approx 2t/\sqrt{\pi}$, which implies

$$I(z \to 0, \mu) = \frac{J}{4\pi\kappa} \frac{\sqrt{\pi} H}{2h} \left\{1 - \exp\left[-\frac{\tau_0}{|\mu|} \frac{2h}{\sqrt{\pi} H}\right]\right\}. \tag{5.25}$$

Defining a "dust-compactness" parameter

$$\lambda \equiv \frac{2h}{\sqrt{\pi} H}, \tag{5.26}$$

the corresponding energy density at $z \to 0$ is given by

$$\begin{aligned} c\mathcal{E}_0 &= \frac{J}{\kappa} \frac{1}{\lambda} \left\{1 - \int_1^\infty \frac{\exp\left[-\tau_0 \lambda x\right]}{x^2} dx\right\} \\ &= \frac{J}{\kappa} \frac{1}{\lambda} \left\{1 - E_2\left[\tau_0 \lambda\right]\right\}. \end{aligned} \tag{5.27}$$

Equations (5.18) and (5.27) give the ionization rate ζ_{H_2} in the limits $z \gg h$ and $z \to 0$, respectively. To provide a continuous expression for ζ_{H_2}, we smoothly connect the two limiting forms,

$$\begin{aligned} \zeta_{\mathrm{H}_2}(z) = (1 - f(z)) &\left\{\frac{J\Sigma_g}{2} E_1\left[\tau_0 \,\mathrm{erf}\left(\frac{z}{\sqrt{2}H}\right)\right]\right\} \\ &+ f(z) \left\{\frac{J}{\kappa} \frac{1}{\lambda} \left\{1 - E_2\left[\tau_0 \lambda\right]\right\}\right\}, \end{aligned} \tag{5.28}$$

where f is a continuous function, e.g., $f = \exp[-z^2/2h^2]$. In the limit $\lambda \to 0$, Equation (5.28) provides the solution for a disk model where all of the dust has settled to the midplane. In

limit $\lambda \to 1$, we recover the solution for the well-mixed disk (Section 5.4.1).

Figure 5.2 (b) shows the ionization rate due to mm-grains (containing 85% of the dust mass) approximated as a thin slab from Equation (5.28). In panel (c) we combine the results in (b) with the well-mixed calculation for small grains (15% of all dust mass) following Section 5.4.1, thereby producing a "hybrid" model. At large heights and large radii, the thin-slab solution reproduces the full solution (a) quite well, though slightly overestimates ($\sim 30 - 60\%$) the ionization inside $R < 50$ AU near the midplane.

5.4.2.2 Bidirectional Escape Approximation

As an alternate approach, we consider only the vertical column of emitters/absorbers, essentially assuming that radiation travels only in the z-direction. This simplification provides the solution after evaluating only one integral in addition to τ, and thus allows us to consider more complex/non-analytic dust and gas distributions. In this "bidirectional escape" approximation, the ionization rate has the form

$$\zeta_{\mathrm{H_2}}(z) = \frac{J}{2}\frac{\kappa\langle m\rangle}{W_{\mathrm{H_2}}}\left\{\int_0^{\infty}\rho_g(z)\left(\frac{100}{f_g(z)}\right)\exp\left[-\tau(z)\right]dz + \int_0^{-\infty}\rho_g(z)\left(\frac{100}{f_g(z)}\right)\exp\left[-\tau(z)\right]dz\right\}. \tag{5.29}$$

where $\tau_{\pm}$ are given by Equation (5.13). Although this approximation is somewhat crude, the solution can be readily evaluated via numerical integration, where the emissivity J is given by Equation (5.2). Figure 5.2 (d) compares this bidirectional approximation to the plane-parallel calculation for the same dust density profile. In general, the bidirectional calculation underestimates the ionization rate by a factor of ~ 1.5, with the discrepancy growing to a factor of ~ 2 for $R \geq 300$ AU.

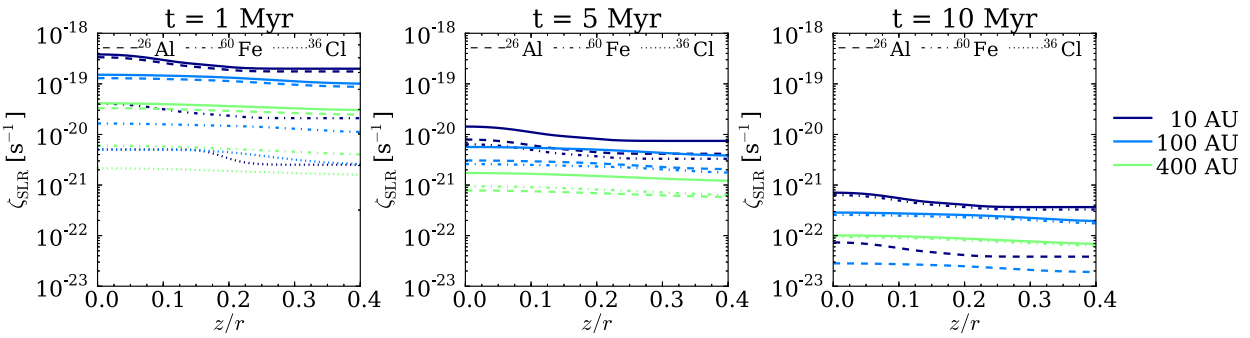

Figure 5.3 Same as Figure 5.1, at the indicated time after $t = 0$ such that the ionizing reservoir has been partially exhausted. For $t < 5$ Myr, the ionization rate is set by ^{26}Al-decay. At later times (right, $t = 10$ Myr) the longer-lived ^{60}Fe provides the ionization, although at a reduced rate due to its lower abundance and longer decay time.

5.4.3 Time Dependence

Technically, the abundances of the SLRs evolve with time, with half-lives $t_{\rm half} \sim 1$ Myr, comparable to disk evolution timescales. We have calculated the ionization rates for the unsettled disk at $t = 1, 5$ and 10 Myr, to compare with the $t = 0$ calculations from Section 5.4 (Figure 5.1); these results are presented in Figure 5.3. At early times, ^{26}Al and ^{36}Cl are the dominant ionizing agents; after ~ 5 Myr, however, the longer-lived though less abundant ^{60}Fe determines the ionization rate $\zeta_{\rm SLR}$. At even longer times, long-lived radionuclides such as ^{40}K ($t_{\rm half} \sim 1.28$ Gyr; *Umebayashi et al.*, 2013) provide the largest contribution. However, because the ionization rate is inversely proportional to $t_{\rm half}$, long-lived radionuclides only produce ionization rates of order $\zeta_{\rm H_2} \lesssim 10^{-22}$ s^{-1}.

Figure 5.4 plots the ionization rate $\zeta_{\rm SLR}$ calculated at the disk midplane ($z = 0$) versus vertical disk surface density at several times. We have fitted power-laws (shown in gray in Figure 5.4) to the ionization rates from all three SLR species to facilitate their use. For the well-mixed disk, the rate $\zeta_{\rm H_2}$, as a function of disk surface density and time, is given by

$$\zeta_{\rm H_2}(r) = \left(2.5 \times 10^{-19}\ {\rm s}^{-1}\right) \left(\frac{1}{2}\right)^{1.04t} \left(\frac{\Sigma(r)}{\rm g\ cm^{-2}}\right)^{-0.27}, \tag{5.30}$$

where time, t, is given in Myr.

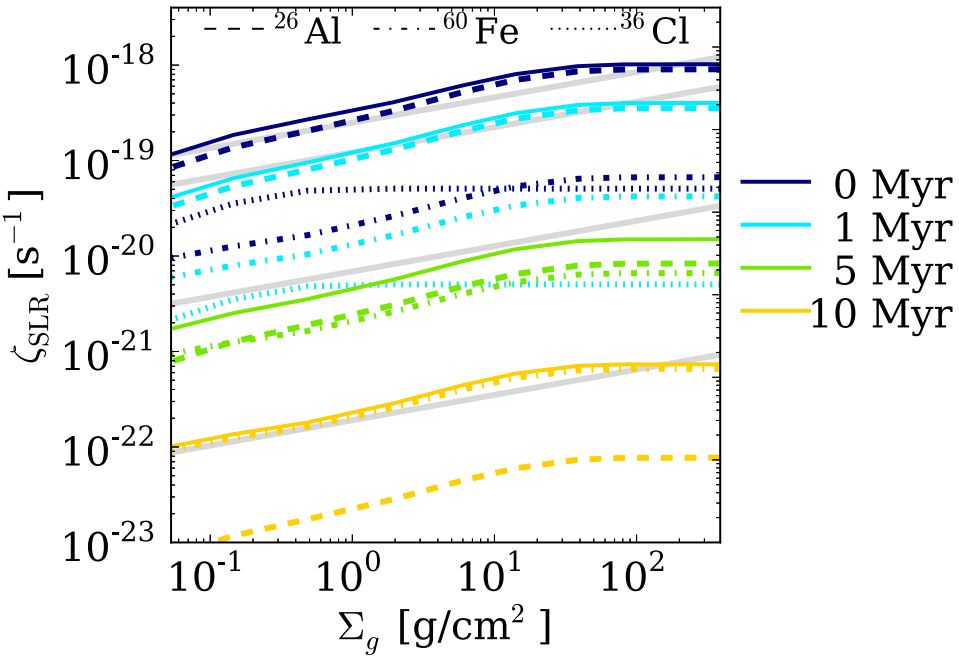

Figure 5.4 Ionization rate per H_2 in the midplane as a function of disk surface density at the indicated times. We fit these results using a simple power-law versus surface density, normalized with to a time-dependent constant (gray lines), see Equation (5.30).

5.5 Discussion

This work has made two simplifying assumptions that warrant further consideration. First, we have used a single opacity to simplify the calculations. In reality, the photons and particles will have their energies degraded as they collide with the gas. For Compton-scattered photons, the change in γ-ray energy for $E_\gamma < m_e c^2$ is approximately $\Delta E \propto {E_\gamma}^2$ (*Rybicki and Lightman*, 1979). This energy degradation results in an energy spectrum of the form $I(E_\gamma) \approx E_\gamma \; dN/dE \approx E_\gamma / \Delta E \propto 1/E_\gamma$, from which we may compute a weighted opacity for photons that lose all of their energy through scattering in the disk,

$$\langle \kappa \rangle \equiv \frac{\int_0^{E_i} \kappa(E_\gamma) I dE}{\int_0^{E_i} I dE} \, . \tag{5.31}$$

At sufficiently low energies, below $E_\gamma < 30$ keV, the dominant absorption mechanism becomes photoabsorption, at which point the photon has lost nearly all of its initial energy $E_i \sim 1$ MeV. The Compton-weighted opacity for a 1.808 MeV photon is $\langle \kappa \rangle \sim 0.19$ cm^2 g^{-1}, larger than its initial cross section, $\kappa_i \sim 0.08$ cm^2 g^{-1}, which increases the derived ionization rate by factors of 4% (12%) at $r = 10$ AU (400 AU).

Another major simplification comes from our treatment of the positrons in ^{26}Al decay. Currently we assume that all energetic particles are emitted locally and can then escape. According to *Umebayashi et al.* (2013), the positron will first lose its energy to primarily collisional ionization until it comes to rest, at which point it will annihilate with an electron and produce two 0.511 MeV γ-rays. However, the cross section for absorption of the γ-rays is less than that of the original positrons. For disk regions where positrons escape in our simplified treatment, these γ-rays escape even more readily, and thus make smaller contributions to the ionization rate.

5.6 Conclusion

This Chapter carries out radiative transfer calculations for the decay products of short-lived radionuclides in circumstellar disks. These SLRs provide an important contribution to the ionization rates, which in turn affect disk chemistry and physics. We provide simple analytic expressions for the ionization rates due to SLR decay. For well-mixed disks, the ionization rate $\zeta_{\rm SLR}(r,z)$ can be found analytically and is given by Equation (5.12). The radial dependence is controlled by the surface density profile, which determines the optical depths through Equations (5.13) and (5.14). Complications arise as disks evolve, including dust settling and a decrease in the SLR abundances. We provide two approximations for disks with settled dust layers: The first treatment considers the dust as a thin uniform layer; the ionization rate is given by Equation (5.28), where the dust-compactness parameter λ determines the degree of settling (Equation (5.26)). This approximation scheme is accurate to tens of percent, and becomes exact for a well-mixed disk. For completeness, we develop a simpler approximation that considers radiation propagation in the vertical directions only (Section 5.4.2.2), as is commonly done for calculations of CR ionization rates. Finally, we provide a fit to the midplane ionization rates as a function of surface density and time (Equation (5.30)). While this function can be applied over the entire vertical structure, it formally overestimates $\zeta_{\rm H_2}^{\rm SLR}$ at the disk surface. In this regime, however, other ionization sources (e.g., stellar X-ray photoionization of H_2) will dominate, so that our approximation remains satisfactory.

A full treatment of this problem requires Monte Carlo or other numerical methods, including energy losses, angle-dependent scattering, energy-dependent radiative transfer, and more sophisticated density distributions. Although these generalizations should be incorporated in future work, the analytic expressions derived herein provide useful and accurate estimates for the ionization rates due to SLR decay, and can thus be used in a wide variety of physical and chemical disk models.

5.7 Acknowledgments

LIC and EAB gratefully acknowledge support from NSF grant AST-1008800.

CHAPTER VI

Exclusion of Cosmic Rays in Protoplanetary Disks. II. Chemical Gradients and Observational Signatures

6.1 Preface

The following work appears in the Astrophysical Journal, Volume 794, 123, 23 pp. (2014). The work is co-authored by Edwin A. Bergin[1] and Fred C. Adams[2]. The paper is copyright 2014, the American Astronomical Society, reproduced here under the non-exclusive right of republication granted by the AAS to the author(s) of the paper.

6.2 Abstract

The chemical properties of protoplanetary disks are especially sensitive to their ionization environment. Sources of molecular gas ionization include cosmic rays, stellar X-rays and short-lived radionuclides, each of which varies with location in the disk. This behavior leads to a significant amount of chemical structure, especially in molecular ion abundances, which is imprinted in their submillimeter rotational line emission. Using an observationally motivated disk model, we make predictions for the dependence of chemical abundances

[1]Department of Astronomy, University of Michigan, 500 Church St, Ann Arbor, MI 48109
[2]Department of Physics, University of Michigan, 450 Church St, Ann Arbor, MI 48109

on the assumed properties of the ionizing field. We calculate the emergent line intensity for abundant molecular ions and simulate sensitive observations with the Atacama Large Millimeter/Sub-millimeter Array (ALMA) for a disk at $D = 100$ pc. The models readily distinguish between high ionization rates ($\zeta \gtrsim 10^{-17}$ s^{-1} per H_2) and below, but it becomes difficult to distinguish between low ionization models when $\zeta \lesssim 10^{-19}$ s^{-1}. We find that H_2D^+ emission is not detectable for sub-interstellar CR rates with ALMA (6h integration), and that N_2D^+ emission may be a more sensitive tracer of midplane ionization. HCO^+ traces X-rays and high CR rates ($\zeta_{CR} \gtrsim 10^{-17}$ s^{-1}), and provides a handle on the warm molecular ionization properties where CO is present in the gas. Furthermore, species like HCO^+, which emits from a wide radial region and samples a large gradient in temperature, can exhibit ring-like emission as a consequence of low-lying rotational level de-excitation near the star. This finding highlights a scenario where rings are not necessarily structural or chemical in nature, but simply a result of the underlying line excitation properties.

6.3 Introduction

Ionization plays an important role in setting thermal (e.g., *Glassgold et al.*, 2004), dynamical (*Balbus and Hawley*, 1991; *Gammie*, 1996; *Matsumura and Pudritz*, 2003), and chemical (e.g., *Semenov et al.*, 2004; *Öberg et al.*, 2011d) properties of protoplanetary disks. The chemistry occurring in the bulk mass of disks is especially sensitive to ionization for two reasons: (i) in the cold gas, ion-neutral reactions are the most efficient means towards chemical complexity, and (ii) in the ices, the crucial hydrogenation reactions (*Tielens and Hagen*, 1982; *Hasegawa et al.*, 1992a) are fueled by hydrogen atoms that are extracted by ionization of molecular H_2. The dominant ionization processes in disks are photoionization from stellar and interstellar UV and X-ray radiation, thermal ionization, ionization by the decay products of short-lived radionuclides (SLRs), and cosmic ray (CR) ionization. Additionally, the cluster environment can provide a source of ionization on the outer surface of the disk from interstellar FUV, which can exceed that of the galactic average interstellar FUV

by a factor of $\gtrsim 3000$ (*Fatuzzo and Adams*, 2008). Of these sources, CRs and potentially SLR decay provide ionization in the densest and coldest layers of the disk, where UV and X-rays are highly attenuated. However, it is unclear as to whether or not CRs are actually present at rates derived for the interstellar medium (ISM), i.e., $\zeta_{\rm CR} \sim (1-5) \times 10^{-17}$ s^{-1} in dense gas and $\zeta_{\rm CR} \sim (1-8) \times 10^{-16}$ s^{-1} in the diffuse ISM (*Dalgarno*, 2006, and references therein). Modulation of the CR flux can occur as a result of exclusion by natal stellar winds as explored in detail in Chapter 4 and discussed in *Glassgold* (1999); *Aikawa and Herbst* (1999a) and *Fromang et al.* (2002), in addition to exclusion by magnetic fields (*Dolginov and Stepinski*, 1994; *Padovani and Galli*, 2011; *Fatuzzo and Adams*, 2014). At these reduced levels, the ionization from SLR decay products becomes as important, and perhaps even more so, than that of CRs.

In the present work, we set out to determine the chemical imprint of individual ionization processes in a generic protoplanetary disk model. We outline how observations of molecular species can be used as a blueprint to constrain the underlying ionization properties of the disk's dense molecular gas. More specifically, we focus on the impact of the assumed CR flux on molecular abundances in tandem with a detailed treatment of ionization by SLRs and stellar X-rays, including a Monte Carlo treatment of the scattered X-ray radiation field. We extend these results to make testable predictions for future sensitive observations with the Atacama Large Millimeter/Submillimeter Array (ALMA) of molecular ion emission in protoplanetary disks. Such predictions will help more accurately determine not only the ionization fraction in disks, which is important for constraining models of turbulence and chemistry, but also the *source* of ionization traced by a given molecular ion and transition.

Current detections of molecular ions in disks include N_2H^+, HCO^+, and DCO^+ (e.g., *Dutrey et al.*, 1997; *van Dishoeck et al.*, 2003; *Thi et al.*, 2004; *Öberg et al.*, 2010, 2011c). The elusive H_2D^+ has yet to be detected in a disk, with reported detections of the $(1_{10}-1_{11})$ line towards DM Tau and TW Hya (*Ceccarelli et al.*, 2004) not confirmed by reanalysis or more sensitive observations (*Guilloteau et al.*, 2006; *Qi et al.*, 2008; *Chapillon et al.*, 2011).

The H_2D^+ upper limits nonetheless provide some constraints on the midplane ionization rate. *Chapillon et al.* (2011) investigated chemical models incorporating deuterium chemistry and find models with midplane ionization rates below $\zeta_{\rm total} < 3\times10^{-17}$ s^{-1} are required to explain the line's non-detection. Strictly speaking, CRs are the primary midplane ionizing agent considered by *Chapillon et al.* (2011), though we note this value more generally provides a limit on the *total* ionization rate, which is expected to be primarily due to SLRs and CRs in the H_2D^+ emitting gas, discussed in more detail below. We note that the deuterium chemistry of H_2D^+, specifically the reactions leading back to H_3^+, are sensitive to the ortho-to-para ratio of both H_3^+ and H_2 (*Chapillon et al.*, 2011; *Hugo et al.*, 2009; *Albertsson et al.*, 2014), which we include in this work (see §6.6.1). Furthermore, H_2D^+ can undergo deuterium substitution towards the fully substituted and unobservable D_3^+ (*Walmsley et al.*, 2004), which complicates the interpretation of H_2D^+ measurements in determining ionization from H_2D^+. Such progressive D-substitution may point towards future difficulty in detection experiments of what would otherwise be a useful tracer of ionization and cold chemistry. This point further emphasizes the utility of chemical models in the interpretation of molecular ion emission as a proxy for measuring disk ionization rates.

The Chapter is structured as follows: In Sections §6.4 and §6.5, we review the physical model and the sources of ionization considered. In Section §6.6.1 we describe the updated chemical reaction network used to predict the molecular abundances, and Section §6.6.2 examines the chemical abundance variations between the different ionization models. Section §6.7 makes predictions for sensitive, high-spatial resolution submillimeter observations that can be used to determine and to distinguish between the important ionization mechanisms. In Section §6.8, we discuss the effects of a more X-ray luminous source, time-decay of radionuclides, disk gas mass, and the impact of disk magnetic fields. In Section §6.9, we summarize our results and discuss their implications.

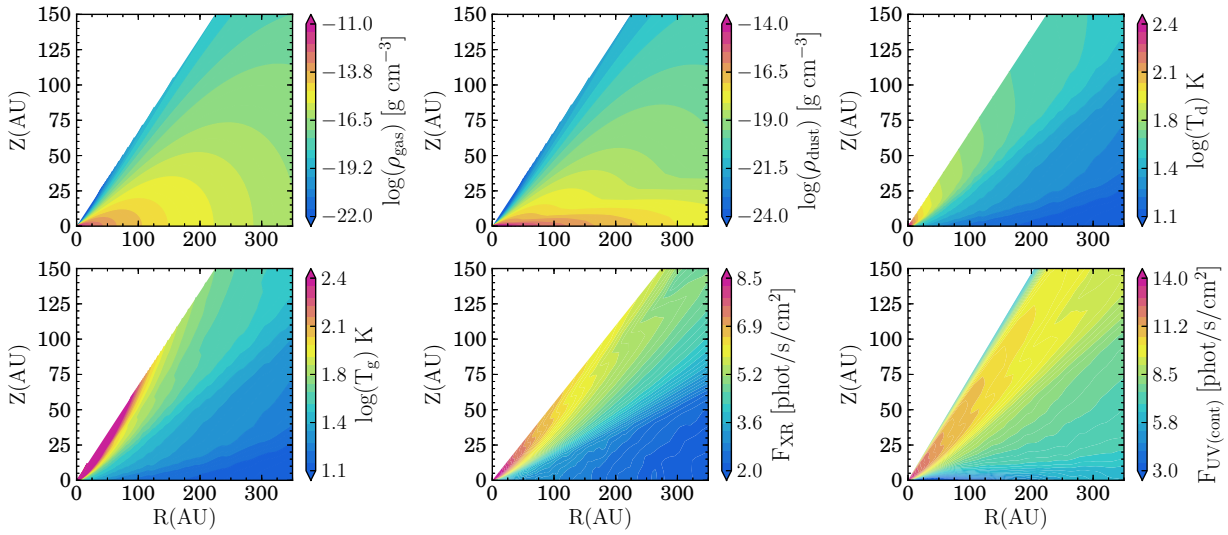

Figure 6.1 Disk model used for the chemical calculations. *Top row, left to right:* i) gas density, ii) settled dust density, iii) dust temperature. *Bottom row, left to right:* i) gas temperature, ii) integrated X-ray radiation field and iii) FUV radiation field from the central star. The FUV flux is integrated between $930 - 2000$ Å using the observed TW Hydra FUV spectrum (*Herczeg et al.*, 2002, 2004), including Ly-α. The X-ray luminosity is $L_{\rm XR} = 10^{29.5}$ erg s^{-1} integrated between $E_{\rm XR} = 0.1 - 10$ keV.

6.4 The Physical Model

We refer the reader to a detailed description of the disk model parameters in Chapter 4, and review only the main aspects of the model below. The fiducial disk mass is $M_d \sim 0.04$ M$_\odot$ within a $R_d = 400$ AU radius, where the vertical structure and geometrical parameters (i.e. flaring) are typical of observed protoplanetary disks (*Andrews et al.*, 2011). The gas and dust surface densities follow a power law with an exponential taper at the outer edge (*Hughes et al.*, 2008; *Andrews et al.*, 2011) and the dust is heated via passive irradiation from the central K5V star with $T_{\rm eff} = 4300$ K with the code TORUS (*Harries*, 2000; *Harries et al.*, 2004; *Kurosawa et al.*, 2004; *Pinte et al.*, 2009). The gas temperature is calculated from a fitting function calibrated to detailed thermochemical models of disks heated by FUV photons from the central star (Simon Bruderer in private communication, 2013). In the heating calculation, we consider only the central star's FUV field (described in §6.5.1). The

Table 6.1. Stellar and disk model parameters.

Stellar Model	
Stellar Mass	1.06 $M_\odot$
Stellar Radius	1.83 $R_\odot$
Stellar T_{eff}	4300 K
L_{UV}	2.9 $\times 10^{31}$ erg/s [a]
L_{XR}	$10^{29.5}$ erg/s
Disk Model	
R_{inner}	0.1 AU
R_{outer}	400 AU
M_{dust}	3.9 $\times 10^{-4}$ $M_\odot$
M_{gas}	0.039 $M_\odot$

[a] As computed from the observed FUV spectrum of TW Hya integrated between 930 and 2000 Å (*Herczeg et al.*, 2002, 2004).

vertical distribution of dust is broken up into two populations to simulate grain growth, with a population of large millimeter grains concentrated at the geometrical center of the disk (the midplane) and a population of "atmosphere" micron-sized grains distributed over larger scale heights. The gas and small micron-sized grains follow the same scale height (see Chapter 4 for details, as well as the dust optical properties). Figure 6.1 shows the disk density, thermal and stellar radiation fields, and Table 6.1 outlines the main physical parameters of our model.

6.5 Ionization Sources

Star/disk systems are subject to a variety of ionization sources, including FUV and X-ray radiation from the central stars, short-lived radionuclides, and CRs. These ionization sources are not constant in time or in space. Instead, they are expected to vary with the local environment, from system to system, and display time dependence. Some environments include ionizing radiation from nearby (more massive) stars (see the review of *Adams*,

2010), although this complication is left for future work. This section outlines the physical mechanisms that contribute to the disk ionization rate and the ranges of values considered at present.

6.5.1 Stellar Photoionization

T Tauri stars are known to be X-ray luminous with X-ray luminosities typically ranging $L_{\rm XR} \sim 10^{29} - 10^{31}$ erg s^{-1} (e.g., *Feigelson and Decampli*, 1981a; *Feigelson et al.*, 1993; *Telleschi et al.*, 2007). Consequently, the disk's X-ray ionization properties are perhaps the best (observationally) constrained ionization agent present in the disk molecular gas. That said, the permeability of the disk gas to X-rays is unknown owing to uncertainties in the disk mass (the column density) and composition (opacity) of the absorbing materials. The biggest uncertainty in the X-ray opacity is in the time-dependent effects of dust settling, which redistributes and removes the absorbing material from the upper layers. More specifically, by removing dust mass from the upper layers the opacity shifts from a well-mixed gas and dust regime to a gas-dominated opacity. For *Asplund et al.* (2009) abundances, the change in opacity corresponds to a factor of two decrease in absorption cross section between the well-mixed and fully settled cases at $E_{\rm XR} = 1$ keV (*Bethell and Bergin*, 2011b). However, with knowledge of the star's X-ray luminosity, it may be possible to shed light on the permeability of the disk atmosphere to X-rays with the proposed molecular tracers in this work (see §6.6.2).

We calculate the stellar FUV and X-ray radiation fields as a function of position and wavelength within the disk using a Monte Carlo treatment described in *Bethell and Bergin* (2011a). For FUV transfer, we consider the dust model's position-dependent opacities and compute the absorption and scattering on dust grains. In addition to the radiative transfer through the dust, we calculate the Lyman-α line transfer, where photons scatter isotropically off atomic hydrogen present at the disk surface. Treatment of Lyman-α is important as this line has been observed to carry $\sim 80 - 90\%$ of the total FUV flux (*Herczeg et al.*, 2004; *Schindhelm et al.*, 2012; *France et al.*, 2014); as a consequence of its scattering properties,

the Lyman-α photons are able to penetrate deeper into the disk gas than the rest of the primarily dust-scattered FUV photons (*Bethell and Bergin*, 2011a). Because the present Chapter is mainly focused on understanding the ionization properties of the dense molecular gas, we hold the FUV radiation field constant in the models presented here since FUV mainly contributes to the ionization in the lower density surface layers where, for example, C^+ emission originates. The assumed incident FUV spectrum is that of TW Hydra (*Herczeg et al.*, 2002, 2004), the closest and least extincted T Tauri star along the line of sight, $d = 55$ pc (*Perryman et al.*, 1997). In this work, we do not include the interstellar FUV radiation field as a source of ionization in the dense gas, but it is expected to play a role in the cluster environment where the external FUV field can be many thousands of G_0 (*Fatuzzo and Adams*, 2008), where G_0 is the mean value for the ISM (*Habing*, 1968; *Draine*, 1978). A G_0=1 has a less significant effect on the chemistry since a small amount of UV opacity from small grains restricts the UV penetration to an outer shell on the disk surface, which is dwarfed by scattered UV from star itself (see Fig. 3 of Chapter 4). A similar ionization study should be carried out for more extreme cluster environments, where the high UV field will be accompanied by a higher SLR abundance and potentially CR abundance in the vicinity of massive stars.

The specific (energy-dependent) X-ray fluxes are calculated using the same code as was used for the FUV (*Bethell and Bergin*, 2011a) where we instead adopt the updated X-ray absorption gas and dust opacities of *Bethell and Bergin* (2011b). We note that the model has been updated since Chapter 4, where the dust-reduced opacity in the upper layers (90% reduction in dust, or "e0p1") was originally assumed to be uniform throughout the disk. We have since updated this calculation to take into account our knowledge of the local gas-to-dust mass ratio. We determine the absorption opacity due to gas and dust individually at each location in the disk from the *Bethell and Bergin* (2011b) cross sections. The X-ray scattering is dominated by Thomson scattering and approximately isotropic (i.e., photons are scattered equally in the backwards and forwards directions). For the primary model,

we assume a characteristic T Tauri star X-ray luminosity of $L_{\rm XR} = 10^{29.5}$ erg s^{-1} with the quiescent X-ray spectral template given in Chapter 4.

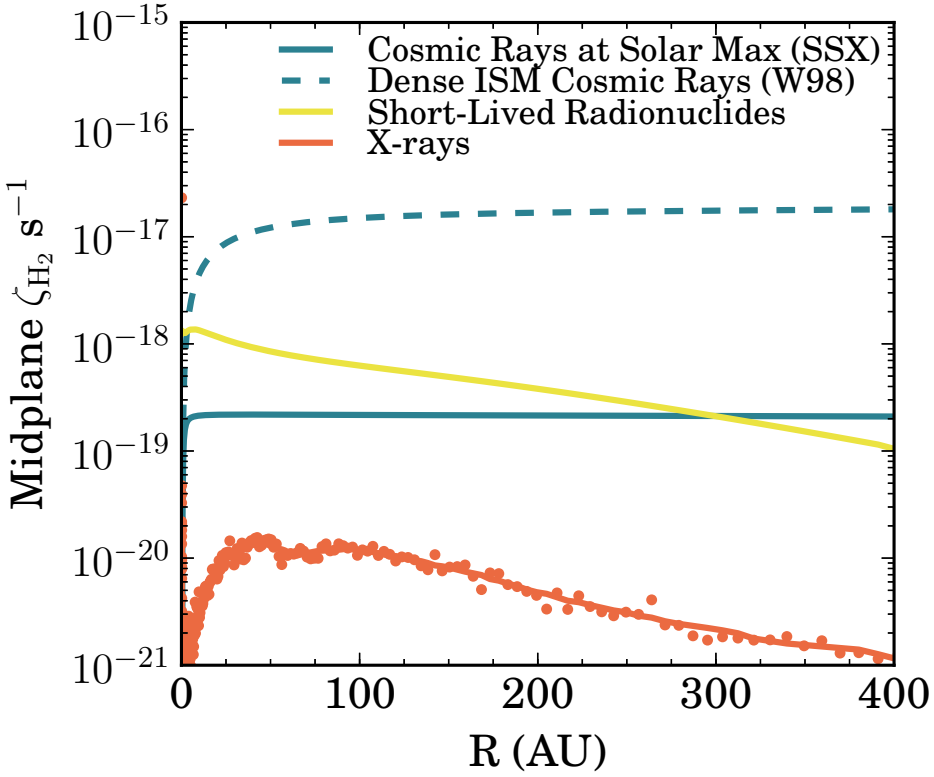

Figure 6.2 Sources of H_2 ionization present in the midplane as a function of disk radius. The orange points are the result of our Monte Carlo calculation and are dominated by intermediate energy X-ray photons, typically $5 - 7$ keV. The solid blue-green line is the cosmic ray ionization rate including the modulation of stellar winds for the present-day Sun at solar maximum. The CR value typically assumed for disk chemical models is shown in dashed blue-green for comparison. The yellow line shows the initial contribution from short-lived radionuclide ionization, predominantly ^{26}Al. The radial decrease in SLR ionization is due to losses of SLR decay products, which escape the disk. The effective half-life of the SLR curve is $t_{\rm half} \sim 1$ Myr.

The most abundant low energy X-rays ($E \sim 1$ keV) are also the most easily attenuated, and consequently do not contribute to the dense midplane ionization. The most important X-rays in the densest gas are typically of intermediate energies, between $5 - 7$ keV, which are less numerous but can more readily penetrate the gas and dust. We emphasize that a detailed treatment of X-ray scattering is crucial in understanding disk ionization, otherwise there would be no X-ray photons in the midplane (*Igea and Glassgold*, 1999; *Ercolano and*

Glassgold, 2013, Chapter 4). Correspondingly, the scattered X-ray radiation field provides the absolute floor to the midplane ionization rate in the absence of CRs and SLRs (see Figure 6.2). In the Figure, the initial rise in midplane X-ray intensity occurs as the disk surface density drops (becomes more optically thin), while the fall-off beyond $R \sim 50$ AU is simply geometrical dilution. The X-ray ionization floor falls in the range $\zeta_{\rm XR} \sim (1 - 10) \times 10^{-21}$ s^{-1}. For a more massive or denser disk than the one considered here, the role of X-rays can be diminished in the midplane by more extreme gas extinction. On the other hand, a star with higher X-ray luminosity would have a proportionally higher $\zeta_{\rm XR}$ depending upon the shape of the stellar X-ray spectrum (see also §6.8.1).

6.5.2 Short-Lived Radionuclide Ionization

The disk ionization contribution from the decay of SLRs has been studied extensively (*Consolmagno and Jokipii*, 1978; *Umebayashi and Nakano*, 1981; *Finocchi and Gail*, 1997; *Umebayashi and Nakano*, 2009; *Umebayashi et al.*, 2013, see also Chapter 4). The initial abundances of radioactive species within a typical protoplanetary disk are uncertain but can be estimated for the case of the protosolar disk from isotopic abundance measurements in meteorites (e.g., *Wasserburg et al.*, 2006, and references therein). Whether these values are representative of all disks is unknown; however, the frequency of differentiated extrasolar asteroids seem to indicate that the young Solar System was at least not atypical in its SLR content (*Jura et al.*, 2013), a hypothesis which models successfully reproduce (*Vasileiadis et al.*, 2013). Moreover, recent work indicates that both direct (disk) SLR injection in clusters and distributed SLR enrichment in molecular clouds can produce abundances comparable to those inferred for the early Solar Nebula (*Adams et al.*, 2014).

Time evolution of abundances adds further uncertainty in estimating the SLR contribution to the ionization budget in disks. The characteristic half-life of the ensemble of important SLRs, primarily ^{26}Al ($t_{\rm half} = 0.74$ Myr; *Schramm*, 1971; *MacPherson et al.*, 1995;

Umebayashi and Nakano, 2009) and ^{60}Fe ($t_{\rm half}$ = 2.6 Myr[3]; *Rugel et al.*, 2009) corresponds to approximately $t_{\rm half} \sim 1.2$ Myr (Appendix A). This implies that for disks aged 5 Myr, the contribution from SLRs is reduced by nearly 80%, and consequently scattered X-rays and SLRs would contribute to the midplane ionization at a similar magnitude outside of $R > 50$ AU (Fig. 6.2). Inside this radius, the SLR contribution exceeds that of X-rays due to the high attenuation of X-ray photons in the inner disk midplane.

Another complication is that a substantial fraction of the SLR decay products, e.g., beta particles and γ-rays, escape the disk prior to ionizing the gas when surface densities drop below $\Sigma_g \sim 1 - 10$ g cm^{-2} so that not all of the available energy is deposited locally. The present model incorporates the effects of γ-ray, β^+ and β^- loss in the outer disk (described in Chapter 5) for the settled disk slab model. We note that the main chemical model results presented in §6.6.2 assume the SLR ionization rate is constant with time, which is acceptable for disks with $t < 1$ Myr or less. We relax this requirement in §6.8.2 where we consider SLR time evolution within the chemical calculation itself.

6.5.3 Cosmic Ray Ionization

Ionization by cosmic rays at the interstellar rate ($1 - 5 \times 10^{-17}$ s^{-1}) is a commonly assumed ingredient in models of disk chemistry and physics. However, detection limits of H_2D^+ emission suggest that the ionization rate is actually *lower* than expected for the dense ISM, pointing to some variety of additional attenuation. One possible explanation is CR exclusion by natal stellar winds, i.e, an analogue to the modern day "Heliosphere." Within the Heliosphere, the solar wind strongly modulates CRs, especially those below $E_{\rm CR} \sim 100$ MeV. Pre-main-sequence stars such as T Tauri stars are significantly more

[3]We note that in Chapter 5, the value assumed for the ^{60}Fe half-life predates *Rugel et al.* (2009), where the original value of $t_{\rm half} = 1.5$ Myr used in Chapter 4 originates from *Kutschera et al.* (1984). Once the ^{26}Al has been depleted after approximately $t > 5$ Myr, ^{60}Fe is the primary contributor to SLR ionization. However at this epoch, the ionization attributed to scattered stellar X-rays begins to exceed that of the SLR contribution (see Fig 6.2), and correspondingly the change in chemical properties or ionization fractions are not expected to be large for the updated half-life. Nonetheless, we have included an updated Figure 4 from

magnetically active, have high rotation rates, and high mass loss rates, all of which may drive high levels of CR exclusion at all particle energies. Models of the Gyr-old Sun show significant modulation even at late times (*Svensmark*, 2006; *Cohen et al.*, 2012), corresponding to incident CR ionization rates in the range $\zeta_{\rm CR} \sim (3 - 100) \times 10^{-22}$ s^{-1}. In Chapter 4, we present a simple model of a scaled-up Heliosphere, i.e. a "T-Tauriosphere," to estimate the degree to which a T Tauri star could potentially exclude CRs with winds, and how this exclusion is imprinted on the ionization state of the disk. In the instance of relatively mild modern-day solar winds at solar minimum, the ionization rate by CRs at the disk surface is reduced to just $\zeta_{\rm CR} \lesssim 10^{-18}$ s^{-1}. This value is already over an order of magnitude below the typically assumed (dense gas) interstellar rate. At solar maximum, the ionization rate at the disk surface is reduced to $\zeta_{\rm CR} \sim 10^{-19}$ s^{-1} (see Figure 6.2). If young, energetic stellar winds are *even more efficient* at sweeping away CRs, the CR ionization rate will drop below the solar maximum value at which point SLRs now become the primary midplane ionization contributor, where $\zeta_{\rm SLR} \sim (1 - 10) \times 10^{-19}$ s^{-1} for $t < 1$ Myr.

While the "T-Tauriosphere" models explored in Chapter 4 were simple scaled up versions of the modern day solar wind, the spectra reflect the general behavior we expect under more extreme stellar wind conditions such as those explored in *Cohen et al.* (2012), where low energy CRs are excluded most severely, and high energy CRs ($E > 1$ GeV) are only weakly modulated. Here we explore two wind-modulated CR ionization models, including the present-day Sun (Solar System Maximum: SSX) and a scaled-up exclusion model (T Tauri Maximum: TTX) as presented in Chapter 4. These models provide a realistic framework that allows us to quantify how the chemistry is affected by modulated incident CR fluxes. We note that the wind modulation affects the incident spectrum and consequently the ionization rate *at the disk surface*, in addition to attenuation by the disk gas, where the typical attenuating surface density is $\Sigma_g \sim 100$ g cm^{-2} (*Umebayashi and Nakano*, 1981). Additional opacity can arise from magnetic mirroring and magnetic irregularities in the disk, which we discuss

Table 6.2. CR model ionization rates for $N(H_2) \leq 10^{25}$ cm^{-2}.

Model	ID	ζ_{CR}
Moskalenko et al. (2002)	M02	6.8×10^{-16} s^{-1}
Webber (1998)	W98	2×10^{-17} s^{-1}
Solar System Maximum	SSX	1.6×10^{-19} s^{-1}
T Tauri Maximum	TTX	1.1×10^{-22} s^{-1}

further in §6.9 (see also *Dolginov and Stepinski*, 1994; *Padovani and Galli*, 2011; *Fatuzzo and Adams*, 2014).

For the scaled up (TTX) CR model discussed in Chapter 4, the ionization rate due to CR drops below that of X-rays *at all radii*, and the TTX models correspond to a purely X-ray dominated disk for models without SLR ionization. Table 6.2 provides characteristic rates in the disk surface layers for the different CR wind modulation models considered in this work. In addition to the wind modulated SSX and TTX spectra, we examine two "ISM-like" models, M02 (*Moskalenko et al.*, 2002) and W98 (*Webber*, 1998). W98 is the closest model to what is typically assumed in models of disk chemistry, $\zeta_{CR} \sim 2 \times 10^{-17}$ s^{-1}, while the M02 ionization rate is characteristic of CR ionization rates measured from H_3^+ in the diffuse ISM (*Indriolo and McCall*, 2012), which are unattenuated. For disks without a significant amount of surrounding nebulous gas, such as TW Hya, the M02 model may be more representative of the interstellar (completely unmodulated) CR rate.

6.6 The Chemical Network

The chemical nature of a parcel of interstellar gas and ice is highly sensitive to the properties of its environment. These properties include the radiation field intensity, grain size and volume density (regulating freeze-out and desorption), gas/dust temperatures and densities. In cold gas ($T < 100$ K), the gas-phase chemistry is particularly sensitive to the gas

Chapter 5 and new fits to the midplane ionization rate in Appendix A of this manuscript.

ionization fraction, as ion-neutral reactions are the most important (i.e., quickest) gas phase reactions that take place (*Herbst and Klemperer*, 1973). The geometry of disks, ranging between lower density, warm ionized surfaces to predominantly neutral, cold midplanes provides a diversity of physical conditions, which are directly translated into a rich chemical environment. Conversely, observations of the chemical composition of disks provide clues into the underlying physical environment and therefore are a powerful observational tool to help understand the important physics governing these systems. In the following section we examine how the chemical properties of disks, particularly the molecular ions, react to different assumptions regarding ionization processes, and how they may be used as diagnostic tools.

6.6.1 Chemical Model

The physical model and stellar UV and X-ray radiation fields provide the backbone on which we solve for the time-dependent chemical abundances with the *Fogel et al.* (2011) disk chemistry code. This chemical reaction network is based upon the OSU gas-phase network (*Smith et al.*, 2004), where *Fogel et al.* (2011) substantially expanded the network to include important processes such as thermal and non-thermal sublimation, photodissociation, freeze-out onto grains, CO and H_2 (and isotopologues) self-shielding, and stellar and non-stellar ionization of H_2 and helium. The code is calculated as 1+1D, where different disk radii are treated independently and self-shielding is considered in the vertical direction. The code is run in parallel with the publicly available GNU Parallel software (*Tange*, 2011). We note that in the calculation of the temperature structure and UV transfer, we consider the spatial dependence of the grain size populations in detail. The grain-surface chemistry, however, is fixed to a single "typical" grain-size of $r_g = 0.1\mu$m, where the underlying assumption is that the small grains dominate the surface area and are most important for the chemistry. Because the gas and small grains are uniformly distributed, this approximation is justified in the present work; however, we would nonetheless be "missing" surface area in the midplane

where the 1mm grains are concentrated. We note, though, that this correction should be small considering that small grains are present throughout the disk at all scale-heights. We furthermore note that the physical size of r_g is not the important quantity, but rather this number translates into an effective grain surface area per unit volume in the chemical code (e.g., 7.5×10^{-3} μm^2 cm^{-3} at $n_{\rm H_2} = 10^{10}$ cm^{-3}). Nonetheless, future work should explore more than two size populations, including their vertical distribution in the disk (for example, in the formalism of *Dullemond and Dominik*, 2004) and how these will affect the grain-chemistry.

In order to make predictions for deuterated molecular ions, we have added to the *Fogel et al.* (2011) network a simple deuterium chemistry to predict the abundances of H_2D^+ and N_2D^+, which become enriched relative to the main isotopologue due to a chemical favorability towards the heavier isotopologue at low ($T < 50$ K) temperatures (*Millar et al.*, 1989). Even though DCO^+ is part of the network through the H_2D^++ CO formation pathway, we do not make predictions for the DCO^+ abundances in the present work; the chemistry of DCO^+ depends sensitively on the deuterated carbon chemistry, for which we have not included a complete network. Instead, the network is designed to reliably predict the relatively simpler H_2D^+ and closely related N_2D^+ chemistry. An important facet of the H_2D^+ chemistry is that the reaction rates depend strongly on the ortho-to-para ratio of the reactants, H_2 and H_3^+, and their isotopologues (*Pagani et al.*, 2009; *Hugo et al.*, 2009; *Chapillon et al.*, 2011). We approximate this behavior by assuming that the ortho-to-para ratio is locally *thermal* for H_2D^+ and include the ortho-to-para fraction as weights on the net reaction rate. In the following prescription we designate f_o^1 (f_p^1) as the fraction of H_2 in the ortho (para) state, and f_o^2 (f_p^2) as the fraction of H_2D^+ in the ortho (para) state. The weighted reaction rate coefficients for (o)rtho and (p)ara H_2 and H_2D^+ is:

$$\begin{aligned} R(T) =& R^{\rm oo}(T) f_{\rm o}^1(T) f_{\rm o}^2(T) + \\ & R^{\rm op}(T) f_{\rm o}^1(T) f_{\rm p}^2(T) + ..., \end{aligned} \tag{6.1}$$

where $f_o^1 + f_p^1 = 1$, $f_o^2 + f_p^2 = 1$, and $R^{oo}(T)$ is the reaction rate coefficient for reactions between o-H_2 and o-H_2D^+, for example. The o/p ratio of H_2 is given by

$$\begin{aligned} \mathrm{o/p}_{\mathrm{H_2}}(T_{\mathrm{gas}}) =& 5.3534 \times 10^{-3} + \\ & \frac{(3.0346 - 5.3534 \times 10^{-3})}{[1 + (96.5330/T_{\mathrm{gas}})^{3.5096}]}, \end{aligned} \tag{6.2}$$

for gas at temperatures above $T_g \geq 80$ K and for temperatures below that value,

$$\mathrm{o/p}_{\mathrm{H_2}}(T_{\mathrm{gas}}) = 9 \exp{(-170.5/T_{\mathrm{gas}})}. \tag{6.3}$$

Flower et al. (2006) finds that at very low temperatures ($T_g \lesssim 10$ K) the ortho-to-para ratio of H_2 exceeds the Boltzmann value, and to approximate this behavior we set a floor to the o/p ratio of H_2 at 10^{-3} that limits Eq. (6.3) from dropping below this value. The o/p ratio of H_2D^+ is given by

$$\begin{aligned} \mathrm{o/p}_{\mathrm{H_2D^+}}(T_{\mathrm{gas}}) =& -1.6977 \times 10^{-2} + \\ & \frac{(3.0375 + 1.6977 \times 10^{-2})}{[1 + (47.9640/T_{\mathrm{gas}})^{3.0692}]}, \end{aligned} \tag{6.4}$$

where both o/p formalisms in Eqs. (6.2) and (6.4) are from *Lee and Bergin* (2014), submitted.

In the chemical network, the deuterium extension to the reaction set – for the most part – mirrors the main isotopologues, and we assume statistical branching ratios where necessary. While the ionization of H_2 and helium are the first step towards the molecular ion chemistry, we do allow for HD and D_2 to be directly ionized by X-rays, CRs and SLRs, assuming the same cross sections as for H_2. The self-shielding functions for HD and D_2 are from *Wolcott-Green and Haiman* (2011). For the reactions where rates are known for the deuterated isotopologue, we incorporate values from the literature for H_2D^+ electron recombination and reactions with atomic H (*Roberts et al.*, 2004), H^+ and D^+ reactions with atomic/molecular hydrogen/deuterium, DCO^+, N_2D^+ reactions with H (*Roberts and*

Millar, 2000), and neutral-neutral warm water-formation deuterium reactions including their significant barriers (*Bergin et al.*, 1999). While we include the spin information for the H_2 + H_2D^+ reaction rates, the endothermicity of the back reactions for the overall less abundant heavier isotopologues, HD_2^+ and D_3^+ are taken to be a single value in the network, 187 K and 341 K, respectively (*Roberts et al.*, 2004). In addition to the standard set of gas-phase reactions in the original network, we include a simple grain-surface chemistry allowing for H_2/HD/D_2, H_2O/HDO, and H_2CO/HDCO formation on grain surfaces through hydrogenation (*Hasegawa et al.*, 1992a) and CO_2 formation through reactions of CO with OH and O with barriers (*Garrod and Pauly*, 2011). In total, the full network spans over $\sim$ 6200 reactions and $\sim$ 600 species.

The initial chemical abundances are listed in Table 6.3 and are for the most part adopted from *Fogel et al.* (2011) based upon the dark cloud model of *Aikawa and Herbst* (1999b). The abundances of CS and SO have been adjusted to the observationally derived abundances of the TMC-1 dark cloud from *Bachiller et al.* (1990) originally compiled in *Guelin* (1988) and *Rydbeck et al.* (1980). Together, CS and SO constitute the main sulfur reservoir with an abundance relative to hydrogen number totaling $\sim 10^{-8}$. The atomic (ionized) sulfur, S^+, is reduced to a low value, where we assume 10^{-11}. The motivation behind the total reduced sulfur abundance, $\sim 10^{-8}$ rather than the diffuse ISM value of $\sim 10^{-6}$, comes from the observation that the volatile sulfur abundance in dense clouds is far lower than that of the diffuse ISM (*Joseph et al.*, 1986; *Tieftrunk et al.*, 1994). These findings were confirmed by observations of molecular sulfur-bearing species including CS and SO (e.g., *Langer et al.*, 1996; *Wakelam et al.*, 2004) where the molecular abundances measured in dense clouds are far less than those predicted by chemical calculations for a diffuse ISM sulfur abundance (*Hatchell et al.*, 1998; *Wakelam et al.*, 2004). In particular, *Wakelam et al.* (2011) find that based upon chemical modeling of dense (high mass) cores, the volatile sulfur abundance is found to be even further substantially reduced, where the observations account for an abundance of sulfur totaling $2 \times 10^{-9} - 5 \times 10^{-8}$ relative to hydrogen across four

sources. The interpretation is that the sulfur has been converted into a more refractory form, i.e., a "sulfur-rich residuum" (*Wakelam et al.*, 2004), and is not chemically available to produce volatile sulfur-bearing molecules. Evidence of high levels of atomic sulfur in shocked gas near Class 0 protostars further supports this scenario, where in one explanation the observed sulfur atoms are sputtered from the sulfur-rich residuum (*Anderson et al.*, 2013). Likewise, the ionized metal abundances of Si^+, Mg^+, and Fe^+ have been reduced to low levels (10^{-11}) based upon the chemical modeling results of *Maret and Bergin* (2007) for the B68 pre-stellar core. The HD abundance is based upon the protosolar bulk value, where D/H in HD is $2.0 \pm 0.35 \times 10^{-5}$ (*Geiss and Gloeckler*, 2003). The H_2D^+, HD_2^+, and D_3^+ abundances are estimated from *Walmsley et al.* (2004) for the small (0.025 μm) grain case at high ($n_{H_2} = 10^7$ cm^{-3}) density. Regarding the nitrogen abundances, we note that in these models, the initial abundance of nitrogen is primary atomic. Had we begun with a larger fraction molecular nitrogen, the overall N_2H^+ abundance would increase but the shape of the column density profile remains largely unchanged (*Schwarz and Bergin*, 2014, and Chapter 7 of this thesis). Starting off with a larger fraction of ammonia, for example, tends to reduce the overall N_2H^+ abundance across the bulk disk (outside of the ammonia snowline) by removing nitrogen from the gas-phase. Consequently, the shape of the column density profile of N_2H^+ is still sensitive to the CR ionization rate even without additional information on the disk nitrogen abundances.

6.6.2 Chemical Abundance Results

In this model framework, we compute the time-dependent chemistry as a function of radial and vertical position within the disk. The molecular abundances for a select set of ALMA observable molecular ions and of CO after $t = 1$ Myr of chemical evolution are shown in Figure 6.3. The column headings indicate the underlying CR ionization model as described in §6.5.3 (see also Table 6.2) with the X-ray luminosity fixed ($L_{XR} = 10^{29.5}$ erg s^{-1}). In addition to the abundances as a function of spatial position, we provide the vertically

Table 6.3. Initial chemical abundances, χ.

Species	$\log(\chi)$	Species	$\log(\chi)$
H_2	5.00×10^{-1}	H_2O(gr)	2.50×10^{-4}
He	1.40×10^{-1}	N	2.25×10^{-5}
CN	6.00×10^{-8}	H_3^+	1.00×10^{-8}
CS	4.00×10^{-9}	SO	5.00×10^{-9}
Si^+	1.00×10^{-11}	S^+	1.00×10^{-11}
Mg^+	1.00×10^{-11}	Fe^+	1.00×10^{-11}
C^+	1.00×10^{-9}	CO	1.00×10^{-4}
N_2	1.00×10^{-6}	C	7.00×10^{-7}
NH_3	8.00×10^{-8}	HCN	2.00×10^{-8}
HCO^+	9.00×10^{-9}	H_2CO	8.00×10^{-9}
HD	2.00×10^{-5}	H_2D^+	1.30×10^{-10}
$HD_2{}^+$	1.00×10^{-10}	$D_3{}^+$	2.00×10^{-10}
C_2H	8.00×10^{-9}		

integrated column density, shown in Figure 6.4.

In general, for decreasing CR ionization, the midplane ion abundances drop precipitously while the X-ray dominated surface layers are unchanged across CR models. For example, the important dense ionization tracers, H_2D^+ and N_2D^+, are highly abundant ($\chi \sim 10^{-11}$ relative to H_2) in the midplane for CR ionization rates exceeding $\zeta_{\rm CR} \gtrsim 10^{-17}$ s^{-1}, but drop in abundance by more than three orders of magnitude for SSX modulated rates and below.

It is important to point out that the TTX model provides a unique chemical picture of a *purely X-ray dominated* disk. In the instance of a modulated CR rate and either (i) a lack of abundant SLRs or (ii) an old (> 5 Myr) disk in which the initial reservoir of SLRs has decayed away ($< 3\%$ remaining), the scattered intermediate energy ($5-7$ keV) X-ray photons set the absolute floor to the ionization rate, with magnitude $\zeta_{\rm XR} \sim (1 - 10) \times 10^{-21}$ s^{-1} for a stellar X-ray luminosity of $L_{\rm XR} = 10^{29.5}$ erg s^{-1}. In the TTX model, the midplane abundances of molecular ions are at their minimum (see especially H_2D^+, HD_2^+, and N_2D^+in Figure 6.4). Correspondingly, H_2D^+ and HD_2^+ have column densities typically *three orders of magnitude less* than if CRs are present at ISM levels and will unfortunately be difficult to detect observationally.

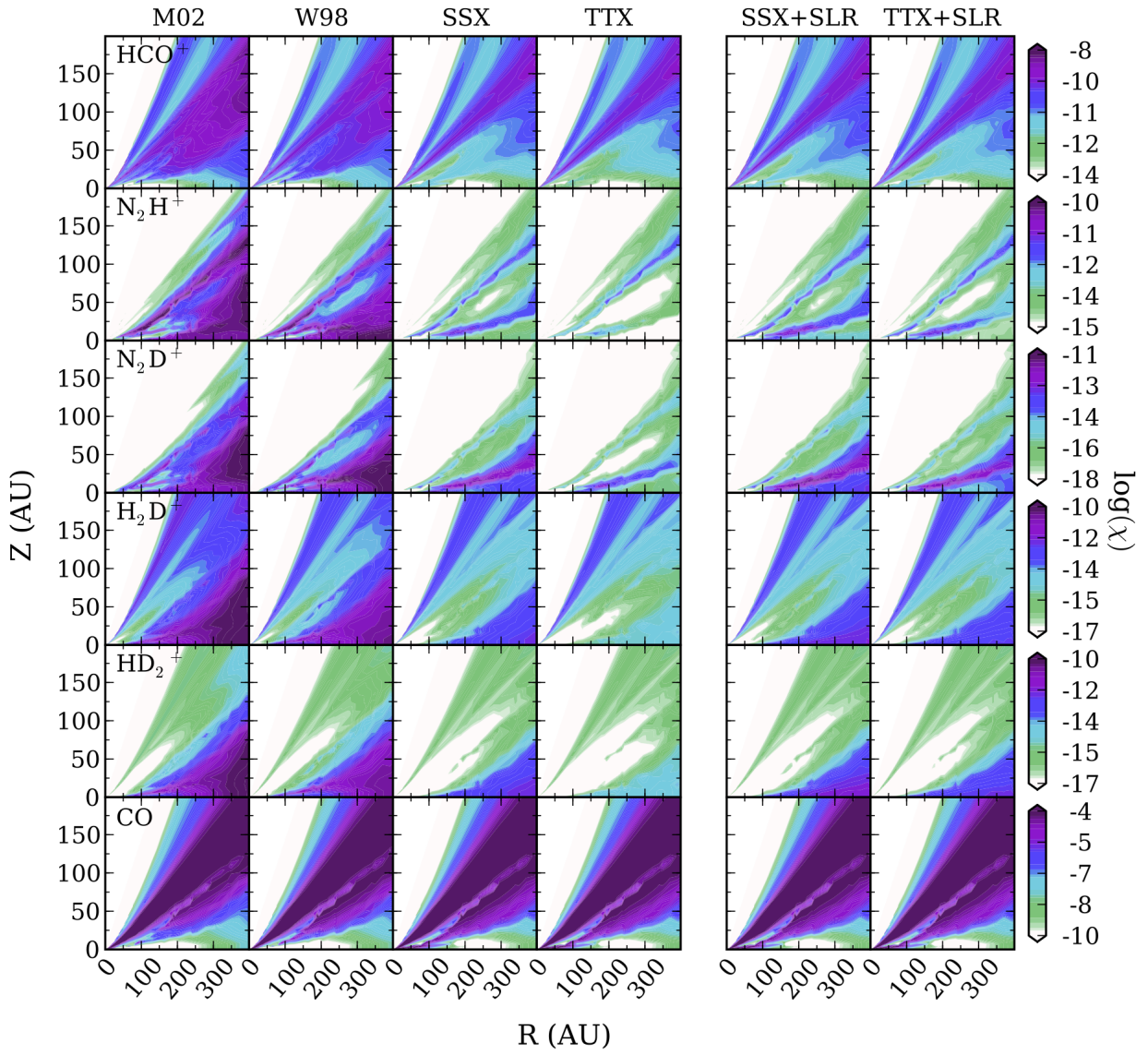

Figure 6.3 Disk chemical abundances relative to H_2 as a function of radius and height, where $R, Z = (0,0)$ AU is the location of the central star. Abundances are shown at time $t = 1$ Myr of chemical evolution. Columns correspond to different CR/SLR ionization models for a fixed X-ray luminosity, and rows are different molecular abundances as labeled on the leftmost column. Specific CR and/or SLR ionization model is indicated at the top of each column. The two rightmost columns include contribution from the decay of short-lived radionuclides adding at most $\zeta_{\rm SLR} \sim 10^{18}$ s^{-1} to the total H_2 ionization (see Figure 6.2). Their inclusion provides a floor for the molecular ion abundance (see especially N_2H^+).

In the rightmost two columns of Figure 6.3, we include (static) contribution from SLR ionization, which provides an ionization rate floor of magnitude $\zeta_{\rm SLR} \sim (1 - 10) \times 10^{-19}$ s^{-1}

for fixed initial solar nebula-like SLR abundances (*Finocchi and Gail*, 1997) of ^{26}Al, ^{36}Cl, and ^{60}Fe. The vertical and radial profile of the SLR ionization rate is taken from the settled disk model presented in Chapter 5 (hybrid dust slab, see Chapter 5 Figure 2 as well as Figure 6.2 in the present chapter). For the case of SSX+SLR, the two sources contribute similarly to the total H_2 and helium ionization, so chemically there is little change with the inclusion of SLRs, especially in the inner disk. The TTX+SLR model, however, increases the total ionization such that the molecular ion abundances resemble the SSX runs inside of $R \sim 200$ AU. Consequently, distinguishing between a SLR and CR driven chemistry will be challenging. Outside of $R \sim 200$ AU, however, the SLR losses become important and the TTX+SLR model drops off more steeply than the SSX model, such as can be seen in H_2D^+.

Focusing now on the individual ions, the column density of HCO^+ changes by an order of magnitude between the high ($\zeta_{CR} \gtrsim 10^{-17}$ s^{-1}) and low CR models. The low CR models pile up at a constant HCO^+ column, which physically corresponds to the minimum amount of HCO^+ provided by X-ray ionization in this model. In the absence of interstellar CR, *the bulk of the HCO$^+$ column is therefore sensitive to only the stellar X-ray ionizing radiation* (see §6.8.1). A second layer of HCO^+ forms at $z/r \sim 0.2$, above the vertical CO freeze-out region, when CRs are present (models W98 and M02). This layer all but disappears for the SSX and TTX models, pointing to the potential utility of disk vertical structure observations in understanding the underlying ionization environment. It is important to note that even though we do not vary the stellar UV field in this work, for very high UV fields the CO that would otherwise form HCO^+ can be photo-dissociated and photo-ionized, thus forming C^+ in abundance. Thus the HCO^+ will be indirectly UV sensitive, particularly for UV luminous Herbig Ae/Be stars (*Jonkheid et al.*, 2007), which can be orders of magnitude brighter than T Tauri stars, or in the case of extremely externally irradiated disks. Nonetheless, the general trends over different ionization models should still hold, albeit with a lower overall HCO^+ column. Moreover, while the HCO^+ column can provide constraints on the ionization rates exceeding $\zeta_{CR} \gtrsim 10^{-17}$ s^{-1}, the HCO^+ is not very sensitive to lower CR rates due to

its precursor, CO, freezing out in the CR dominated region. Moreover, the HCO^+ column densities for the W98 and M02 models have a second peak in column density at $R \sim 200$ AU not seen for the low CR models. The second peak is actually a consequence of a deficit of CO at $R \sim 50$ AU, seen in the same plot. Because HCO^+ forms directly from CO, it is sensitive to the CO chemistry, both freeze-out and CO chemical processing as is the case for the W98 and M02 models.

The N_2H^+ column shows a three order of magnitude spread between a high CR rate (M02) and an X-ray only disk (TTX), with one order of magnitude variation between the different low CR models (SSX and TTX) and is a potential candidate as a midplane ionization tracer. One caveat in using N_2H^+ is that a tenuous ($\chi \sim 10^{-11}$) surface layer of N_2H^+ is sustained from the high X-ray photon flux (see Figure 6.3) even in the presence of CO, which is the major reactant of N_2H^+. For more X-ray luminous stars, the surface N_2H^+ may contribute more to total column and mask the midplane abundances. Alternatively, the contribution from the surface N_2H^+ can be reduced if the N_2 binding energy is higher than 855 K, i.e., the N_2 value when CO and N_2 ice are well-mixed where the CO binding energy is the same, 855 K (*Öberg et al.*, 2005). Such is the case for an N_2 ice layered on an H_2O ice substrate (*Collings et al.*, 2004), but this surface N_2H^+ is never completely absent in any of our models.

The deuterated molecular ions considered here, H_2D^+, N_2D^+ and HD_2^+, show a promising sensitivity to the low ionization models, spanning many orders of magnitude in their column densities. Observations of these species will be essential for measuring midplane ionization, especially in the absence of CRs. This result is a natural consequence of the pathways towards deuterated isotopologues being favored at low temperatures, resulting in their overabundance relative to the main isotopologue in cold ($T < 50$ K) gas. Naturally, the same gas is also the least affected by X-ray ionization, and therefore these species allow us to peer through the X-ray dominated upper layers directly to the midplane.

In addition to the ions, we plot the CO abundance and column density (Figures 6.3 and 6.4). CO is a commonly used tracer of gas mass assuming an ISM conversion factor of CO

to hydrogen mass of 10^{-4} and is frequently used to determine chemical abundances per H_2 from an observed column of optically thin gas. There is evidence, however, that the CO abundance may be lower, and hence gas masses from CO may be underestimated (*Favre et al.*, 2013). A possible reason for the low observed abundance is that CO is chemically eroded over time by reactions with He^+. The majority of the carbon returns back to CO eventually, but some non-zero fraction of the carbon is recycled into other carbon-bearing molecules, reducing the CO abundance over time (*Bergin et al.*, 2014; *Furuya and Aikawa*, 2014). For the highly ionized CR models W98 and M02, the abundance of CO is visibly reduced near the inner disk midplane at around $R \sim 100$ AU due to an increased abundance of He^+ and consequently a speed-up of the CO erosion process. The column density plot (Figure 6.4) also reflects this behavior in the M02 and W98 models and is an example of how ions can have a long-lasting effect even on abundant neutral species. We emphasize that the layered structure of CO induced by the ionization-chemistry in the abundance plot (Fig. 6.3) may be smeared out in the presence of turbulent motions of the gas (*Semenov and Wiebe*, 2011; *Furuya and Aikawa*, 2014), which is beyond the scope of the current Chapter but should be explored in future work.

6.7 Line Emission Modeling

The chemical models demonstrate a sensitive link between abundances (and column densities) and ionization properties of the disk. For example, the HCO^+ and N_2H^+ column densities typically are sensitive to stellar X-rays, though not exclusively for high interstellar CR ionization rates. The deuterated ions trace deeper gas, and probe ionization properties near the midplane, tracing ionization due to CRs and SLRs. In this section we show how these effects are imprinted on the molecular emission and how excitation effects and opacity can "mask" the molecular column densities that allow us to discriminate between models. From these emission models, we simulate realistic ALMA observations to determine the utility of emission line tracers as probes of individual ionizing agents.

6.7.1 Line Radiative Transfer

For our molecular ion abundance results (§6.6.1), we have simulated observations of the ground-accessible submillimeter transitions of each species considered here. The strength of the line emission depends on both the total column of material as well as the temperature of the emissive gas within the column. To simplify the problem, we have simulated the emergent line intensity assuming the disk is observed face-on at a distance of $D = 100$ pc. The line radiation transfer is carried out with LIME (*Brinch and Hogerheijde*, 2010) where we create simulated "perfect" images of the line emission in 100 m s^{-1} channels in pixels of size 0.02″ (2 AU), which is much smaller than our desired resolution in the ALMA simulations. For gas motions, we assume the gas is in Keplerian rotation about the star, and we include a turbulent doppler B-parameter of $v_{\rm dop} = 100$ m s^{-1}, as observations indicate that the turbulent broadening in disks is small (*Hughes et al.*, 2011).

For the HCO^+ and N_2H^+ emission models, we calculate the level populations in non-LTE with the collision rates of *Flower* (1999) as compiled in the Leiden LAMDA database (*Schöier et al.*, 2005). For the latter we do not separate out the hyperfine structure lines, and hence refer to the transitions by their rotational-J states. Given that the collisional rates for N_2D^+ are unknown, we treat the N_2D^+ level populations as in local thermodynamic equilibrium (LTE), which is a satisfactory approximation as the critical density of the $(3-2)$ and $(4-3)$ transitions are $n_{\rm crit} \sim 2 \times 10^5$ cm^{-3} and $\sim 8 \times 10^5$ cm^{-3}, respectively, as estimated from the *Flower* (1999) collision rates for HCO^+ and line parameters (Einstein A-coefficients, frequencies, statistical weights) from the JPL Database[4] (*Pickett et al.*, 1998), originally measured in *Anderson et al.* (1977); *Sastry et al.* (1981). We note that *Hugo et al.* (2009) provide inelastic collisional rates for the excitation of H_2D^+; however, to simplify the calculations we assume the H_2D^+ level populations are also in LTE. This assumption is appropriate as the H_2D^+ emission originates from dense gas exceeding $n_{H_2} > 10^8$ cm^{-3},

[4]http://spec.jpl.nasa.gov/

much larger than the critical density for o-H_2D^+ ($1_{10} - 1_{11}$), $n_{\rm crit} \sim 10^5$ cm^{-3} (*Hugo et al.*, 2009).

For the carbon and oxygen isotopes, we adopt $^{16}O/^{18}O = 500$ (*Kahane et al.*, 1992; *Prantzos et al.*, 1996) and $^{12}C/^{13}C = 60$ (*Keene et al.*, 1998). The deuterium isotopologues of the molecular ions are calculated within the code where the main gas reservoir (molecular hydrogen) has initially $D/H = 2 \times 10^{-5}$ (see §6.6.1). Leiden LAMDA formatted H_2D^+ and N_2D^+ input files were compiled from the CDMS database[5] (*Müller et al.*, 2001, 2005) and from the JPL database, where the primary literature regarding the line parameters can be found in *Saito et al.* (1985); *Amano and Hirao* (2005); *Yonezu et al.* (2009) for H_2D^+. All simulations are carried out using the same dust distribution and opacities from the physical structure model, where the continuum is subsequently subtracted from the resulting line emission profiles.

6.7.1.1 Line Opacity

The LIME code is capable of providing physical line intensities, e.g., Jansky/pixel and Kelvin, as well as the line optical depth, τ_ν. In Figure 6.5, we show the line-center, vertical optical depth τ_0 through the disk of the simulated transitions (direct from the emission model, i.e., no beam convolution) as a function of cylindrical disk radius. The HCO^+ isotopologues are for the most part thin ($\tau_0 < 1$), while N_2H^+ ($4-3$) and ($3-2$) reach $\tau_0 \sim 5$ just beyond the CO snowline for the W98 and M02 CR models. Observations of $H^{13}CO^+$ (3-2) and HCO^+ (3-2) are reported in *Öberg et al.* (2011d) towards DM Tau. The disk integrated flux ratio of the (3-2) transition for the $^{12}C/^{13}C$ isotopologues is ~ 7.6, and assuming a respective isotope ratio of 60 (*Keene et al.*, 1998), corresponds to an $H^{13}CO^+$ (3-2) optical depth of $\tau = 0.14$. Though this value is optically thin, it is nonetheless higher than the values from our models. Potential explanations include a potentially higher X-ray luminosity from the

[5]http://www.astro.uni-koeln.de/cdms/catalog

star, which is unknown, or that the 19 AU inner cavity (*Calvet et al.*, 2005; *Andrews et al.*, 2011) may permit the X-rays to more directly ionize the outer disk gas. The N_2D^+ and H_2D^+ lines are thin throughout the disk for all models. $C^{18}O$ is thick, with $\tau_0 \gtrsim 1$ at all radii, though the CO opacity drops slightly near the star where high CR+X-ray ionization chemically destroys CO with He^+ more quickly than it is replenished. We emphasize that the molecular ion opacities may be higher for higher ionization rates or if the column of gas is larger for a more massive disk, and vice versa for lower mass models (see discussion in §6.8.3).

The HCO^+ isotopologues show a peak in their opacity offset from the radial center of the disk, where the column is highest (see Fig. 6.4). The relative height between the central peak and the outer broad $100-300$ AU peak is due to a combination of column density and excitation. The ring-like feature is exaggerated for low rotational J lines such as the $(3-2)$ transition where depopulation becomes important towards hotter inner disk gas, whereas $H^{13}CO^+$ $(5-4)$ appears more centrally peaked.

The N_2H^+ lines have two main emission features, where the inner ring is caused by a contribution of stellar X-rays and CR ionization in tandem with the CO condensation front, while the outer tail at $R \sim 300$ AU is fueled by primarily CR ionization. The H_2D^+ optical depth also peaks in this same outer region in the models where CR ionization is active. The N_2D^+ has a somewhat complicated τ_0 profile, which is reflected in the N_2D^+ column densities (Fig 6.4). The high CR ionization models sustain N_2D^+ co-spatial with N_2H^+ and, when combined with warm temperatures close to the upper-state excitation temperatures ($E_u = 22.2$ K and 37.0 K for $J = 3$ and $J = 4$ rotational levels, respectively), leads to N_2D^+ emission inside of $R < 100$ AU.

6.7.2 Simulated ALMA Observations

From the LIME emission models described in §6.7.1, we simulate full-science ALMA observations for the ground-based accessible transitions of $HC^{18}O^+$, $H^{13}CO^+$, N_2H^+, N_2D^+,

Table 6.4. CASA Simulation Parameters.

Emission Line	12-m Configuration[6] (12-m + 7-m Beam)	Sensitivity[7] (mJy)
$HC^{18}O^+$ $(3-2)$	03 (1.28″)	1.0
$HC^{18}O^+$ $(4-3)$	03 (0.96″)	1.4
$H^{13}CO^+$ $(3-2)$	10 (0.33″)	0.97
$H^{13}CO^+$ $(4-3)$	10 (0.25″)	1.4
$H^{13}CO^+$ $(5-4)$	10 (0.20″)	3.6
N_2H^+ $(3-2)$	10 (0.31″)	1.3
N_2H^+ $(4-3)$	10 (0.24″)	2.6
N_2D^+ $(3-2)$	01 (1.55″)	1.3
N_2D^+ $(4-3)$	01 (1.16″)	1.3
o-$H_2D^+$$(1_{10}-1_{11})$	01 (0.96″)	2.5

[a]http://casaguides.nrao.edu/index.php?title=Antenna_List Beam averaged over major and minor axes from the combined 12-m and ACA observations.

[b]$6.1h$ in 0.2 km/s bins from the ALMA Sensitivity Calculator.

and H_2D^+. The full set of emission lines considered at present are listed in Table 6.4. We note there are additional lines that are accessible by ALMA that we chose not to include, such as N_2D^+ (5-4) and HD_2^+ $(1_{10}-1_{01})$, because these lines were unobservable for all emission models considered. The full-science array is comprised of fifty 12-m antennas, twelve 7-m antennas, and four 12-m antennas, i.e., the total power (TP) array, where the 7-m and TP arrays are referred to as the Atacama Compact Array (ACA). For each of the line models we assume the same set of simulated observing parameters, and note that in some instances there are more efficient (i.e., less ALMA time) means to achieve the same goals. The specific settings for actual observations should be tailored to the specific target and specific line being studied.

6.7.2.1 Observational Parameters

The simulations presented here reflect $6h$ of total on-sky time with one of the 12-m array configurations and an ACA 7-m observation. While the choice of $6h$ is somewhat arbitrary,

it represents a relatively "deep" observation, and ideally one would target more than one emission line towards a given source in the same proposal. Thus this length of time may be somewhat optimistic, but is designed to detect the lines with high signal-to-noise. Some of the lines are undetectable for low ionization models as is the case for H_2D^+, and thus deeper observations would be needed to detect the line if that specific model reflects the true properties of the disk. In that case, going to a different tracer such as N_2D^+ may be a better choice than a deeper observation of a weak line. Furthermore, these results can be approximately scaled for sources at different distances and the estimated signal-to-noise can be adjusted for different observation times.

Regarding antenna configurations, for stronger emission lines, such as $H^{13}CO^+$, and N_2H^+, we choose somewhat more extended 12-m configurations (see Table 6.4), while for weaker lines, we simulate the most extended configuration that still provides high signal-to-noise if possible, which in some instances is the most compact, least-resolved full-operations configuration, denoted 01. We include ACA 7-m observations because the maximum scale of the $R = 400$ AU disk at $d = 100$ pc on the sky is $8''$, and for the higher frequency ($\nu > 300$ GHz) lines considered here, the 7-m array recovers the flux at all scales without the need for the TP array. At lower frequencies, a second 12-m configuration can be used instead to recover all of the flux in significantly less time than for the 7-m observations, which is clearly the better – and default – option for on-sky ALMA observations. Additionally, the long duration of the simulated observations fills out the UV coverage and, due to sky-projection effects, can decrease the minimum baseline, allowing for slightly larger maximum recoverable scales.

In summary, the simulations presented here are designed to show the sensitivity of the emission line observations to chemical signatures of ionization processes in disks. These results provide a primer to aid in quantifying the contribution of different physical processes to disk ionization, a crucial ingredient in models of disk chemistry. We note that the specific choice of observing parameters will depend upon properties of the source, the ALMA cycle,

which determines the available antenna configurations, and the lines targeted. Figure 6.6 illustrates the full process beginning with LIME emission models to creating ALMA on-sky simulations for two example emission lines. Rather than showing images or channel maps for every emission line/model considered both in model emission (§6.7.1) and CASA simulations, we instead present our results as circularly averaged visibility amplitudes and circularly averaged integrated line intensity cuts in sky coordinates, which facilitates easy comparison between observations of different ionization models for a given emission line.

6.7.2.2 ALMA Sensitivity Calculation

To calculate the uncertainty on the ALMA measurements, we use the uncertainties from the ALMA sensitivity calculator[8], which set the width of the shaded regions in the image plots (rightmost column of Figures 6.7 and 6.8). We do not simulate thermal noise within the CASA simulations themselves to save computational time. To estimate the error on individual baselines at each time sampling (defined by integration time, which was $t_{\rm int}$ = 1000s for the simulations), we scale the sensitivity calculator's uncertainty σ_0 by $\sigma_i = \sigma_0\sqrt{N_A(N_A-1)}\sqrt{N_{\rm time}}\sqrt{N_{\rm pol}}$, where N_A is the number of antennas (50 for the 12-m array and 12 for the 7-m array), $N_{\rm time}$ is the number of time samplings during the course of the simulated observation's integration time (e.g., $t_{\rm obs} = 22000s = 6.1h$ on the 12-m array such that $N_{\rm time}$=22) and $N_{\rm pol}$ = 2 is the number of polarizations, where the emission is unpolarized. We note that if we had chosen a smaller (larger) sampling time within a factor of a few, we would have correspondingly more (less) points to bin over, and the final error on the binned measurement is not very sensitive to the choice of sampling time. From the full measurement set, we bin the velocity-integrated visibility amplitudes by projected UV distance. The uncertainty on the binned value (the mean) is taken to be the error on the individual measurements divided by the number of points within the UV distance bin,

[8]https://almascience.nrao.edu/proposing/sensitivity-calculator

$\sigma_A = \sigma_i/\sqrt{N_{\rm bin}}$, where $N_{\rm bin}$ is typically $\gtrsim 100$.

6.7.2.3 Emission Model Results

We present the primary results of the ALMA simulated observations in Figures 6.7 and 6.8. The CR ionization models described in §6.5.3 are indicated by line color, where purple represents the highest, diffuse ISM CR rate, while the blue curve is representative of an X-ray dominated chemistry. The identifier of the full-operations array used to simulate each set of data is indicated in parenthesis next to the name of the species (see Table 6.4 for equivalent angular resolution). The left and right columns are different representations of the same simulated data. The left column shows the visibility amplitudes integrated over the line (Jy km s^{-1}) where the quantity "integrated amplitude" corresponds to the fact that we have integrated over the channels that contain line flux rather than averaging, which is often done for continuum amplitudes. The visibility amplitude plots are labeled with a dashed green vertical line indicating the maximum recoverable scale for the 12-m array observations alone. The dashed red vertical line indicates the minimum scale sampled by the 7-m array. We note that the minimum baseline indicated by the green line may be less than what would be predicted for the same array based upon the physical baselines due to sky-projection effects mentioned previously. The right column shows the brightness profile of the reconstructed (cleaned) images on the sky, where θ is relative to the position of the central star and $1'' = 100$ AU. To create the profiles, we average ten radial slices across the face of the disk. The noise reflects the sensitivity on a single cut, but in practice averaging over slices can further reduce the noise on the profile.

The HCO^+ isotopologues' line emission (Figure 6.7) is sensitive to both the stellar X-rays and the high CR ionization models (M02 and W98 in purple and yellow respectively). This behavior is reflected in the column densities (Figure 6.4) and in the simulated observations, both in the visibilities and reconstructed images. The line intensity is indistinguishable for lower CR rates for models TTX and SSX, green and blue, where stellar X-rays – and not

CRs – set the minimum HCO^+ abundance in this particular model. The high M02 CR rates form a clear emission ring (i.e. the HCO^+ emission peaks offset from the star) for the $(3-2)$ transition, less prominently seen in the $(4-3)$. The reason that the $(3-2)$ emission is brightest away from the column density peak is due to excitation of the line, which has an upper state energy of $E_u \sim 25$ K. The abundant HCO^+ gas inside of $R \lesssim 50$ AU has temperatures typically exceeding 100 K. At this point, higher J-states of $H^{13}CO^+$ and $HC^{18}O^+$ become more populated, thereby de-populating the J = 3 levels and decreasing the column of emissive gas, behavior reflected in the line optical depths (Figure 6.5) and emission plots (Figure 6.7). For higher rotational transitions of $H^{13}CO^+$, $(4-3)$ and $(5-4)$, there is an inner ($\theta < 0.5''$) peak in the simulated observations (Figure 6.7) due to a confluence of high X-ray rates and abundant gas-phase CO. This feature is also present in the underlying $HC^{18}O^+$ abundances, but the lower spatial resolution simulations adopted for $HC^{18}O^+$ (see Table 6.4) do not resolve the inner 50 AU. In summary, the HCO^+ emission sensitively traces i) stellar X-ray processes and ii) high CR fluxes, but is limited in its capacity as a midplane tracer due to CO freeze-out in the outer disk. Furthermore, the low-J HCO^+ behavior highlights a situation in which observations of emission rings are *excitation effects,* rather than chemical or physical structure, such as a planet or a snowline.

N_2H^+ is expected to arise from cold gas where its destroyer, CO, is frozen out at temperatures below $T < 20$ K (*Aikawa et al.*, 2001; *Bergin et al.*, 2002; *Jørgensen et al.*, 2004). Nevertheless, in the strongly irradiated X-ray layers we find that some N_2H^+ is sustained even in the presence of CO. Consequently, its strength as a diagnostic tool of midplane ionization is somewhat decreased by potential confusion with surface N_2H^+ emission. As shown in Figure 6.8, the high ionization and low ionization models are clearly discernible, while the SSX and TTX models are – in a relative sense – far more difficult to tell apart. We note N_2H^+ may nonetheless have utility as a midplane ionization tracer, and that the SSX and TTX models are both observable and differ by a factor of ~ 7 in brightness (see the zoom-in in Figure 6.9), but detailed modeling may be required to estimate the potential

X-ray contribution to the N_2H^+ column density. An additional caveat in using N_2H^+ as an ionization tracer is that its emission can be partially optically thick (if not completely, $\tau \sim 5$; Fig. 6.5). Indeed, the high interstellar CR models, M02 and W98, have similar emission line strengths because the column densities are quite large, and the correspondingly thick emission lines are no longer sensitive to column density. Therefore, in this model, N_2H^+ observations would help distinguish between disks where CRs are present or where they are excluded, e.g., by winds, however it is perhaps not a precise tool for determining CR rates below $\zeta_{\rm CR} \sim 10^{-19}$ s^{-1} for this particular disk structure. In Figure 6.8, we note that even though the SSX model emission is substantially lower than that of the W98 and M02 models, it nonetheless is still detectable. The width of the radial profile corresponds to the ALMA sensitivity, and thus disks with SSX-level of CR ionization are detectable at the 3σ and 6σ level for the $(4-3)$ and $(3-2)$ transitions of N_2H^+, respectively. Given the N_2H^+abundance's concurrent chemical dependence on temperature, a warmer disk where the N_2H^+ abundance peaks further from the X-ray bright star may allow N_2H^+ to be a more sensitive tracer of non-stellar ionizing processes and be less optically thick at the emission peak due to lower outer disk gas densities.

N_2D^+ shows interesting emission behavior such that the M02 models show *less* N_2D^+ emission than the more weakly CR-ionized W98 models (Figure 6.8). This behavior is reflected in the column densities (Fig. 6.4) and the abundances (Fig. 6.3). More specifically, the M02 N_2D^+ models show a deficit in abundance relative to the W98 models centered at $R \sim 200$ AU. The inner N_2D^+ gas is co-spatial with the high N_2H^+ (fueled by X-ray flux) and with the boundary of the H_2D^+ abundant region ($T < 50$ K), creating an N_2D^+ layer. This layer is reflected in the W98 models as well. At intermediate distance radii $R \sim 150-300$ AU, the M02 models show an N_2D^+ deficit as a direct consequence of the high degree of CR ionization in the presence of cold gas where freeze-out becomes important. The combination of ionization and cold gas drives important non-equilibrium chemistry. More specifically, the nitrogen is not being recycled back into N_2H^+ but instead sequestered into

nitrogen bearing ices like NH_3, HCN and NO, and therefore is not available as N_2 in the gas to reform N_2H^+ and N_2D^+. This process is an analogue to a similar sequence that may occur for CO (*Bergin et al.*, 2014). In the M02 model, these pathways are specifically triggered by M02's high CR flux, but a factor of ~ 10 brighter X-ray luminosity would have a similar effect (see §6.8.1).

The true utility of N_2D^+ is highlighted at low CR ionization rates. The SSX models are clearly distinguishable from the TTX models, which is reflected in the emission plane for both $(3-2)$ and $(4-3)$ and in the column density plane. N_2D^+ emission is always very optically thin, making it a direct tracer of column regardless of CR rate. The difference between the SSX and TTX line intensities is a factor of about ~ 20, more than double that of N_2H^+, allowing these CR models to be more easily disentangled than with N_2H^+.

Finally, H_2D^+ is a commonly used cold ionization tracer. However, as can be seen in Figure 6.8, its emission is only detectable for interstellar CR rates or higher, owing to its weak line strength. For ionization rates at or below $\zeta_{\rm CR} \lesssim 10^{-19}$ s^{-1}, the H_2D^+ $(1_{10}-1_{11})$ is undetectable even for full ALMA operations, and therefore it is only a useful tracer of interstellar CR rates, if they are present. These results are consistent with existing limits on the observed H_2D^+ column towards the TW Hya protoplanetary disk (*Chapillon et al.*, 2011; *Qi et al.*, 2008); however, such limits are much higher than all of the line strengths predicted here and thus more sensitive observations are required to determine if CRs are present with H_2D^+ as a tracer. The utility of H_2D^+ is highlighted when used in tandem with N_2D^+. As mentioned above, N_2D^+ decreases in brightness for both high ionization rates (when the precursors of N_2D^+ are chemically destroyed) and low ionization rates (when N_2D^+ is not produced). Observations of H_2D^+ in conjunction with N_2D^+ would allow one to break the degeneracy between these scenarios.

In Figure 6.9, we show simulated ALMA observations for the models including SLRs (no time decay) for the SSX and TTX models. The N_2H^+ and N_2D^+ lines are the only tracers for which there may be a measurable difference for the low ionization models. From these

plots it is apparent that distinguishing between CR fueled chemistry and SLR chemistry is extremely difficult. Additional factors such as – highly uncertain – disk ages will be necessary to determine fractional contributions. Alternatively, if an otherwise unexpected "jump" in ionization is seen, e.g., at the boundary of a T-Tauriosphere, then the contribution from each component can be determined unambiguously. Without this additional information, however, measurements of dense gas ionization using emission line tracers will most likely reflect a combination of both CR and SLR effects.

6.8 Further Considerations

In this section, we relax certain assumptions of our model and explore how our model results depend upon these additional parameters, including X-ray luminosity, temporal decay of SLRs, and the assumed mass of the disk.

6.8.1 Higher X-ray Luminosity

The results presented in Figures 6.7–6.9 consider a single X-ray luminosity, $L_{\rm XR} = 10^{29.5}$ erg s^{-1}. To understand the sensitivity of the lines to X-ray ionization, we have computed an additional chemical model for a ten-fold increase in X-ray luminosity for three spectral shapes: (1) the same "quiescent" spectral shape for the baseline model, solid line; (2) a harder X-ray spectrum as was used in Chapter 4, with the same normalized luminosity as model (1), dashed line; and (3) the hard X-ray spectrum normalized to have the same X-ray flux at 1 keV as model (1), dotted line. The results of these higher X-ray luminosity models are shown in Figure 6.10, where the standard model is shown as the gray solid line and the elevated models are shown in black.

The high X-ray ionization rate changes the HCO^+ column density most significantly in the inner $R < 100$ AU for the M02 and W98 models; for the outer disk there is a reduced effect as the contribution by CRs is more important. For the reduced CR models, the HCO^+ column density is enhanced throughout the disk by a factor of 3-4. This trend is explained

by the balance between ionization and recombination, such that the steady state abundance of ions (or electrons) is proportional to $\propto \sqrt{\zeta/(\alpha n_{\rm H_2})}$, where α is the recombination rate and $n_{\rm H_2}$ is the number density of H_2. With everything else constant, a factor of ten increase in ionization results in a factor of $\sqrt{10} \approx 3$ increase in the abundance and consequently column density. Consequently, owing to the sensitivity of HCO^+ to the X-ray ionization field, observations of optically thin isotopologues of HCO^+ may help put constraints on the permeability (optical depth) of the disk gas and dust to X-ray photoionization if the stellar X-ray luminosity is known. Furthermore, additional constraints on the disk gas mass combined with X-ray measurements would provide an approximate measure of the opacity due to dust and gas in the X-ray irradiated layers. Variations induced by the difference in spectral templates (black lines) are smaller, typically a factor of 1.2-1.8 in the TTX models. The hard X-ray spectrum considered in (2) (dashed line) even has a slightly lower molecular ion column density compared to the softer X-ray spectrum of (1) owing to the initial destruction of CO and N_2 by hard X-ray generated He^+. Model (3), i.e., the spectrum normalized at 1 keV with model (1), has a slightly higher energy integrated luminosity, 1.7 times that of models (1) and (2), at which point production overtakes the destruction of precursors. The N_2H^+, N_2D^+, and H_2D^+ column densities do not become sensitive to variations in the X-ray luminosity and spectrum until very low CR rates, primarily TTX, where most of the ionization in these cases comes from stellar X-rays. The flat increase in ionization for the TTX models is a consequence of high X-ray ionization rates near the star and slow recombination at large radii, where the drop in density (recombination) balances the decrease in X-ray flux with distance from the star.

6.8.2 Short-Lived Radionuclide Time Decay

Another simplifying assumption made in the chemical abundance calculations in Figures 6.3 and 6.4 was the use of a constant, non-decaying SLR ionization rate for the models including radionuclide ionization sources. From the results presented in Chapter 5 (see also

Appendix A), the ensemble of short-lived radionuclides that dominate the ionization, namely ^{26}Al and ^{60}Fe, have an effective net half-life of approximately $t_{\rm half} \sim 1.2$ Myr (see §6.5.2 for further details). For disk lifetimes up to 1 Myr, the change in ionization rate is correspondingly less than a factor of two, but can become significant for older disks (> 3 Myr). To simulate the decay of ionizing SLRs with time within the disk chemistry code, we have created a model where the SLR ionization rate is now time-dependent internal to the chemical calculations and the total (ensemble) rate decays with a 1.2 Myr half-life (Appendix A), as a simple first order approximation. In reality, the specific radionuclide decay products (i.e., γ-rays, β^+ particles, etc.) will evolve as each parent nuclide decays, i.e., ^{26}Al versus ^{60}Fe and will result in different amounts of energy deposited or lost depending upon the ionization cross sections and the decay rate of the parent nuclide. The changeover from a ^{26}Al dominated SLR rate to ^{60}Fe rate happens at around 5 Myr, and so strictly speaking a more detailed treatment that is beyond the scope of this Chapter would separate the individual contributions. We note that in addition to time variation, there will be variation between the starting abundances of SLRs between disks. In this analysis we assume solar nebula-like abundances from Chapter 5.

Figure 6.11 shows the effect of time-decaying SLRs on molecular column densities for the two lowest CR ionization models, SSX and TTX, where the change is most significant. The Figure 6.11 column densities are shown at $t = 3$ Myr of time evolution instead of 1 Myr, which corresponds to a decrease of nearly an order of magnitude in the SLR ionization rate. We show the model for fixed initial SLR abundances (blue), for CR only (orange), and a time-decaying SLR ionization rate (magenta). The inclusion of time-dependence for the SLRs *does not sensitively affect* the SSX model, which carries similar contribution from both CR and SLR ionization (at $t = 0$ Myr). In other words, in the absence of SLRs, the CRs provide similar levels of ionization in the SSX case. The CR "absent" TTX models (Figure 6.11, right) are far more sensitive to the change in SLR rate, where the time decay changes the column densities of N_2D^+, H_2D^+, and HD_2^+ by at least an order of magnitude.

Note the HCO^+ column is insensitive to differences in the SLR model assumptions, regardless of CR rate, as is expected by an X-ray dominated chemistry.

6.8.3 Dependence on Disk Mass

The results of our study are for a particular disk model (§6.4) and disk mass (M_g = 0.04 $M_\odot$). Observed protoplanetary disks show significant diversity in mass, diameter, stellar properties and environment (*Williams and Cieza*, 2011b). It is therefore interesting to quantify the sensitivity of these results to the specific choice of disk mass. To test this scenario, we take our standard model and find the chemical signatures for a disk of half mass ($M_g = 0.02$ $M_\odot$) and double mass ($M_g = 0.08$ $M_\odot$). To facilitate a simple comparison, we do not change the UV radiation field or temperature structure, but we do recompute the X-ray and CR ionization field. In reality, an increase or decrease by a factor of ~ 2 in density would change the disk opacity and would result in a correspondingly cooler (warmer) disk by $\lesssim 10\%$ in dust temperature. In the present section we focus on the abundances determined from the column densities; however, we note that the emission line ratios for a particular species will also reflect the change in local temperature due to the mass change. Furthermore, a larger (smaller) mass also would make for a more (less) UV/X-ray shielded disk. However, by changing a single parameter we may investigate, in this case, the role of more or less efficient ion-recombination and how this effect plays into the measured abundances (see §6.8.4 for temperature dependence). We leave the geometrical parameters of the disk unchanged such that the disk density scales with the change in mass. CRs are slightly more excluded by the higher gas column (not a large overall effect) and we do not consider SLRs here. A higher disk mass will trap more SLR decay products prior to loss but it is only a small effect ($\sim 1.2\times$ more ionization; see Chapter 5).

In Figure 6.12, we show the column of the indicated molecular ion, N_i, normalized to the column of model CO, $N_{\rm CO}$, which acts as our observable mass-reference. Observations of optically thin lines provide their respective total (line-of-sight integrated) column densities.

However, when one wants to determine relative abundances, typically to H_2, a normalization quantity is required. The total gas mass can be inferred from millimeter dust emission or from molecular gas traced by CO, in both cases requiring a calibrated conversion factor. Both methods have substantial caveats. The millimeter-wave dust emission evolves as the underlying population of dust evolves via grain growth, making the dust-to-gas conversion factor a time-dependent quantity. The CO abundance relative to H_2 likewise can be unreliable, both owing to freeze-out at low temperatures and chemical processing initiated by ionization (*Bergin et al.*, 2014), though this process may be slowed by vertical mixing (*Furuya and Aikawa*, 2014) and by grain growth through decreased surface area for freeze-out (*Bergin et al.*, 2014). Ideally a less chemically reactive mass tracer like HD should be used for normalization, if available (*Bergin et al.*, 2013). Nonetheless, given limited data on HD in protoplanetary disks, we provide column densities relative to the CO traced gas column, a far more widely available gas mass probe. In practice, CO column densities are extracted from optically thin isotopologues such as $C^{18}O$, however we emphasize that even $C^{18}O$ has a minimum optical depth of $\tau \sim 1$ at line center in this particular model (see Fig. 6.5). To determine the CO column observationally, one must consider either i) more rarified CO isotopes than $C^{18}O$ or ii) emission restricted to the line-wings to ensure the line is thin. In this analysis, the column densities of both the ions and of CO are taken directly from the chemical models.

In general, for the intermediate ionization rate models, W98 and SSX, the molecular ion abundance is not very sensitive to changes in the disk mass (formally density). Most importantly, the abundances are far more sensitive to the CR ionization rate than they are to the disk mass. Nonetheless, some variation does exist, where in Figure 6.12 the line thickness increases for increasing disk mass. HCO^+ in particular shows a decrease in abundance with disk mass across all CR models. These results can be understood by the same relation discussed in §6.8.1, where the ion abundance is proportional to $\sqrt{\zeta/(\alpha n_{\rm H_2})}$. In terms of column densities, the ratio of the ion-species to CO is then approximately given

by $N_i/N_{\rm CO} \sim \chi_i N_{\rm H_2}/\chi_{\rm CO} N_{\rm H_2} = \chi_i/\chi_{\rm CO} = \chi_{\rm CO}^{-1}\sqrt{\zeta/(\alpha n_{\rm H_2})}$. For a more massive disk, $\zeta_{\rm XR}$ decreases due to increased gas opacity, and $n_{\rm H_2}$ increases as the mass increases. Thus the quantity $\zeta/n_{\rm H_2}$ will decrease for increasing mass, reducing the ion abundance, explaining the general trend for all of the molecular ions considered here.

Two special cases are the high M02 CR rate (leftmost column) and the low TTX CR rate (rightmost column). Generally speaking, the M02 CR models tend to damp out the change in X-ray ionization, $\zeta_{\rm XR}$, leaving $\sqrt{n_{\rm H_2}^{-1}}$ as the dominant term. M02 shows substantially more variation than can be attributed to changes in $n_{\rm H_2}$ or in X-ray flux, otherwise the variation would be seen in W98 as well. This behavior can be understood by looking towards the denominator of the abundance ratio: $\chi_{\rm CO}$. As seen in the column density plots in Figure 6.4, the CO abundance is decreased due to chemical processing, and this deficit is reflected in the column integrated abundance, especially for H_2D^+ and HD_2^+, which are far more spread out in abundance than the W98 and SSX models in Figure 6.12.

TTX is also a special case because the molecular ion abundances are very sensitive to the X-ray ionization rate, its only ionizing source. Thus TTX is far more sensitive to the mass of the disk because $N_i/N_{\rm CO}$ depends sensitively on both $\zeta_{\rm XR}$ and $n_{\rm H_2}$. Regardless, we note that the abundance spread over different mass models – even for the TTX case – is far less than the spread resulting from different ionization rates. We thus conclude that ionization (X-ray, CR and SLRs) is the more important quantity regulating ion abundances, not disk gas mass.

6.8.4 Dependence on Stellar Spectral Type

The chemical properties of disks are especially sensitive to the dust and gas temperatures, which are set by irradiation from the central star at radii beyond the inner $R \sim 1$ AU, i.e., the region where accretion heating becomes significant. The temperature in the warm molecular layer is especially important in regulating the observable gas-phase chemistry (*Aikawa et al.*, 2002). To explore the chemical dependence on the temperature of the central star, we

recompute our baseline chemical model for a central star with $T_{\rm eff}$ = 6000 K, where all other structural parameters are held fixed. At R = 15 AU, the disk surface (z/r = 0.3) temperature increases substantially from $T_d \sim 100$ K to ~ 140 K. The warm molecular layer (z/r = 0.1) increases from T_d = 40 K to 55 K, and the midplane increases by ΔT_d = 10 K from 30 K to 40 K. This substantial increase in temperature has a sizable effect on the abundance profiles as shown in Figure 6.13. Specifically, the increase in disk temperature pushes out the CO snow line, resulting in a larger abundance of CO in the inner disk, and a thicker layer of CO radially across the entire disk. The HCO^+ column densities in Figure 6.13 for the M02 and W98 (high CR flux) cases reflect the enhanced HCO^+ production from the additional CO. However, the effect is mediated by the same chemical processing of CO as discussed in §6.6.2 and §6.8.3, where for the warmer star, CO processing occurs deeper in the dense layers of the disk, closer to the midplane, and thereby has a larger effect on the total column of CO than for the cooler star. HCO^+ for the low CR-ionization cases, SSX and TTX, shows a decrease in the outer disk, beyond $R > 250$ AU, due to the combination of CO reprocessing happening deeper in the warmer disk and the simultaneous loss of non-thermal CR desorption, enabling rapid carbon sequestration from CO into other ices.

For all CR-ionization models, the column density of N_2H^+ shows a decrease in the inner $R < 100$ AU and a surplus beyond $R > 150$ AU in the cold versus warm disk model. The inner deficit is a direct result of the enhanced inner disk CO abundance and increased destruction rate. The outer enhancement follows from the increased gas-phase N_2 abundance in the warmer disk model where it would otherwise freeze out, thereby enabling N_2H^+ formation. This process operates in tandem with the loss of CO in the dense gas due to reprocessing, reducing one of the primary destruction agents of N_2H^+. The N_2D^+ column density shows similar morphological changes as N_2H^+ where it is pushed further out radially; however, its abundance is simultaneously affected by the net reduction in deuterium-bearing species in the warm gas and the immediate loss of H_2D^+ relative to H_3^+. The H_2D^+ column density has the same drop in the inner disk due to the increased CO abundance and overall

warmer gas temperatures, though the change is less severe in the outer disk mainly because its precursor, H_2, does not freeze-out in either model.

The warmer disk model not only changes the chemical properties of the disk, but also the observational strategy necessary to experimentally determine the disk ionization processes, especially that of CRs. In the cold disk case, all molecular ions considered here were able to distinguish between high (M02 and W98) and low (SSX and below) CR fluxes outside of $R > 50$ AU; however, the column density of these species are less sensitive to changes at lower ionization rates due to freeze-out of CO and N_2. For the warm disk, the CO freeze-out region is pushed further out radially and the HCO^+ column density becomes more sensitive to the CR ionization rate outside of the X-ray dominated region ($R > 50$ AU). At $R \sim 175$ AU, the SSX and TTX CR ionization rates are indistinguishable for the cold disk model because of CO freeze-out, but in the warm disk case, there is a $\sim 60\%$ difference between the SSX and TTX models. While this difference is not sufficient to measure the ionization rate to great accuracy for this particular model, a warm disk around a more X-ray faint star (or a less X-ray permeable disk) may engender conditions favorable for optically thin HCO^+ isotopologue emission tracing *CR-dominated* layers down to low CR flux-levels. N_2H^+ and N_2D^+ remain sensitive observational tracers of the CR ionization rate at both high and low CR fluxes beyond $R > 100$ AU, where the warm disk acts to increase the "dynamic range" between the model column densities due to the reduced N_2 freeze-out. For example, the variation in N_2H^+ column density between SSX and TTX models was approximately one order of magnitude or less in the fiducial cold disk (see Figure 6.4). The warm disk increases the fractional difference to over two orders of magnitude in N_2H^+ and the same behavior holds true for N_2D^+. Thus warmer disks may allow us to estimate more precisely the CR ionization rate by mediating the effects of freeze-out and increasing the overall column. One potential caveat is that the radially larger "snowline" makes for a higher disk-averaged CO column and disk-integrated CO opacity compared to a cooler disk. In this case, even rarer CO isotopes than $C^{18}O$ may be necessary to interpret the HCO^+ column densities or to

use as a proxy for gas mass. It is also important to point out that the emission is not only sensitive to the column but also the emitting temperature, and therefore the particular transition or transitions targeted should also take into account the inherent temperature of the disk as estimated by the stellar luminosity.

6.8.5 Disk Magnetic "Opacity" to Cosmic Ray Ionization

The CR contribution to disk ionization in both magnitude and scope is the least observationally constrained parameter in disks. A cosmic ray ionization rate of $\zeta_{\rm CR} \gtrsim 3 \times 10^{-17}$ s^{-1}, consistent with dense ISM values, was ruled out by *Chapillon et al.* (2011) using observations of H_2D^+. There are a few possible explanations for the low CR rates inferred. The present work focuses on the possibility of wind-modulated *incident* CR ionization rates due to the presence of an analogue to the Solar System's heliosphere. Within this paradigm we have ignored radial variations in the GCR rate that may include (i) a gradual increase (1%/AU) in the CR rate with radius where modulation is weaker further out in the disk (Chapter 4) and (ii) an edge to the region of CR-modulation, i.e, a Heliopause. As compared to the negative ionization gradient expected for SLR ionization, (i) would create a positive ionization gradient, though the two effects are similar ($\sim$ 1 order of magnitude) and may conspire to cancel each other out. The other important radial effect is the extent of the wind-modulation zone, the "T-Tauriosphere." We have assumed the disk is fully enclosed, but if winds can only punch out the inner tens of AU, perhaps by magnetic trapping of the winds (*Turner et al.*, 2014b), the region of exclusion may be much smaller. Alternatively, if the winds dominate, they could perhaps encircle a much larger region, hundreds to thousands of AU in size due to the high gas densities (and correspondingly higher ram pressures) of early stellar winds.

Magnetic fields provide an additional source of "opacity" to CRs in two ways: (i) for funnel-shaped magnetic field configurations seen in protostars (e.g., *Girart et al.*, 2006), the magnetic field can mirror at most 50% of the CRs away (see also *Padovani and Galli*, 2011) and (ii) the presence of magnetic irregularities with size scales near the CR gyro-

radius can scatter CRs (*Cesarsky and Volk*, 1978). Both effects can act in tandem, where magnetic irregularities on an hourglass magnetic field configuration can further enhance the fraction of mirrored particles (*Fatuzzo and Adams*, 2014). The role of CR exclusion by magnetic irregularities induced by disk gas turbulence has been explored in *Dolginov and Stepinski* (1994). It was found that modest magnetic field strengths with imposed turbulent irregularities significantly impeded the CR rate in the disk, such that only $20-30\%$ of CRs reach depths corresponding to the disk scale height at all radii beyond the inner few AU. Including irregularities causes the CR ionization rate to decay very quickly with vertical depth towards the midplane (see Eq. (9) of *Dolginov and Stepinski*, 1994), thus removing CRs entirely by the midplane. Plugging in the numbers typical of our own disk model, we find that magnetic irregularities act to reduce the CR rate at the midplane by six orders of magnitude at 100 AU compared to the CR rate at the disk surface. Furthermore, both winds *and* magnetic effects can operate simultaneously, such that the winds reduce the *incident* CR ionization rate and disk magnetic irregularities substantially curtail the CR propagation *internal* to the disk, much faster the classically assumed penetration depth of 100 g cm$^{-}2$ (*Umebayashi and Nakano*, 1981).

The two scenarios, winds and "magnetic opacity," act similarly to reduce the CR flux in the disk's midplane but where they differ is in the *surface*. While we have touted the HCO^+ isotopologue emission as an excellent X-ray tracer, it is still sensitive to the higher CR ionization rate models considered here (with $\zeta_{\rm CR} \gtrsim 10^{-17}$ s^{-1}, i.e., M02 and W98). If winds are modulating the CR ionization, we would expect the HCO^+ emission to reflect a uniformly low CR rate regardless of height. If magnetic irregularities dominate the attenuation of CRs, then the CR ionization rate should be normal in the HCO^+ traced upper layers and absent in the midplane. To conduct such an experiment however, requires reasonably good constraints on the stellar X-ray luminosity and distributions of density and temperature in the disk, as both of these are expected to affect the HCO^+ emission (§6.8.1 and §6.8.3, respectively). Alternatively, if neither of these effects are important, wind modulation nor

magnetic effects, then the ionization should be $\zeta_{\rm CR} \gtrsim 10^{-17}$ s^{-1} in the outer disk and the more weakly emissive, difficult species to observe, like H_2D^+, can help provide constraints on midplane ionization.

6.9 Discussion and Conclusions

Using a generic, observationally motivated model of a T Tauri protoplanetary disk, we present chemical abundance models and simulated submillimeter emission line observations that can be used as a blueprint to constrain the detailed ionization environment within the gas disk. In particular, sensitive ($\sim 6h$) ALMA observations of nearby protoplanetary disks ($D \sim 100$ pc) will readily be able to distinguish between systems with high, interstellar CR ionization levels ($\zeta_{\rm CR} \gtrsim 10^{-17}$ s^{-1}) and those with low (sub-interstellar) ionization levels, though determining very low CR rates ($\zeta_{\rm CR} \lesssim 10^{-20}$ s^{-1}) will be made difficult by weak emission from molecular tracers and X-rays providing a lower ionization limit that may hide the effects of CRs. We emphasize that the chemical results presented here demonstrate *relative* trends across different ionization models and that the physical structure of the disk and properties of the star will determine how the chemical abundances measured directly map to ionization properties of the disk in an absolute sense. Consequently, creating detailed models of particular sources with as many observational constraints as possible will be crucial to mapping out the ionization in detail for any particular system.

We highlight the molecular ions that are useful tracers of specific ionizing agents in dense gas, e.g., the warm, X-ray irradiated molecular surface through HCO^+ or the cold, dense SLR and/or CR dominated midplane through N_2D^+ and H_2D^+. Moreover, by isolating individual ionization sources, whether by central stellar processes or otherwise, we can use these results to observationally quantify the relative importance of each ionizing agent to the total ionization state of the disk gas. Better constraints on the underlying ionization environment inform models of turbulence via the ionization-dependent magneto-rotational instability (*Balbus and Hawley*, 1991) and models of disk chemistry via ion-neutral and grain

surface reactions. In other words, dense gas ionization drives both the fundamental processes that govern both the formation (by potentially regulating turbulence-free "dead zones") and chemical make-up of planetary systems.

In particular, the least observationally constrained ionizing agents present in disks are those which dominate the midplane ionization – CRs and SLRs. More specifically, the CR rate incident on a protoplanetary disk is unknown and may be strongly modulated by winds and/or magnetic fields. Without CRs, the total midplane ionization rate is reduced by at least one to two orders of magnitude depending upon radial location and the degree to which SLR ionization contributes, which becomes the primary midplane ionization source in the absence of CRs (see also Chapter 4). High spatial resolution observations may furthermore reveal radial structure (e.g., gradients) in the CR rate with distance from the star, potentially belying the presence of an analogue heliosphere to that of the Solar System. The molecular tracers outlined in this Chapter thus provide signposts of the presence or absence of important physical processes related to disk ionization. In summary, the main results of this work are:

1. Chemical abundances of different molecular ions trace different ionizing agents (and regions) in our fiducial disk model. The abundance variation is born out in their submillimeter emission, and thus the lines discussed here can be used as diagnostic observational tools of disk ionization.

2. Optically thin isotopes of HCO^+ trace primarily the incident X-ray ionizing flux, in particular X-rays with energies $E_{\rm XR} \sim 5 - 7$ keV. For a generally warmer disk, the CO snow line may exist further out, and in this scenario, radially extended (resolved) HCO^+ emission may be sensitive to midplane ionization sources, i.e., CRs and SLRs.

3. N_2H^+ is sensitive to both cold ionization processes (CRs and SLRs) and warm ($T >$ 20 K) gas ionization via stellar X-rays and is likely moderately optically thick inside $R \lesssim 200$ AU (τ of a few). This behavior makes for somewhat difficult direct interpre-

tation, requiring detailed chemical/line emission models and multiple transitions.

4. We find that the cold gas ionization tracer H_2D^+ becomes undetectable in a $6h$ full ALMA observation at $D = 100$ pc for CR ionization rates below solar maximum (SSX models). To detect the amount of H_2D^+ present in our models at the level of $\zeta_{CR} \sim 10^{-19}$ s^{-1}, at least an order of magnitude more sensitive observations would be required, or a less distant disk such as TW Hya.

5. N_2D^+, rather than H_2D^+ is a more sensitive tracer of midplane ionization due to CRs and SLRs and the least sensitive to stellar X-rays. N_2D^+ can be used to measure ionization levels even at low CR rates ($\zeta_{CR} \lesssim 10^{-19}$ s^{-1}) and should be detectable with ALMA in a reasonable amount of time ($< 10h$).

6. Cosmic rays may be excluded by wind processes or internal/external magnetic processes (or both), but combined observations of surface ionization tracers such as HCO^+ isotopologues and midplane tracers like N_2D^+ will help illuminate the CR-exclusion mechanism that dominates (see §6.8.5).

7. Short-lived radionuclides are an important contributor to the ionization in disks, exceeding that of scattered stellar X-rays within the first few Myr. If CRs are not present, N_2D^+ should still be detectable for young disks due to the SLR contribution, but its emission will fade over the disk lifetime.

8. It will be very difficult to tell apart SLR ionization from CR ionization for measured midplane ionization rates of $\zeta \sim (1 - 10) \times 10^{-19}$ s^{-1}. A negative ionization gradient with radius would indicate a SLR dominated chemistry (SLRs can escape the tenuous outer disk radii), while a flat or positive gradient (if the inner disk is very dense with $\Sigma_g > 100$ g cm^{-2}) may point to a CR dominated chemistry.

9. The mass-normalized column density of ions (with respect to HD, CO, or dust) is far more sensitive to the CR ionization rate than to the mass of the disk itself, where we

have considered disk masses spanning the range $M_g = 0.02 - 0.08$ $M_\odot$.

10. Not all emission "rings" trace physical deficits in abundance or structure. Large temperature gradients present in disks can result in low-J rotational lines peaking offset from the star due to de-excitation in warm gas, such as can happen with HCO^+ for high CR rates.

This Chapter provides a viable starting point to study the ionization sources acting in circumstellar disks and their corresponding chemical signatures. However, this work must be carried forward in several ways. First, the ionization models used here are preliminary. We need to construct more detailed models for how CRs are suppressed by both T Tauri winds and magnetic field fluctuations; we also need improved assessments of the ionization rates provided by background cluster environments. On another front, both existing and upcoming submillimeter facilities will provide important constraints on the actual ionization levels realized in these systems and will determine which molecules provide the most information. With improved theoretical and observational input, the chemical signatures considered here can then be revisited. In the end, we will thus obtain a good working understanding of both the relevant ionization processes and the chemical structure of planet forming disks. This information, in turn, can then be used to constrain disk evolution. More specifically, the chemical structure of the disk determines the locations of both the dead zones (where MRI cannot operate) and chemical gradients in the gas and ice, and these structures greatly influence the accompanying processes of disk accretion and planet formation.

6.10 Acknowledgements

The authors thank the anonymous referee and editor for their comments and suggestions, which have greatly improved the quality of this manuscript. This work was supported by NSF grant AST-1008800.

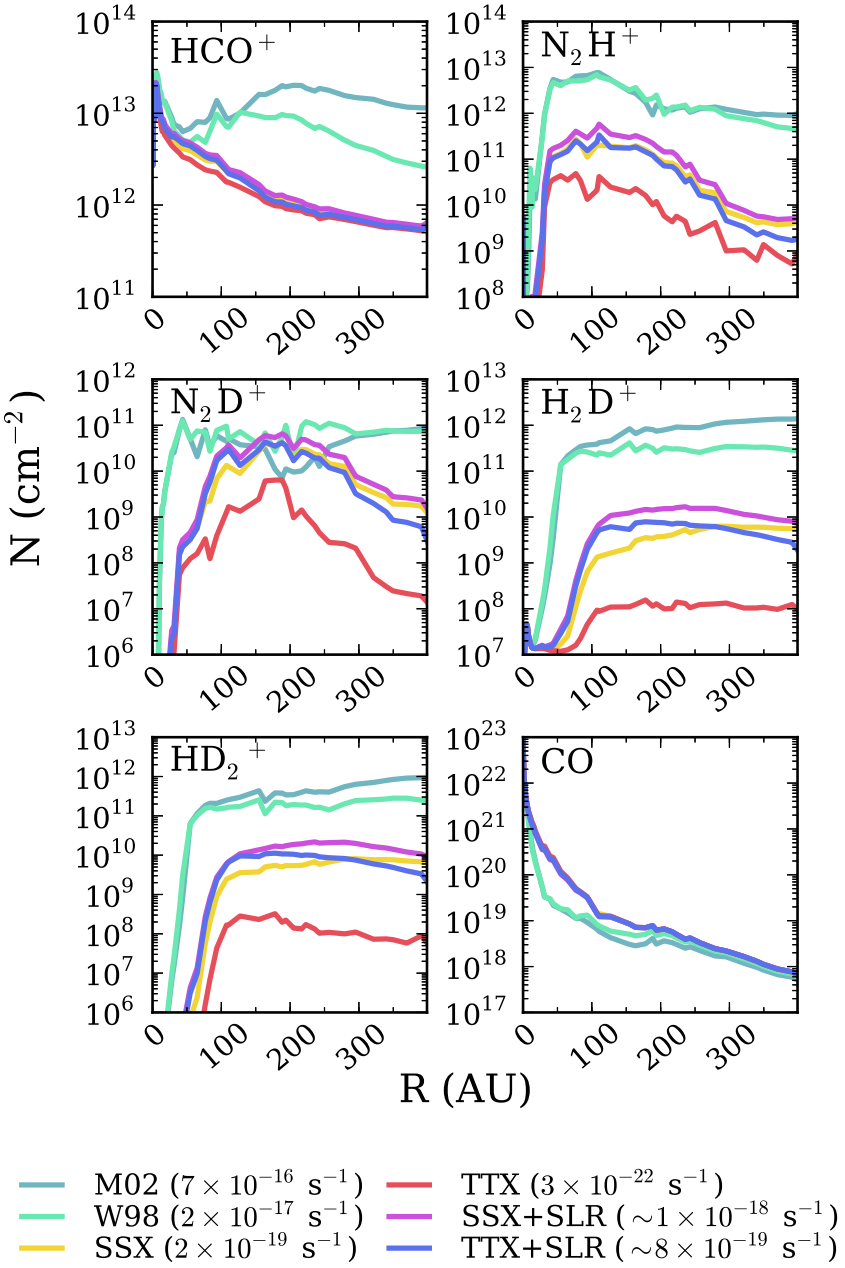

Figure 6.4 Vertically integrated column densities (cm^{-2}) of the indicated species as dependent upon the magnitude of non-stellar ionization sources. Line color indicates CR/SLR ionization model with the approximate ζ_{H_2} s^{-1} value for the incident CR ionization rates (plus SLR, if applicable), where the X-ray luminosity is fixed as $L_{XR} = 10^{29.5}$ erg s^{-1}. HCO^+ and N_2H^+ reach a "floor" in their column density from a stellar X-ray ionization baseline. X-rays contribute less to N_2D^+, H_2D^+, and HD_2^+ and so their column density is more sensitive to both the high and low ($\zeta_{CR} \lesssim 10^{-19}$ s^{-1}) ionization models. CO column densities are provided in the lower right, and at high cosmic ray ionization rates the CO abundance is eroded by reactions with He^+.

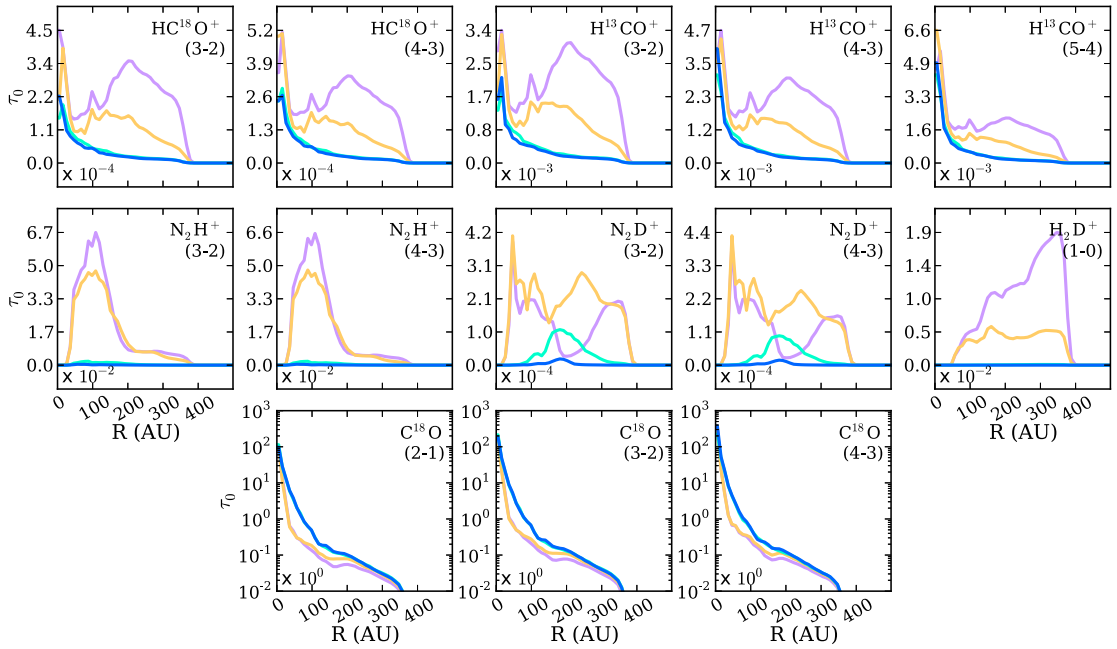

Figure 6.5 Face-on line center optical depth (τ_0) of the labeled emission lines as a function of radial distance from the star. The y-axis values are to be multiplied by the value in the lower left corner of each plot. The emission lines for the most part are optically thin except in the case of N_2H^+ $(4-3)$ and $(3-2)$, which reaches τ_0 of a few inside of $R < 200$ AU. $C^{18}O$, a commonly used tracer of gas-mass, is optically thick for most of the disk, and therefore either a more optically thin isotopologue is needed or sensitive observations of the line wings where the gas may become thin to use $C^{18}O$ as a potential mass normalizer. Colors correspond to M02: purple, W98: yellow, SSX: blue, and TTX: green.

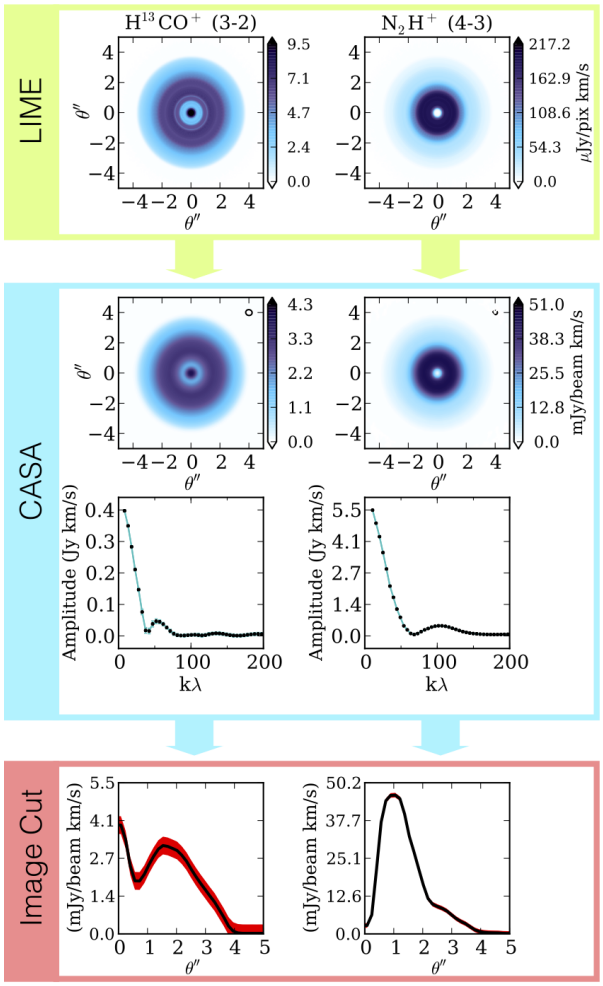

Figure 6.6 Schematic illustrating the calculation of simulated observations. *Top:* The face-on line emission models calculated from the chemical abundance models (Fig. 6.3) using the radiative transfer code LIME (*Brinch and Hogerheijde*, 2010) in non-LTE where available. Line emission models are in units of μJy/pixel and are observed at a distance of $d = 100$ pc. *Middle:* Using CASA's simobserve task, we simulate observations with the full 12m ALMA array plus the 7m ACA array. UV-binned visibility amplitudes integrated over velocity and on-sky emission shown, $1'' = 100$ AU. *Bottom:* Cuts across the on-sky emission from the cleaned simulated observations, see text for details. Error bars (sensitivity) are estimated from the ALMA sensitivity calculator values assuming a 6.1h observation in 100 km/s channels. Average beam size is $0.33''$ and $0.24''$ for the left and right plots, respectively.

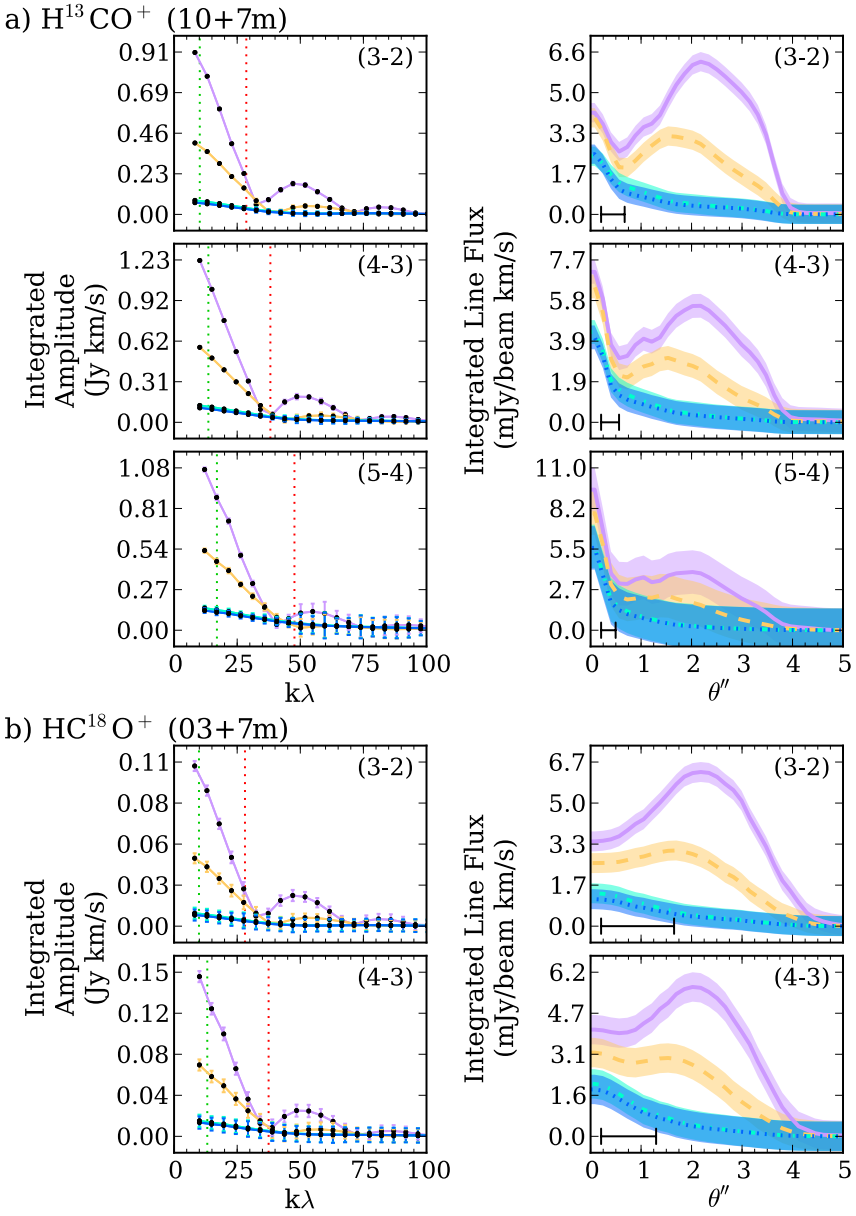

Figure 6.7 ALMA simulations for the observable transitions of the indicated molecular ions. Line color represents different CR ionization models: M02 (purple), W98 (yellow), SSX (cyan), and TTX (blue). The simulated antenna configuration used in CASA's simobserve task is indicated in parenthesis (## + 7m). *Left:* Velocity-integrated visibility amplitudes. The dashed vertical green line corresponds to the minimum baseline from the 12-m observations, which can be less than the physical separation of the antennas due to sky projection. The red dashed line is the maximum baseline sampled by the 7-m observations. *Right:* reconstructed image profiles in sky-coordinates integrated over velocity. Synthesized beam indicated by the black bar. Width of the lines corresponds to the sensitivity of the simulated observations.

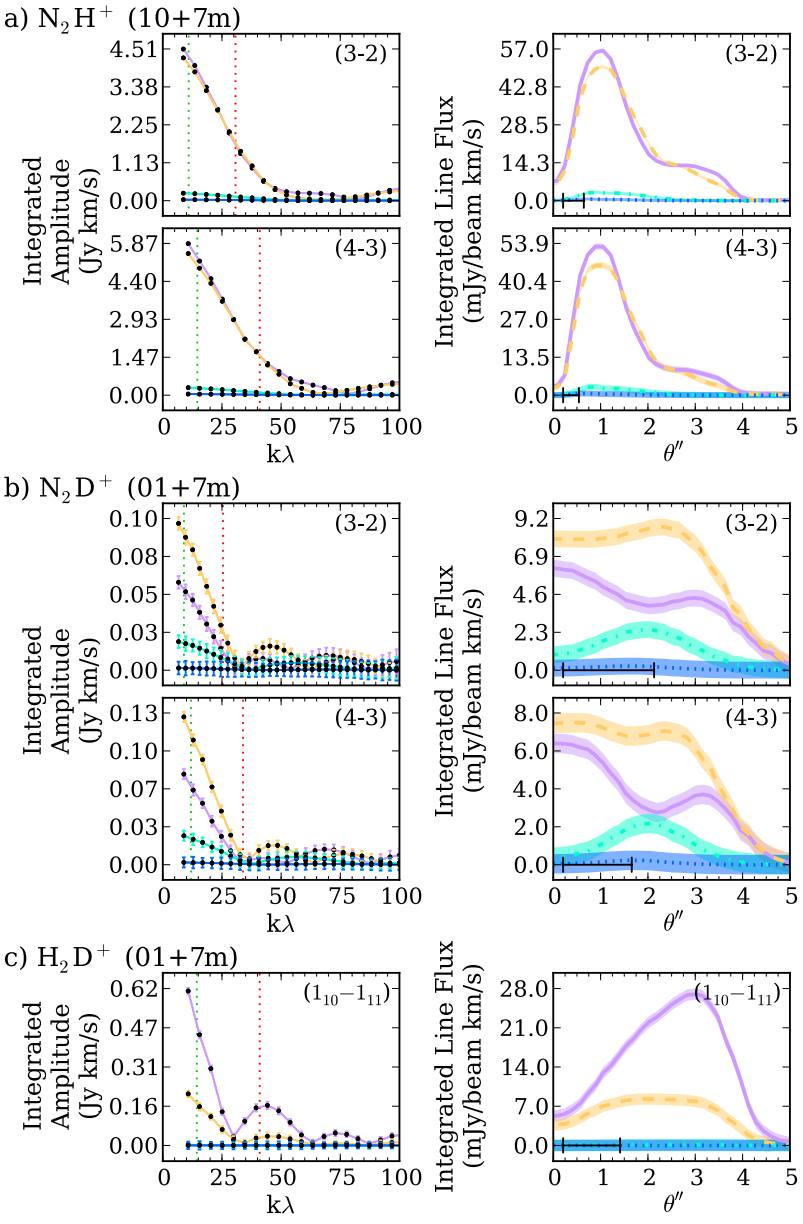

Figure 6.8 The same as Fig. 6.7, for "cold gas" ions typically tracing gas below $T \lesssim 50$ K. H_2D^+ is unobservable for our models with ionization rates of $\zeta_{CR} \lesssim 2 \times 10^{-18}$ s^{-1}. Consequently, N_2D^+ is the only molecular ion which allows for some differentiation between ionization rates below $\zeta_{CR} \lesssim 10^{-18}$ s^{-1}, as seen clearly in the visibilities, especially for the N_2D^+ (4-3) transition. The high CR ionization rate models overlap for N_2H^+ because the line becomes very optically thick. We note, that while weak, the SSX model is detectable in both the $(4-3)$ and $(3-2)$ transitions of N_2H^+ at the 3 and 6σ levels, respectively. See also Figure 6.9 for a zoom-in on the low ionization models.

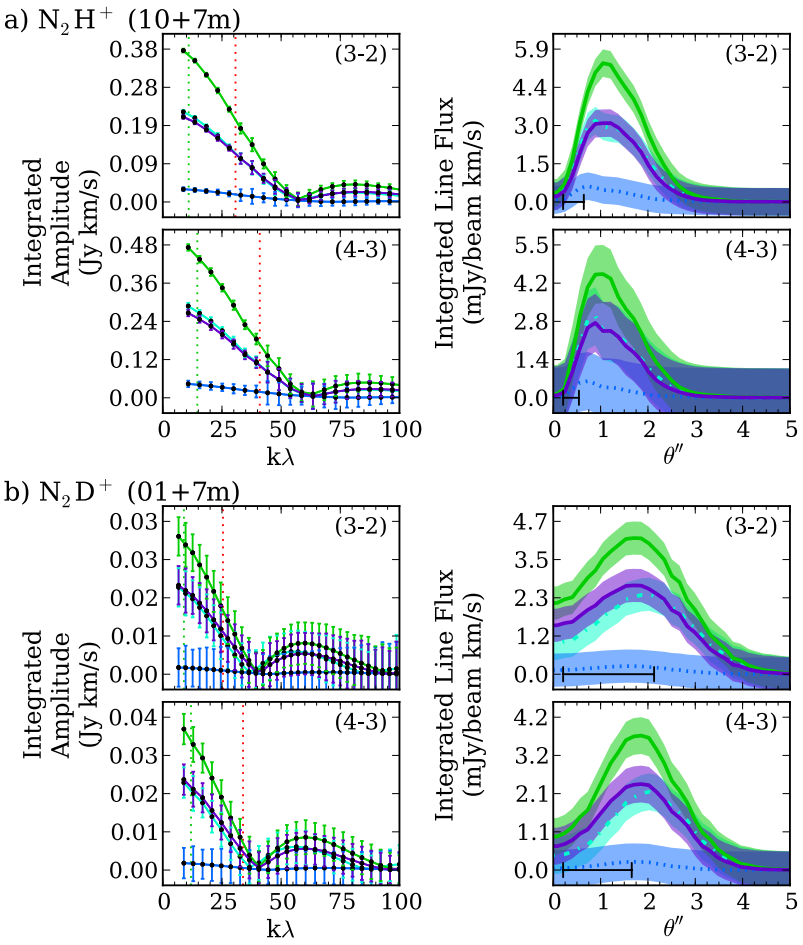

Figure 6.9 ALMA simulations of the low CR ionization rate models with and without a constant SLR ionization rate. Only the low ionization models are shown for clarity. Figure quantities are the same as Figure 6.7. The CR-only models are shown as TTX: blue and SSX: cyan. The same CR models now including SLR ionization are shown in green and purple, respectively. As can be seen from both visibility curves and sky-emission, the inclusion of SLR ionization does not significantly change the profile or intensity of the lines shown. A TTX model with SLR ionization (purple) would be difficult to distinguish from an SSX model without SLRs (cyan).

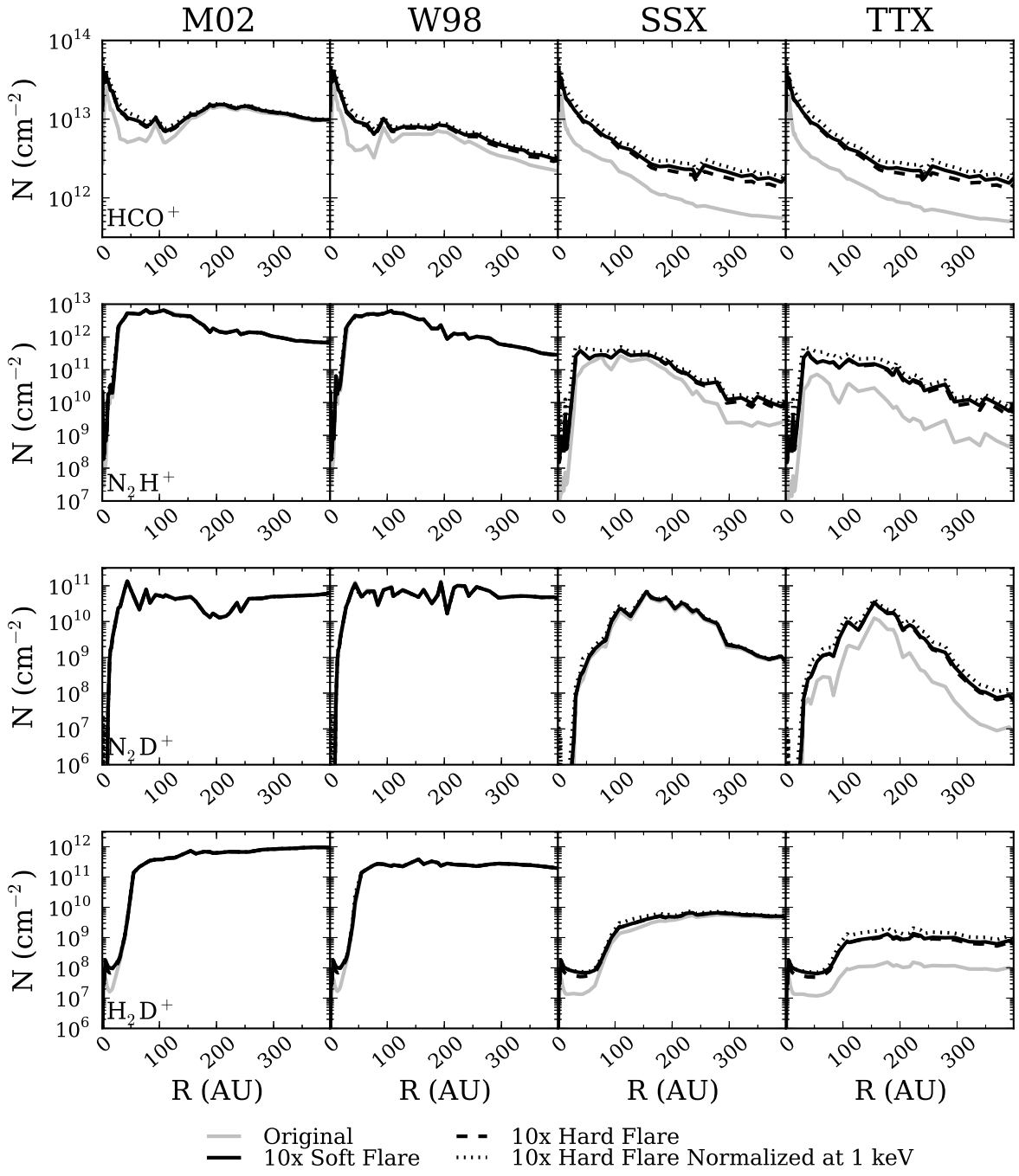

Figure 6.10 Chemical models for $L_{\rm XR} = 10^{29.5}$ erg s^{-1} (gray solid lines) and enhanced to $L_{\rm XR} = 10^{30.5}$ erg s^{-1} (black lines). Rows correspond to the indicated molecules on the left, and columns correspond to the CR models as labeled at the top of the figure. For the enhanced models, the three line styles correspond to different X-ray spectra. The solid black line holds the spectral shape fixed and increases the overall luminosity by a factor of 10. The dashed black line corresponds to a harder X-ray spectrum with the same normalized luminosity as the solid line. The dotted line is a model with the same 1 keV flux as the solid black line, but with a hard spectral template increasing $L_{\rm XR}$ by 1.7.

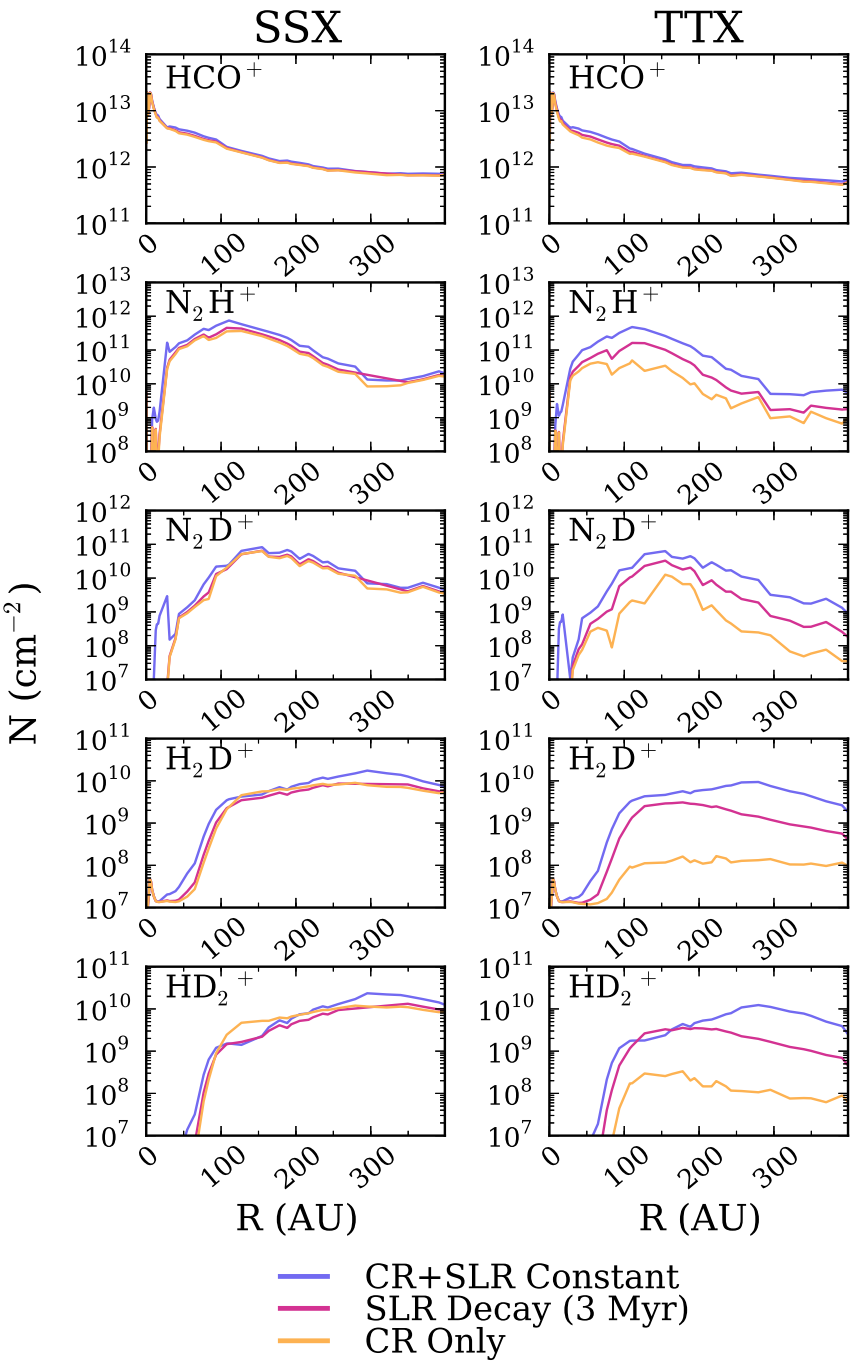

Figure 6.11 Column density dependence on SLR ionization with time dependence. All curves are shown at $t = 3$ Myr of chemical evolution. The blue line shows a model with CRs and a fixed SLR ionization rate set by the initial value, no time decay included. Magenta curves include a decay on the SLR ionization rate with a half-life of $t_{\rm half} \sim 1.2$ Myr (Chapter 5). The yellow line shows the column density in the absence of SLR ionization.

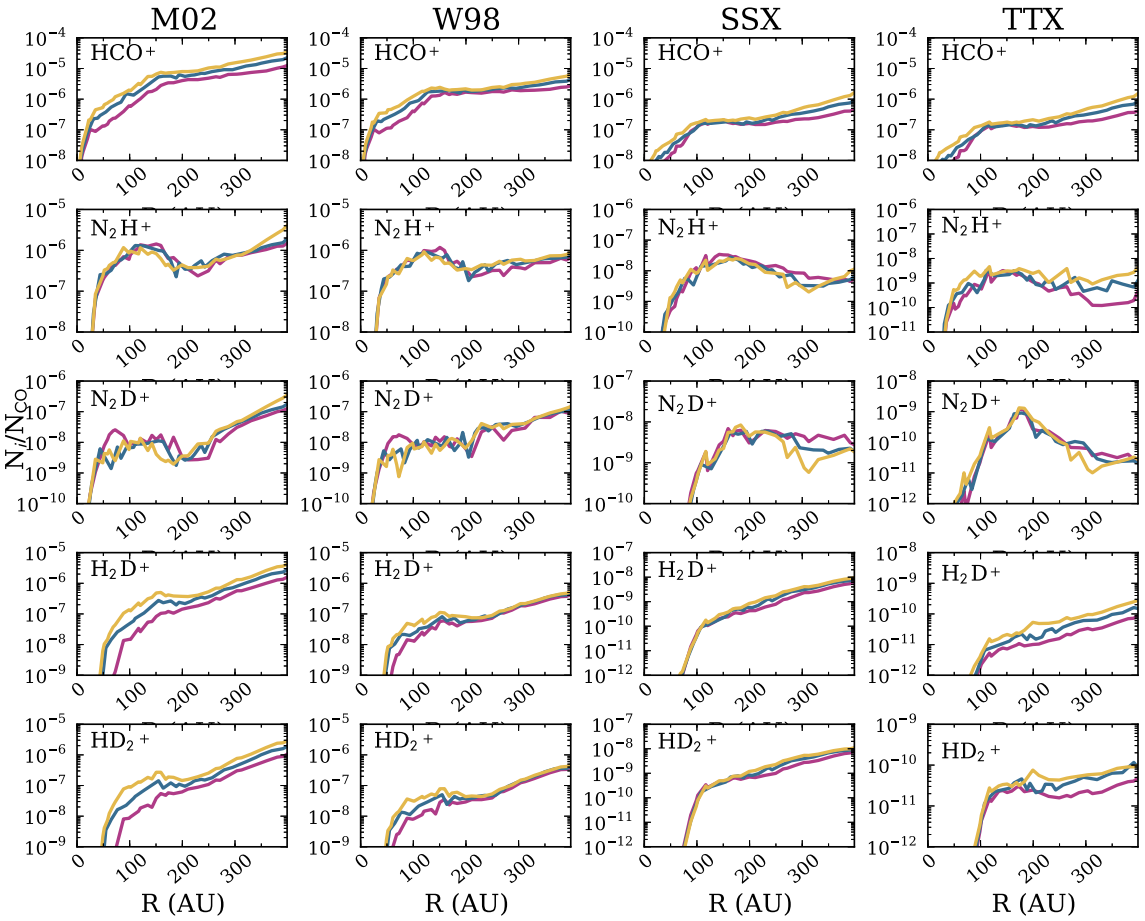

Figure 6.12 Column-derived abundances of the indicated molecular ions, normalized to CO as a function of disk radius. Colors represent disk mass, where yellow, blue and magenta correspond to 0.5×, 1×, and 2× disk gas mass models. CR models are as indicated in the column headings. Changes in the normalized column densities of a given molecular ion for different disk masses are, in general, far smaller than changes across different CR ionization rates. Ionization decreases as one goes from left to right. See text for details and discussion.

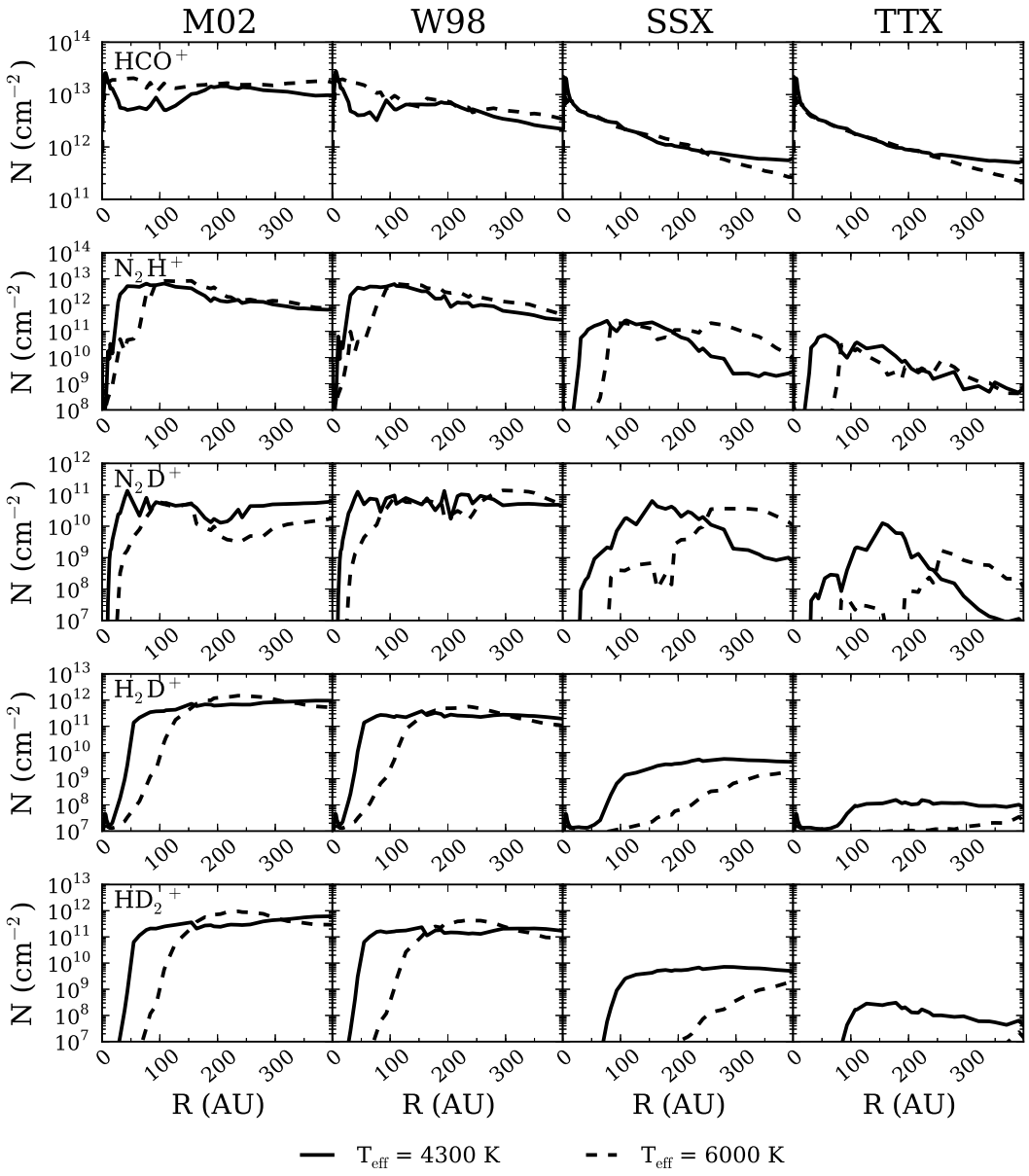

Figure 6.13 Vertical column densities of select species as a function of stellar spectral type. Solid lines correspond to the fiducial disk model with stellar effective temperature of $T_{\rm eff}$ = 4300 K. Dashed lines show column densities for the warmer (more luminous) central star, $T_{\rm eff}$ = 6000 K. See discussion in §6.8.4 for details.

CHAPTER VII

Constraining the X-ray and Cosmic Ray Ionization Chemistry of the TW Hya Protoplanetary Disk: Evidence for a Sub-interstellar Cosmic Ray Rate

7.1 Preface

The following work appears in the Astrophysical Journal, Volume 799, 204, 18 pp. (2015). The work is co-authored by Edwin A. Bergin,[1] Chunhua Qi,[2] Fred C. Adams,[3], and Karin I. Öberg,[4] The paper is copyright 2015, the American Astronomical Society, reproduced here under the non-exclusive right of republication granted by the AAS to the author(s) of the paper.

7.2 Abstract

We present an observational and theoretical study of the primary ionizing agents (cosmic rays and X-rays) in the TW Hya protoplanetary disk. We use a set of resolved and unresolved observations of molecular ions and other molecular species, encompassing eleven lines total,

[1]Department of Astronomy, University of Michigan, 1085 S. University Ave., Ann Arbor, MI 48109
[2]Harvard-Smithsonian Center for Astrophysics, 60 Garden Street, Cambridge, MA 02138
[3]Department of Physics, University of Michigan, 450 Church St, Ann Arbor, MI 48109
[4]Harvard-Smithsonian Center for Astrophysics, 60 Garden Street, Cambridge, MA 02138

in concert with a grid of disk chemistry models. The molecular ion constraints comprise new data from the Submillimeter Array on HCO^+, acquired at unprecedented spatial resolution, and data from the literature, including ALMA observations of N_2H^+. We vary the model incident CR flux and stellar X-ray spectra and find that TW Hya's HCO^+ and N_2H^+ emission are best fit by a moderately hard X-ray spectra, as would be expected during the "flaring" state of the star, and a low CR ionization rate, $\zeta_{\rm CR} \lesssim 10^{-19}$ s^{-1}. This low CR rate is the first indication of the presence of CR exclusion by winds and/or magnetic fields in an actively accreting T Tauri disk system. With this new constraint, our best fit ionization structure predicts a low turbulence "dead-zone" extending from the inner edge of the disk out to $50 - 65$ AU. This region coincides with an observed concentration of millimeter grains, and we propose that the inner region of TW Hya is a dust (and possibly planet) growth factory as predicted by previous theoretical work.

7.3 Introduction

Gas-rich circumstellar disks around young stars are the formation sites of planetary systems. The physical conditions of this circumstellar material, including density, temperature, and ionization, all play an important role in setting the dynamical and chemical properties of the disk. In particular, ionization has a central role in governing disk turbulence and chemistry within the cold ($T < 100$ K) planet-forming gas. The turbulence of disks with masses comparable to our own minimum mass solar nebula ($\lesssim 0.05$ M$_\odot$; *Weidenschilling*, 1977) is thought to be driven by the magnetorotational instability (MRI; e.g., *Velikhov*, 1959; *Balbus and Hawley*, 1991; *Stone et al.*, 1996; *Wardle*, 1999; *Sano et al.*, 2000; *Sano and Stone*, 2002; *Fleming and Stone*, 2003; *Bai and Stone*, 2011). MRI requires the disk to be sufficiently ionized such that the bulk, predominantly neutral gas can couple to the magnetic field lines, thereby "stirring" the gas. Regions of the disk quiescent to such turbulence, i.e., "dead-zones," have been posited as safe-havens for efficient planetesimal formation (*Gressel et al.*, 2012), as well as an efficient "stopping mechanism" against Type I and II migration

(e.g., *Matsumura and Pudritz*, 2005; *Matsumura et al.*, 2007). With regards to molecular composition, ionization drives the most efficient chemical processes in the cold, dense regions of disks, both in the gas by ion-neutral chemical pathways (*Herbst and Klemperer*, 1973) and through ionization-derived hydrogenation reactions on ice-coated grain surfaces (*Tielens and Hagen*, 1982; *Hasegawa et al.*, 1992a; *Garrod et al.*, 2008). For the same reason, ionization plays a pivotal role in facilitating (or hindering) deuterium fractionation reactions in the gas or on cold grain surfaces (*Aikawa and Herbst*, 1999a, Chapter 8). Consequently, ionization is central to the chemical and physical fate of protoplanetary disks and ultimately the planets they form.

The primary sources of dense gas ionization in disks are X-rays, cosmic rays (CRs) and the decay of short-lived radionuclides (SLRs). Classical T Tauri (CTT) stars are exceptionally X-ray bright (10^{28} erg s^{-1} cm^{-2} $\lesssim L_{\rm XR} \lesssim$ 10^{34} erg s^{-1} cm^{-2}; *Feigelson et al.*, 2002) and often time-variable sources. X-ray flaring activity in CTTs is commonly associated with an overall hardening of the X-ray spectrum, where relatively more energy is output at $E_{\rm XR} \gtrsim 2$ keV (*Skinner et al.*, 1997). These harder X-ray photons are particularly important in setting the disk ionization as they are not easily impeded by intervening material between the star and the disk (i.e., by a stellar/disk wind) and are not as efficiently stopped within the disk itself compared to less-energetic $E_{\rm XR} \sim 1$ keV photons (*Glassgold et al.*, 1997).

In very dense gas ($n_{\rm H_2} \gtrsim 10^9$ cm^{-3}), where X-rays are strongly attenuated, the primary sources of ionization available are external galactic CRs and the internal decay of short-lived radionuclides (SLRs). In the dense interstellar medium, CRs ionize at a rate exceeding a few times 10^{-17} s^{-1} and perhaps an order of magnitude or more higher in the diffuse gas (*Indriolo and McCall*, 2012). However, in the presence of stellar winds and/or magnetic fields, the incident CR rate can be substantially reduced by orders of magnitude (*Dolginov and Stepinski*, 1994; *Padovani et al.*, 2013; *Fatuzzo and Adams*, 2014, and Chapter 4 of this thesis).

SLRs are provided by massive stars that enrich the dense molecular gas from which young

stars (and disks) form. In addition, certain species including ^{36}Cl and, to some extent, ^{26}Al (e.g., *Gounelle et al.*, 2001) can be provided by grain-surface spallation via energetic particles from the central star; however, the dominant species at 1 Myr, ^{26}Al, is primarily formed by external sources (see reviews by *Adams*, 2010; *Dauphas and Chaussidon*, 2011, and references therein). The presence of SLRs in the young Solar Nebula is inferred from the Solar System's meteoritic record, but the contribution towards disk ionization from SLR decay is uncertain, owing to unknown initial abundances, inherent time-decay over the lifetime of the disk, and an uncertain "injection" point prior to or after disk formation, or perhaps both (e.g., *Ouellette et al.*, 2007, 2010; *Adams et al.*, 2014). SLR ionization may also be reduced by the escape of ionizing agents, i.e., the decay products, from the tenuous outer disk (Chapter 5).

All of these effects act together to make a rich ionization environment with substantial spatial variation. The individual importance of each of these physical processes has been debated for decades (*Gammie*, 1996; *Igea and Glassgold*, 1999). For the gas thermal structure in the upper layers, understanding the heating contribution by X-rays, UV irradiation and to a lesser extent the CR flux is necessary (e.g. *Glassgold et al.*, 2004; *Jonkheid et al.*, 2004; *Kamp and Dullemond*, 2004; *Gorti and Hollenbach*, 2009; *Glassgold et al.*, 2012; *Bruderer et al.*, 2012). In determining the extent of the disk that is unstable to MRI (i.e., is turbulent), the question is often what minimum ionization fraction is required. CRs, given their ability to penetrate disk gas down to $\lesssim 100$ g cm^{-2}, were the original focus of *Gammie* (1996) in determining the thickness of the MRI active layer. However, given the intensity of the young star as an X-ray source and including the important effects of X-ray scattering, *Igea and Glassgold* (1999) argued that the disk could be turbulent everywhere beyond 5 AU (inside of which X-rays are too highly attenuated) even in the absence of CRs. With the arrival of spatially and spectrally resolved high signal-to-noise data on molecular ions, many of these questions should be possible to resolve through the coupling of detailed models and observations.

In Chapter 6, we explored the sensitivity of disk ion chemistry to different ionization

scenarios using a generic T Tauri disk model. In the present Chapter, we apply these results to a particular protoplanetary disk, TW Hya. TW Hya's proximity ($d = 55 \pm 9$ pc; *Webb et al.*, 1999; *van Leeuwen*, 2007), face-on inclination ($i \sim 7 \pm 1°$; *Qi et al.*, 2004), and general isolation from ambient molecular gas (*Rucinski and Krautter*, 1983; *Feigelson*, 1996; *Hoff et al.*, 1998; *Tachihara et al.*, 2009), together provide a clear view into the chemical and physical properties of TW Hya's circumstellar material. This favorable orientation combined with a rich observed gas-phase chemistry (CN, HCN, DCN, H_2O, HD, and H_2CO; *Kastner et al.*, 1997; *van Zadelhoff et al.*, 2001; *Qi et al.*, 2008; *Hogerheijde et al.*, 2011; *Öberg et al.*, 2012; *Bergin et al.*, 2013; *Qi et al.*, 2013a) and numerous detections of molecular ion emission (N_2H^+ HCO^+, $H^{13}CO^+$, and DCO^+; *Kastner et al.*, 1997; *van Zadelhoff et al.*, 2001; *Wilner et al.*, 2003; *van Dishoeck et al.*, 2003; *Qi et al.*, 2008, 2013a) make for fertile ground to study the disk's ionization chemistry. In this work, we combine new and archival data with detailed theoretical simulations of disk ionization chemistry to unravel the origin of the molecular ion emission along with its distribution within the TW Hya protoplanetary disk.

In §7.4, we present the observational constraints, including new data from the Submillimeter Array (SMA). We describe the gas and dust physical model along with the chemical code in §7.5. In §7.5.3 we outline the grid of ionization parameters, where we specifically vary the shape of the incident X-ray spectrum and incident CR ionization rate. We calculate chemical models across the grid and perform simulated observations (§7.5.4) for direct comparison to the data. We present our findings in §7.6, discuss their implications for the TW Hya disk structure in §7.7 and summarize in §7.8.

7.4 Observations

7.4.1 Submillimeter Array Data

The HCO^+ (3-2) observations of TW Hydra were made with the SMA (*Ho et al.*, 2004) located atop Mauna Kea on April 12, 2012 in the very extended (VEX) configuration with 7

antennas under excellent sky conditions, $\tau_{225\mathrm{GHz}} \lesssim 0.04$. Titan was used for flux calibration, the quasars J1147-382 and J1037-295 were used for gain calibration and 3C279 for passband calibration. The line was observed with 256 channels in chunk s04, where the chunk width is 104 MHz, corresponding to a velocity resolution of $\Delta v = 0.46$ km s^{-1}. All data were phase- and amplitude-calibrated using the MIR software package[5]. All continuum and spectral line maps were then generated and CLEANed using the MIRIAD software package with natural weighting. The synthesized VEX beam for the HCO^+ observation is $(\theta_{\mathrm{maj}} \times \theta_{\mathrm{min}}) = (0.64'' \times 0.36'')$ with a position angle PA $= 17.3°$, where the RMS noise on the line is 85 mJy/beam. We have also combined the new VEX HCO^+ track with shorter spacing data from compact and extended tracks (*Qi et al.*, 2008, observed between 2005-2006) to improve the imaging fidelity. The synthesized beam for the combined measurement set is $0.69'' \times 0.39''$, PA $= 16.9°$, with an RMS of 60 mJy/beam. The 1σ continuum sensitivity at 267 GHz is 1.6 mJy beam^{-1} ($0.63'' \times 0.35''$ beam) and 2.3 mJy beam^{-1} ($0.65'' \times 0.37''$ beam) beam in the VEX-only and combined observations, respectively. The decrease in sensitivity in the latter is a result of poorer atmospheric conditions for the extended and compact tracks. Figure 7.1 shows the velocity integrated line flux for the combined and VEX-only data sets.

Observations of the $H^{13}CO^+$ $(3-2)$ line were made on 2014 April 8 using six out of eight 6-m antennas of the SMA in the extended configuration with projected baselines ranging from 8 to 165 meters. The tuning was centered on the $H^{13}CO^+$ $(3-2)$ line at 260.255339 GHz in chunk S23. The observing loops used J1037-295 as the gain calibrator. The bandpass response was calibrated using observations of 3C279. Flux calibration was done using observations of Titan and Callisto. The derived flux of J1037-295 at the time of the observations was 0.70 Jy. The spatially integrated $H^{13}CO^+$ $(3-2)$ and HCO^+ $(3-2)$ spectra are shown in Figure 7.2.

[5]http://www.cfa.harvard.edu/∼cqi/mircook.html

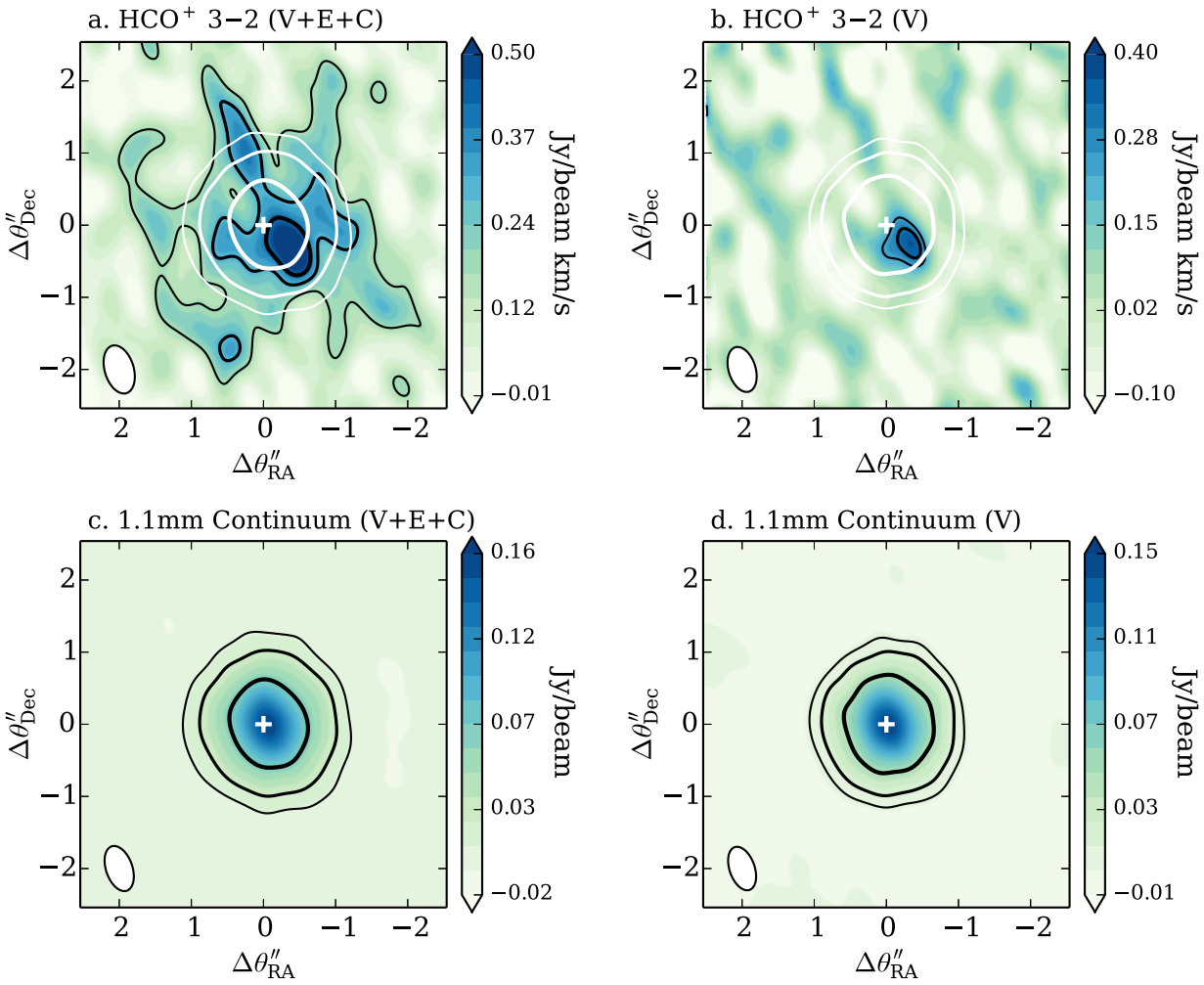

Figure 7.1 TW Hya velocity integrated HCO^+ $(3-2)$ (*top*) and 1.1 mm continuum (*bottom*) observations. The combined SMA very-extended, extended and compact array data in panels (a) and (c) show the almost symmetric large scale structure of the HCO^+ emission, while the very-extended data in panels (b) and (d) show the small-scale deviation from axis-symmetry in HCO^+. White crosshairs mark the continuum phase center and overlaid white contours trace the continuum contours. Black contours mark 3σ, 5σ and 7σ in the HCO^+ panels with 1σ=60 mJy beam^{-1} km s^{-1} (*left*) and 85 mJy beam^{-1} km s^{-1} (*right*). Continuum contours are 3σ, 10σ and 30σ, where $1\sigma = 2.3$ mJy beam^{-1} (*left*) and $1\sigma = 1.6$ mJy beam^{-1} (*right*). The beam is shown in the lower-left of each panel.

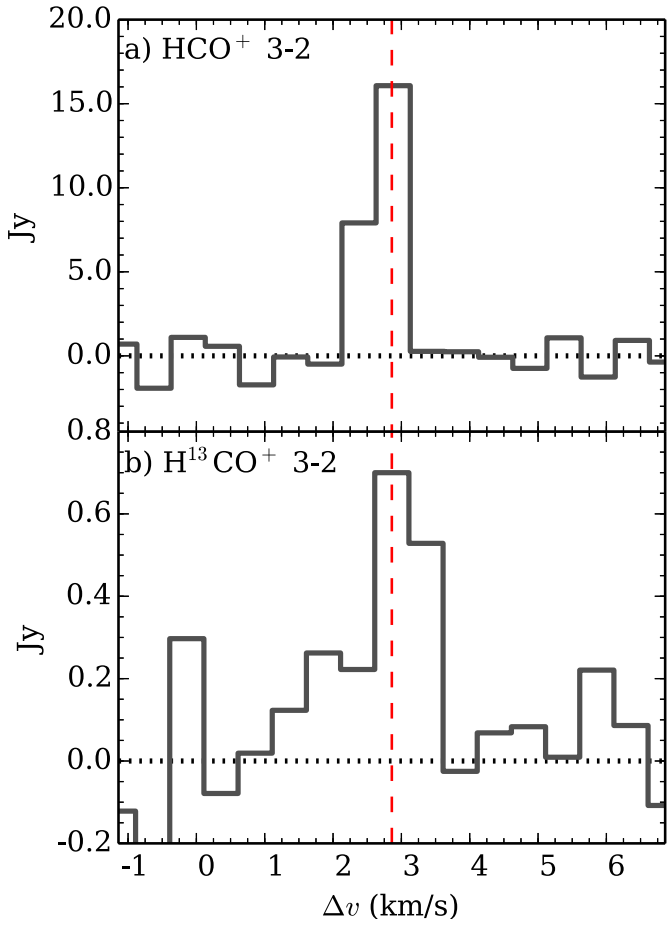

Figure 7.2 Spatially integrated spectra over an 8″ region, where the vertical red line indicates TW Hya's intrinsic velocity $V_{\rm LSR}$=2.86 km s^{-1}. *Top:* HCO^+ $(3-2)$ from the combined (V+E+C) data set. *Bottom:* $H^{13}CO^+$ $(3-2)$ from the extended configuration observations.

7.4.2 Archival Data

In addition to the new HCO^+ $(3-2)$ and $H^{13}CO^+$ $(3-2)$ data, we have compiled molecular ion emission line observations from archives and the literature (Table 7.1). HCO^+ $(1-0)$ and $(4-3)$ line data was extracted from ALMA Science Verification observations. The HCO^+ $(1-0)$ line was observed in Band 3 on May 13-14, 2011 with ten 12-m antennas for a total of 3.7 hours. Titan, 3C279, and J1037-295 were used for flux, gain and phase calibration, respectively. The HCO^+ $(4-3)$ line was observed in Band 7 on April 22, 2011 in three scheduling blocks for a total of 4.5 hours. Nine 12-m antennas were available during the observations; however, one antenna had to be flagged. The same calibrators were used as in the HCO^+ $(1-0)$ observations. Further information regarding the observations is provided at the ALMA Science Verification website[6]. From the publicly available calibrated data, we extract the flux from an $8''$ region for both lines.

$H^{13}CO^+$ $(4-3)$, N_2H^+ $(3-2)$ and $(4-3)$ have been observed with the SMA and ALMA, respectively (*Qi et al.*, 2008, 2013a,b). Integrated line fluxes were extracted from the spectral image cubes using an 8" box to be consistent with the new and archival HCO^+ data. In addition to these molecular line data, we have made use of the published HD, CO and HCN fluxes listed in in Table 7.1 to calibrate and verify the developed TW Hya disk chemistry model.

All reported noise in Table 7.1 combines in quadrature the random noise on the data and an absolute flux uncertainty of 15%. We note that as a result the detections are individually *more significant*, i.e., have higher signal to noise as determined from random noise, than the table implies. See section §7.5.4 for a detailed discussion regarding the "Recover All?" column.

[6]https://almascience.nrao.edu/alma-data/science-verification

Table 7.1. Spectrally integrated TW Hya line fluxes used to constrain the physical model. Reported uncertainties on the molecular ions include statistical errors and a 15% systematic uncertainty in the absolute flux scale.

Line	Integrated Line Flux (Jy km/s)	Beam (maj × min, PA)	Reference	Recover all?
HCO^+ $(1-0)$	0.85 ± 0.14	$(4.2'' \times 2.9'', 72°)$	ALMA 2011.0.00001.SV.	Y
HCO^+ $(3-2)$	12.9 ± 2.12	$(0.69'' \times 0.39'', 16.9°)$	This work.	Y
HCO^+ $(4-3)$	23.3 ± 3.5	$(1.7'' \times 1.6'', 18°)$	ALMA 2011.0.00001.SV.	N
$H^{13}CO^+$ $(3-2)$	0.7 ± 0.18	$(1.81'' \times 0.90'', 15.6°)$	This work	Y
$H^{13}CO^+$ $(4-3)$	1.1 ± 0.41	$(4.1'' \times 1.8'', 3.3°)$	*Qi et al.* (2008)	N
N_2H^+ $(3-2)$	2.2 ± 0.46	$(3.5'' \times 2.0'', 10°)$	*Qi et al.* (2013a)	Y
N_2H^+ $(4-3)$	4.6 ± 0.7	$(0.63'' \times 0.59'', -18°)$	*Qi et al.* (2013b)	N
HD $(1-0)$	70.6 ± 7.8	$(9.4'' \times 9.4'')$	*Bergin et al.* (2013)	Y
$C^{18}O$ $(2-1)$	0.68 ± 0.18	$(2.8'' \times 1.9'', -1.3°)$	*Favre et al.* (2013)	Y
			Qi et al. (2013b)	Y
^{13}CO $(2-1)$	2.76 ± 0.18	$(2.7'' \times 1.8'', -3°)$	*Favre et al.* (2013)	Y
			Qi et al. (2013b)	Y
HCN $(3-2)$	8.5 ± 1.7	$(1.6'' \times 1.1'', -0.5°)$	*Qi et al.* (2008)	Y

7.5 Modeling

To evaluate what constraints the molecular ion observations provide on the ionization agents active in the TW Hya disk requires 1) a physical model of the TW Hya protoplanetary disk, 2) a disk chemistry code, and 3) the application of this code to the physical model under a range of ionizing conditions. Informed by previous model efforts (e.g., *Calvet et al.*, 2002; *Thi et al.*, 2010b; *Gorti et al.*, 2011; *Andrews et al.*, 2012; *Menu et al.*, 2014) and directly building on *Bergin et al.* (2013), we have constructed a new physical model of the TW Hya disk, which focuses on the aspects of most importance to the molecular ion chemistry, i.e. the distribution of cold gas and small dust grains. The details of the modeling process are described in Appendix D as well as the sensitivity of our conclusion on the chosen disk structure, and we review only the main features of the model here.

7.5.1 Physical Structure

The dust structure is derived from fitting the spectral energy distribution, where we include settling by defining two dust populations of small (atmosphere) and large (midplane) grains, with the latter concentrated near the midplane, i.e. it is parameterized as having a smaller scale height. The outer disk radius of our full model is taken to be $R_{\rm out} = 200$ AU as determined from the CO gas disk and scattered light images tracing the small dust (*Andrews et al.*, 2012; *Krist et al.*, 2000; *Trilling et al.*, 2001; *Weinberger et al.*, 2002; *Roberge et al.*, 2005; *Debes et al.*, 2013). We do not account for the observed radial variation between the two dust populations, i.e., the concentration of large grains inside of $R \sim 60$ AU (*Andrews et al.*, 2012), since the explored chemistry depends mainly on the small dust grain population, which dominate the total surface area of grains (see §7.5.2).

We assume the gas is co-distributed with the small grains following a power-law with an exponential taper beyond $R > 150$ AU (see Appendix F for structure dependence) and cut off at an outer disk radius of 200 AU. We estimate the total mass in gas from the *Herschel* detection of HD (*Bergin et al.*, 2013), by varying the disk-integrated gas-to-dust mass ratio, i.e., the gas-to-dust ratio calculated from the column density is constant, but the local gas-to-dust ratio varies with height (due to settling). The resulting disk gas mass in our model is $M_g = 0.04$ $M_\odot$ with an uncertainty of 0.02 $M_\odot$ (see Appendix D). The gas temperatures are estimated from the UV radiation field throughout the disk (S. Bruderer, in private communication and Appendix D). The gas and dust distributions of our physical models are shown in Figure 7.3.

7.5.2 Disk Chemistry

We employ a time-dependent chemical code specifically tailored to the disk chemical environment (*Fogel et al.*, 2011). The code solves the input reaction network based on the input disk physical parameters and initial chemical abundances. The baseline chemical reaction network of *Fogel et al.* (2011) is built from the OSU gas-phase network (*Smith et al.*,

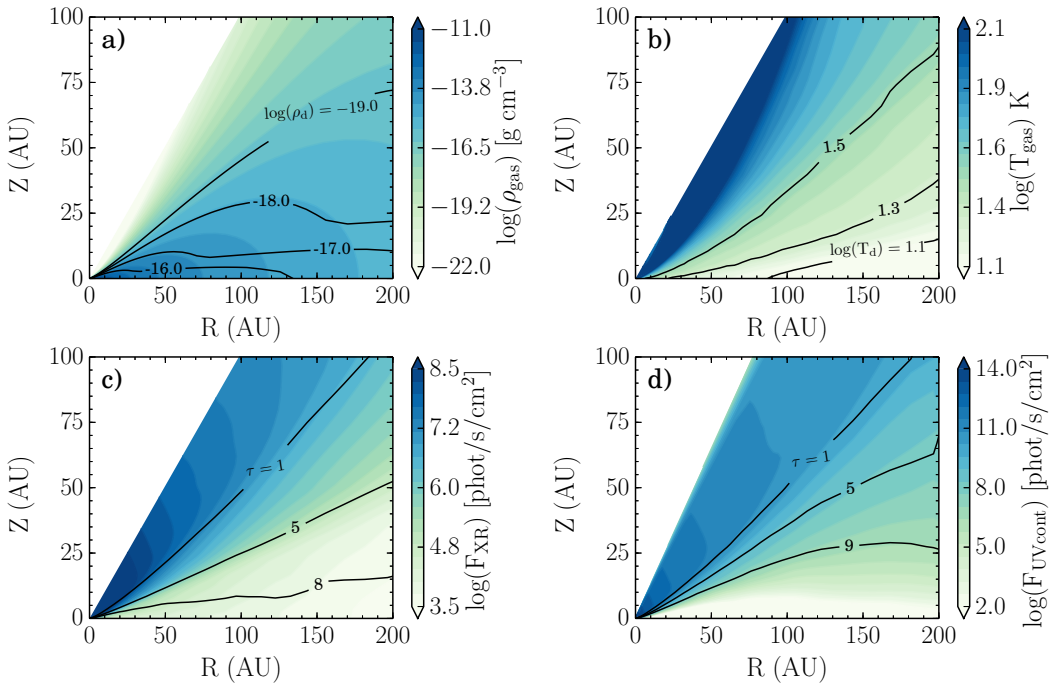

Figure 7.3 TW Hya physical model constrained from the SED and HD observations (see Appendix F). The filled contours in panels a) and b) are the gas density and temperature, respectively. The overlaid contour lines in a) and b) show the corresponding dust density and temperature. Panel c) plots the integrated X-ray flux between 1-20 keV with lines of wavelength integrated optical depth over plotted. Similarly, panel d) shows the wavelength integrated UV flux along with corresponding UV optical depth.

2004) and includes neutral-neutral, ion-neutral, ion recombination with grains/electrons, freeze-out, thermal and non-thermal desorption via UV photons and CRs, photodissociation, photoionization, X-ray induced UV, self-shielding of CO and H_2, and water and H_2 grain-surface formation. The expanded network (Chapter 6) also includes simple deuterium reactions to form H_2D^+ and HDO, and self-shielding of HD and D_2. The grain-surface formation reactions are also extended in the present work to include additional pathways for grain surface chemistry in the formalism of *Hasegawa et al.* (1992a) for a small subset of species (77 reactions total), forming H_2/HD/D_2, H_2O/HDO, H_2CO, CH_3OH, CH_4, CO_2, N_2, N_2H_2, HNO, NH_3, HCN, OCN, and H_2CN. The total network includes 6284 reactions and 665 species. The initial chemical abundances input into our model are discussed in Appendix E (see Table E.1).

We constrain the CO and nitrogen abundances using observations of CO and HCN (see Appendix E for more details). Regarding CO, motivated by the results of *Favre et al.* (2013) where CO is highly depleted in $\geq$ 20 K gas by $1-2$ orders of magnitude, we manually change (reduce) the initial CO abundance until our models reproduce the CO isotopologue observations after 1 Myr of chemical evolution. Chemical processes within the disk naturally remove CO from the gas over time by converting CO into more complex carbon-bearing ices (*Bergin et al.*, 2014); however, we find that starting with a "normal" CO abundance of $\chi(\mathrm{CO}) = 10^{-4}$ and allowing the chemistry to evolve over $3-10$ Myr does not alone sufficiently reduce the CO abundance to match the observed $C^{18}O$ and ^{13}CO observations. This finding implies that some type of additional CO depletion is necessary. Possible mechanisms include CO chemical conversion to organic ices at even earlier stages, prior to disk formation (i.e., the disk does not start out with $\chi(\mathrm{CO}) = 10^{-4}$) or, alternatively, freeze-out of CO-derived ices in the disk combined with rapid settling of large, ice-coated grains to the midplane, which can remove carbon and oxygen from the upper layers of the disk. With our present simple reduction models, we confirm the low gas-phase CO abundance posited in *Favre et al.* (2013), where we derive a CO abundance of $\chi(\mathrm{CO}) = 10^{-6}$ relative to H_2 (traced by HD).

The chemical calculations are explicitly non-equilibrium, and as such, there is some uncertainty on what "chemical time" to adopt when comparing model results with observations. Time "zero" in the chemical code corresponds to a fixed physical structure with uniform input abundances set by Table E.1 at every location in the disk. As time progresses there is a net gas-phase depletion because there are several "sinks" in the network, where energetic He^+ atoms break molecular bonds and gradually form more complex species with higher grain-surface binding energies than the parent molecule (for the case of CO, see *Bergin et al.*, 2014, and §E.1).

The time for this sequestration process is related to the freeze-out time, which is directly proportional to the typical size of grains assuming a constant gas-to-dust mass ratio (e.g., *Aikawa et al.*, 1996). Specifically, larger grains have less surface area per unit volume of gas than smaller grains, i.e., the total surface area per unit volume is $\sigma_g(r)n_g(r_g) \propto r_g^2 r_g^{-3.5} = r_g^{-1.5}$, where n_g is the volume number density of grains and σ_g is the surface area of a single grain. Therefore, as grains grow larger, the surface area of grains drops and molecule collisions with grains are less frequent, slowing down the chemical time for freeze-out. Likewise, settling removes some fraction of the dust mass from the upper layers and correspondingly, dust surface area, also slowing down the rate of subsequent freeze-out. Grain growth and settling therefore slow the chemistry's natural tendency to sequester volatiles into more complex ices, and an old disk with large grains can look like a young disk with small grains. Thus grain growth can reduce the "chemical age" as compared to the physical (stellar) age.

In the present model, owing to the settled nature of the disk, we reduce the "chemically active" surface area of grains to 3% of its standard value, i.e., compared to a uniform gas-to-dust mixture (mass ratio of 100) and grains typically $r_g = 0.1$ μm in size, the default assumption of the *Fogel et al.* (2011) model. Because the typical grain surface area is a single parameter in the model, we cannot increase the surface area in the midplane where the larger ($\geq$ 1mm) grains will collect. However, these larger grains contribute negligibly to the surface area compared to the small grains, which are also present throughout the

midplane (e.g., *Dullemond and Dominik*, 2004). This change in grain surface area increases the time-scale for freeze-out by a factor of ~ 30.

Taking these factors into consideration and the unknown age of the TW Hya star and disk system of $\sim 3 - 10$ Myr (*Barrado Y Navascués*, 2006; *Vacca and Sandell*, 2011), we opt to examine the time-evolved chemical abundances at 1 Myr, when the ion-chemistry has leveled to an approximate steady-state. Because we cannot take into account the time-evolving grain size and its changing spatial distribution simultaneously with the time evolution of the chemistry along with uncertainties in stellar ages, calibrating the chemical evolution using molecular line observations is a better approach to assessing the current evolutionary state of the TW Hya molecular gas disk. In this light, the present model is verified as appropriate to the current chemical evolutionary stage of TW Hya using neutral gas constraints, CO and HCN, as described in Appendix E.

7.5.3 Ionization

The primary sources of ionization considered in this work are X-rays, CRs, and UV photoionization. X-rays and CRs are the most important for the ionization of the dense molecular gas, where both are capable of ionizing H_2 and helium. Both the incident CR flux and the implementation of X-rays (motivated by X-ray observations of the source) are the primary free parameters of our modeling efforts and are described in detail below. We *do not* include the ionization contribution from the decay of SLRs, owing to the advanced age of TW Hya (3-12 Myr; *Webb et al.*, 1999; *Barrado Y Navascués*, 2006; *Mentuch et al.*, 2008; *Vacca and Sandell*, 2011; *Weinberger et al.*, 2013) and its relative isolation from recent massive star formation, though see §7.6.3 for additional discussion.

7.5.3.1 CR Ionization

The CR ionization rate, $\zeta_{\rm CR}$, is a free parameter in the present study, where we have adopted the results of Chapter 4 to construct five input cosmic ray models. These models

Table 7.2. Incident CR model ionization rates, $\zeta_{\rm CR}$.

Model	ID	$\zeta_{\rm CR}$
Moskalenko et al. (2002)	M02	6.8×10^{-16} s^{-1}
Webber (1998)	W98	2×10^{-17} s^{-1}
Solar System Minimum	SSM	1.1×10^{-18} s^{-1}
Solar System Maximum	SSX	1.6×10^{-19} s^{-1}
T Tauri Minimum	TTM	7.0×10^{-21} s^{-1}

consist of empirically motivated CR particle spectra and include self-consistent energy decay with depth (i.e., surface density). The CR attenuation is taken in the vertical direction for ease of calculation in the chemical models. In Table 7.2 we provide the incident CR ionization rate at the surface of the disk (prior to attenuation by the gas itself). Details regarding the calculation of $\zeta_{\rm CR}$ and the functional form of the decay with surface density can be found in Chapter 4. In summary, the *Moskalenko et al.* (2002) (M02) ionization rate is similar to that determined for the diffuse ISM, the *Webber* (1998) (W98) rate is consistent with values for the dense, molecular ISM, and Solar System Minimum (SSM) and Solar System Maximum (SSX) are the present day CR fluxes at 1 AU. T Tauri Minimum is an "extreme" modulation case, extrapolated from the solar values.

7.5.3.2 X-ray Ionization

The efficiency of X-rays to ionize a disk depends both on the total flux and the hardness of the spectra. TW Hya has a substantial measured X-ray luminosity of $L_{\rm XR} \sim 2 \times 10^{30}$ erg cm^{-2} s^{-1} (e.g., *Kastner et al.*, 1999; *Raassen*, 2009; *Brickhouse et al.*, 2010), assuming a distance of $d = 55$ pc. This flux has been observed to double or triple during X-ray flares over periods of hours (*Kastner et al.*, 2002; *Brickhouse et al.*, 2010) at a cadence of less than a day (*Kastner et al.*, 1999).

The quiescent state X-ray spectrum is well-fit by a two temperature plasma model with characteristic temperatures of $2 - 3$ MK and $10 - 12$ MK (*Kastner et al.*, 1999; *Brickhouse*

et al., 2010), which are associated with X-ray emission from the accretion shock (*Calvet and Gullbring*, 1998; *Kastner et al.*, 1999, 2002; *Stelzer and Schmitt*, 2004; *Brickhouse et al.*, 2010; *Dupree et al.*, 2012), and coronal emission from hot plasma (e.g., *Lamzin*, 1999; *Güdel and Telleschi*, 2007; *Brickhouse et al.*, 2010), respectively. During flares, hints of a hard X-ray excess have been observed by *Kastner et al.* (1999). *Kastner et al.* (2002) and *Brickhouse et al.* (2010) also found that during independent flaring events, harder energy bands and high temperature diagnostics were affected by the flare while the soft component was not.

Despite the exquisite data available on X-ray fluxes and spectra toward TW Hya, its impact on ionization and chemistry is highly uncertain. First, the shape of the spectrum beyond $E_{\rm XR} \sim 3$ keV (the very photons that ionize the bulk gas) in both the quiescent and flaring states is not directly known. Second, the variability of the X-ray flux and possibly spectrum occurs on small enough time scales that the chemistry may not be able to reset between flares, and may thus reflect the flared state of TW Hya dependent on the relevant timescales. For ion chemistry the relevant time scale is the electron recombination rate. The typical electron recombination rate coefficient is of order $\alpha_{\rm rec} \sim 1 \times 10^{-7}$ cm^3 s^{-1}. The electron density at the inner disk surface, $R = 30$ AU, $Z = 12$ AU (i.e., above the $\tau_{\rm XR} \sim 1$; Figure 7.3), is approximately $n_e \sim 10$ cm^{-3}, resulting in a recombination time of $t_{\rm rec} \sim (\alpha_{\rm rec} n_e)^{-1} = 12$ days. Therefore, if the flaring time scale is on the order of days, the chemistry may not have time to "reset" between flares.

To address this issue, we treat the X-ray flux and spectrum as a free parameter in our model. We construct four low-resolution X-ray templates with XSPEC[7], where the baseline "quiescent" X-ray model is the two component plasma model (raymond) derived by *Kastner et al.* (1999), with 1.7 MK and 9.7 MK components (these components are similar to those found in the detailed spectroscopic study of *Brickhouse et al.* (2010)). The luminosity in the quiescent template is $L_{\rm XR} = 1.5 \times 10^{30}$ erg cm^{-2} s^{-1}. To approximate the X-ray flaring state,

[7]http://heasarc.gsfc.nasa.gov/xanadu/xspec/.

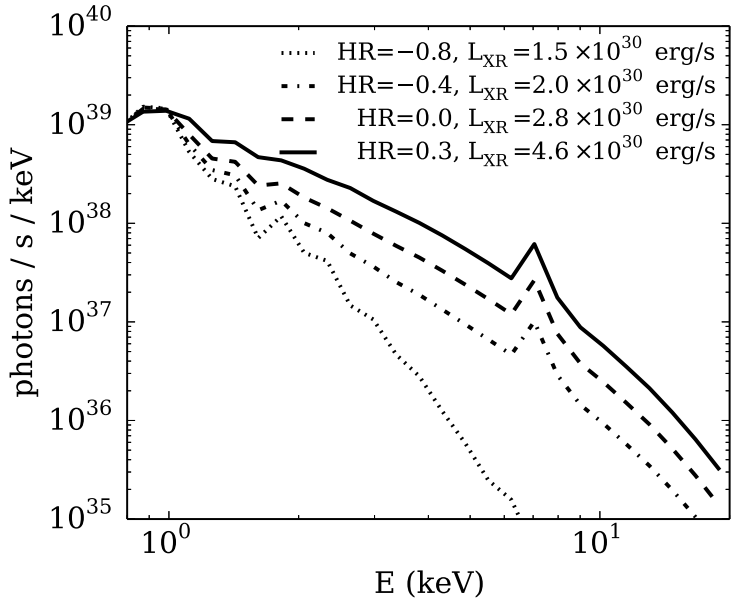

Figure 7.4 Template X-ray spectra for the ionization model grid, where the softest X-ray spectrum (i.e., the quiescent template), HR = −0.8, is motivated by the observations of *Kastner et al.* (1999, 2002), while the other spectra are artificially hardened to simulate different degrees of "flaring" spectral states.

on top of the quiescent spectrum we add an artificial hard component at 4 keV, changing the relative amounts of hard-to-soft X-rays and thus decreasing the overall spectral slope (Figure 7.4).

We fix the soft X-ray flux at 1 keV across the four spectra based upon the results that the low temperature, softer X-ray component is unaffected by the observed flares. Between the four spectra considered here, the integrated X-ray luminosity changes by a factor of just ~ 3 (see Figure 7.4 legend); however, the specific flux at the hard X-ray tail ($E_{\rm XR} \gtrsim 5$ keV) changes by an order of magnitude. All but the highest energy flaring spectrum are consistent within the error bars of the data presented in *Kastner et al.* (1999). We identify the four models by their X-ray hardness ratio, which is defined as the ratio $(L_{\rm soft} - L_{\rm hard}) \,/\, (L_{\rm soft} + L_{\rm hard})$ where $L_{\rm soft}$ is the X-ray luminosity between $0.5 - 2.0$ keV in erg s^{-1} and $L_{\rm hard}$ is the equivalent between $2.0 - 10$ keV. More negative numbers are soft X-ray dominated, while more positive numbers are hard X-ray dominated.

We calculate the X-ray propagation throughout the disk for energies of $E_{\rm XR} = 1 -$

20 keV in 1 keV intervals as described in Chapter 4 with the Monte Carlo code presented in *Bethell and Bergin* (2011a). The absorption cross-sections are provided in *Bethell and Bergin* (2011b) and the X-ray scattering is dominated by Thompson scattering. Next, we apply the template spectra in Figure 7.4 to determine the X-ray radiation field as a function of energy and position within the disk, which is the input for the chemical calculations. The X-rays primarily ionize H_2 and He, where we adopt the ionization cross-sections provided in *Yan et al.* (1998), integrated over the local X-ray spectrum. The same *Bethell and Bergin* (2011a) code is also used for the UV calculations (see Chapter 6 for our treatment of the Lyman-α transfer and §D.2). The energy-integrated X-ray and UV field ($930 - 2000$ Å) are shown in Figure 7.3c and 7.3d, respectively, along with their total optical depth.

7.5.4 Line Radiative Transfer and Synthetic Observations

The set of five CR models (§7.5.3.1) and four X-ray models (§7.5.3.2) forms a grid of twenty different ionization profiles for a fixed physical (density and temperature) structure (Appendix D). For each model, we calculate the time-dependent chemistry as described in §7.5.2. To enable model-data comparison, we then calculate the emergent line emission from the abundances and model physical conditions assuming a distance of $d = 55$ pc and, for cases where spatial filtering cannot be excluded, we also simulate the particular observations.

The line radiative transfer is computed using the LIME code (*Brinch and Hogerheijde*, 2010) in non-LTE where available[8]. We consider two components to the gas velocity: i) Keplerian rotation around the star based on the stellar mass and viewing geometry ($i \sim 7°$) and ii) the gas turbulent velocity, i.e., the doppler-B parameter. We adopt a turbulent velocity of 40 m s^{-1} based on the observed upper limit from *Hughes et al.* (2011). The end product of the LIME simulations are data cubes, i.e., two dimensions on the plane of the sky and a third in velocity. Since carbon and oxygen isotopologues are not considered

[8]Collisional rates for HCO^+, $H^{13}CO^+$ and N_2H^+ are compiled at the Leiden LAMDA database (*Schöier et al.*, 2005), where the primary literature for the spectroscopic data is *Anderson et al.* (1977); *Sastry et al.*

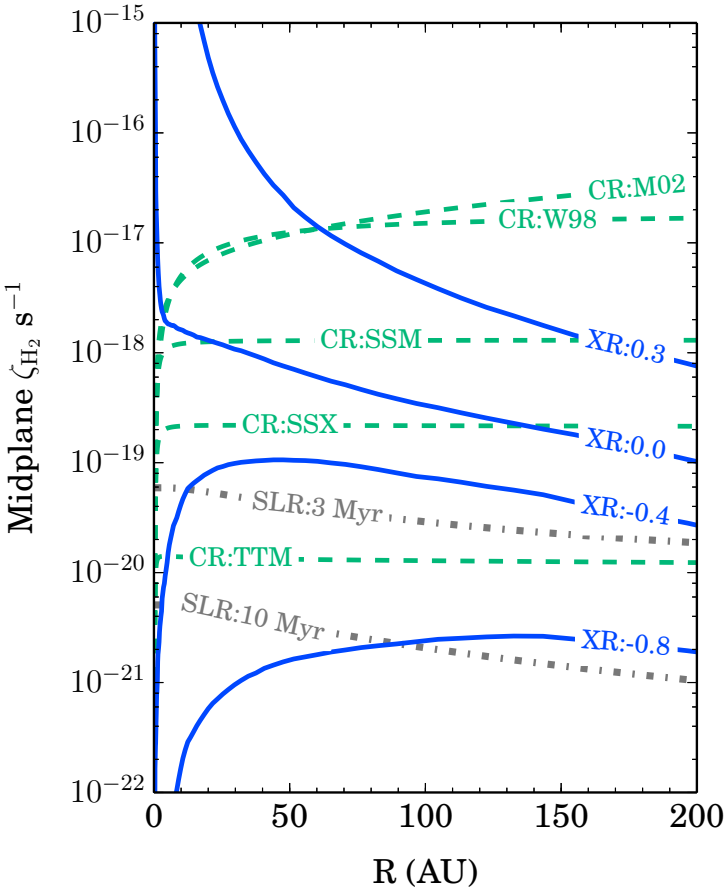

Figure 7.5 H_2 ionization rate in the midplane ($z = 0$ AU) due to X-rays (XR), cosmic rays (CR) and short-lived radionuclides (SLR). Incident (unattenuated) CR fluxes are listed in Table 7.2. X-rays are labeled by their hardness ratio (see also Figure 7.4 for the incident spectra). SLR rates are determined from the initial solar nebular abundances with the indicated decay time (and no late stage injection).

independently in the chemical network, their abundances are calculated based on the main isotopologues using a fixed ratio of $^{12}C/^{13}C = 70 \pm 10$ and $^{18}O/^{16}O = 540 \pm 30$ (*Henkel et al.*, 1994; *Prantzos et al.*, 1996) appropriate for the local ISM. For all lines, we simulate the line and continuum emission simultaneously with the dust and gas co-spatial within the framework of the physical model. We then use self-consistent dust opacities from the radiative transfer and UV modeling, and then subtract off the continuum emission when comparing the line fluxes.

The calculated line emission fluxes are compared to observations to determine the goodness of fit of the chemical simulations. This can be done directly using the LIME output for lines observed for the observations that have sufficient short spacings to not have any flux resolved out, marked as 'Recover all?'='yes' in Table 7.1. Exceptions to this are the $(4-3)$ rotational lines of HCO^+, $H^{13}CO^+$, and N_2H^+. For these lines, we make synthetic observations using the `simobserve` task in CASA[9] and the specific array configurations used for these SMA and ALMA observations. The HCO^+ $(4-3)$ and N_2H^+ $(4-3)$ were both observed as part of ALMA Early Science operations, where the former was a Science Verification target and the latter was reported in *Qi et al.* (2013b). Because the array configurations during these observations were non-standard, we used the original data to create the observation specific array configurations for the `simobserve` task. From the simulated visibilities we reconstruct the on-sky image using `clean` with natural weighting. The simulated beam from the reconstructed images is $(4.1'' \times 1.97'')$ and $(0.66'' \times 0.56'')$ for HCO^+ $(4-3)$ and N_2H^+ $(4-3)$, respectively, which are in good agreement with the beams from the observations (see Table 7.1). Likewise, the CASA simulations for the SMA $H^{13}CO^+$ $(4-3)$ with a beam of $(4.1'' \times 1.97'')$ reasonably agrees with the observed beam.

For all lines except HCO^+ $(3-2)$ and N_2H^+ $(4-3)$, we only compare spatially/spectrally integrated line fluxes. To determine quality of fit, we combine the uncertainties on the

(1981); *Botschwina et al.* (1993); *Flower* (1999).

[9]http://casa.nrao.edu/

original observations in quadrature with a 10% uncertainty from the stochastic point-casting uncertainty of the LIME code (*Brinch and Hogerheijde*, 2010). For the uncertainty of the two $H^{13}CO^+$ rotational lines, we also include a 14.3% uncertainty for the isotopologue ratio of $^{12}C/^{13}C = 70 \pm 10$.

For the best spatially resolved data, HCO^+ $(3-2)$ and N_2H^+ $(4-3)$, we directly compare the observed emission profile on the plane of the sky to the model emission profile. To assess the fit to the model emission profiles, we measure the difference between the model and observed line fluxes in units of the integrated σ (Jy/beam km s^{-1}) over the angular extent of the disk. From this difference, we determine the radial difference in units of the uncertainty on the line flux, $\sigma(R)$. From this profile, we determine a disk-averaged σ between the model and observation by integrating over the disk area, $\int 2\pi\Delta\sigma(\theta)\theta d\theta / \int 2\pi\theta d\theta$, which implicitly weights towards the outer disk because it covers more of the total emission area. For both HCO^+ $(3-2)$ and N_2H^+ $(4-3)$ we integrate out to $\Delta\theta = 3''$ from the stellar position, beyond which the emission drops off substantially.

7.6 Results

7.6.1 HCO^+ Spatial Distribution

The HCO^+ $(3-2)$ velocity integrated line emission for the combined data set and the VEX data set are shown in Figure 7.1 together with the simultaneously observed continuum data. The VEX data clearly deviates from axisymmetry, and while less pronounced, this deviation is also recovered in the combined image. The VEX emission excess is separated from the phase center by the size of the $\sim$25 AU beam and seems to be unresolved. In the combined image, the feature shows up as a 3σ enhancement as compared to the emission profile across the rest of the disk at the same radial distance. The emission contributes approximately $\sim 15-20\%$ of the overall disk-integrated HCO^+ $(3-2)$ flux, which is a substantial amount of the total emission confined to a very small region. The possible origin of this asymmetry is

discussed in §7.7.3. While the asymmetry is not the focus of the present Chapter, equipped with this additional spatial information, we are able to exclude the southwest quadrant from the ionization fitting as it does not reflect the majority of the disk properties. The three other quadrants are assumed to be representative of the axisymmetric HCO^+ $(3-2)$ emission profile. The remaining HCO^+ lines, $(1-0)$, $(4-3)$ and the isotopologues, were observed at lower spatial resolution (see Table 7.1, and as a result, we are unable to correct their emission for such an asymmetry if it is a long-lived feature. These observations highlight the utility of high spatial resolution observations even for the study of bulk gas chemical properties.

7.6.2 Model Grid Results

The contribution of the different X-ray and cosmic ray models to the disk midplane ionization level is shown in Figure 7.5. We also plot the contribution from two SLR realizations assuming an age of 3 Myr and 10 Myr with Solar System-like initial SLR abundances (see Chapter 5 for details). The relative importance of CR and X-rays for H_2 ionization clearly depends both on the CR attenuation and the X-ray hardness. In its quiescent state, even the most attenuated cosmic rays dominate the X-ray ionization level throughout the disk. Moderate hardening/flaring of the X-ray spectra results in an X-ray dominated ionization profile in the inner disk, and for the hardest X-ray spectra, X-rays drive ionization throughout the disk for all cases with any CR attenuation. SLRs only contribute to the ionization level if the CRs are extremely attenuated and the star displays no X-ray flaring activity, justifying their exclusion from the model calculations.

Figure 7.6 shows the chemistry model results in terms of HCO^+ and N_2H^+ radial column density profiles for the full grid of models i.e. the grid of 4×5 X-ray and cosmic ray flux levels. Increasing X-ray hardness generally increases the HCO^+ and N_2H^+ column densities. CR ionization does not strongly affect the HCO^+ column profile but does change the shape of N_2H^+, going from more centrally peaked column densities to radially flatter with increasing CR flux, similar to what was seen in the parameter study in Chapter 6 for a generic T Tauri

disk model.

7.6.3 Constraints on Ionizing Agents

From the chemical models discussed in the previous section and the emission line analysis detailed in §7.6.2, we can now compare the observations in Table 7.1 to the simulated molecular emission. The agreement between models and observed data is evaluated based on disk integrated fluxes for all lines except HCO^+ $(3-2)$ and N_2H^+ $(4-3)$, where the latter are fit based upon their radial emission profile (§7.5.4). The results of this comparison are presented in Figure 7.7. For each considered emission line, agreement is classified as within 1σ, 2σ, 3σ or as a poor fit between the observation and model. We also classify the overall quality of fit to each model in terms of 1) midplane ionization as probed by N_2H^+ lines and 2) surface ionization tracers, i.e. HCO^+ lines. Finally, the total quality of fit is determined based on the fit to midplane and surface ionization levels weighted equally, which implies that individual N_2H^+ lines are weighted more heavily than individual HCO^+ lines for the final metric. Based upon these numbers, the best fit and acceptable fit models to both surface and midplane tracers are boxed in Figure 7.7.

Interestingly, all of the acceptable models have *sub-interstellar CR ionization rates*, $\zeta_{\rm CR} \lesssim 10^{-18}$ s^{-1}. The best fit models, SSX and TTM, have $\zeta_{\rm CR} \lesssim 10^{-19}$ s^{-1}. Additionally, these two models also have an X-ray spectral hardness ratio of -0.4, which is harder than TW Hya's quiescent X-ray state, -0.8, from the modelled observations of *Kastner et al.* (1999). This result implies that the chemistry seems to reflect an elevated X-ray ionization state perhaps as a result of the well-characterized frequent flaring behavior of the star (*Kastner et al.*, 2002; *Brickhouse et al.*, 2010).

The quality of fit is especially apparent in the emission profile fitting of HCO^+ $(3-2)$ and N_2H^+ $(4-3)$, shown in Figures 7.8 and 7.9 and described in §7.5.4. To evaluate the model goodness of fit for the relevant wedges in Figure 7.7, the HCO^+ $(3-2)$ emission line models are convolved with a $(0.69'' \times 0.39'')$ Gaussian beam, while the N_2H^+ $(4-3)$ profile

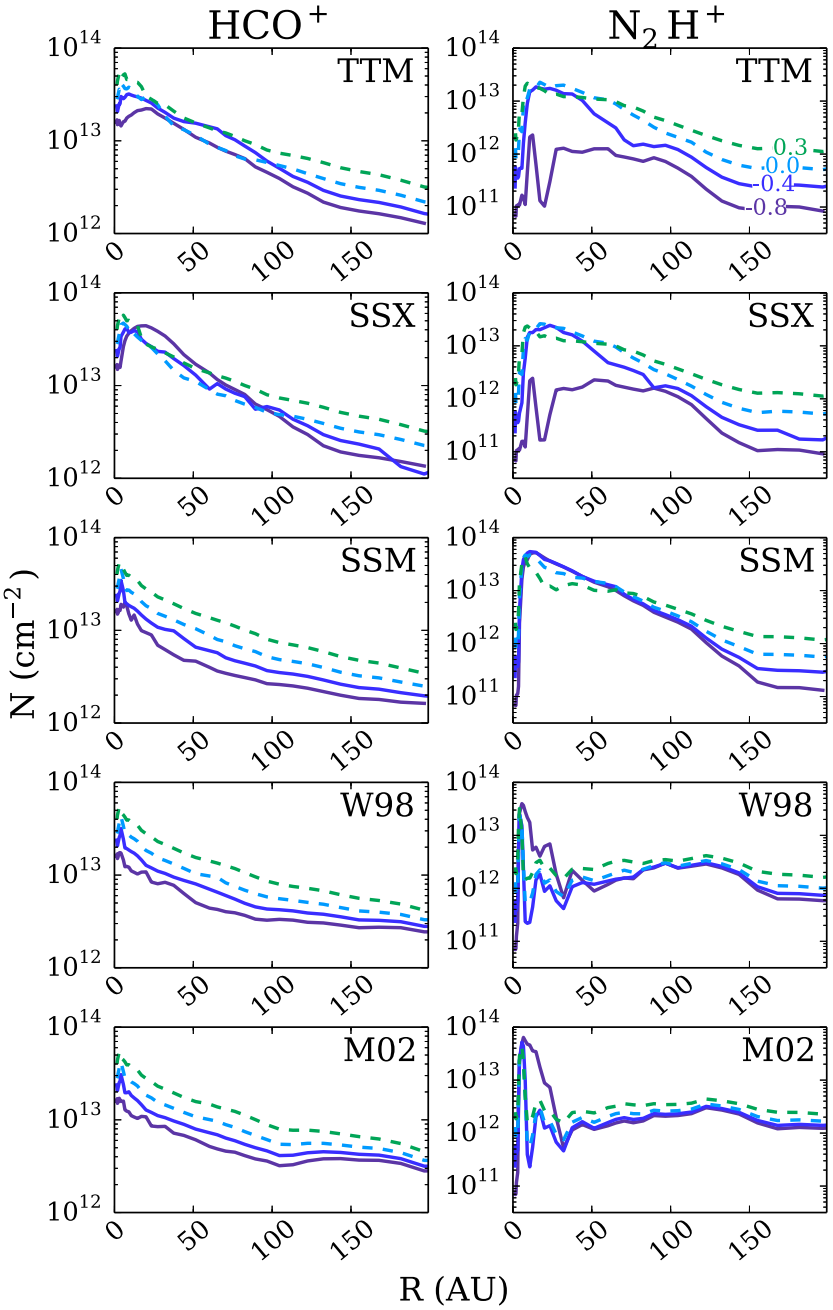

Figure 7.6 Vertically integrated column densities of HCO^+ (left) and N_2H^+ (right) versus disk radius. Individual panels show increasing CR ionization rates from top to bottom. In each panel, variations due to changes in the X-ray spectral hardness are shown by the different lines as labeled in the top right panel. The dashed lines indicate hard X-ray spectra, 0.0 and 0.3, while the solid lines are the softer X-ray spectra, −0.8 and −0.4.

is measured from the CASA simulations discussed above. Both the observations and models are averaged over deprojected annuli assuming an inclination of $i = 7°$. The HCO^+ $(3-2)$ profile excludes the southwest quadrant from the annular averaging, along with the inner $0.3''$, due to the significant asymmetry present there.

Most models reproduce the radial distribution of HCO^+ $(3-2)$, while the N_2H^+ $(4-3)$ spatial structure is more discriminatory between models. Specifically, Figure 7.9 shows that the N_2H^+ $(4-3)$ ring discovered by *Qi et al.* (2013b) is narrow and the emission drops off steeply beyond the peak at $\theta \sim 0.7''$. These observed features are only reproduced by low, modulated CR models and moderately hardened X-ray spectra. The broad N_2H^+ emission extending to large angular scales in the high CR case is due to non-thermal desorption of N_2 ice coupled with slower outer disk freeze-out times in the presence of CR ionization of H_2. This exclusion of high CR models is independent of the specifics of the assumed disk density and temperature profile (Appendix F). There is thus very good agreement between the best-fit model derived from line flux comparisons and the spatial profiles of individual lines.

It is apparent from Figure 7.7 that the best fit models reproduce the N_2H^+ emission better than the HCO^+ emission on the whole. The HCO^+ lines other than $(3-2)$ are better fit by very hard X-ray spectra (HR: 0.3) or a high CR rate and HR of 0.0 or 0.3, and the models generally under predict the HCO^+ emission for all lines except the $(3-2)$ transition. Some of this under prediction may be explained by the observed asymmetric excess in the $(3-2)$ image (Fig. 7.1), which we were able to remove from the HCO^+ $(3-2)$ flux before model-data comparison, but may contribute significantly to the other line fluxes. A second source of error is the uniform reduction of the CO abundance (see Appendix E.1). There could be substantial spatial structure in the gas-phase CO abundance distribution, which is the precursor for HCO^+ formation. A third source of error is probably the details of the temperature structure, since the optically thin $H^{13}CO^+$ lines, which should trace the column well, are better reproduced by the model than the optically thick low-spatial resolution lines,

which should trace the disk (surface) temperature. There is clearly a need for future detailed thermal structure modeling using more higher resolution HCO^+ and CO data that can be used to optimize the temperature and chemical/physical structure simultaneously.

7.7 Discussion

7.7.1 The Ionization Environment of TW Hya

From the emission modeling, we find that the CR ionization rate is substantially suppressed at all disk radii, with especially strong limits on the outer disk. One possible explanation is exclusion by young stellar winds as an analogue to the Solar System's heliosphere, i.e., a T-Tauriosphere. As was shown in Chapter 4 as well as *Svensmark* (2006); *Cohen et al.* (2012), winds from young stars should be efficient CR excluders if they operate over a large enough region of the disk. Alternatively, if such winds are highly collimated by, e.g., magnetic fields, their covering fraction may be too small to shield the disk. Whether disk winds are also capable of excluding CRs should be explored in future work. If stellar or disk winds are the primary exclusion mechanism, they must operate well beyond the outer 200 AU gas disk radius, and the corresponding T-Tauriosphere, must be at least this large (see discussion in Chapter 4).

CRs can also be repelled by mirroring via external magnetic fields linking the disk to the parent cloud, especially if there are irregularities in the field lines (*Padovani et al.*, 2013; *Fatuzzo and Adams*, 2014). Given TW Hya's relative isolation from molecular cloud material, it is uncertain whether such a large-scale environmental magnetic field exists. Turbulent magnetic fields within the disk can also act as an additional source of energy loss for the CR particles if they are present (*Dolginov and Stepinski*, 1994); however, the disk must be sufficiently turbulent (and thus MRI-active) to support such a configuration.

The ionization rate derived for the midplane gas, $\zeta_{\rm CR} \lesssim 10^{-19}$ s^{-1}, is, strictly speaking, a limit on *all* sources of ionization, including that due to SLRs and the scattered X-ray field

in the midplane. If TW Hya had similar SLR abundances to the Solar Nebula and without significant additional late-stage SLR pollution by massive stars (*Adams et al.*, 2014), the contribution from SLR ionization in TW Hya falls below the X-ray ionization rate in the midplane, or $\zeta_{\rm XR} = (2.3 - 10) \times 10^{-20}$ s^{-1}, at $\gtrsim 3$ Myr. For our best fit model, the scattered X-rays alone exceed the contribution from SLR ionization; thus further constraining the ionization rate due to SLR ionization will be difficult. Ionization tracers of the inner disk ($R < 10$ AU) midplane may help put more stringent limits on the dense gas ionization in the region where X-rays are highly attenuated and SLRs may dominate. Such small scales will be readily accessible by ALMA in the near future either with direct imaging or by using velocity information to spectrally resolve the inner disk.

The overall picture of TW Hya's relatively high surface ionization rate and ion-poor midplane is consistent with previous theoretical (e.g. *Gammie*, 1996; *Glassgold et al.*, 1997; *Igea and Glassgold*, 1999; *Semenov et al.*, 2004; *Semenov*, 2010; *Semenov and Wiebe*, 2011) and observational (*Kastner et al.*, 1997; *Qi et al.*, 2003; *Dutrey et al.*, 2007; *Öberg et al.*, 2011d) studies of disk ionization. With the IRAM Plateau de Bure Interferometry, *Dutrey et al.* (2007) conducted a search for N_2H^+ and HCO^+ (and isotopologues) to measure the ionization state of three protoplanetary disks in a similar manner to the present Chapter. While the PdBI data had lower resolution and lower signal-to-noise, the N_2H^+ observations of the three disks indicate a distinct drop at large radii, similar to what was found in the resolved TW Hya N_2H^+ $(4-3)$ observations (see Fig. 7.9). Similar to our own findings (c.f. Chapter 6), the *Dutrey et al.* (2007) chemical models with CRs show a rise in N_2H^+ column in the outer disk that is not present in the data (see their Figure 6). We attribute this rise in the models to outer disk CR ionization and decreased ion-recombination efficiency. While the lower signal-to-noise data presented in *Dutrey et al.* (2007) cannot definitively point to a CR-poor environment, these observations may hint that TW Hya's low CR environment is a common feature of protoplanetary disks.

7.7.2 Dead-zones, Dust Growth and Accretion

From our best fit ionization models we can estimate the size of the magneto-rotational instability (MRI) "dead" regions in the disk in a similar fashion to Chapter 4. In contrast to Chapter 4, we directly measure the ionization fraction from the chemical models, where the electron abundance is exactly equal to the ion abundance for a charge neutral disk. From the spatial ion abundances (equivalently the ion fraction), we estimate the magnetic Reynolds number, Re, and ambipolar diffusion coefficient, Am, to determine the approximate location of the MRI active versus dead layers. In Figure 7.10, we plot the electron abundance as filled contours.

We note that the electron abundance is slightly higher at the outer disk midplane in the present models than the steady-state estimate, $\chi_e = \sqrt{\zeta \alpha n(\mathrm{H}_2)}$, predicts because of the low densities and correspondingly longer recombination time-scales in the outer disk. We choose a critical Re for the disk to be dead as $Re \leq 3300$ (where MRI active lies outside of the area inclosed by the thick purple line), but we also show $Re = 1000$ and $Re = 5000$ on the same plot, demonstrating that the Re-determined dead-zone is not very sensitive to this choice. Critical $Am < 0.1$ (below which the disk is stable against the MRI) is indicated by the region inside of the orange lines, and is mainly confined to a layer between the highly ionized surface and the outer disk midplane outside of $R > 100$ AU (see grey contours of Fig. 7.10). Formally the disk must satisfy both $Am > 0.1$ and $Re > 3300$ to be active; however, the importance of the Am criteria is affected by the strength and direction of the disk magnetic field, which is unconstrained here. Therefore we focus on Re to approximately estimate the minimum region where the disk is dead versus active.

For the two best fit models, SSX and TTM (HR $= -0.4$), the Re criteria results in a MRI dead region that extends from the inner disk out to 50 AU and 65 AU in the midplane (see Figure 7.10). This specific zone is of particular significance as it coincides with a region of concentrated large (mm/cm-sized) grains. *Wilner et al.* (2000) reported observations of TW Hya with the Very Large Array (VLA) where 7 mm continuum emission was found

to be concentrated within a $R \sim 50$ AU radius along with an unresolved 3.6 cm detection within a $\sim 1.12'' \times 0.93''$ (62×51 AU) beam. *Wilner et al.* (2005) reported 3.6 cm continuum observations at higher spatial ($0.15''$) resolution and found that the emission was concentrated in a region of tens of AU in size. Deep 870 μm observations with the Submillimeter Array (SMA) show similar morphology, where grains are concentrated within $R \sim 60$ AU of the parent star (*Andrews et al.*, 2012), also seen in CARMA 1.3 mm observations where *Isella et al.* (2009) find a disk radius of ~ 73 AU.

The co-spatial location of the dead-zone with the large grains is perhaps not coincidental. *Gressel et al.* (2012) argue that the decrease in turbulent activity within a dead-zone leads to the survival and growth embedded planetesimals, and thus may facilitate the growth of planets. Additionally *Matsumura and Pudritz* (2005) and *Matsumura et al.* (2007) argue that the presence of dead-zones may also halt rapid inward migration, leading to long-term survival of the planetesimal bodies. We note there are certainly other explanations for the dust concentration and the sharpness of the mm-grain outer edge, in particular as a natural outcome of the velocity dependence of radial drift (c.f., *Birnstiel and Andrews*, 2014); however, a change in the disk turbulent properties resulting from a dead-zone may facilitate further dust growth via sticking collisions within this region.

If such substantial dead-zone exists, it may also pose a problem for disk accretion onto the central star. TW Hya is a relatively low accretor ($\sim 10^{-9}$ $M_\odot$ yr^{-1}; *Alencar and Batalha*, 2002; *Herczeg et al.*, 2004; *Ingleby et al.*, 2013) supporting the continued existence of its gas-disk at a relatively old age; however, accretion must nonetheless proceed. *Gammie* (1996) found that accretion can be sustained within a layer closer to the disk surface ($\Sigma_g <$ 100 g cm^{-2}, limited by CR penetration) and in this case, estimate an accretion rate of $\dot{M} \sim 10^{-8}$ $M_\odot$ yr^{-1}. Parts of the dead-zone can also potentially become "undead" when reactivated by adjacent turbulent gas (*Turner and Sano*, 2008), in which case the accretion flow in these regions is reduced compared to the active zone but is not zero. *Lesur et al.* (2014) found inclusion of the Hall effect in MHD shearing box simulations can support

efficient accretion onto the star $\dot{M} \lesssim 10^{-7}$ $M_\odot$ yr^{-1}, even for poorly ionized disks, with laminar flow through the dead zone, supporting the hypothesis that dead-zones may be beneficial to dust growth and planetesimal formation. Thus the dead-zone may not entirely inhibit disk accretion, though the relationship between massive, extended dead-zones and mass/angular momentum transfer should be studied further.

7.7.3 HCO^+ Asymmetry

Our new SMA observations reveals a significant small-scale asymmetric emission excess of HCO^+. While a detailed analysis of this particular feature is left to future work, there are a few plausible explanations for its origin. The enhancement may be related to a local change in vertical structure, either due to a asymmetric pressure bump or the crest of a spiral arm. The local increase in scale-height increases the surface area over which the disk can intercept stellar irradiation (*Jang-Condell*, 2008, 2009) including that of X-rays, leading to a local over-production of HCO^+. This scenario would also explain why the same feature does not appear in N_2H^+, which originates deeper in the disk, hidden from surface irregularities. Alternatively, the presence of an accreting protoplanet still embedded within the disk might locally heat the gas, increasing the local CO abundance near the midplane and produce deep HCO^+; however, the $(3-2)$ transition is likely optically thick and does not directly trace the dense gas where planets are expected to form. The feature may also be temporal in nature, where the same stellar X-ray flares that are known to occur with some frequency may also be related to energetic expulsions from the central star, i.e., coronal mass ejections, that may impinge upon and ionize disk gas directly. All of these scenarios are worth further explanation are beyond the scope of this Chapter, but hint at interesting chemical structure in the TW Hya disk that should be followed up with high resolution observations.

7.8 Conclusions

We have constrained the ionization environment of the TW Hya disk using molecular ion observations and a calibrated physical model of the TW Hya dust and gas circumstellar disk, on which we vary the incident ionizing flux of X-rays and CRs. We find that the ionization rate due to CRs is quite low ($\zeta_{\rm H_2} \lesssim 10^{-19}$ s^{-1}), and that the X-ray flares seem to have a lasting chemical effect on the disk. We note that the limit for the CR rate is more than two orders of magnitude less than that derived for the dense interstellar medium. We emphasize that the particular mechanism via which CR exclusion happens does not matter, but that the chemistry indicates that the CR flux is significantly lower than the canonical values throughout the full radial extent of the disk. The main results of this Chapter are summarized as follows:

1. The total outer disk ionization rate in the disk midplane is below $\zeta_{\rm H_2} \lesssim 10^{-19}$ s^{-1}. This values formally puts limits on the combined CR, SLR and X-ray ionization rate throughout the disk midplane. X-rays at the $\zeta_{\rm XR} \sim 10^{-19}$ s^{-1} level likely dominate the inner disk midplane and perhaps the outer disk at 2.3×10^{-20} s^{-1}. Due to the likely dominant contribution from scattered stellar X-rays at the midplane, it will be difficult to measure the CR and SLR ionization rate in the TW Hya disk directly. This limit implies that the CR ionization rate in the outer disk is at least two orders of magnitude below that of the ISM.

2. The HCO^+ traces a slightly flared state of TW Hya (HR: -0.4) rather than the quiescent X-ray spectrum (HR: -0.8). Additional detailed modeling of the thermal structure with resolved CO observations will help improve the fit to the optically thick HCO^+ lines, including the $(1-0)$ rotational transitions.

3. We make the first observational prediction of the dead-zone size, and based on the magnetic Reynolds' number, the expected dead-zone coincides with a region of known large grain concentration in the disk out to 60 AU. A dead-zone of this size is consistent

with the long lifetime of the gas disk in this system.

4. The HCO^+ $(3-2)$ emission reveals slight asymmetry, which alone contributes $\sim 20\%$ of the overall flux. Resolved observations, where available, are thus extremely helpful when trying to understand the bulk disk properties.

In closing, we note that this study provides the strongest constraints to date on the sources of ionization in protoplanetary disks (at least for those constraints derived from imaging observations of ionized molecular species). A wide variety of ionization sources are thought to contribute, including stellar X-rays, SLRs, CRs, and ionizing radiation from the background star-forming environment. This work shows observationally that CRs can indeed be excluded from disks, as proposed previously on theoretical grounds (see, e.g., *Padovani et al.*, 2013; *Fatuzzo and Adams*, 2014), and provides an estimate for the extent of the dead zone (compare *Gammie* (1996) with *Igea and Glassgold* (1999)). Given the availability of new instruments and facilities, this study marks only the beginning of an important research program that will provide future observational constraints on disk physics.

7.9 Acknowledgements

The authors wish to thank the anonymous referee and editor for their helpful comments. LIC and EAB acknowledge grant AST-1008800 and KO acknowledges support from the Simons Collaboration on the Origins of Life (SCOL) program. CQ acknowledges grant NASA Origins of Solar Systems, Grant Number NNX11AK63G. The Atacama Large Millimeter/submillimeter Array (ALMA), an international astronomy facility, is a partnership of Europe, North America and East Asia in cooperation with the Republic of Chile. This Chapter makes use of the following ALMA Science Verification data: ADS/JAO.ALMA#2011.0.00001.SV.

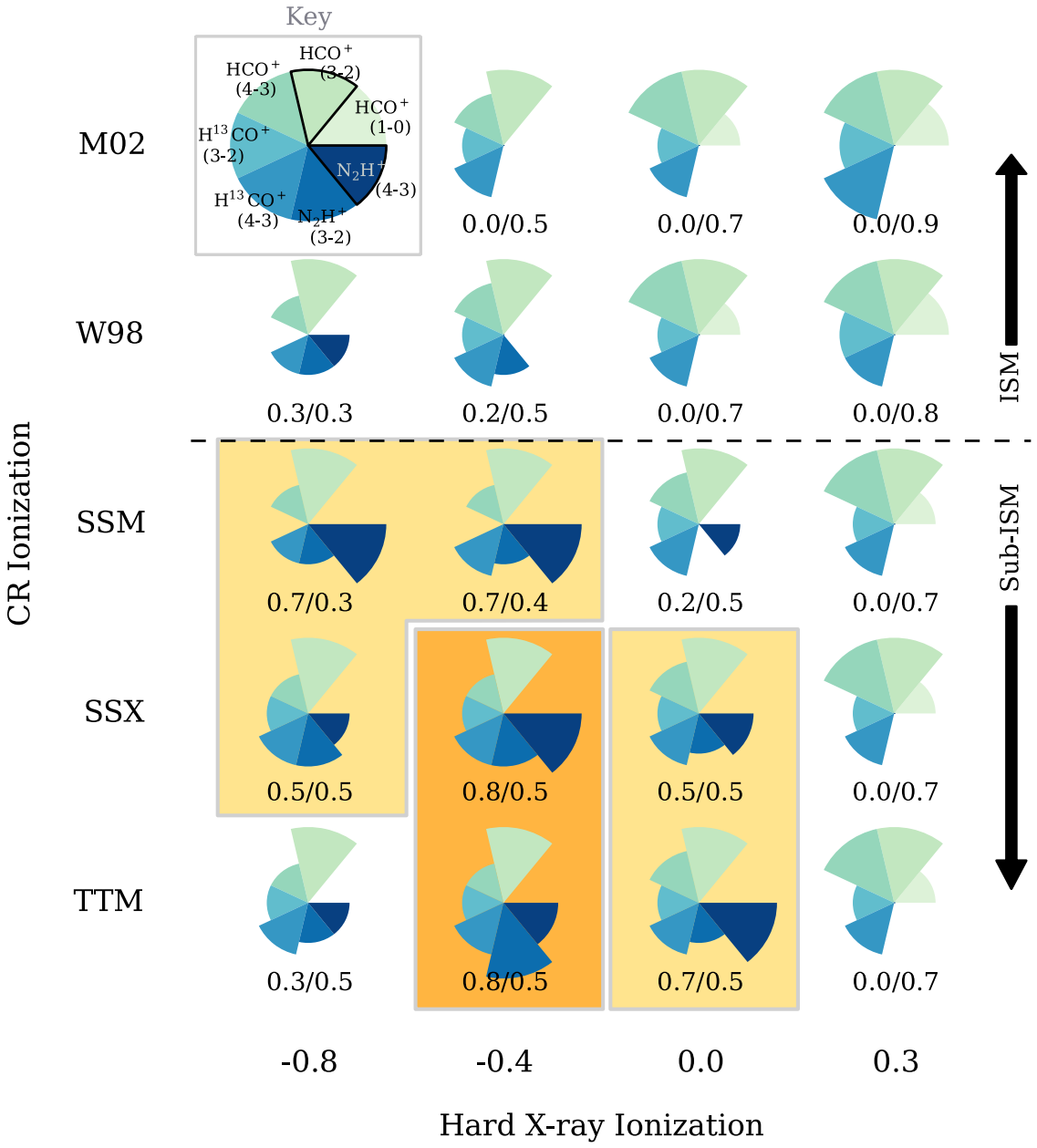

Figure 7.7 Ionization model goodness-of-fit for the lines indicated in the key (top-left). The size of the wedge indicates how closely the model matches the data, where the largest wedge matches within 1σ (i.e., the best), the second and third smaller wedges indicate the model matches the data within 2σ and 3σ of the observations, respectively. *No wedge implies the model and data do not match within* 3σ. The wedges that are boxed in black in the key indicate lines that are fit by their emission profile rather than their integrated line flux. Columns are X-ray ionization increasing from left to right (see Fig. 7.4), while rows are CR ionization decreasing from the top down (see Table 7.2). The two numbers under each pie chart measure the goodness of fit to HCO^+ and N_2H^+ line fluxes, respectively. We box in orange the best fit models, where the darkest orange corresponds to the best-fit model.

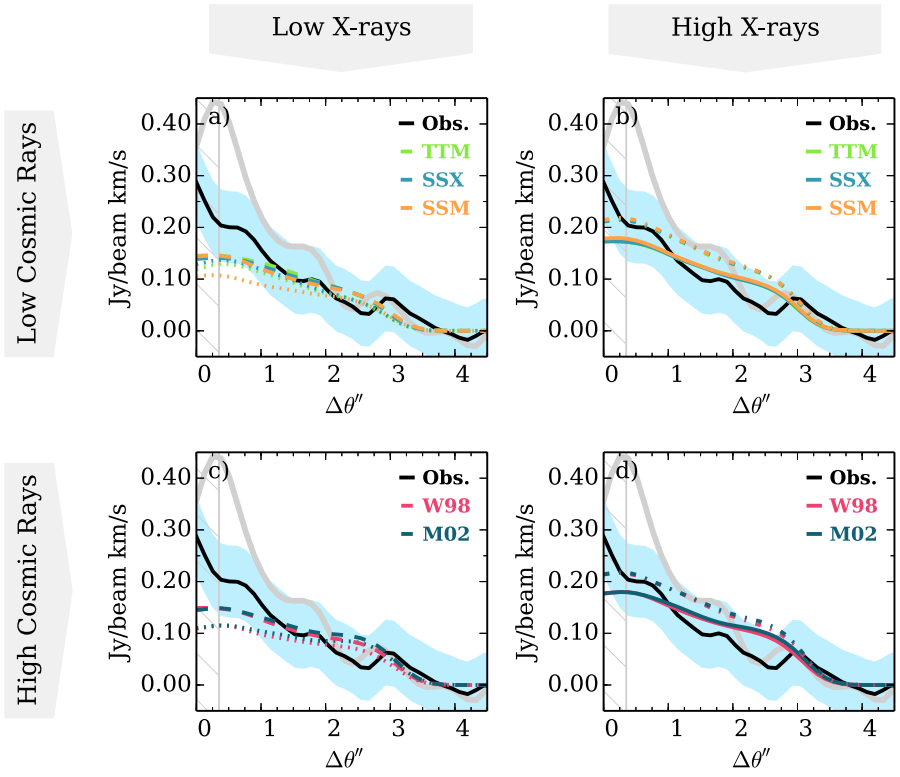

Figure 7.8 Integrated line intensity profile of HCO^+ $(3-2)$ versus angular distance from the star for the ionization models (colored lines) and the observed profile (solid black line). We have divided the models into low, modulated CR ionization rate models (top) and high, interstellar CR ionization rate models (bottom). The line style indicates the X-ray spectral hardness ratio (Fig. 7.4) where the two softer X-ray spectra are shown on the left panels: dotted (-0.8) and dashed (-0.4); and the two harder X-ray spectra are shown on the right: solid (0.0) and dot-dashed (0.3). The inner vertical region hatched in gray in the HCO^+ profiles designates the part of the disk that is contaminated by the asymmetric feature (shown as the solid gray profile), which is excluded from the fitting.

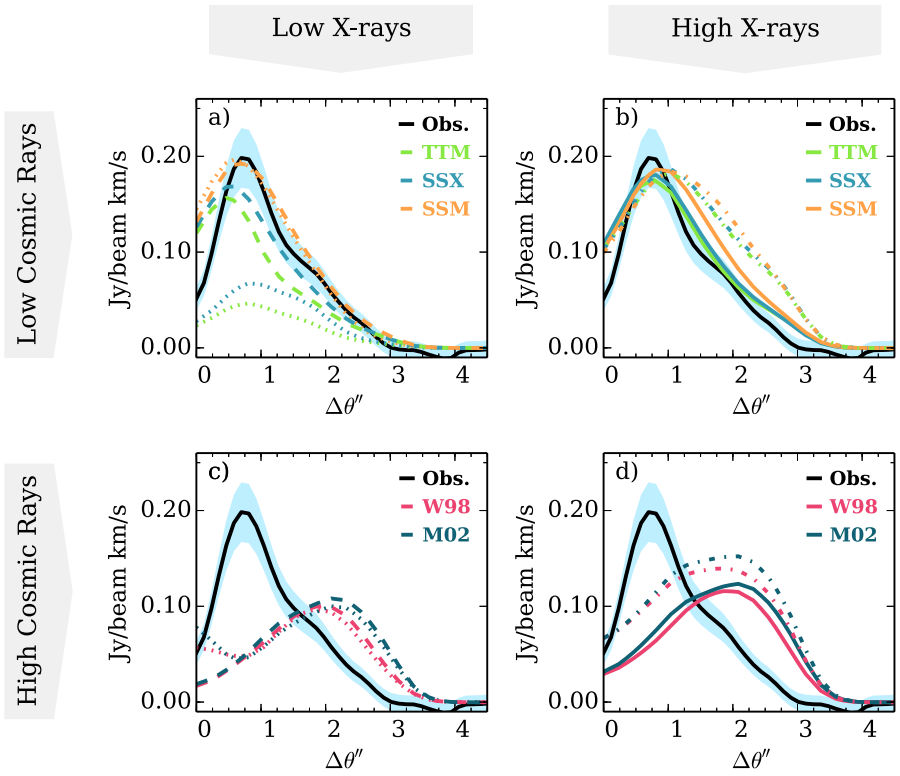

Figure 7.9 Integrated line intensity profile of N_2H^+ $(4-3)$ versus angular distance from the star for the ionization models (colored lines) and the observed profile (solid black line). The panels are divided up as in Figure 7.8. The low CR models (top) are generally a better fit to the observed N_2H^+ $(4-3)$ profile in tandem with a slightly harder X-ray profile, where the dashed line (top left panel, -0.4) or the solid line (top right panel, 0.0) provide a good fit.

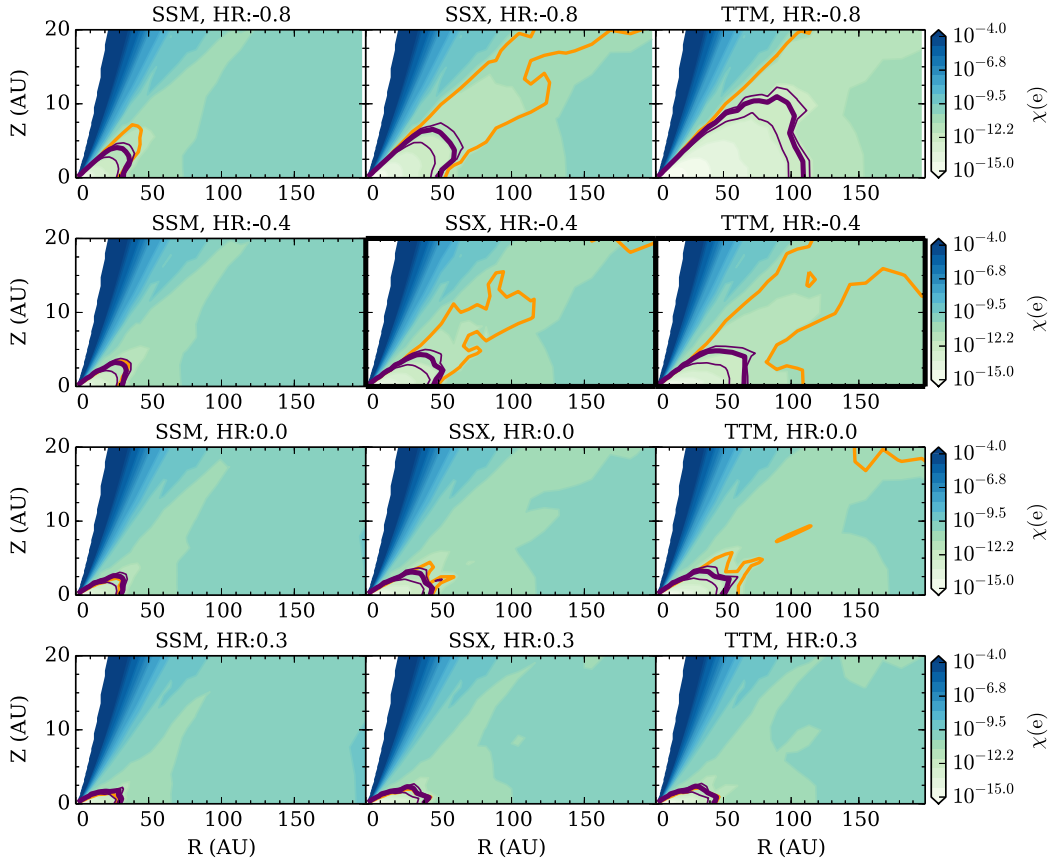

Figure 7.10 Estimates of the dead-zone size as determined from the chemical calculations (the electron abundances at 1 Myr; see Section 7.5.2). The MRI-dead region is determined from the Reynolds number ($Re < 3000$, dark purple) and from the ambipolar diffusion parameter ($Am < 0.1$, orange) following *Perez-Becker and Chiang* (2011a) and Chapter 4 of this thesis. The ambipolar diffusion criteria formally depends upon the strength of the magnetic field, which is unconstrained here, and so we emphasize that the Reynolds number (purple) provides the minimum predicted dead-zone size in this formalism. For the best fit models, the dead-zone extends to $R = 50$ AU and $R = 65$ AU for the SSX and TTM models (black-boxed panels).

CHAPTER VIII

The ancient heritage of water ice in the solar system

8.1 Preface

The following work appears in Science, Volume 345, Issue 6204, pp. 1590-1593 (2014). The work is co-authored by Edwin A. Bergin,[1] Conel M. O'D. Alexander,[2] Fujun Du,[3] Dawn Graninger,[4] Karin I. Öberg,[5] and Tim Harries.[6]

8.2 Abstract

Identifying the source of Earth's water is central to understanding the origins of life-fostering environments and to assessing the prevalence of such environments in space. Water throughout the solar system exhibits deuterium-to-hydrogen enrichments, a fossil relic of low-temperature, ion-derived chemistry within either (i) the parent molecular cloud or (ii) the solar nebula protoplanetary disk. Utilizing a comprehensive treatment of disk ionization, we

[1]Department of Astronomy, University of Michigan, 1085 S. University Ave., Ann Arbor, MI 48109
[2]DTM, Carnegie Institution of Washington, Washington, DC 20015
[3]Department of Astronomy, University of Michigan, 1085 S. University Ave., Ann Arbor, MI 48109
[4]Harvard-Smithsonian Center for Astrophysics, 60 Garden Street, Cambridge, MA 02138
[5]Harvard-Smithsonian Center for Astrophysics, 60 Garden Street, Cambridge, MA 02138
[6]Department of Physics and Astronomy, University of Exeter, Stocker Road, Exeter, EX4 4QL, UK

find that ion-driven deuterium pathways are inefficient, curtailing the disk's deuterated water formation and its viability as the sole source for the solar system's water. This finding implies that if the solar system's formation was typical, abundant interstellar ices are available to all nascent planetary systems.

8.3 Introduction

Water is ubiquitous across the solar system, in cometary ices, terrestrial oceans, the icy moons of the giant planets, and in the shadowed basins of Mercury (*Encrenaz*, 2008; *Lawrence et al.*, 2013). Water has left its mark in hydrated minerals in meteorites, in lunar basalts (*Barnes et al.*, 2014) and in martian melt-inclusions (*Usui et al.*, 2012). The presence of liquid water facilitated the emergence of life on Earth, and thus understanding the origin(s) of water throughout the solar system is a key goal of astrobiology. Comets and asteroids (traced by meteorites) remain the most primitive objects, providing a natural "time capsule" of the conditions present during the epoch of planet formation. Their compositions reflect those of the gas, dust, and – most importantly – ices encircling the Sun at its birth, i.e., the solar nebula protoplanetary disk. There remains an open question, however, as to when and where these ices formed, whether they i) originated in the dense interstellar medium (ISM) in the cold molecular cloud core prior to the Sun's formation, or ii) are products of reprocessing within the solar nebula (*Robert et al.*, 2000; *Ceccarelli et al.*, 2014; *van Dishoeck et al.*, 2014). Scenario i) would imply that abundant interstellar ices, including water and presolar organic material, are incorporated into all planet-forming disks. By contrast, local formation within the solar nebula in scenario ii) would potentially result in large water abundance variations from stellar system to system, dependent upon the properties of the star and disk.

In this work, we aim to constrain the formation environment of the solar system's water using deuterium fractionation as our chemical tracer. Water is enriched in deuterium relative to hydrogen (D/H) compared to the initial bulk solar composition across a wide range of solar system bodies, including comets, (*Bockelée-Morvan et al.*, 1998; *Eberhardt et al.*, 1995),

terrestrial and ancient Martian water (*Usui et al.*, 2012), and hydrated minerals in meteorites (*Alexander et al.*, 2012). The amount of deuterium relative to hydrogen of a molecule depends on its formation environment, and thus the D/H fraction in water, $[D/H]_{H_2O}$, can be used to differentiate between the proposed source environments. Interstellar ices, as revealed by sublimation in close proximity to forming young stars, also exhibit high degrees of deuterium-enrichment, $\sim 2 - 30\times$ that of terrestrial water (*Dartois et al.*, 2003; *Coutens et al.*, 2012; *Persson et al.*, 2012, 2014). It is unknown to what extent these extremely deuterated, interstellar ices are incorporated into planetesimals or if instead the interstellar chemical record is erased by reprocessing during the formation of the disk (*Visser et al.*, 2009b; *Yang et al.*, 2013). Owing to its high binding energy to grain surfaces, theoretical models predict that water is delivered from the dense molecular cloud to the disk primarily as ice with some fraction sublimated at the accretion shock in the inner tens of astronomical units (AU) (*Visser et al.*, 2009b). If a substantial fraction of the interstellar water is thermally reprocessed, the interstellar deuterated record could then be erased. In this instance, the disk is left as primary source for (re-)creating the deuterium-enriched water present throughout our solar system.

The key ingredients necessary to form water with high D/H are cold temperatures, oxygen, and a molecular hydrogen (H_2) ionization source. The two primary chemical pathways for making deuterated water are: (i) gas-phase ion-neutral reactions primarily through H_2D^+, and (ii) grain-surface formation (ices) from ionization-generated hydrogen and deuterium atoms from H_2. Both reaction pathways depend critically on the formation of H_2D^+. In particular, the gas-phase channel (i) involves the reaction of H_2D^+ ions with atomic oxygen or OH through a sequence of steps to form H_2DO^+, which recombines to form a water molecule. The grain-surface channel (ii) is powered by H_2D^+ recombination with electrons or grains, which liberates hydrogen and deuterium atoms that react with oxygen atoms on cold dust grains. H_2D^+ becomes enriched relative to H_3^+ due to the deuterated-isotopologue being energetically favored at low temperatures. There is an energy barrier ΔE_1 to return to H_3^+,

i.e., $H_3^+ + HD \rightleftharpoons H_2D^+ + H_2 + \Delta E_1$, where $\Delta E_1 \sim 124$ K, though the precise value depends upon the nuclear spin of the reactants and products (see Appendix G). The relatively modest value of ΔE_1 restricts deuterium enrichments in $H_3{}^+$ to the coldest gas, $T \lesssim 50$ K. Thus, deuterium-enriched water formation requires the right mix of environmental conditions: cold gas, gas-phase oxygen and ionization.

The conditions in the dense interstellar medium, i.e., the cloud core, readily satisfy these requirements, where temperatures are typically $T \sim 10$ K and ionization is provided via galactic cosmic rays (GCRs). In this regard, the conditions in the core and in the outermost regions of the solar nebula are often thought of as analogous (*Aikawa and Herbst*, 1999a). This is because the outskirts of protoplanetary disks typically contain the coldest ($T \lesssim 30$ K), lowest density gas, and are often assumed to be fully permeated by GCRs. However, the efficacy of GCRs as ionizing sources in protoplanetary disks has been called into question due to the deflection of GCRs by the stellar winds produced by young stars (Chapter 4). Even the mild, modern-day solar wind reduces the GCR ionization rate, $\zeta_{\rm GCR}$, by a factor of ~ 100 below that of the unshielded ISM. Limits on protoplanetary disks' molecular ion emission indicate low GCR ionization rates, $\zeta_{\rm GCR} \leq 3 \times 10^{-17}$ s^{-1} (*Chapillon et al.*, 2011). In the absence of GCRs, disk midplane ionization is instead provided by scattered X-ray photons from the central star and the decay of short-lived radionuclides (SLRs), where the latter's influence decreases with time (*Umebayashi et al.*, 2013). In addition, the core-disk analogy breaks down with regard to gas density. At the outermost radius of the protosolar gaseous disk, $R_{\rm out} \sim 50 - 80$ AU (Appendix G), the typical disk density is $n \sim 10^{10}$ cm^{-3}. This value is approximately five orders-of-magnitude higher than typical values within the interstellar molecular core (*Minamidani et al.*, 2011). The steady state ion abundance is proportional to $\sqrt{\zeta/n}$, where ζ is the ionization rate and n is the volumetric gas (hydrogen) density. For a constant ionization rate, a density increase of 10^5 corresponds to χ_i being a factor of ~ 300 below that expected in the ISM. Thus, wind or magnetically driven deflection of ionizing GCRs, coupled with high gas densities will strongly inhibit the disk from generating

deuterium enrichments through the standard cold chemical reactions (i) and (ii), described above.

To test the disk hypothesis, we explore whether ionization-driven chemistry within the disk alone is capable of producing the deuterium-enriched water that was present in the early solar system. We have constructed a comprehensive model of disk ionization, including detailed radiative transfer, reduced GCR ionization and SLR decay. To simulate the "reset" scenario, i.e., all interstellar deuterium enhancement is initially lost, we start with unenriched water with bulk solar D/H composition, $[\mathrm{D/H}]_{\mathrm{H_2}} = 2.0 \pm 0.35 \times 10^{-5}$ (*Geiss and Gloeckler*, 2003), and quantify the maximum amount of deuterated water produced by chemical processes in a static protoplanetary disk over 1 Myr of evolution. The goal is to determine whether or not the conditions present in the solar nebula were capable of producing at minimum the measured isotopically enriched water in meteorites, ocean water (VSMOW), and comets (see Figure 8.3). We do not attempt to address the eventual fate of this water by additional processing, i.e., by radial or vertical mixing, which tends to reduce the bulk D/H ratio in water (*Willacy and Woods*, 2009; *Albertsson et al.*, 2014).

Instead, our emphasis is on the physical mechanism necessary for D/H enrichment: ionization. We illustrate the suite of ionization processes considered in the traditional picture of disk ionization (Figure 8.3a) alongside a schematic for our new model (Figure fig:8n2b). More specifically, we include "solar-maximum" levels of GCR wind-modulation for the incident GCR rate, a factor of ~ 300 below that of the ISM, Monte Carlo propagation of X-ray photoabsorption and scattering, and ionization by SLR decay products, including losses in the low density ($\Sigma_{\mathrm{gas}} \lesssim 10$ g cm^{-2}) regions of the disk (Appendix G). The total H_2 ionization rate is shown in Figures 8.3c and 8.3d. It can be seen that while the warm surface layers ($\Sigma_{\mathrm{gas}} \lesssim 1$ g cm^{-2}) are strongly ionized by stellar X-rays, $\zeta_{\mathrm{XR}} \gtrsim 10^{-15}$ s^{-1}, the midplane is comparatively devoid of ionization due to the modulation of incident GCRs (Figure 8.3d).

To compute molecular abundances, we compile a simplified deuterium reaction network designed to robustly predict the D/H in water resulting from gas-phase and grain-surface

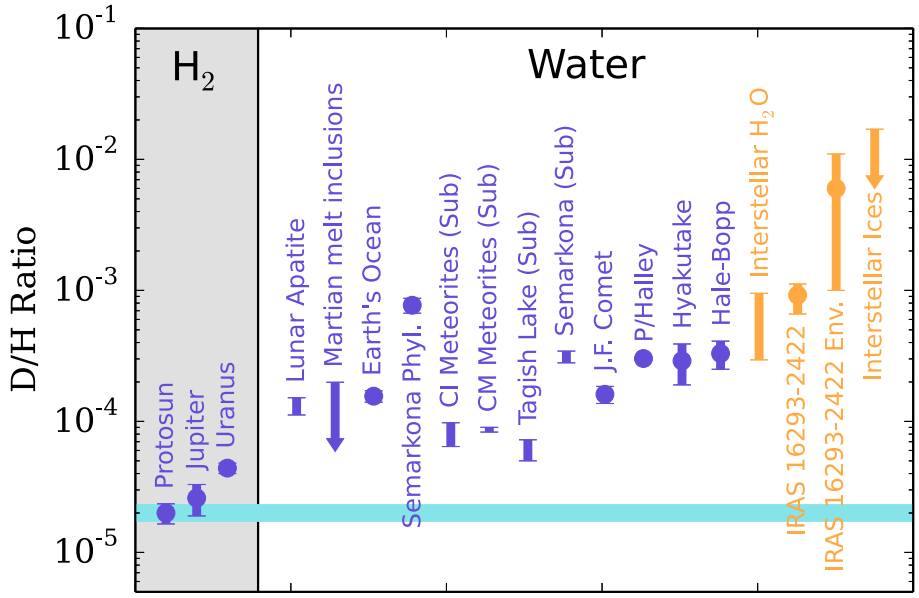

Figure 8.1 Atomic D/H ratios in solar system (*purple*) and interstellar (*yellow*) sources separated into bulk H_2 and water. Points indicate single measurements, bars without points are ranges over multiple measurements, and arrows correspond to limits. D/H in the bulk gas (i.e., solar) is indicated as a horizontal blue bar. References are provided in Appendix G, Table G.4.

chemistry (Appendix G). We include both ion-neutral and the hot-phase neutral-neutral water chemistry (*Bergin et al.*, 1995), as well as self-shielding by HD and D_2, in addition to the standard chemical network (Appendix G). We include an updated treatment of the inherently surface-dependent CO freeze-out process motivated by new laboratory data on CO ice binding energies (Appendix G). CO freeze-out is important for the present study as CO regulates the amount of oxygen present in gas above $T > 17$ K and available for new water formation. We place the majority of volatile carbon in CO and the rest of the oxygen not in CO in water ice (*Visser et al.*, 2009b) (see Appendix G for additional runs). We examine the final D/H of water ice after 1 Myr of chemical evolution, i.e., the approximate lifetime of the gas-rich disk and, correspondingly, the duration over which the disk is able to build up deuterated water (see Figure 8.3). The ions are most abundant in the upper, X-ray-dominated surface layers, whose temperatures are too warm for significant deuterium enrichment in $[D/H]_{H_3^+}$. The bulk ice mass is closest to the cold midplane, where only a

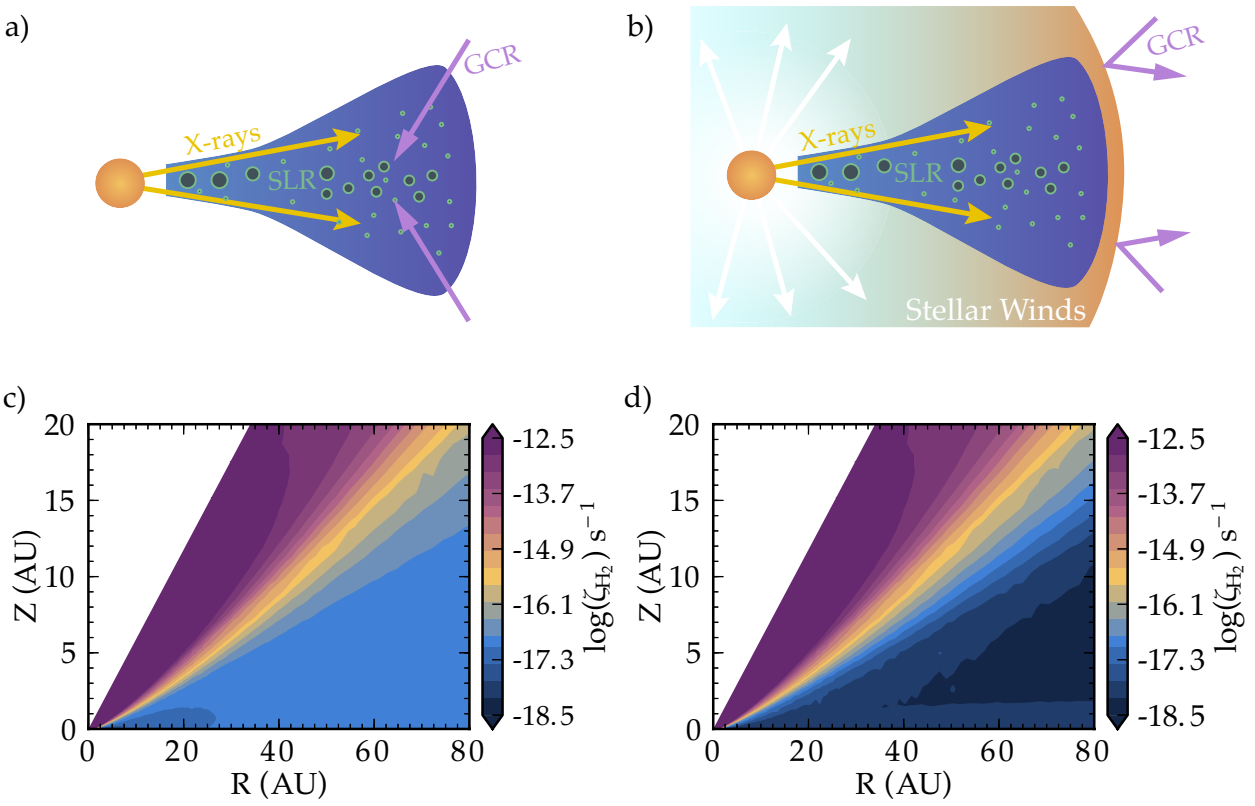

Figure 8.2 Schematic of energetic disk ionization sources (*top row*) and the calculated total H_2 ionization rate (*bottom row*). Panels are: **(a)** a "standard" disk ionization model driven by X-rays and GCRs; **(b)** ionization conditions under the influence of a Sun-like wind at solar maximum, now dominated by X-rays in the surface and SLRs in the midplane; **(c)** calculated H_2 ionization rates for the scenario depicted in Panel (a); and **(d)** calculated H_2 ionization rates from the scenario depicted in Panel (b) and that used within the present Chapter.

meager amount (per unit volume) of H_3^+ and H_2D^+ remain in the gas, a consequence of low ionization rates and high densities.

In addition to spatial abundances, we provide ratios of the vertically integrated column densities of both ions and ices (Figure 8.3, bottom). The choice of VSMOW as a benchmark is somewhat arbitrary considering that comets exceed [D/H] in VSMOW by factors of 1-3× and meteorites have typically lower values, a factor $\sim$ 2 less (Figure 8.3). The column-derived $[D/H]_{H_3^+}$ approaches – but does not reach – VSMOW after 1 Myr at the outer edge of the disk. Moreover, most of the molecules that contribute to the column density ratio of

$[D/H]_{H_3^+}$ arise in an intermediate layer of cold ($T_{\rm gas} \sim 30 - 40$ K) gas where X-ray photons are still present. However, it is readily apparent that this enrichment does not translate into $[D/H]_{H_2O}$. The most deuterium-enriched water, $[D/H]_{H_2O} = 3 \times 10^{-5}$, is co-located with the enriched layer of $[D/H]_{H_3^+}$; however, the water is considerably less enriched than the ions. Over the lifetime of the disk, the gas-phase and grain-surface chemical pathways do not produce deuterated water ices in significant quantities. The low water production is due to a combination of (i) a lack of sufficient ionization to maintain significant amounts of H_2D^+ in the gas, and (ii) a lack of atomic oxygen in the gas, locked up in ices. We do find a super-deuterated layer of water at the disk surface ($[D/H]_{H_2O} = 5 \times 10^{-3}$). This layer is a direct consequence of selective self-shielding of HD relative to H_2, which leads to an over abundance of atomic D relative to H. Selective self-shielding is also the cause of $[D/H]_{H_3^+}$ falling below the initial bulk gas value inside of $R < 40$ AU. This layer does not, however, contribute significantly to the vertically integrated $[D/H]_{H_2O}$ (bottom panels in Figure 8.3).

In summary, using a detailed physical ionization model, updated treatment of oxygen-bearing (CO) ice chemistry, and a simplified deuterium chemical network, we find that chemical processes in disks are not efficient at producing significant levels of highly deuterated water. Our model predicts that disk chemistry can only produce a volume-integrated $[D/H]_{H_2O} \lesssim 2.1 \times 10^{-5}$, which is only slightly enriched from the bulk solar value (2×10^{-5}). In terms of column density, we find that even in the most radially distant (coldest) regions water only attains $[D/H]_{H_2O} \lesssim 2.5 \times 10^{-5}$. This finding implies that ion-chemistry within the disk cannot create the deuterium-enriched water present during the epoch of planet formation. When we begin our models with interstellar $[D/H]_{H_2O} \sim 10^{-3}$, however, it is hard to "erase" D/H ratios with low-temperature disk chemistry alone. A number of studies have invoked turbulent mixing of gas in the radial and/or vertical directions, which can reduce inner-disk deuterium enrichments in water (*Willacy and Woods*, 2009; *Furuya et al.*, 2013; *Albertsson et al.*, 2014). Moreover, a common feature of such models is that they begin with high levels of deuterated water, as high as $[D/H]_{H_2O} \sim 10^{-2}$. In general,

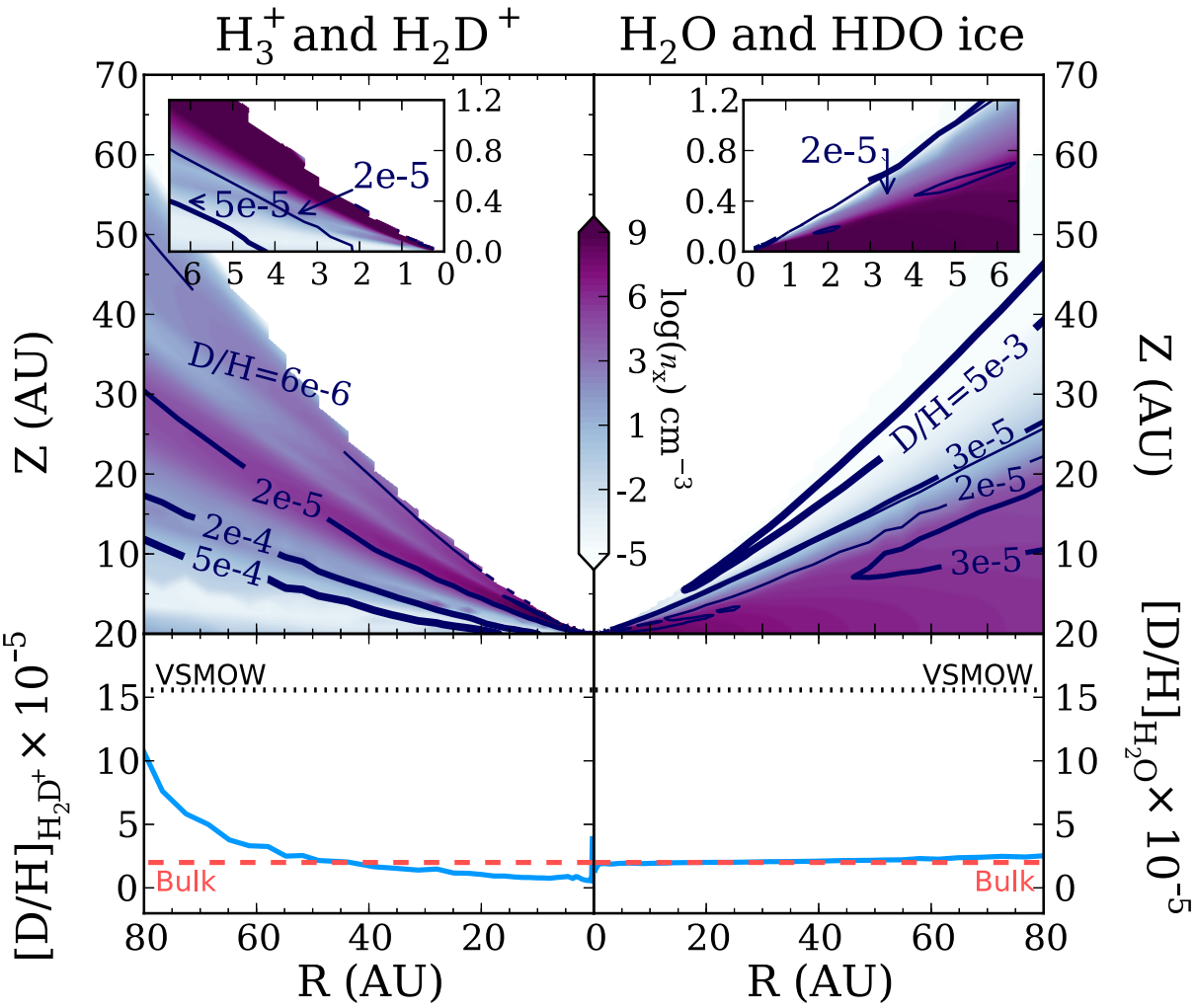

Figure 8.3 Chemical abundances and column densities for the drivers of the deuterium enrichment, the ions; and the corresponding products, the ices. Volume densities (cm^{-3}) of all labeled isotopologues for H_3^+ (left) and water (right) in filled purple contours. Solid contour lines indicate local D/H and are as labeled. The color scale applies to both the left and right halves of the plot. Insets zoom-in on the inner disk with the same axes units. Bottom panel plots show the vertically integrated D/H ratio of column densities versus radius. The bulk gas (protosolar) value is labeled by the red dashed line, and the Earth's ocean value (VSMOW) is labeled with the black dotted line.

mixing in the vertical direction transports highly deuterium-enriched ices from the shielded midplane into the X-ray and UV irradiated warm surface layers (*Ciesla and Sandford*, 2012; *Ciesla*, 2014) where they can be reprocessed to lower D/H. Ices transported radially inward, either entrained by gas accretion or subjected to radial migration, evaporate in the

warm and dense inner disk and isotopically reequilibrate with H_2 or ion-neutral chemistry in hot ($T > 100$ K) gas. With our updated disk ionization model, we can now exclude chemical processes within the disk as an enrichment source term and conclude that the solar nebula accreted and retained some amount of pristine interstellar ices. One potential explanation is that during the formation of the disk, there was an early high temperature episode followed by continued infall from deuterium-enriched interstellar ices (*Yang et al.*, 2013). If we ignore the negligible contribution to deuterated water formation from the disk, we can estimate the fraction of water in a particular solar system body, X, that is presolar, $f_{\rm ISM} = ({\rm D/H_X} - {\rm D/H_\odot}) \,/\, ({\rm D/H_{ISM}} - {\rm D/H_\odot})$, where $\rm D/H_X$ refers to $[\rm D/H]_{H_2O}$ in X and $\rm D/H_\odot = 2 \times 10^{-5}$. Water in the ISM ranges from a limit of $[\rm D/H]_{H_2O} < 2 \times 10^{-3}$ in interstellar ice (*Dartois et al.*, 2003) to $[\rm D/H]_{H_2O} = (3-5) \times 10^{-4}$ for low-mass protostars, i.e., analogs to the Sun's formation environment (*Persson et al.*, 2014). If the former, higher value reflects the ices accreted by the solar nebular disk, then at the very least, terrestrial oceans and comets should contain $\gtrsim 7\%$ and $\gtrsim 14\%$ interstellar water, respectively. If the low-mass protostellar values are representative, the numbers become $30-50\%$ for terrestrial oceans and $60-100\%$ for comets. Thus a significant fraction of the solar system's water predates the Sun. These findings imply that some amount of interstellar ice survived the formation of the solar system and was incorporated into planetesimal bodies. Consequently, if the formation of the solar nebula was typical, our work implies that interstellar ices from the parent molecular cloud core, including the most fundamental life-fostering ingredient, water, are widely available to all young planetary systems.

8.4 Acknowledgements

LIC and EAB acknowledge support by NSF grant AST-1008800 and the Rackham Predoctoral Fellowship (LIC). CA was partially supported by NASA Astrobiology grant NNA09DA81A and by NASA Cosmochemistry grant NNX11AG67G. FD was supported by NASA grant NNX12A193G. TJH was supported by STFC grant ST/J001627/1.

CHAPTER IX

In Conclusion

When I began graduate school in the Fall of 2009, it was an exciting and eventful time both within the Bergin research group (the "nerd club") and for protoplanetary disk science at large. During this time a senior graduate student in the group, Jeffrey Fogel, was completing a major effort to develop a detailed chemical model tailored to the disk environment (*Fogel*, 2011). Simultaneously, a former postdoctoral researcher, Thomas Bethell, was working on developing an important Monte Carlo X-ray and UV radiative transfer code to calculate the high energy radiation field propagation throughout the disk (*Bethell and Bergin*, 2011a). Overlapping with these excellent researchers allowed me to learn firsthand the inner workings of these codes from their authors, an invaluable experience during these first few years. Their instruction has enabled me to further develop and improve the codes' utility, for which this very thesis is a testament. In addition, I have had the pleasure of passing along the codes and associated knowledge to fellow graduate students at University of Michigan and other institutions, to further their use, development, and impact.

Simultaneously during this time, excitement was building across the field as the Atacama Large Millimeter Array (ALMA) approached its inaugural early science phase, where the first open call for proposals was made in 2011. During the years leading up to ALMA Cycle 0 (and even after the fact), research talks would routinely end with the claim "... and all of these questions will be answered with ALMA." With ALMA would come orders of

magnitude increases in sensitivity, spatial resolution, and spectral resolution; it was (and is) an exhilarating time. With every new data set, there are new questions, new things to find. The recent image of the dust disk of HL Tau released in November 2014 was no exception, with sharply ringed dust lanes centered on the young star (see Figure IX and the subsequent analysis presented in *The ALMA Partnership et al.*, 2015).

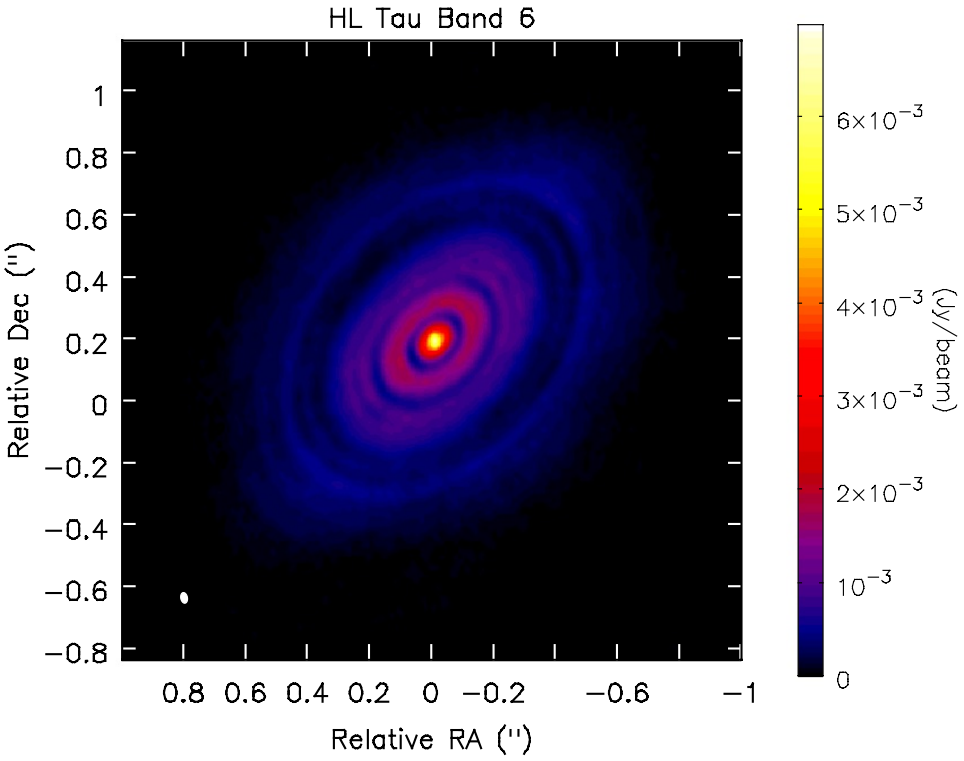

Figure 9.1 Band 6 (1.3 mm) image of HL Tau as taken with ALMA during the long baseline commissioning campaign. One potential interpretation of the rings' origin is sculpting/shepherding by newly formed planets.

The work presented in this thesis is a culmination of the efforts of many people, together developing very powerful theoretical tools that in concert provide a nearly complete framework to study the physical and chemical properties of protoplanetary disks. With these tools, we have made realistic theoretical predictions for future ALMA observations, and we have applied the modeling techniques to ground- and space-based data from the SMA, *Herschel*, and ALMA, among others, as reported in this thesis. Below we summarize the main findings

of this body of work (Section 9.1) and highlight future areas of study (Section 9.2).

9.1 Summary of Findings

9.1.1 Chemistry in the Presence of Planetary Sculpting

The first part of this thesis focuses on the chemical impact of local, planet-induced structure in the disk. In particular, I have made theoretical predictions of signatures of transition disk chemistry (Chapter 2), which are being independently confirmed with very high resolution sub-mm observations (e.g., *Brown et al.*, 2012; *van der Marel et al.*, 2014). More recently, I have completed a pilot study of the fully 3D chemical effects of heating from an embedded, luminous protoplanet within a disk gap (Chapter 3). The planet directly heats the otherwise cold icy disk midplane, sublimating ices and creating a gas-phase signature. The planet has the strongest effect on ices with 30-40 K sublimation temperatures, especially HCN. We found that the sublimation due to a luminous planet would be a detectable effect in less than 10 hours of ALMA time with lines of HCN and $H^{13}CN$ ($J = 8 - 7$ at 690 GHz).

9.1.2 Ionization Processes in Planet-Forming Disks

The observable molecular abundances and physical properties of the disk (i.e., turbulence, accretion, heating) sensitively depend on the environmental conditions, including density, UV irradiation, and energetic ionization. As part of this thesis, I have focused on the role of high energy ionizing agents ($E > 13.6$ eV) in regulating disk chemistry and gas ionization fraction. The primary sources of disk ionization include X-rays, cosmic rays (CRs) and short-lived radionuclides (SLRs). X-rays from the central star mainly ionize the surface but can penetrate deeper regions in the disk during energetic flares. Cosmic rays are thought to dominate the outer disk ionization budget especially at the midplane; however, they are efficiently stopped by stellar or disk winds along with background magnetic fields. To estimate the cosmic ray ionization rate under the influence of winds, I developed template

"extreme" wind-modulated CR spectra based on solar system data along with self-consistent energy losses as CRs propagate through the molecular gas disk (Chapter 4). In the absence of CRs, SLRs sustain low-level ionization in the midplane, initially $\zeta_{\rm SLR} \sim 1-10\times10^{-19}$ s^{-1} per H_2, decaying in strength with an ensemble half-life of approximately ~ 1.2 Myr. Moreover, taking into account the propagation of SLR decay products ($\sim$Mev-energy γ-rays, $\beta^{\pm}$), SLR ionization suffers substantial losses in the lower density outer disk where decay products readily escape (Chapter 5).

We applied these findings to a parameter space study of disk chemistry under a wide range of ionization scenarios as described in Chapter 6 and examined how the molecular ion abundances change under different ionization source assumptions. We made testable predictions for high resolution observations with ALMA to use as a blueprint for mapping the spatial structure of ionizing agents. For example, midplane ionization due to SLRs will fall off with radial distance, owing to outer-disk losses. Conversely, midplane ionization by CRs (if present) will have the opposite behavior, where they are unattenuated by the outer disk but are stopped by high gas surface densities ($\gtrsim 100$ g cm^{-2}; *Umebayashi and Nakano*, 1981) in the inner disk. These are *testable* implications for which I was awarded ALMA Cycle 2 time as principle investigator (in-progress; 30% completion) with *Swift* X-ray monitoring to study ionization at high spatial resolution (see future work below).

9.1.3 Ionization in the TW Hya Disk: Tentative First Detection an Extrasolar Heliosphere?

Some of the theoretical predictions made in Chapter 4 are within reach of current submillimeter facilities. I was awarded time on the Submillimeter Array atop Mauna Kea to study the ionization chemistry at high resolution ($\sim 0\farcs5$ in the array's very-extended configuration) in the molecular layer of the TW Hya disk. I complemented these observations with existing submillimeter observations, for a total of 11 molecular line constraints. I explored a total of 20 different ionization models (4 stellar X-ray models based on observations and 5 cosmic

ray models) and found that the low CR models systematically fit the data better than the high, ISM-like CR rates, i.e., $\zeta_{CR} \geq 10^{-17}$ s^{-1} per H_2. Specifically, ISM CR models were too "chemically destructive" in the inner disk, and produced ion-fractions that were too high in the outer disk to match observations.

There are two potential explanations for the low measured CR rate: (1) exclusion by stellar or disk winds or (2) deflection by turbulent magnetic fields embedded in the disk (*Dolginov and Stepinski*, 1994). While the viability of each of these mechanisms remains to be tested, the recent discovery of highly ordered, strong mm-polarization by *Stephens et al.* (2014) in HL Tau may suggest that disk magnetic fields are not entirely turbulent/random as required for (2). If winds (1) are confirmed to be the primary driver of the CR exclusion, this would be the first detection of an extrasolar heliosphere analogue.

9.1.4 Water in Protoplanetary Disks

One of the most interesting molecules from an astrobiological perspective is water. The chemistry of water is intimately tied with ionization, where its formation in cold gas and on grain surfaces both hinge on the presence of ions. I led a modeling effort described in Chapter 8 to shed light on the origins of water, specifically heavy water, in the solar system. Solar system bodies are well-known to be characteristically enriched in HDO/H_2O, and there is a longstanding debate as to whether this feature is inherited from deuterium-enriched interstellar gas or a product of synthesis in the disk after a "chemical reset" upon disk formation. We took a different approach to the problem and asked the first-order question: how much heavy water does disk chemistry alone produce, starting with no initial deuterium enrichment? I applied the detailed disk ionization model presented in Chapter 3 and found that disk chemistry was unable to reproduce HDO/H_2O in solar system bodies. This result implies that some degree of deuterated interstellar ices, including water, were inherited (and preserved) from the parent molecular cloud during the solar system's formation. These results have interesting astrobiological consequences, namely that interstellar water ice may

be ubiquitously available to all forming planetary systems.

9.2 Future Directions

Looking ahead, there are many avenues to build on the present work. Regarding ionization, higher resolution studies are necessary, with more ion line observations in more disk systems needed to understand what the typical ionization properties of a disk are. We have an active ALMA program to map the ionization across a massive younger disk, IM Lupi, which we have combined with a *Swift* space telescope program to monitor the stellar X-ray activity. The data for this project are currently being taken and are scheduled for completion by the end of September. In addition, I will carry out a larger survey of disk ionization to gather better statistics on disk ionization properties at different evolutionary stages and in different stellar environments. I also plan to push forward on time domain chemistry, where the time-variable energetic stellar properties, especially in the X-rays, may cause a lasting effect on the chemistry as we found for TW Hya (Chapter 7).

I am currently applying a similar time-domain chemical analysis to expand upon the models of disk chemistry under the influence of a planet (Chapter 3), now including the effects of differential rotation. This work will confirm whether or not our basic assumption of rapid chemical adjustment by freeze-out and adsorption hold with more complex models. These models will also allow us to look at longer term chemical affects where the products created by the planet are not destroyed rapidly, potentially resulting in molecular rings or arcs.

I will also apply our theoretical findings for the chemistry of embedded protoplanets to use ALMA to search for planets embedded in their parent disks. Molecular line observations of planets in disks will allow us to obtain critical information about the local physical conditions near the planet, including temperature and velocity. Likewise, we will be able to characterize the local chemistry of the region from which the planet is accreting, where the heating may, for example, alter C/O ratios in the gas versus the ice, fundamentally changing important

physical properties about the resulting planet itself (*Madhusudhan*, 2012).

Finally, we will expand our work on deuterium enrichment of water in disks to explore similar consequences for the organic deuterium chemistry. While deuterium enrichment of water is driven primarily by H_2D^+, the ion CH_2D^+ is instead responsible for setting the organic deuterium enrichment. This distinction is important as the CH_2D^+/CH_3^+ can become highly enriched, even in warm gas, due to the different in zero point energies compared to H_2D^+/H_3^+ (*Roueff et al.*, 2013). Furthermore, I am part of multiple efforts to directly detect HDO in a disk for the first time using ALMA. This measurement would put important constraints on the D/H ratio in water in the cold photodesorbed layers of the disk, and would finally connect our knowledge of the D/H ratio in water in the interstellar medium to that within the solar system.

Together these studies will enable us to get a better handle on important disk physical processes and the underlying chemistry of disks, to put together a more complete picture of the planet formation process.

APPENDICES

APPENDIX A

Approximation for the Interstellar Radiation Field

To determine the extent of the ionization contribution from the ISRF we take a "brute-force" approach and coarsely sample our model on a cartesian grid. From each point in this subsample, we integrate outward along lines of sight evenly spaced over 4π steradians assuming azimuthal disk symmetry. To sample 4π steradians uniformly is not trivial, and we adopt here the "spiral-point technique," see *Saff and Kuijlaars* (1997) for further details and specifically their Equation 8. From these N_a sampled rays we compute a weighted effective optical depth due to extinction by dust,

$$\tau_{\rm eff} = -\ln\left[\sum_{a}^{N_a} \frac{1}{N_a} \exp\left(-\tau_a\right)\right], \tag{A.1}$$

in all directions. The resulting flux is then simply $F_{\rm ISRF} = 1.6 \times 10^{-3}\ G_0 \exp\left(-\tau_{\rm eff}\right)$ erg s^{-1} cm^{-2}. The expression above yields a scalar measure of the interstellar UV absorption by dust from all directions to a given point in the disk. Note that this method includes only 1D absorption in a given direction and neglects dust scattering.

APPENDIX B

Sulfur Chemistry

Even though sulfur is less abundant than carbon, it less effectively self-shields and therefore sees the interstellar FUV field deeper in the disk than carbon. At the temperatures present in the outer disk, $T_g \lesssim 20$ K, most of the S will be locked up in SO and CS on grains and carbon in CO ice. Visualizing the outer disk as an irradiated slab, there are two dominant ionization fronts: the CO(gr) $\rightarrow$ CO $\rightarrow$ C $\rightarrow$ C^+ and CS/SO(gr) $\rightarrow$ CS/SO $\rightarrow$ S $\rightarrow$ S^+. The location of the ion–neutral transition depends on the intensity of the photodesorbing and photodissociating FUV flux and the recombination rates. For continuum photo-processes, the determining factor is dust attenuation in the outer disk if small grains are present. Because CO is very efficient at self shielding, the carbon ionization front traces a thin "onion-layer" of C^+ near the disk surface. While sulfur is less abundant than carbon, it does not self-shield as efficiently (in fact, small grains are more efficient, see *Perez-Becker and Chiang*, 2011b), and as a result, sulfur can be ionized at higher column densities than carbon, setting the deep ionization-front at the UV dust-attenuation limit. Thus, while stellar FUV photoionization of carbon dominates the surface layers and the inner disk, sulfur supplies the FUV-derived ions in the outer disk.

Carbon is ionized by FUV photons with 912–1109 Å, while sulfur is ionized for photons of λ 912–1198 Å, which is equivalent to 7% and 10% of the interstellar FUV flux between

Table B.1. Reduced sulfur network adapted from the OSU gas-phase chemical network (March 2008; *Smith et al.*, 2004).

Reactants		Products	Rate κ (cm^3 s^{-1} unless noted)
$H_3^+ + CO$	$\longrightarrow$	$HCO^+ + H_2$	$\kappa_1 = 1.61 \times 10^{-9}$
$H_3^+ + O$	$\longrightarrow$	H_3O^+	$\kappa_2 = 8.00 \times 10^{-10}$
$S + OH$	$\longrightarrow$	$SO + H$	$\kappa_3 = 6.60 \times 10^{-11}$
$H_3^+ + e^-$	$\longrightarrow$	$H_2 + H$ or $3H$	$\alpha_1 = 6.70 \times 10^{-8} \left[\frac{T_g}{300\ \mathrm{K}}\right]^{-0.52}$
$H_3O^+ + e^-$	$\longrightarrow$	$OH + H_2$	$\alpha_2 = \frac{2}{3} \times 2.60 \times 10^{-7} \left[\frac{T_g}{300\ \mathrm{K}}\right]^{-0.5}$
$SII + e^-$	$\longrightarrow$	S	$\alpha_3 = 3.90 \times 10^{-12} \left[\frac{T_g}{300\ \mathrm{K}}\right]^{-0.63}$
$SO + gr$	$\longrightarrow$	$SO(gr) + gr$	$f_1 = 3.14 \times 10^{-10} \left[\frac{8kT_g}{\pi m_{SO}}\right]^{0.5}$
$S + gr$	$\longrightarrow$	$S(gr) + gr$	$f_2 = 3.14 \times 10^{-10} \left[\frac{8kT_g}{\pi m_{S}}\right]^{0.5}$
$SO(gr) + T$	$\longrightarrow$	SO	$R_1 = 1.32 \times 10^{12} \times \exp\left[\frac{-3.34 \times 10^3\ \mathrm{K}}{T_d}\right]\ \mathrm{s}^{-1}$
$S(gr) + T$	$\longrightarrow$	S	$R_2 = 9.29 \times 10^{11} \times \exp\left[\frac{-1.10 \times 10^3\ \mathrm{K}}{T_d}\right]\ \mathrm{s}^{-1}$
$SO(gr) + \gamma_{UV}$	$\longrightarrow$	SO	$\Gamma_{D1} = 10^{-3}\sigma_g / N_{sites}\ \mathrm{s}^{-1}$
$S(gr) + \gamma_{UV}$	$\longrightarrow$	S	$\Gamma_{D2} = 10^{-3}\sigma_g / N_{sites}\ \mathrm{s}^{-1}$
$SO + \gamma_{UV}$	$\longrightarrow$	$S + O$	$\Gamma_{SO} = 3.30 \times 10^{-10} G_0\ \mathrm{s}^{-1}$
$OH + \gamma_{UV}$	$\longrightarrow$	$O + H$	$\Gamma_{OH} = 1.68 \times 10^{-10} G_0\ \mathrm{s}^{-1}$
$S + \gamma_{UV}$	$\longrightarrow$	$SII + e^-$	$\Gamma_{PI} = 7.20 \times 10^{-10} G_0\ \mathrm{s}^{-1}$

912 – 2000 Å, respectively. Combining the stellar and interstellar UV fields, we then solve for the steady-state S^+ abundance taking into account the pathways and rates listed in Table B.1 (from the OSU gas-grain network; *Smith et al.*, 2004), as well as the total sulfur abundance: $S_{tot} = S + SII + SO + SO(gr) + S(gr)$. To simplify the problem the electron abundance is computed from Eq. (4.10), which intrinsically assumes most electrons come from ionization of H_2, and we furthermore set the oxygen abundance to be $\chi_O = 10^{-10}$, consistent with the outer disk where most oxygen is in molecular gas or ice (*Fogel et al.*, 2011). We tested values ranging between $\chi_O = 10^{-9} - 10^{-12}$ and find that the result does not depend strongly on the assumed oxygen abundance. Additionally, we set the CO abundance to be $\chi_{CO} = \chi_C \equiv 1.4 \times 10^{-4}$. In the following equations, number density (cm^{-3}) of a particular species is denoted by brackets around the species name, e.g., [CO]. First, we compute directly the steady state abundances of H_3^+ and H_3O^+:

$$\left[H_3^+\right] = \frac{\zeta_{H_2}[H_2]}{\kappa_1[CO] + \alpha_1[e^-] + \kappa_2[O]},$$
$$\left[H_3O^+\right] = \frac{\kappa_2[H_3^+][O]}{\alpha_2[e^-]}.$$

In steady state, the S^+ number density can be rearranged into a quadratic form, A $[S^+]^2$ + B $[S^+]$ + C = 0, where the coefficients are defined as follows:

$$A = -\frac{\kappa_3\alpha_3[e^-]}{\Gamma_{PI}}\left(1 + E\frac{\alpha_3[e^-]}{\Gamma_{PI}}\right),$$
$$B = \left[\frac{\kappa_3\alpha_3[e^-][S_{tot}]}{\Gamma_{PI}} - \left(1 + E\frac{\alpha_3[e^-]}{\Gamma_{PI}}\right)\Gamma_{OH} - D\frac{\alpha_2\alpha_3\kappa_3\left[H_3O^+\right][e^-]^2}{\Gamma_{PI}\Gamma_{SO}}\right], \text{ and}$$
$$C = \Gamma_{OH}[S_{tot}];$$

with D and E defined as:

$$\mathrm{D} = \left[1 + \frac{f_1[\mathrm{gr}]}{\Gamma_{\mathrm{D1}} + R_1}\right] \text{ and}$$
$$\mathrm{E} = \left[1 + \frac{f_2[\mathrm{gr}]}{\Gamma_{\mathrm{D2}} + R_2}\right].$$

Upon solving the quadratic equation for $[\mathrm{S}^+]$, the corresponding abundances of the other species can be computed straightforwardly:

$$[\mathrm{S}] = \frac{\alpha_3[\mathrm{S}^+][\mathrm{e}^-]}{\Gamma_{\mathrm{PI}}},$$
$$[\mathrm{OH}] = \frac{\alpha_2[\mathrm{H_3O}^+][\mathrm{e}^-]}{\kappa_3[\mathrm{S}] + \Gamma_{\mathrm{OH}}},$$
$$[\mathrm{SO}] = \frac{\kappa_3[\mathrm{OH}][\mathrm{S}]}{\Gamma_{\mathrm{SO}}},$$
$$[\mathrm{SO(gr)}] = \frac{f_1[\mathrm{SO}][\mathrm{gr}]}{\Gamma_{\mathrm{D1}} + R_1}, \text{ and}$$
$$[\mathrm{S(gr)}] = \frac{f_2[\mathrm{S}][\mathrm{gr}]}{\Gamma_{\mathrm{D2}} + R_2}.$$

In this treatment, we have significantly simplified the sulfur chemistry by excluding the formation of other S-bearing species such as CS. In general, by allowing sulfur to take other pathways to form species such as CS, more sulfur will be tied up in gas or ice phase molecules and will be less available for photoionization, pushing the ion-front closer to the disk surface. For a detailed treatment of this problem, both the chemistry and multidirectional self-shielding of molecules such as CO and sulfur need to be considered in detail. This approximation, however, gives a simple expression for the ionization contribution from S^+ in the outer irradiated region in the disk.

APPENDIX C

Updated Short-Lived Radionuclide Rates

We provide fits to the midplane ionization rate in Chapter 5 as a function of vertical surface density and time. We note, however, that the previous work assumed a somewhat short half-life for ^{60}Fe, $t_{\rm half} = 1.49 \pm 0.27$ Myr from *Kutschera et al.* (1984). This value was revised in *Rugel et al.* (2009) to be $t_{\rm half} = 2.62 \pm 0.04$ for a larger ^{60}Fe sample. In the present work we recalculate the SLR ionization rate in the same method as described in Chapter 5 adopting the revised ^{60}Fe half-life. The effect only becomes important after a disk life-time of 5 Myr. At this evolutionary time, the scattered stellar X-rays begin to dominate over the SLR contribution. Consequently, the net disk ionization properties should not be strongly sensitive to the specific ^{60}Fe half-life used.

Nevertheless, in the interest of completeness, we provide updated SLR ionization rate calculations versus disk surface density in Figure C.1. Colors indicate the time from "disk formation," i.e., the epoch when the initial measured SLR abundances were set. We re-fit the ionization rate curves using a power law (grey lines), which are described by

$$\zeta_{\rm H_2}(r) = \left(2.1 \times 10^{-19}\ {\rm s}^{-1}\right) \left(\frac{1}{2}\right)^{t/1.2} \left(\frac{\Sigma(r)}{\rm g\ cm^{-2}}\right)^{0.26}, \tag{C.1}$$

where time, t, is given in Myr. This equation is an updated version of Equation (30) in Chapter 5. The change in the half-life of the SLR ensemble increases from $\sim$ 1 Myr to

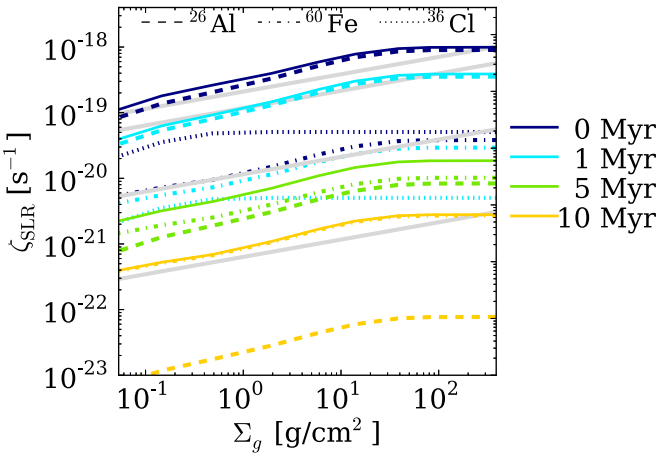

Figure C.1 Same as Fig. 4 of Chapter 5. Short-lived radionuclide H_2 ionization rate in the disk midplane as a function of *vertical* gas surface density and time (from the initial event suppling the SLR abundances, approximately the formation time of the disk). Grey lines indicate the new fits to the values provided by Eq. (C.1).

1.2 Myr, meaning that SLRs can play an important role in the absence of CRs for a slightly longer span of the disk's lifetime. We emphasize that the abundances of SLRs will vary from source to source. This variation will change the leading coefficient of Eq. (C.1 by at least of factor of two in both directions.

APPENDIX D

Physical Structure

D.1 Dust Model

We calibrate the disk physical density and temperature structure by fitting TW Hya's spectral energy distribution (SED). References for the SED photometry are provided in the Figure D.2 caption, originally compiled by *Andrews et al.* (2012). We adopt the same parametric density profile presented in Chapter 4 Eqs. (1-4), adapted from *Andrews et al.* (2011). In essence, the gas and dust surface densities, $\Sigma_{g,d}$, are described by radial power-laws with an exponential taper, while the density, $\rho_{g,d}$, is taken to be vertically Gaussian. Moreover, we break the dust into two populations, one of small "atmosphere" grains with radii $r_g = 0.005 - 1\mu$m distributed over the full (gas) scale height of the disk, and a second of larger midplane grains, $r_g = 0.005 - 1$mm, concentrated near the midplane. The former contains 10% of the total dust mass, while the latter contains the remaining 90%. This larger population is designed to simulate the effects of settling due to grain-growth, a feature common of observed protoplanetary disks (*Furlan et al.*, 2006). Both large and small dust populations have an MRN size distribution (*Mathis et al.*, 1977), where the number of grains scales with the size of grain as $n_g \propto r_g^{-3.5}$. We assume a mixed dust composition with

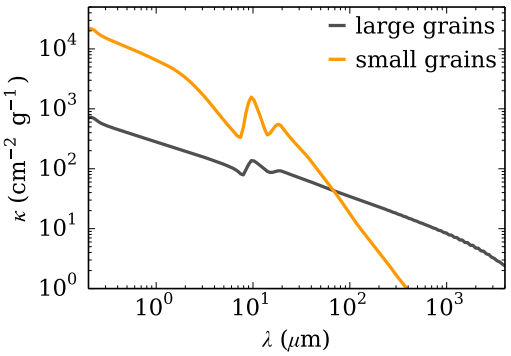

Figure D.1 Dust opacities for the two dust populations used in our SED model. Small grains (atmosphere) have a maximum grain size of 1 μm, while the large grain population has a maximum wavelength of 1 mm. Opacities are plotted as a cross section per unit dust mass in grams.

80% astronomical silicates and 20% graphite by mass. The model opacities are shown in Figure D.1. Similar to Eqs. (1-4) of Chapter 4, our best fit model has a *total* dust surface density of

$$\Sigma_d(R) = 0.04 \text{ g cm}^{-2} \left(\frac{R}{R_c}\right)^{-1} \exp\left[-\frac{R}{R_c}\right], \tag{D.1}$$

and a scale height for small grains (and gas) following

$$h(R) = 15 \text{ AU} \left(\frac{R}{R_c}\right)^{0.3}, \tag{D.2}$$

where the critical radius is $R_c = 150$ AU. The density of the small and large grain populations are described by

$$\rho_s(R,Z) = \frac{(1-f)\Sigma_d}{\sqrt{2\pi}Rh} \exp\left[-\frac{1}{2}\left(\frac{Z}{h}\right)^2\right], \tag{D.3}$$

and

$$\rho_l(R,Z) = \frac{f\Sigma_d}{\sqrt{2\pi}R\chi h} \exp\left[-\frac{1}{2}\left(\frac{Z}{\chi h}\right)^2\right], \tag{D.4}$$

respectively, where the fraction of mass in large grains is $f = 0.9$ and the large grains concentrated over $\chi = 0.2$ the scale height of the small grains, h. Z corresponds to the vertical distance from the midplane where R and Z are in cylindrical coordinates.

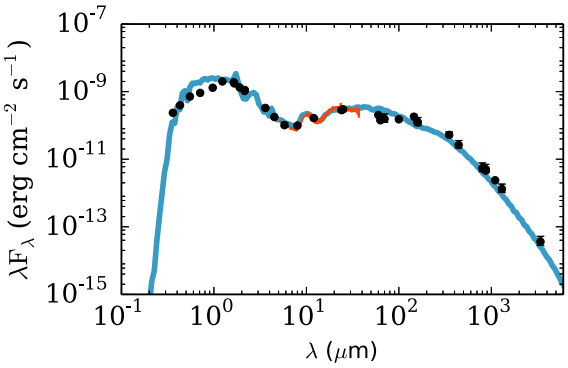

Figure D.2 Our best fit spectral energy distribution (blue line) from the combined star and disk of TW Hya. Black points (with error bars) are individual photometric measurements taken from the literature (*Weintraub et al.*, 2000; *Mekkaden*, 1998; *Cutri et al.*, 2003; *Hartmann et al.*, 2005; *Low et al.*, 2005; *Thi et al.*, 2010b; *Andrews et al.*, 2012; *Weintraub et al.*, 1989a; *Qi et al.*, 2004; *Wilner et al.*, 2003, 2000). TW Hya's Spitzer IRS spectrum is over-plotted in orange (*Uchida et al.*, 2004).

We use the radiative transfer code TORUS (*Harries*, 2000; *Harries et al.*, 2004; *Kurosawa et al.*, 2004; *Pinte et al.*, 2009) to calculate the dust temperatures and emergent SED assuming dust radiative equilibrium where heating is dominated by the central star. We adopt the following stellar parameters for TW Hya: $T_{\rm eff} = 4110$ K, $M_* = 0.8$ M$_\odot$, $R_* = 1.04$ R$_\odot$ (*Andrews et al.*, 2012). The total mass of dust with grain sizes up to 1 mm in our best fit model is $M_d = 4 \times 10^{-4}$ M$_\odot$. There may certainly be larger "pebbles," boulders, or even planetesimals; however, the SED modeling is not sensitive to these. We present the best fit SED model in Figure D.2. The corresponding dust density and temperature models are shown as solid contour lines in Figures 7.3a and 7.3b.

D.2 Gas Model

The SED fitting formally constrains the distribution of dust grains. To constrain the total *gas* mass in the TW Hya protoplanetary disk, we use the *Herschel* detection of hydrogen deuteride, HD, to directly probe the gas reservoir (*Bergin et al.*, 2013). This is especially crucial for TW Hya's disk, as the more widely used molecular gas probe, CO, is measured to be depleted in warm gas, i.e., in addition to CO freeze-out (*Favre et al.*, 2013, see also

Sec. E.1). Because HD does not freeze-out and the HD to H_2 ratio is approximately constant and well constrained within the local bubble ($HD/H_2 = 3 \pm 0.2 \times 10^{-5}$; *Linsky*, 1998), HD is a chemically "simple" species, differing mainly from H_2 with regards to UV self-shielding.

To calibrate our model's gas mass using HD, we start from the dust-derived physical structure and assume the gas density and small grains are distributed over the same scale height and are vertically Gaussian (filled contours in Fig. 7.3a). Furthermore, we must assume a gas-to-dust mass conversion factor where, because gas and dust are not uniformly vertically distributed due to settling, we compare the vertically integrated quantities, $f_g = \Sigma_g/\Sigma_d$, with $f_g = 100$ for dense interstellar gas.

To calculate the HD emission, we must also estimate the gas temperature and dust opacity at 112 μ. HD is particularly sensitive to the gas temperature due to the high upper state energy of the $J = 1$ rotational level. In the upper layers of the disk, the gas temperature can exceed the dust temperature, i.e., become "decoupled" due to less efficient gas cooling. We estimate the gas temperature by using a fitting function calibrated to thermochemical models of FUV heating from the central star (S. Bruderer, in private communication 2013). Based on a grid of physical structures and FUV field strengths, the detailed heating and cooling balance was solved (e.g., *Bruderer*, 2013) to determine the gas thermal decoupling from the dust in the disk atmosphere where $A_V = 1 - 3$. Based on these models, S. Bruderer estimates a parameterized fit to the gas temperature based on the local FUV strength and gas density. We emphasize that the main results of this Chapter, the ions, are not sensitive to the gas temperatures as most of the molecular ion emission comes from deeper layers and, correspondingly, higher A_V. To determine the FUV radiation field throughout the disk, we use a Monte Carlo technique to calculate the wavelength-dependent UV field including both absorption and scattering on dust, in addition to the transfer of Lyman-α photons (*Bethell and Bergin*, 2011a). Special treatment of Lyman-α radiative transfer is important as these photons will resonantly scatter on atomic hydrogen atoms, greatly enhancing the scattered radiation field deep in the disk compared to the primarily forward-scattering dust.

Furthermore, Lyman-α carries $\sim 85\%$ of the FUV flux below 2000 Å (*Herczeg et al.*, 2004). The UV optical properties are taken from the dust model described in §7.7.2, and we use the measured TW Hya FUV fluxes from *Herczeg et al.* (2002, 2004) assuming a distance of $d = 55$ pc. The calculated FUV radiation field integrated over wavelength is shown in Figure 7.3d, and the resulting gas temperature structure is shown in Figure 7.3b as filled color contours. For the most part $T_g = T_d$ (see contour lines), however the gas temperature becomes decoupled from the dust by more than $\Delta T > 10$ K in the layer where $z/r \gtrsim 0.4$.

In addition to the gas temperature, the HD emission is sensitive to the vertical structure of the dust as the dust disk becomes optically thick at 112 μm. Consequently, the HD emission is sensitive to the specific dust opacity for which we must assume a single value. The weighted average of the two large and small populations corresponds to an opacity per gram of dust of $\kappa_{\rm mix}(112\ \mu{\rm m}) = 30\ {\rm cm}^2\ {\rm g}^{-1}$.

From the gas and dust density and temperature model, we compute the baseline chemistry for HD (see details of the chemical code in §7.5.2) to primarily determine how much HD is dissociated in the upper layers before self-shielding takes hold. Because HD does not freeze-out, the HD abundance is effectively constant throughout the disk below the UV self shielding layer ($z/r \sim 0.4$). From the calculated HD abundances, we then compute the emergent HD $(1-0)$ line intensity assuming the emission is in LTE (see §7.5.4 for details on the radiative transfer). We then adjust the gas-to-dust ratio, f_g, until we find agreement with the observed HD flux, $\int F_{\rm HD} dv = 70.6 \pm 7.8$ Jy km s^{-1} (*Bergin et al.*, 2013). With a vertically integrated gas-to-dust mass ratio of $f_g = \Sigma_g/\Sigma_d = 75 - 100$ ($M_g = 0.03 - 0.04$ M$_\odot$), we find good agreement with the observed value, where our 0.04 M$_\odot$ model predicts $\int F_{\rm HD} dv = 76.6$ Jy km s^{-1}. We note, however, that slightly less massive ($M_g = 0.02$ M$_\odot$) but warmer disk or perhaps a more massive ($M_g = 0.05$ M$_\odot$) but cooler disk can also reproduce the observations, so in the present framework, we find that TW Hya's gas mass is $M_g = 0.04 \pm 0.02$ M$_\odot$. This value can be further refined with better observational constraints on the overall vertical density and thermal structure. The gas mass derived here

is slightly less than the mass provided by *Bergin et al.* (2013), $M_g > 0.05$ $M_\odot$, and is chiefly due to differences in the gas temperature calculation and underlying disk model assumed.

APPENDIX E

Neutral Gas Constraints

E.1 Neutral Gas Constraints: CO

In the ISM, CO is the second-most abundant gas phase molecule after H_2. In the ISM, CO has an abundance of $\chi(\mathrm{CO}) = 10^{-4}$ and participates in a wide range of chemical reactions. However, recent observations indicate that CO is substantially reduced in warm ($T \gtrsim 20$ K) gas where the CO abundance relative to H_2 was found to be $\chi(\mathrm{CO}) = (1 - 10) \times 10^{-6}$ (*Andrews et al.*, 2012; *Favre et al.*, 2013). *Williams and Best* (2014) indirectly confirm this finding by deriving a gas mass from CO isotopologue observations of $M_g = 5 \times 10^{-4}$, a factor of ~ 100 less than the HD derived gas mass. One potential explanation for this large CO deficit is through CO dissociation by He^+, where some fraction of the carbon from CO to be put into other neutral species with higher grain-surface binding energies than that of CO. This process can happen at early stages prior to the formation of the disk, activated by CR ionization, or at later stages in the disk's warm molecular layer initiated by stellar X-ray ionization (*Semenov et al.*, 2004; *Bergin et al.*, 2013). To robustly make predictions for HCO^+ abundances, which forms from CO via

$$H_3^+ + \mathrm{CO} \rightarrow \mathrm{HCO}^+ + H_2, \tag{E.1}$$

we must include the CO deficit in our model. We initially ran models where the initial (input) CO abundance is set at $\chi(\mathrm{CO}) = 1 \times 10^{-6}$, and the rest of the carbon is put into strongly bound, carbon-bearing ices, e.g., methanol. However, even in this instance the carbon in methanol ice was recycled back into gas phase CO in less than 1 Myr in the layers where UV photons are present. Even when we artificially increased the binding energy of methanol, the carbon nevertheless made its way back into gas phase CO, and over-produced the observed CO emission (i.e., the CO abundance after 1 Myr was far too high to explain the observations).

In the end, we found that the only way to reproduce the low CO abundance was to reduce the CO abundance and explicitly *not* put it into one of the existing network species, thereby net reducing the amount of *reactive* carbon. The physical interpretation behind this finding is that the carbon no longer in gaseous CO has gone on to form something similar to macromolecular organic ices. In the presence of UV irradiation, such material is less likely to non-thermally desorb, and are more likely to break up into radical ices, where the products remain on the grains (and are not returned to the gas) and are thought to be key to forming important biogenic organic material.

Taking two models with different CR ionization rates (SSX and W98, §7.5.3.1), we i) vary the *initial* CO abundance, ii) calculate the final CO abundance after 1 Myr, and iii) compute the ^{13}CO and C^{18}O emergent line emission (see §7.5.4). We compare these values to the observations (*Favre et al.*, 2013, see also Table 7.1). Figure E.1 shows the ratio of the observed flux to the model flux for different CO initial conditions. The model which simultaneously best fits ^{13}CO and C^{18}O is one where $\chi(\mathrm{CO}) = 1 \times 10^{-6}$, though CO abundances between $\chi(\mathrm{CO}) = (5 - 20) \times 10^{-7}$ can fit either ^{13}CO or C^{18}O. The main differences between the present work and *Favre et al.* (2013) is that we are using a new model and a different method to calculate gas temperature. We confirm the *Favre et al.* (2013) result that the CO abundance is substantially lower than the canonical $\chi(\mathrm{CO}) = 10^{-4}$ in the warm gas by approximately a factor of ~ 100.

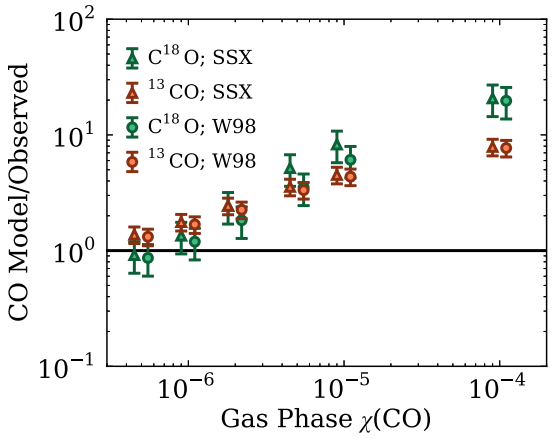

Figure E.1 Comparison between the simulated $C^{18}O$ (2-1) and ^{13}CO (2-1) line intensities and the observed values (see Table 7.1) for different gas-phase CO abundances. The canonical CO abundance, $\chi(CO) = 10^{-4}$ over predicts the observed fluxes by approximately an order of magnitude and is also optically thick – inconsistent with the observations. A gas-phase CO abundance of $\chi(CO) = 10^{-6}$ or perhaps lower is a better match to the data, in agreement with the findings of *Andrews et al.* (2012) and *Favre et al.* (2013).

E.2 Neutral Gas Constraints: HCN

Motivated by the work of *Schwarz and Bergin* (2014, submitted), the initial abundances of nitrogen also play an important role in the chemical outcome of nitrogen bearing species, including HCN, NH_3 and N_2H^+. Because N_2H^+ is simultaneously affected by ionization and CO abundance, the neutral species provide a cleaner test of the initial nitrogen abundances in this model. Described in more detail in *Schwarz and Bergin* (2014, submitted), the final nitrogen molecular abundances are most sensitive to the following broad groupings of initial nitrogen reservoirs, namely the amount of NH_3 ice, N_2, and N and/or single-N containing molecules. The species HCN has been previously detected in the TW Hya disk, and thus we use this molecule as a probe of the initial nitrogen portioning in the disk; however, we note that this is only one line and that future more detailed modeling and additional observations will greatly help but additional constraints on the nitrogen assay in disks.

In the midplane, since we use a static disk model, the chemistry is such that the abundance of NH_3 ice in the midplane is often very similar to that which was assumed initially,

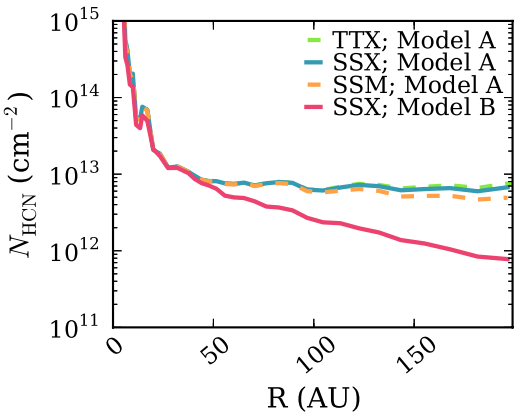

Figure E.2 The dependence on different initial nitrogen conditions of the HCN abundance after 1 Myr of chemical evolution. The initial abundances relative to total H of major nitrogen-bearing species (with abundance $\chi \geq 10^{-7}$) are as follows. Model A: $\chi(\mathrm{NH_3}$ ice$) = 9.16 \times 10^{-6}$, $\chi(\mathrm{N_2}) = 2.5 \times 10^{-6}$, and $\chi(\mathrm{N}) = 5.1 \times 10^{-6}$. Model B: $\chi(\mathrm{NH_3}$ ice$) = 7.91 \times 10^{-6}$, $\chi(\mathrm{N_2}) = 5.7 \times 10^{-6}$, and $\chi(\mathrm{N}) = 1 \times 10^{-7}$. Variations between initial nitrogen abundances exceed variations due to different assumed ionization rates (dotted lines, Model A). See Section E.2 for details.

i.e., the ices are not rapidly reprocessed. In this light, we can look to cometary $\mathrm{NH_3/H_2O}$ ratios to put an upper limit on the $\mathrm{NH_3}$ ice abundance. Typical ammonia abundances for comets have percentages of $0.1 - 1.5\%$ relative to water (*Bockelée-Morvan et al.*, 2004; *Biver et al.*, 2012). Evidence from protostellar $\mathrm{NH_3}$ ice abundances, typically $\sim 3\%$ (*Öberg et al.*, 2011a) and comets gives an approximate range for the amount of nitrogen locked up in ices and thus provides a crude handle on the nitrogen partitioning in the disk. In Figure E.2 we show two models considered where Model A has more ammonia ice (less reactive nitrogen)

The initial $\mathrm{N_2}$ abundance directly affects $\mathrm{N_2H^+}$; however, its effect is predictable. The overall column density profile may shift up or down, but the shape of the $\mathrm{N_2H^+}$ column density versus radius stays the same. The $\mathrm{N_2}$ and $\mathrm{NH_3}$ binding energies assumed in the model are 1220 K and 3080 K, respectively. The final nitrogen abundances determined from the HCN emission are listed in Table E.1.

Table E.1. Chemical model initial abundances relative to total number of H-atoms.

Species	χ	Species	χ
H_2	5.00×10^{-1}	H_2O(gr)	2.50×10^{-4}
HDO(gr)	1.00×10^{-8}	He	1.40×10^{-1}
CN	6.60×10^{-8}	HCN	1.00×10^{-8}
N	5.10×10^{-6}	NH_3(gr)	9.90×10^{-6}
N_2	1.00×10^{-6}	H_3^+	1.00×10^{-8}
CS	4.00×10^{-9}	SO	5.00×10^{-9}
Si^+	1.00×10^{-11}	S^+	1.00×10^{-11}
Mg^+	1.00×10^{-11}	Fe^+	1.00×10^{-11}
C^+	1.00×10^{-9}	CH_4	1.00×10^{-7}
Grain	6.00×10^{-12}	CO	1.00×10^{-6}
C	7.00×10^{-7}	HCO^+	9.00×10^{-9}
HD	1.50×10^{-5}	H_2D^+	1.30×10^{-10}
HD_2^+	1.00×10^{-10}	D_3^+	2.00×10^{-10}
C_2H	8.00×10^{-9}		

APPENDIX F

Model Comparison

It is important to quantify the model dependency of the results of Chapter 7. To determine how our results depend on the disk physical structure, we repeat our experiment using the detailed model of *Andrews et al.* (2012). The *Andrews et al.* (2012) model fits the dust distribution in detail, and fits the CO $(3-2)$ profile. Because CO $(3-2)$ is thick, the gas model primarily reflects the disk temperature profile versus radius. However, the best fit model in that work found a significantly smaller taper radius for the gas disk, i.e., the critical radius, where $r_c = 35$ AU for the sA model, which could still fit the distributed CO gas out to 200 AU. The model in the present work, for comparison, has a taper at $r_c = 150$ AU, dropping off instead at the edge of the CO and scattered light disk.

Consequently, there is a substantial difference in the mass distribution between the two models, and the disk mass itself (which is an order of magnitude smaller for the *Andrews et al.* (2012) model). The mass/density difference is most pronounced at the outer disk, at the same radii where N_2H^+ $(4-3)$ is dropping off. By comparing the two models, we can test whether or not the N_2H^+ distribution is a mass effect or an ionization effect. In Figure F.1, we show the normalized N_2H^+ column density for the outer disk (Fig. F.1a) and the column density of the population of N_2H^+ in the $J = 4$ upper state (which is more closely related to the line emissivity). We have normalized the columns because we have not done any

additional chemical calibration or mass calibration for the *Andrews et al.* (2011) model as were done in the main text, and so there is an overall offset between the two models. From these tests we find that the overall slope of the N_2H^+ column density and emissive column density agree well with the results of the main text for the SSX (reduced CR ionization model), and that even with the reduced outer disk mass in the *Andrews et al.* (2011) model, the N_2H^+ emission distribution is too flat to explain the observations. This behavior is a natural consequence of the drop in outer disk density, where the loss of mass acts to *reduce* the recombination efficiency of ions, and thus there is higher fractional abundance of ions, including N_2H^+, than in our model, which has higher outer disk recombination due to the higher outer disk mass in the present Chapter. Thus the N_2H^+ profile cannot be attributed to a mass effect, and that a reduced CR ionization rate does a better job of explaining the emission distribution for both physical structures.

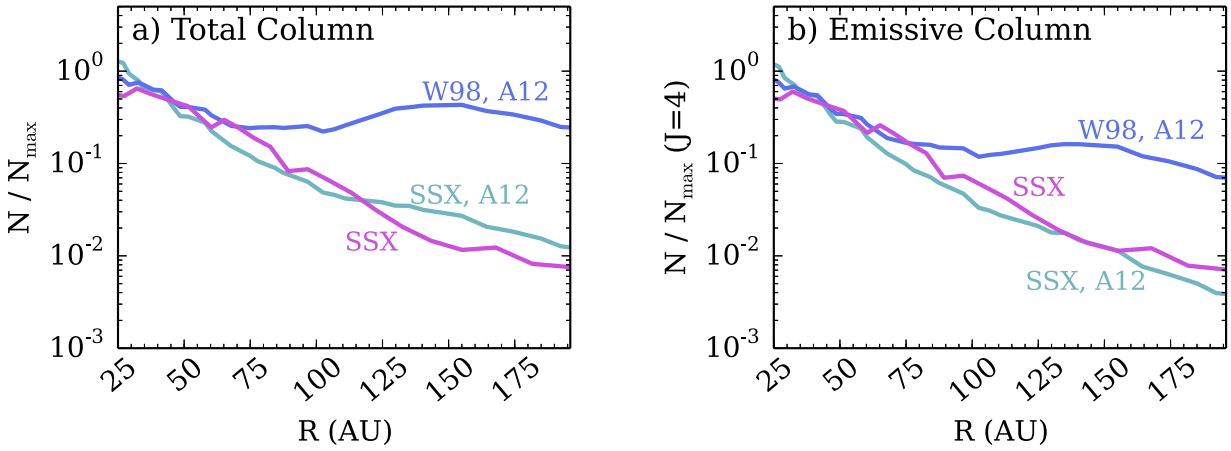

Figure F.1 Chemical model comparison between the disk model assumed in this work (labeled just SSX) and the results for a different underlying disk model from *Andrews et al.* (2012) (lines labeled A12). We find good agreement in the overall slope of the column densities for the low CR ionization model and can exclude the high CR ionization model, W98, which over predicts the outer disk by over an order of magnitude.

APPENDIX G

Physical Model and Supplementary Data

G.1 Physical Model

The disk physical structure adopted for the modeling presented in Chapter 8 is based upon a previously published model of a dust-settled disk (see Chapter 4) with typical geometric and settling structural parameters reflecting a sample of modeled dust continuum observations (*Andrews et al.*, 2011). The model has been truncated from its original outer radius of $R = 400$ AU to have an outer radius of $R = 80$ AU, which reflects the maximal radius of the protosolar disk as determined from dynamical models of the lack of planetesimals on high inclination orbits (*Kretke et al.*, 2012). This corresponds to a modified disk gas mass of $M_{\rm gas} = 0.008$ $M_\odot$ from its original value of $M_{\rm gas} = 0.039$ $M_\odot$, which is still above the total mass in the Solar System's planets (0.002 $M_\odot$) but slightly less than the classical minimum mass solar nebula (MMSN), derived from integrating an assumed gas surface density profile, $M_{\rm MMSN} = 0.01$ $M_\odot$ (*Weidenschilling*, 1977). If the disk is more radially compact, e.g., $R \sim 30 - 50$ AU (*Hersant et al.*, 2001; *Adams*, 2010; *Kretke et al.*, 2012), the disk integrated D/H ratio would be lower as a direct consequence of removing mass where the gas is coldest. In this instance, disk chemical processes, as determined by our model, could provide up to $< 1\%$ of D/H in VSMOW for an outer disk radius of $R = 50$ AU.

We emphasize that we have not attempted to recreate a classical MMSN model but have opted instead to utilize a generic model based upon observations of protoplanetary disks in situ. Two important points regarding the model are as follows. First, the choice of a dust-settled model, chosen based upon the observational inference of a reduction of small grains from the upper layers of planet-forming disks (*Furlan et al.*, 2006), results in the disk being *more* permeable to X-rays, which are scattered by gas and dust, and thus the model adopted at present is *more favorable* towards deuterium fractionation than a well-mixed (uniform gas-to-dust ratio) disk model. Second, because the mass of the disk is slightly lower than the typical MMSN, the average gas density would also be slightly lower than a MMSN model. Thus ion-recombination is proportionally less efficient in a lower mass model, making for a higher steady state abundance of ions present for fractionation. Both of these effects would lead to our fiducial model predicting higher D/H ratios than expected, and therefore our D/H results are likely to be upper limits, i.e., the total fractionation of water in the disk may be lower, and consequently requiring more water to be interstellar in nature. To test the latter scenario, we re-ran all of our chemical models (described in detail below) with a factor of ten reduction in density and all other parameters held constant. There was no significant change in the abundances relative to hydrogen calculated for the low-density model and so the net effect of the disk mass on the chemical results is small.

The dust temperatures are calculated using the radiative transfer code TORUS (*Harries*, 2000; *Harries et al.*, 2004; *Kurosawa et al.*, 2004; *Pinte et al.*, 2009) where we have assumed stellar parameters typical of the Sun at $1 - 3$ Myr as described in the main text. The gas temperatures are computed using a fitting function relating the local strength of the FUV field and disk gas density (*Bruderer et al.*, 2012). The stellar FUV and X-ray radiative transfer is calculated using a 2D Monte Carlo treatment (*Bethell and Bergin*, 2011a,b). For the FUV radiation field we include absorption and scattering from dust in the continuum calculation, as well as resonant scattering off atomic hydrogen for Lyman-α propagation (*Bethell and Bergin*, 2011a). The X-ray treatment includes both photo-absorption and scat-

tering by dust grains and gas (*Bethell and Bergin*, 2011b), which is essential as scattered X-ray photons provide the baseline midplane ionization in the absence of cosmic rays and radionuclide decay. The physical model and radiation fields are shown in Figure G.1.

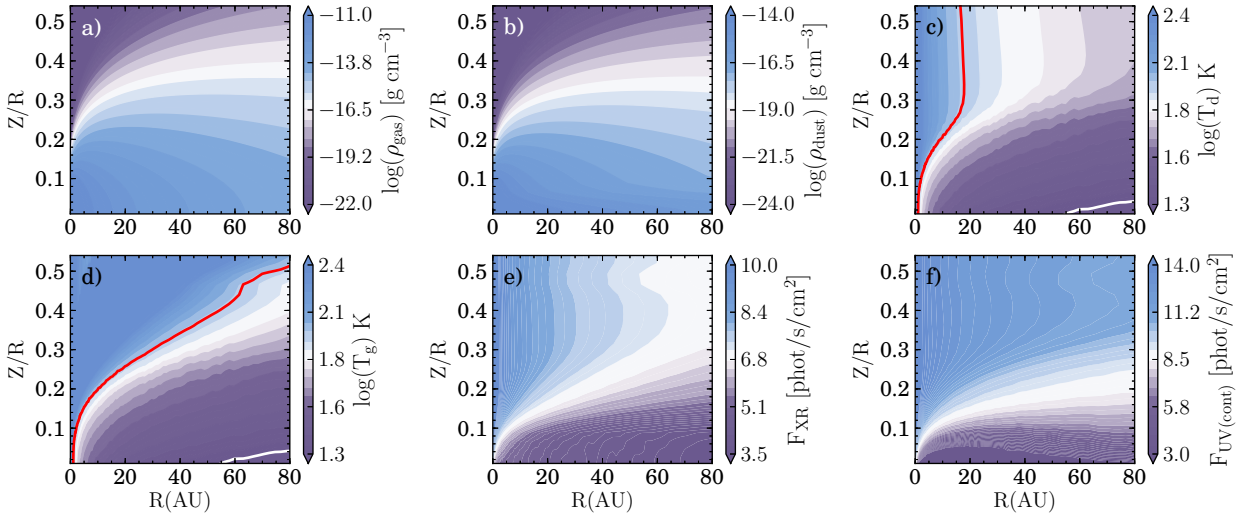

Figure G.1 Disk model assumed. Panels are: a) gas density, b) dust density, c) dust temperature, d) gas temperature, e) spectrally integrated X-ray flux, f) spectrally integrated continuum far UV flux. In panels c) and d) red and white lines delineate $T = 100$ K and $T = 17$ K respectively.

G.2 Non-Stellar Ionization Processes

In addition to X-ray photoionization, our model includes non-stellar ionization from external galactic cosmic rays (GCR) and internal short-lived radionuclide decay. In the Solar System, the solar wind is observed to efficiently modulate the GCR flux within a region known as the Heliosphere, especially at low GCR energies. The net result is over a factor of $\gtrsim 10$ reduction in the GCR ionization rate under *present day* solar minimum conditions. T Tauri stars likewise drive stellar and disk winds, and thus it would not be unexpected for this mechanism to operate at equal or perhaps higher efficiency in the circumstellar environment of a T Tauri star. The GCR ionization rate present in a disk has not yet been directly measured, but limits on the GCR ionization rate from H_2D^+ non-detections

indicate that the GCR rate is sub-interstellar (*Chapillon et al.*, 2011). Because the ionization rate is unknown in the young circumstellar environment, we assume an unattenuated GCR ionization rate of $\zeta_{\rm GCR} = 2 \times 10^{-19}$ s^{-1}, commensurate with the GCR rate under modern day solar maximum conditions (Chapter 4). From the specific solar maximum GCR spectrum we self-consistently vertically propagate GCR protons, including energy dependent losses through the gas disk, thus providing a comprehensive treatment of GCR ionization under the influence of wind modulation. We emphasize that the GCR rate may be lower if winds are even more efficient at excluding cosmic rays from the natal environment, and thus deuterium fractionation powered by GCR ionization may be further hindered.

Within the disk, near the geometrical midplane, contributions from the decay of radioactive particles become another important source of ionization, especially under the instance of GCR modulation. The decay products, primarily γ-rays, positrons and electrons, originate from the decay of ^{26}Al, ^{36}Cl and ^{60}Fe embedded in the refractory (dust) component. For pebbles less than $a_{gr} \leq 1$ cm in size, the decay products can escape the pre-planetesimal prior to losing all of there energy (*Umebayashi and Nakano*, 2009). In the present model, we have included grain-growth up to $a_{gr} = 1$ mm in the dust opacities, and thus we assume that all decay products escape the dust particles and are available for ionization, and the SLR abundances are taken to be the initial abundances present in the protosolar nebula (Chapter 5). Depending on location in the disk and the type of decay product considered, particles can be lost from the gas disk prior to losing all energy to ionization. For example, ^{26}Al β-decay results in the emission of a positron ($\Sigma \sim 0.1$ g cm^{-2}) and energetic MeV photons ($\Sigma \sim 12$ g cm^{-2}), which are each trapped at different disk surface densities and thus different radial locations in the disk. Thus treatment of the losses of the radionuclide decay products is important in a complete picture of disk ionization, especially in the outer ($R > 30$ AU) disk. Furthermore, because our disk is settled, i.e., the dust and gas are no longer uniformly distributed, we calculate the vertical and radial position-dependent decay product losses, treating each decay product individually with regards to the relevant energy

loss mechanism (Chapter 5). We note that if decay products are either trapped within dust particles or if the abundance of SLRs is lower than the protosolar value, the corresponding ionization rate due SLR decay would also be lower, further hindering D-fractionation. In Chapter 8, Figure 8.3 we show both the standard, fully present GCR ionization structure (left) next to our fiducial ionization model adopted in the main text (right), incorporating a mildly wind-excluded incident GCR ionization rate and detailed radionuclide transfer through the gas and dust disk, as described above.

G.3 Chemical Reaction Network

We calculate time-dependent chemical abundances as a function of position throughout the disk utilizing a comprehensive disk chemistry code (*Fogel et al.*, 2011). The backbone of the chemical network is based upon the Ohio State University's gas-phase reaction network (*Smith et al.*, 2004), which has been substantially expanded to include a host of chemical processes important in disks, including photodissociation, freeze-out, thermal and non-thermal sublimation, CO and H_2/HD/D_2 self-shielding (*Wolcott-Green and Haiman*, 2011), stellar and non-stellar ionization of H_2 and Helium (*Fogel et al.*, 2011). In addition to the standard set, which encompasses 5912 reactions and 550 unique species, we have further expanded the network for the present study to include the essential deuterium fractionation reactions surrounding H_2D^+ chemistry, along with HDO. We have also expanded the set to include simple, primarily hydrogenation-based grain surface chemistry (*Hasegawa et al.*, 1992a), which forms HDO/H_2O, HDCO/H_2CO, H_2, HD and D_2. It has been shown that deuterium enrichments are efficient in the gas phase (*Millar et al.*, 1989) and in ices on dust grains (*Tielens*, 1983). An additional fifty species are included in the expanded network, and the full set of reactions totals 6268. The initial abundances in our model relative to total number of hydrogen atoms are listed in Table G.1.

Unless otherwise specified, the majority of the deuterated isotopologue reactions mirror those for the main isotopologues, where we have assumed the same reaction rate coeffi-

Table G.1. Log of the initial chemical abundances, χ, per total number of hydrogen atoms.

Species	log(χ)	Species	log(χ)
H_2	-0.30	H_2O ice	-3.60
HDO ice	-8.00	He	-0.85
N	-4.65	CN	-7.22
H_3^+	-8.00	CS	-8.40
SO	-8.30	Si^+	-11.00
S^+	-11.00	Mg^+	-11.00
Fe^+	-11.00	C^+	-9.00
CO	-4.00	N_2	-6.00
C	-6.15	NH_3	-7.10
HCN	-7.70	HCO^+	-8.05
HD	-4.70	H_2D^+	-9.89
HD_2^+	-10.00	D_3^+	-9.70
C_2H	-8.10		

cients for both, and statistical branching ratios where appropriate. In addition to H_2, HD and D_2 are directly ionized by X-rays, GCRs and SLRs. Specific reaction rates are taken from the literature for the deuterated versions of the following reaction types: (i) $H_3^+ + H_2$, H_3^+ electron recombination and $H_3^+ + H$ (*Roberts et al.*, 2004); (ii) reactions with H^+ and atomic/molecular hydrogen, reactions with deuterated HCO^+, N_2H^+ and atomic hydrogen (*Roberts and Millar*, 2000); and (iii) neutral-neutral warm deuterium reactions with barriers (*Thi et al.*, 2010a).

There is one important exception in reaction set (i) regarding $H_2D^+ + H_2$, where we take into account the ortho- and para- spins of both reactants (*Hugo et al.*, 2009). The ortho- and para- forms are not treated as distinct species but we instead assume that they are present with a thermal abundance ratio following the methods described in Chapter 8. Including the spin information is important, as the energy barrier depends strongly on spin, with the reaction being barrierless if both reactants are ortho-type and $\Delta E_1 = 226$ K if both are para-type, for example. Thus we calculate the local energy barrier for this reaction as a weighted mean of the ortho/para types in our determination of the reaction rate. Finally,

inclusion of the warm fractionation reactions in (iii) did not change our results.

To keep the network relatively chemically simple and transparent, we set out to form only singly deuterated water, HDO. In the gas phase, deuterium enrichments are driven by ion-neutral reactions with H_2D^+, where H_2D^+ reacts with oxygen, eventually leading to H_2DO^+, which can recombine with charged grains and electrons $\sim 25\%$ of the time to form water (the rest of the time it goes to OH and either H or H_2). On the grain surfaces, HDO forms by subsequent hydrogenation of oxygen ice (*Tielens and Hagen*, 1982; *Hasegawa et al.*, 1992a). Oxygen does not need to be "permanently" bound to the surface but simply needs to stay on the surface long enough for a hydrogen to adhere to a grain, sweep out the grain surface, and react with the heavier molecule (in this case, oxygen), which remains largely stationary.

G.4 Binding Energies

For most species, we assume the same binding energies for deuterated and main isotopologues. One exception is that we assume the surface binding energy of physisorbed deuterium is slightly higher (21 K) than hydrogen, $E_b(D) = 471$ K and $E_b(H) = 450$ K (*Caselli et al.*, 2002). The distinction of *physisorbed* hydrogen stems from the observed fact that hydrogen has two main types of bonds on a substrate. Physisorbed hydrogen weakly adheres to a surface by van der Waals forces with binding energies of around $E_b(H) = 450$ K. The second type is a far stronger chemical bond, called chemisorption, and has binding energies typically of order a few eV. Formally each of these bonds corresponds to a different state of hydrogen on the grain surface, but because we do not track individual atoms we approximate this behavior by adopting a significantly higher chemisorption binding energy ($E_b = 3000$ K) with respect to thermal and non-thermal desorption processes but adopt the physisorption energy when calculating the rate of hydrogen grain surface reactions, which proceed through the more mobile atoms.

Another grain-surface facet of this study is a new treatment of the CO binding energy.

CO is the second most abundance molecular volatile after H_2, and has been well studied in its binding properties on various substrates (*Öberg et al.*, 2005; *Collings et al.*, 2004; *Bergin et al.*, 1995). The specific binding energy of CO to a substrate depends on the surface composition, namely if it is coated in water, CO, or CO_2 ices, or bare. The CO on CO binding energy was determined to be $E_b = 855$ K (*Öberg et al.*, 2005), corresponding to a dust temperature of $T_d \sim 17$ K. However, in regions of the disk close to and above this temperature, the surface seen by freshly adsorbed CO molecules will be predominantly non-CO by construction. Again, because we do not track individual ice mantles nor their multi-layered structure, we approximate the binding surface based upon the local temperature. At dust temperatures below $T_d < 25$ K, the ice will be primarily CO-dominated, and thus we adopt a binding energy of $E_b = 855$ K. Between $T_d = 25-50$ K, approximately corresponding to temperatures between the freeze-out temperature of CO_2 down to that of CO, the ice mantle will be primarily CO_2. CO_2 is a gas- and grain-surface product that readily proceeds in our chemical models in the presence of free oxygen or hydroxyl radicals. At temperatures exceeding the freeze-out temperature of CO_2, $T_d > 50$ K, the mantle will be primarily water ice, and above the water ice freeze-out temperature of $T \sim 100$ K, the grains will be mostly bare. The increased binding energy for CO on H_2O has been previously recognized (*Collings et al.*, 2004; *Bergin et al.*, 1995), however the consideration of CO_2 on CO is a new facet in the present study.

The relative binding energies of pure CO, CO on CO_2 ice and CO on H_2O ice were explored using temperature programmed desorption experiments of pure CO ice and thin CO layers on top of CO_2 and H_2O ices. Previous experiments have demonstrated that CO-CO and CO-H_2O binding energies differ substantially (*Collings et al.*, 2003), but less is known about the CO-CO_2 interaction.

The experiments were carried out in a new ultrahigh vacuum (UHV) chamber (custom-made, Pfeiffer Vacuum), evacuated by a Pfeiffer Turbo HiPace 400 pump backed by a DUO 10M rotary vane pump to a base pressure of ~ 10 mbar at room temperature. Ices are

grown on a 2 mm thick IR transparent CsI substrate mounted on an optical ring sample holder through. The sample holder is connected to the cold tip of a closed cycle He cryostat (Model CS204B, Advanced Research Systems, Inc.) capable of cooling the CsI substrate down to 11 K. The cryostat is mounted on the top port of the chamber via a differentially pumped UHV rotary seal (Thermionics RNN-400) that allows 360 degree rotation of the CsI substrate inside the chamber without breaking the vacuum during the experiment. The CsI substrate is mounted onto the nickel-plated OHFC copper sample holder using silver gaskets for good thermal contact. A 50 ohm thermofoil heater is connected to the cryocooler tip so that the temperature of the substrate can be varied between $12-350$ K. The temperature of the substrate is controlled and monitored by a cryogenic temperature controller (Lake Shore Model 335) using two calibrated silicon diode sensors (accuracy of ± 0.1 K), one connected directly to the sample holder and the other near the heater element. During heating, the temperature is increased using a linear heating ramp controlled by a positive feedback loop set using the Lake Shore 335 temperature controller.

Ices were grown onto the sample window using vapor deposition along the surface normal using de-ionized and freeze-thaw purified water, and high-purity CO and CO_2 gas ($> 99\%$ purity guaranteed, which was confirmed by mass spectrometric measurements). The individual ice layer thicknesses were estimated from the deposition time and pressure and then quantified using transmission infrared spectroscopy using a Vertex 70v spectrometer with a liquid nitrogen cooled MCT detector and literature absorption coefficients (*Gerakines et al.*, 1996). In the presented experiments the pure CO ice is 16 monolayers (ML), the layered CO/CO_2 ice is 2/51 ML and the layered CO/H_2O ice is 3/46 ML. That is, in each experiment the ice thickness is sufficient to ensure that the underlying substrate is not affecting the desorption energies, and the top CO layers are thin enough that interactions with the underlying CO_2 and H_2O ices should dominate the desorption temperature of CO.

Following deposition, the ices were heated up using a linear 1 K/min heating ramp and the desorption rate of CO was monitored using a Pfeiffer quadrupole mass spectrometer

(QMG 220M1, mass range 1-100 amu) positioned 40 mm of the CsI substrate. The resulting Temperature Programmed Desorption spectra are shown in Figure G.2. Qualitatively, the

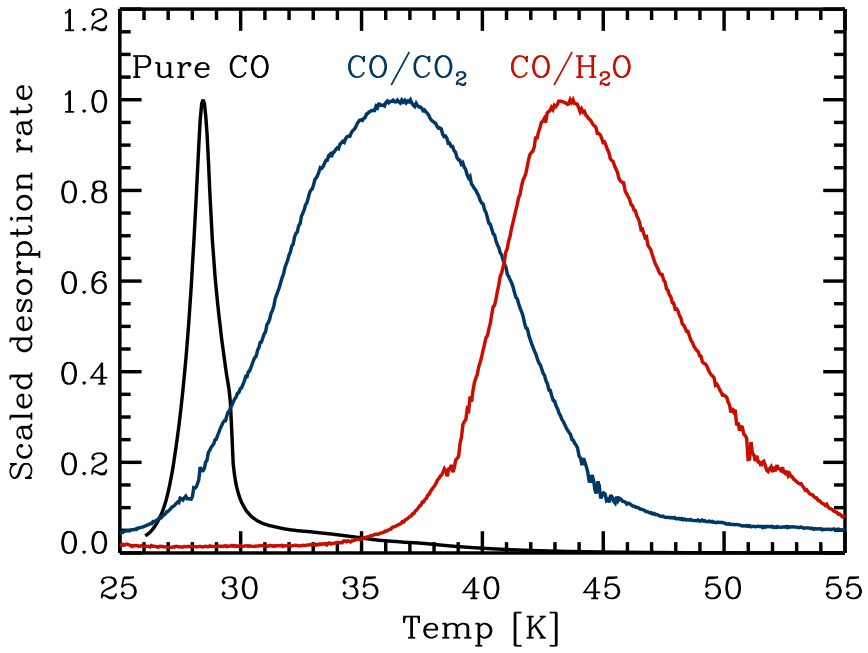

Figure G.2 Temperature programmed desorption spectra of pure CO, CO desorbing off a CO_2 ice, and CO desorbing of an amorphous H_2O ice. The desorption rates have been scaled to a unity peak desorption rate for visibility.

desorption peaks of pure CO, CO_2 and H_2O are clearly separated. The desorption rate of CO peaks at 28.5 K, the CO/CO_2 rate at 37 K, and the CO/H_2O at 44 K. The pure CO and CO/H_2O desorption behavior is consistent with previous studies (*Öberg et al.*, 2005; *Collings et al.*, 2003). The binding energy in Kelvin can be estimated from the peak position (*Attard and Barnes*, 1998), by multiplying the peak desorption rate temperature by 30. This yields binding energies of 855, 1110, and 1320 K for CO-CO, CO-CO_2 and CO-H_2O, respectively. Observe that this is a rather crude estimate and should mainly be used to constrain the relative binding energies of these three systems, while more experiments and more detailed modeling is required to set the absolute scale.

Table G.2. Physical parameters for the chemical model comparison points in the midplane at the specified radii.

	R (AU)	n_H (cm^{-3})	T_g (K)	T_d (K)	Σ (ζ_{H_2}) (s^{-1})	A_V^* (mag)
1	40	3.6×10^{10}	21.6	21.6	1.1×10^{-18}	> 20
2	3	1.8×10^{13}	56.7	56.7	1.5×10^{-18}	> 20

G.5 Chemical Model Tests

In our use of simplified deuterium network, there is concern that we may miss essential low-lying reactions that contribute over the duration of the chemical calculations or act in combination with a handful of other slow reactions that may impact our results. To test this hypothesis, we have extracted the physical parameters (Table G.2) at a representative point at the outer disk midplane ($R = 40$ AU) and the inner disk midplane ($R = 3$ AU) from our disk model and have calculated the corresponding abundances using a more advanced general deuterium chemical network (*Du*, 2012, PhD). The D/H values from our calculations (A) and the point-wise large scale network (B) are shown in Table G.3, where both models start with the same set of initial conditions (Table G.1). For the most part the models are in good agreement, especially regarding the low D/H predicted for water, though some differences do exist. The disparity in H_2D^+/H_3^+ is a consequence of different assumptions for the reaction rates, where we have included the ortho-to-para spin information in the calculation of the rate coefficients (*Hugo et al.*, 2009). In the B-model, $E_b = 124$ K is assumed at both points. The H_2D^+/H_3^+ ratio in both cases is not directly imprinted into the water as a consequence of the oxygen being trapped in water, CO, and CO_2 ices and not available for new water chemistry, and thus the conclusion of little deuteration of water holds.

Table G.3. Independent chemical model comparison results. Table values given with respect to D/H in H_2, i.e. $f[\mathrm{R}] = \mathrm{R}/4 \times 10^{-5}$. A = chemical model presented in the main text; B = complex gas-grain deuterium chemical model (*Du*, 2012, PhD).

	1			2		
Ratio	A	B	A/B	A	B	A/B
$f[H_2D^+/H_3^+]$	115	230	0.5	1.5	6.7	0.2
$f[HDO/H_2O]$	1.0	1.1	0.9	1.0	1.1	0.9

G.6 Further Considerations

In the present section we compare how our choice of model parameters impacts the primary results of Chapter 8. To compare the main results of Chapter 8 to a model with GCRs fully present (unmodulated), we have recomputed our chemical models assuming a typical GCR rate (model type W98; Chapter 4). The results are shown in Figure G.3 The HDO/H_2O ratio in ices is elevated from the main result. The layer of water ice where the D/H ratio is enriched is larger but remains centered on the warm molecular layer. The maximum vertically integrated column of HDO/H_2O in ices approaches $HDO/H_2O \sim 10^{-4}$ at the disk outer edge ($R \sim 80$ AU), which is still below VSMOW ($HDO/H_2O \sim 3 \times 10^{-4} = 2 \times [D/H]_{VSMOW}$). Recent models which include mixing have found that under a fully present GCR ionization rate, the D/H in water approaches $[D/H]_{H_2O} = 2 \times 10^{-3}$ after 1 Myr regardless of initial conditions and thus would allow for the D/H ratio to be mixed up from the molecular hydrogen value (*Furuya et al.*, 2013). Because we do not include mixing we cannot compare with this claim directly, but in the instance of a low GCR ionization rate the efficacy of this process will be significantly curtailed. In their models, oxygen is transported into the deuterium rich midplane to reform water. The timescales for this process in the gas phase are too long compared to the freeze out time for oxygen onto grain surfaces regardless of ionization rate, so water reformation would have to be grain-surface chemistry driven. However, given the

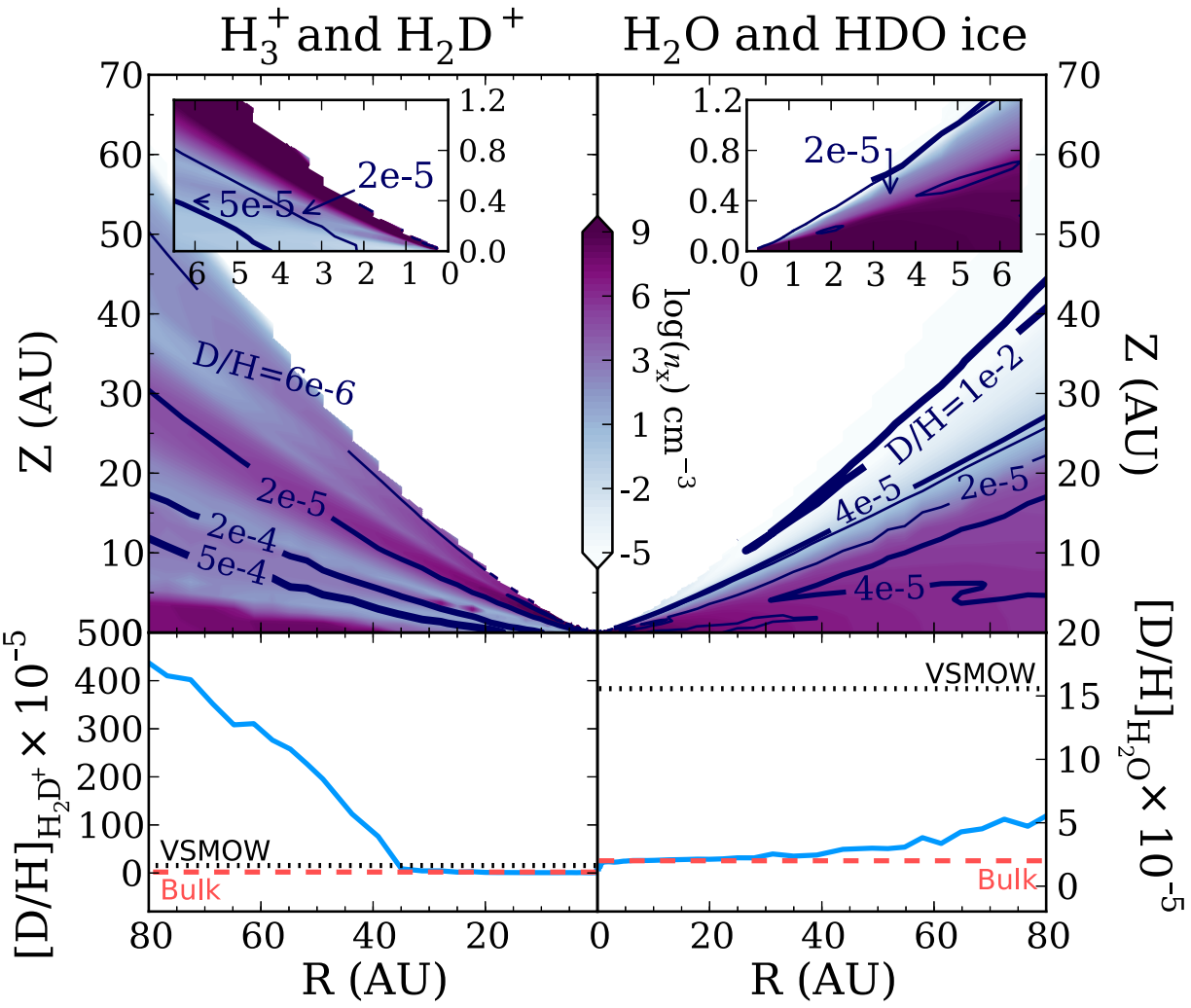

Figure G.3 Abundance and D-fractionation results for a standard ISM GCR rate. The H_3^+ abundance is significantly elevated in the midplane compared to the fiducial model, and thus the vertically integrated D/H in H_2D^+ is substantially higher owing to the cold gas contribution to the column. The D/H in water remains low, however, due to a lack of freely available oxygen for water reformation. Plot labels are the same as for Figure 8.3.

low abundance of hydrogen atoms to fuel hydrogenation (χ[H] $\sim 10^{-13}$ and χ[D] $\sim 10^{-17}$), grain surface reformation of water would not be efficient, and it is instead more favorable for the oxygen (or OH) to react with CO ices abundantly present on the grains to form CO_2 prior to getting doubly hydrogenated to make water, even though to CO reactions have a weak barrier, $E_b \sim 80$ K (*Garrod and Pauly*, 2011).

Another component of our study was that we initiated the chemistry with all oxygen as gas-phase CO and water ice (Table G.1). One could alternatively begin with nearly all oxygen in atomic form, i.e., fully available for chemical processing. We computed a second model assuming the initial abundance of oxygen was $\chi(\mathrm{O}) = 2 \times 10^{-4}$ and $\chi(\mathrm{H_2O\ ice}) = 5 \times 10^{-5}$ with HDO ice scaled appropriately to the protostellar molecular hydrogen D/H value. The results are shown in Figure G.4. As can be seen, the $\mathrm{HDO/H_2O}$ ratio is slightly higher but

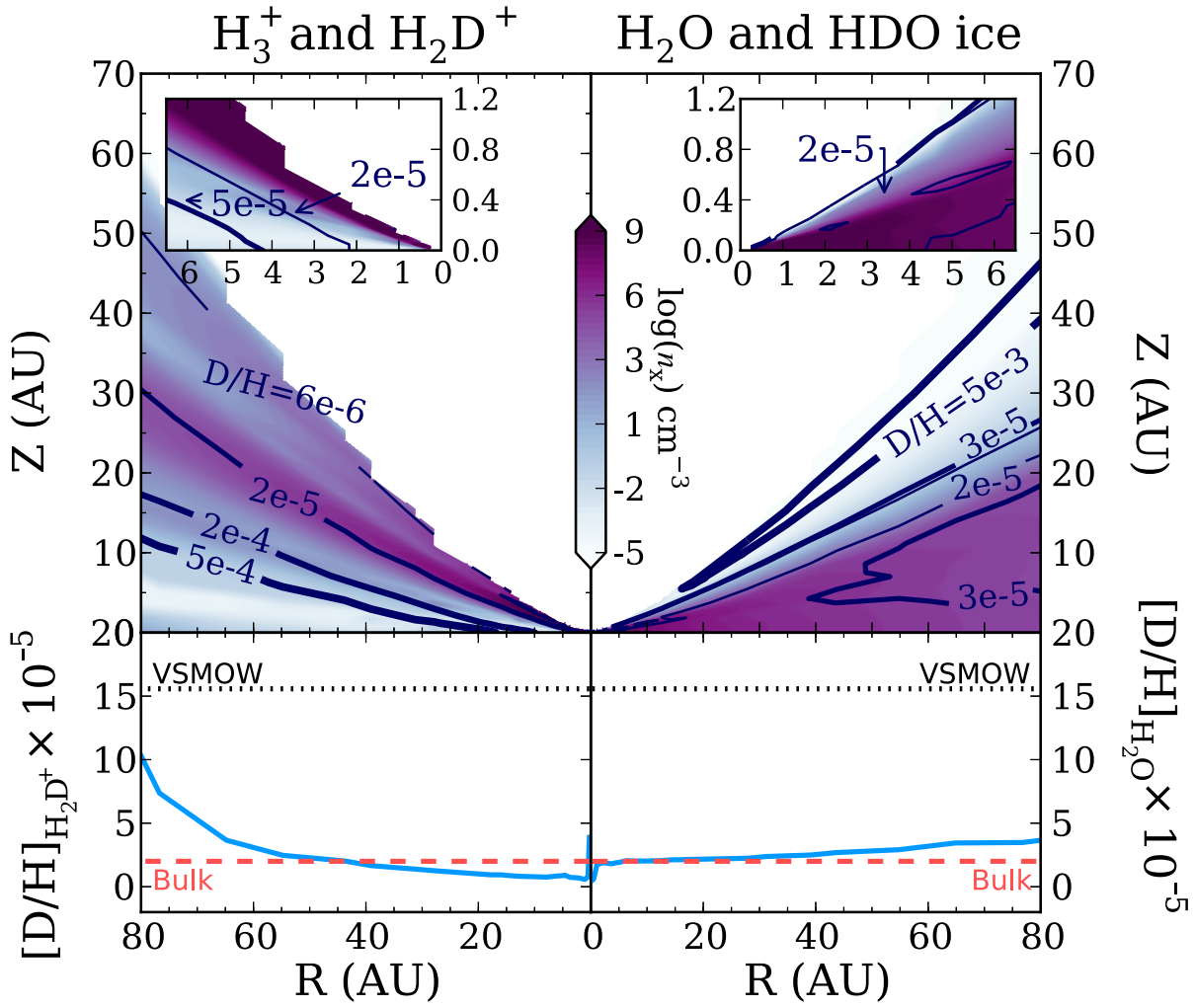

Figure G.4 Test case model where we began initially with most of the oxygen (that is not in CO) in gas-phase atomic O, rather than water ice. Water D/H in ices remains low, even when we begin with atomic oxygen due to a lack of ionization. Thus the models are not strongly sensitive to the initial conditions of the oxygen. Plot labels are the same as for Figure 8.3.

still well below VSMOW, and thus our results regarding D/H in water do not depend strongly on where the oxygen is initially. Furthermore, the model that begins with a substantial fraction of oxygen in atomic form rather than water only increases its water ice abundance by 0.2% at 30 AU in the midplane after 1 Myr. The lack of ionization not only hinders the formation of deuterated water (whose reactants are less abundant an take longer chemical times), but also the formation of the main isotopologue, H_2O, at the midplane. Based on the knowledge that comets are comprised of a significant fraction of water by mass, approximately $\sim 30\%$ (*Greenberg and Li*, 1999) where silicates and refractory carbonaceous material comprise the rest, it seems unlikely that the disk formed from an initially primarily oxygen state, otherwise comets would be CO_2 "snowballs" rather than water "snowballs." Above the midplane, where $z/r \gtrsim 0.15$, the disk is able to convert the oxygen to water where there is sufficient ionization. Nonetheless, the water formed in this gas still has just $[\mathrm{D/H}]_{\mathrm{H_2O}} = 5.3 \times 10^{-5}$ after 1 Myr, more than a factor of 3 below VSMOW.

Thus we find that regardless of initial oxygen abundances, chemical model assumed, and density structure, it is very difficult for disk chemistry alone to produce a significant amount of deuterated water ice (or perhaps any water ice) in the bulk gas at the outer disk, even at the VSMOW level, and thus the deuterium in water must have an interstellar heritage that has been since mixed down with warm deuterium-poor water to the values measured today. Consequently, the survival of deuterium enrichments originating from interstellar ices will depend upon processing during the initial disk formation (*Visser et al.*, 2009b; *Yang et al.*, 2013) and the efficiency of mixing in the solar nebula between the active surface and the inert midplane, in addition to radial mixing with the warm inner ($\lesssim 3$ AU) disk.

Table G.4. D/H values and references from Figure 8.3.

Label	Value	Type	Reference
H_2			
Protosun	$(2.00 \pm 0.35) \times 10^{-5}$	Value	*Geiss and Gloeckler* (2003)
Jupiter	$(2.60 \pm 0.70) \times 10^{-5}$	Value	*Mahaffy et al.* (1998)
Uranus	$(4.40 \pm 0.40) \times 10^{-5}$	Value	*Feuchtgruber et al.* (2013)
Water			
Lunar Apatite	$(1.12 - 1.52) \times 10^{-5}$	Range	*Barnes et al.* (2014)
Martian melt inc.	$\leq 1.99 \times 10^{-4}$	Upp. Lim.	*Usui et al.* (2012)
Semarkona Phyl.	$(7.70 \pm 1.00) \times 10^{-4}$	Value	*Deloule and Robert* (1995)
CI (sub)	$(6.43 - 9.77) \times 10^{-4}$	Range	*Alexander et al.* (2012)
CM (sub)	$(8.29 - 9.01) \times 10^{-4}$	Range	*Alexander et al.* (2012)
Tagish Lake (sub)	$(5.00 - 7.24) \times 10^{-4}$	Range	*Alexander et al.* (2012)
Semarkona (sub)	$(2.80 - 3.44) \times 10^{-4}$	Range	*Alexander et al.* (2012)
J.F. Comet	$(1.61 \pm 0.24) \times 10^{-4}$	Value	*Hartogh et al.* (2011)
P/Halley	$(3.02 \pm 0.07) \times 10^{-4}$	Value	*Eberhardt et al.* (1995)
Hyakutake	$(2.90 \pm 1.00) \times 10^{-4}$	Value	*Bockelée-Morvan et al.* (1998)
Hale-Bopp	$(3.30 \pm 0.80) \times 10^{-4}$	Value	*Meier et al.* (1998)
Interstellar H_2O	$(2.95 - 9.50) \times 10^{-4}$	Range	*Persson et al.* (2014)
IRAS 16293	$9.20^{+2.00}_{-2.60} \times 10^{-4}$	Value	*Persson et al.* (2012)
IRAS 16293 Env.	$(6.00 \pm 5.00) \times 10^{-3}$	Value	*Coutens et al.* (2012)
Interstellar Ices	$\leq 1.70 \times 10^{-2}$	Upp. Lim.	*Parise et al.* (2003)

BIBLIOGRAPHY

BIBLIOGRAPHY

Abramowitz, M., and I. A. Stegun (1972), *Handbook of Mathematical Functions*.

Adams, F. C. (2010), The Birth Environment of the Solar System, *ARA&A*, *48*, 47–85, doi:10.1146/annurev-astro-081309-130830.

Adams, F. C., J. P. Emerson, and G. A. Fuller (1990), Submillimeter photometry and disk masses of T Tauri disk systems, *ApJ*, *357*, 606–620, doi:10.1086/168949.

Adams, F. C., M. Fatuzzo, and L. Holden (2014), Distributions of Short-lived Radioactive Nuclei Produced by Young Embedded Star Clusters, *ApJ*, *789*, 86, doi:10.1088/0004-637X/789/1/86.

Aikawa, Y., and E. Herbst (1999a), Deuterium Fractionation in Protoplanetary Disks, *ApJ*, *526*, 314–326, doi:10.1086/307973.

Aikawa, Y., and E. Herbst (1999b), Molecular evolution in protoplanetary disks. Two-dimensional distributions and column densities of gaseous molecules, *A&A*, *351*, 233–246.

Aikawa, Y., S. M. Miyama, T. Nakano, and T. Umebayashi (1996), Evolution of Molecular Abundance in Gaseous Disks around Young Stars: Depletion of CO Molecules, *ApJ*, *467*, 684, doi:10.1086/177644.

Aikawa, Y., N. Ohashi, S.-i. Inutsuka, E. Herbst, and S. Takakuwa (2001), Molecular Evolution in Collapsing Prestellar Cores, *ApJ*, *552*, 639–653, doi:10.1086/320551.

Aikawa, Y., G. J. van Zadelhoff, E. F. van Dishoeck, and E. Herbst (2002), Warm molecular layers in protoplanetary disks, *A&A*, *386*, 622–632, doi:10.1051/0004-6361:20020037.

Albertsson, T., D. Semenov, and T. Henning (2014), Chemodynamical Deuterium Fractionation in the Early Solar Nebula: The Origin of Water on Earth and in Asteroids and Comets, *ApJ*, *784*, 39, doi:10.1088/0004-637X/784/1/39.

Alencar, S. H. P., and C. Batalha (2002), Variability of Southern T Tauri Stars. II. The Spectral Variability of the Classical T Tauri Star TW Hydrae, *ApJ*, *571*, 378–393, doi:10.1086/339878.

Alexander, C. M. O. D., R. Bowden, M. L. Fogel, K. T. Howard, C. D. K. Herd, and L. R. Nittler (2012), The Provenances of Asteroids, and Their Contributions to the Volatile Inventories of the Terrestrial Planets, *Science*, *337*, 721–, doi:10.1126/science.1223474.

Allamandola, L. J., S. A. Sandford, A. G. G. M. Tielens, and T. M. Herbst (1993), Diamonds in dense molecular clouds - A challenge to the standard interstellar medium paradigm, *Science*, *260*, 64–66, doi:10.1126/science.11538059.

Amano, T., and T. Hirao (2005), Accurate rest frequencies of submillimeter-wave lines of H_2D^+ and D_2H^+, *Journal of Molecular Spectroscopy*, *233*, 7–14, doi:10.1016/j.jms.2005.05.008.

Anderson, D. E., E. A. Bergin, S. Maret, and V. Wakelam (2013), New Constraints on the Sulfur Reservoir in the Dense Interstellar Medium Provided by Spitzer Observations of S I in Shocked Gas, *ApJ*, *779*, 141, doi:10.1088/0004-637X/779/2/141.

Anderson, T. G., T. A. Dixon, N. D. Piltch, R. J. Saykally, P. G. Szanto, and R. C. Woods (1977), Laboratory Rest Frequencies for N2D(+), *ApJ*, *216*, L85, doi:10.1086/182516.

André, P., J. Di Francesco, D. Ward-Thompson, S.-I. Inutsuka, R. E. Pudritz, and J. E. Pineda (2014), From Filamentary Networks to Dense Cores in Molecular Clouds: Toward a New Paradigm for Star Formation, *Protostars and Planets VI*, pp. 27–51, doi:10.2458/azu:uapress:9780816531240-ch002.

Andrews, S. M., D. J. Wilner, A. M. Hughes, C. Qi, and C. P. Dullemond (2009), Protoplanetary Disk Structures in Ophiuchus, *ApJ*, *700*, 1502–1523, doi:10.1088/0004-637X/700/2/1502.

Andrews, S. M., D. J. Wilner, C. Espaillat, A. M. Hughes, C. P. Dullemond, M. K. McClure, C. Qi, and J. M. Brown (2011), Resolved Images of Large Cavities in Protoplanetary Transition Disks, *ApJ*, *732*, 42, doi:10.1088/0004-637X/732/1/42.

Andrews, S. M., et al. (2012), The TW Hya Disk at 870 μm: Comparison of CO and Dust Radial Structures, *ApJ*, *744*, 162, doi:10.1088/0004-637X/744/2/162.

Arnaud, K. A. (1996), XSPEC: The First Ten Years, in *Astronomical Data Analysis Software and Systems V*, *Astronomical Society of the Pacific Conference Series*, vol. 101, edited by G. H. Jacoby and J. Barnes, p. 17.

Arnould, M., G. Paulus, and G. Meynet (1997), Short-lived radionuclide production by non-exploding Wolf-Rayet stars., *A&A*, *321*, 452–464.

Asplund, M., N. Grevesse, A. J. Sauval, and P. Scott (2009), The Chemical Composition of the Sun, *ARA&A*, *47*, 481–522, doi:10.1146/annurev.astro.46.060407.145222.

Attard, G., and C. Barnes (1998), Surfaces, *Oxford Chemistry Primer*, *59*, 96.

Axford, W. I., A. J. Dessler, and B. Gottlieb (1963), Termination of Solar Wind and Solar Magnetic Field., *ApJ*, *137*, 1268, doi:10.1086/147602.

Ayliffe, B. A., and M. R. Bate (2009), Circumplanetary disc properties obtained from radiation hydrodynamical simulations of gas accretion by protoplanets, *MNRAS*, *397*, 657–665, doi:10.1111/j.1365-2966.2009.15002.x.

Ayotte, P., R. S. Smith, K. P. Stevenson, Z. Dohnlek, G. A. Kimmel, and B. D. Kay (2001), Effect of porosity on the adsorption, desorption, trapping, and release of volatile gases by amorphous solid water, *Journal of Geophysical Research: Planets*, *106*(E12), 33,387–33,392, doi:10.1029/2000JE001362.

Bachiller, R., K. M. Menten, and S. del Rio Alvarez (1990), Anatomy of a dark cloud - A multimolecular study of Barnard 1, *A&A*, *236*, 461–471.

Bai, X.-N., and J. M. Stone (2011), Effect of Ambipolar Diffusion on the Nonlinear Evolution of Magnetorotational Instability in Weakly Ionized Disks, *ApJ*, *736*, 144, doi:10.1088/0004-637X/736/2/144.

Balbus, S. A., and J. F. Hawley (1991), A powerful local shear instability in weakly magnetized disks. I - Linear analysis. II - Nonlinear evolution, *ApJ*, *376*, 214–233, doi:10.1086/170270.

Balmaceda, L. A., S. K. Solanki, N. A. Krivova, and S. Foster (2009), A homogeneous database of sunspot areas covering more than 130 years, *Journal of Geophysical Research (Space Physics)*, *114*, A07104, doi:10.1029/2009JA014299.

Barnard, E. E. (1907), On a nebulous groundwork in the constellation Taurus., *ApJ*, *25*, 218–225, doi:10.1086/141434.

Barnes, J. J., R. Tartèse, M. Anand, F. M. McCubbin, I. A. Franchi, N. A. Starkey, and S. S. Russell (2014), The origin of water in the primitive moon as revealed by the lunar highlands samples, *Earth and Planetary Science Letters*, *390*(0), 244 – 252, doi:http://dx.doi.org/10.1016/j.epsl.2014.01.015.

Barrado Y Navascués, D. (2006), On the age of the TW Hydrae association and 2M1207334-393254, *A&A*, *459*, 511–518, doi:10.1051/0004-6361:20065717.

Basri, G., G. W. Marcy, and J. A. Valenti (1992), Limits on the magnetic flux of pre-main-sequence stars, *ApJ*, *390*, 622–633, doi:10.1086/171312.

Beckwith, S., M. F. Skrutskie, B. Zuckerman, and H. M. Dyck (1984), Discovery of solar system-size halos around young stars, *ApJ*, *287*, 793–800, doi:10.1086/162738.

Beckwith, S. V. W., and A. I. Sargent (1993), Molecular line emission from circumstellar disks, *ApJ*, *402*, 280–291, doi:10.1086/172131.

Beckwith, S. V. W., A. I. Sargent, R. S. Chini, and R. Guesten (1990), A survey for circumstellar disks around young stellar objects, *AJ*, *99*, 924–945, doi:10.1086/115385.

Bergin, E., N. Calvet, P. D'Alessio, and G. J. Herczeg (2003), The Effects of UV Continuum and Lyα Radiation on the Chemical Equilibrium of T Tauri Disks, *ApJ*, *591*, L159–L162, doi:10.1086/377148.

Bergin, E., et al. (2004), A New Probe of the Planet-forming Region in T Tauri Disks, *ApJ*, *614*, L133–L136, doi:10.1086/425865.

Bergin, E. A., W. D. Langer, and P. F. Goldsmith (1995), Gas-phase chemistry in dense interstellar clouds including grain surface molecular depletion and desorption, *ApJ*, *441*, 222–243, doi:10.1086/175351.

Bergin, E. A., D. A. Neufeld, and G. J. Melnick (1999), Formation of Interstellar Ices behind Shock Waves, *ApJ*, *510*, L145–L148, doi:10.1086/311817.

Bergin, E. A., J. Alves, T. Huard, and C. J. Lada (2002), N_2H^+ and $C^{18}O$ Depletion in a Cold Dark Cloud, *ApJ*, *570*, L101–L104, doi:10.1086/340950.

Bergin, E. A., Y. Aikawa, G. A. Blake, and E. F. van Dishoeck (2007), The Chemical Evolution of Protoplanetary Disks, *Protostars and Planets V*, pp. 751–766.

Bergin, E. A., L. I. Cleeves, N. Crockett, and G. A. Blake (2014), Exploring the Origins of Carbon in Terrestrial Worlds, *Faraday Discussions*, *168*, 61–79.

Bergin, E. A., et al. (2013), An old disk still capable of forming a planetary system, *Nature*, *493*, 644–646, doi:10.1038/nature11805.

Bethell, T. J., and E. A. Bergin (2011a), The Propagation of Lyα in Evolving Protoplanetary Disks, *ApJ*, *739*, 78, doi:10.1088/0004-637X/739/2/78.

Bethell, T. J., and E. A. Bergin (2011b), Photoelectric Cross-sections of Gas and Dust in Protoplanetary Disks, *ApJ*, *740*, 7, doi:10.1088/0004-637X/740/1/7.

Beuther, H., R. S. Klessen, C. P. Dullemond, and T. Henning (2014), Protostars and Planets VI, *Protostars and Planets VI*, doi:10.2458/azu:uapress:9780816531240.

Birnstiel, T., and S. M. Andrews (2014), On the Outer Edges of Protoplanetary Dust Disks, *ApJ*, *780*, 153, doi:10.1088/0004-637X/780/2/153.

Biver, N., et al. (2012), Ammonia and other parent molecules in comet 10P/Tempel 2 from Herschel/HIFI and ground-based radio observations, *A&A*, *539*, A68, doi:10.1051/0004-6361/201118447.

Blaauw, A. (1964), The O Associations in the Solar Neighborhood, *ARA&A*, *2*, 213, doi:10.1146/annurev.aa.02.090164.001241.

Blaauw, A. (1991), OB Associations and the Fossil Record of Star Formation, in *NATO Advanced Science Institutes (ASI) Series C*, *NATO Advanced Science Institutes (ASI) Series C*, vol. 342, edited by C. J. Lada and N. D. Kylafis, p. 125.

Black, J. H., E. F. van Dishoeck, S. P. Willner, and R. C. Woods (1990), Interstellar absorption lines toward NGC 2264 and AFGL 2591 - Abundances of H2, H3(+), and CO, *ApJ*, *358*, 459–467, doi:10.1086/168999.

Blitz, L. (1993), Giant molecular clouds, in *Protostars and Planets III*, edited by E. H. Levy and J. I. Lunine, pp. 125–161.

Bockelée-Morvan, D., J. Crovisier, M. J. Mumma, and H. A. Weaver (2004), *The composition of cometary volatiles*, pp. 391–423, University of Arizona Press.

Bockelée-Morvan, D., et al. (1998), Deuterated Water in Comet C/1996 B2 (Hyakutake) and Its Implications for the Origin of Comets, *Icarus*, *133*, 147–162, doi:10.1006/icar.1998.5916.

Boogert, A. C. A., A. G. G. M. Tielens, C. Ceccarelli, A. M. S. Boonman, E. F. van Dishoeck, J. V. Keane, D. C. B. Whittet, and T. de Graauw (2000), Infrared observations of hot gas and cold ice toward the low mass protostar Elias 29, *A&A*, *360*, 683–698.

Boogert, A. C. A., M. R. Hogerheijde, C. Ceccarelli, A. G. G. M. Tielens, E. F. van Dishoeck, G. A. Blake, W. B. Latter, and F. Motte (2002), The environment and nature of the class i protostar elias 29: Molecular gas observations and the location of ices, *The Astrophysical Journal*, *570*(2), 708.

Boss, A. P. (1997), Giant planet formation by gravitational instability., *Science*, *276*, 1836–1839, doi:10.1126/science.276.5320.1836.

Botschwina, P., M. Horn, J. Flugge, and S. Seeger (1993), Ab initio calculations on molecules of interest to interstellar cloud chemistry, *J. Chem. Soc., Faraday Trans.*, *89*, 2219–2230, doi:10.1039/FT9938902219.

Bouvier, J., and C. Bertout (1989), Spots on T Tauri stars, *A&A*, *211*, 99–114.

Brauer, F., C. P. Dullemond, and T. Henning (2008), Coagulation, fragmentation and radial motion of solid particles in protoplanetary disks, *A&A*, *480*, 859–877, doi:10.1051/0004-6361:20077759.

Brickhouse, N. S., S. R. Cranmer, A. K. Dupree, G. J. M. Luna, and S. Wolk (2010), A Deep Chandra X-Ray Spectrum of the Accreting Young Star TW Hydrae, *ApJ*, *710*, 1835–1847, doi:10.1088/0004-637X/710/2/1835.

Brinch, C., and M. R. Hogerheijde (2010), LIME - a flexible, non-LTE line excitation and radiation transfer method for millimeter and far-infrared wavelengths, *A&A*, *523*, A25+, doi:10.1051/0004-6361/201015333.

Bringa, E. M., and R. E. Johnson (2004), A New Model for Cosmic-Ray Ion Erosion of Volatiles from Grains in the Interstellar Medium, *The Astrophysical Journal*, *603*(1), 159–164.

Brown, J. M., G. A. Blake, C. Qi, C. P. Dullemond, and D. J. Wilner (2008), Lkh 330: Evidence for dust clearing through resolved submillimeter imaging, *The Astrophysical Journal Letters*, *675*(2), L109.

Brown, J. M., G. J. Herczeg, K. M. Pontoppidan, and E. F. van Dishoeck (2012), A 30 AU Radius CO Gas Hole in the Disk around the Herbig Ae Star Oph IRS 48, *ApJ*, *744*, 116, doi:10.1088/0004-637X/744/2/116.

Bruderer, S. (2013), Survival of molecular gas in cavities of transition disks. I. CO, *A&A*,

559, A46, doi:10.1051/0004-6361/201321171.

Bruderer, S., E. F. van Dishoeck, S. D. Doty, and G. J. Herczeg (2012), The warm gas atmosphere of the HD 100546 disk seen by Herschel. Evidence of a gas-rich, carbon-poor atmosphere?, *A&A*, *541*, A91, doi:10.1051/0004-6361/201118218.

Bryden, G., X. Chen, D. N. C. Lin, R. P. Nelson, and J. C. B. Papaloizou (1999), Tidally Induced Gap Formation in Protostellar Disks: Gap Clearing and Suppression of Protoplanetary Growth, *ApJ*, *514*, 344–367, doi:10.1086/306917.

Burger, R. A., M. S. Potgieter, and B. Heber (2000), Rigidity dependence of cosmic ray proton latitudinal gradients measured by the Ulysses spacecraft: Implications for the diffusion tensor, *J. Geophys. Res.*, *105*, 27,447–27,456, doi:10.1029/2000JA000153.

Burlaga, L. F., N. F. Ness, M. H. Acuña, R. P. Lepping, J. E. P. Connerney, E. C. Stone, and F. B. McDonald (2005), Crossing the Termination Shock into the Heliosheath: Magnetic Fields, *Science*, *309*, 2027–2029, doi:10.1126/science.1117542.

Caballero-Lopez, R. A., and H. Moraal (2004), Limitations of the force field equation to describe cosmic ray modulation, *Journal of Geophysical Research: Space Physics*, *109*(A1), n/a–n/a, doi:10.1029/2003JA010098.

Calvet, N., and P. D'Alessio (2011), *Protoplanetary Disk Structure and Evolution*, pp. 14–54.

Calvet, N., and E. Gullbring (1998), The Structure and Emission of the Accretion Shock in T Tauri Stars, *ApJ*, *509*, 802–818, doi:10.1086/306527.

Calvet, N., A. Patino, G. C. Magris, and P. D'Alessio (1991), Irradiation of accretion disks around young objects. I - Near-infrared CO bands, *ApJ*, *380*, 617–630, doi:10.1086/170618.

Calvet, N., P. D'Alessio, L. Hartmann, D. Wilner, A. Walsh, and M. Sitko (2002), Evidence for a Developing Gap in a 10 Myr Old Protoplanetary Disk, *ApJ*, *568*, 1008–1016, doi:10.1086/339061.

Calvet, N., J. Muzerolle, C. Briceño, J. Hernández, L. Hartmann, J. L. Saucedo, and K. D. Gordon (2004), The Mass Accretion Rates of Intermediate-Mass T Tauri Stars, *AJ*, *128*, 1294–1318, doi:10.1086/422733.

Calvet, N., et al. (2005), Disks in Transition in the Taurus Population: Spitzer IRS Spectra of GM Aurigae and DM Tauri, *ApJ*, *630*, L185–L188, doi:10.1086/491652.

Cameron, A. G. W. (1978), Physics of the primitive solar accretion disk, *Moon and Planets*, *18*, 5–40, doi:10.1007/BF00896696.

Cameron, A. G. W., and J. W. Truran (1977), The supernova trigger for formation of the solar system, *Icarus*, *30*, 447–461, doi:10.1016/0019-1035(77)90101-4.

Carkner, L., E. D. Feigelson, K. Koyama, T. Montmerle, and I. N. Reid (1996), X-Ray-emitting T Tauri Stars in the L1551 Cloud, *ApJ*, *464*, 286, doi:10.1086/177320.

Carr, J. S., and J. R. Najita (2008), Organic Molecules and Water in the Planet Formation Region of Young Circumstellar Disks, *Science*, *319*, 1504–, doi:10.1126/science.1153807.

Caselli, P., C. M. Walmsley, R. Terzieva, and E. Herbst (1998), The Ionization Fraction in Dense Cloud Cores, *ApJ*, *499*, 234, doi:10.1086/305624.

Caselli, P., T. Stantcheva, O. Shalabiea, V. I. Shematovich, and E. Herbst (2002), Deuterium fractionation on interstellar grains studied with modified rate equations and a Monte Carlo approach, *Planet. Space Sci.*, *50*, 1257–1266, doi:10.1016/S0032-0633(02)00092-2.

Ceccarelli, C., C. Dominik, B. Lefloch, P. Caselli, and E. Caux (2004), Detection of H_2D^+: Measuring the Midplane Degree of Ionization in the Disks of DM Tauri and TW Hydrae, *ApJ*, *607*, L51–L54, doi:10.1086/421461.

Ceccarelli, C., P. Caselli, D. Bockelee-Morvan, O. Mousis, S. Pizzarello, F. Robert, and D. Semenov (2014), Deuterium Fractionation: the Ariadne's Thread from the Pre-collapse Phase to Meteorites and Comets today, *Protostars and Planets VI*.

Cesarsky, C. J., and H. J. Volk (1978), Cosmic Ray Penetration into Molecular Clouds, *A&A*, *70*, 367.

Chandrasekhar, S. (1960), The Stability of Non-Dissipative Couette Flow in Hydromagnetics, *Proceedings of the National Academy of Science*, *46*, 253–257, doi:10.1073/pnas.46.2.253.

Chapillon, E., B. Parise, S. Guilloteau, and F. Du (2011), A deep search for H_2D^+ in protoplanetary disks. Perspectives for ALMA, *A&A*, *533*, A143, doi:10.1051/0004-6361/201117354.

Chen, Y.-J., et al. (2015), Formation of S-bearing Species by VUV/EUV Irradiation of H_2S-containing Ice Mixtures: Photon Energy and Carbon Source Effects, *ApJ*, *798*, 80, doi:10.1088/0004-637X/798/2/80.

Ciesla, F. J. (2014), The Phases of Water Ice in the Solar Nebula, *ApJ*, *784*, L1, doi:10.1088/2041-8205/784/1/L1.

Ciesla, F. J., and S. A. Sandford (2012), Organic Synthesis via Irradiation and Warming of Ice Grains in the Solar Nebula, *Science*, *336*, 452–, doi:10.1126/science.1217291.

Cieza, L., et al. (2007), The Spitzer c2d Survey of Weak-Line T Tauri Stars. II. New Constraints on the Timescale for Planet Building, *ApJ*, *667*, 308–328, doi:10.1086/520698.

Cieza, L. A., et al. (2010), The Nature of Transition Circumstellar Disks. I. The Ophiuchus Molecular Cloud, *ApJ*, *712*, 925–941, doi:10.1088/0004-637X/712/2/925.

Cohen, O. (2011), The independency of stellar mass-loss rates on stellar X-ray luminosity and activity level based on solar X-ray flux and solar wind observations, *MNRAS*, *417*, 2592–2600, doi:10.1111/j.1365-2966.2011.19428.x.

Cohen, O., J. J. Drake, and J. Kóta (2012), The Cosmic-Ray Intensity near the Archean Earth, *ApJ*, *760*, 85, doi:10.1088/0004-637X/760/1/85.

Collings, M. P., J. W. Dever, H. J. Fraser, and M. R. S. McCoustra (2003), Laboratory studies of the interaction of carbon monoxide with water ice, *Ap&SS*, *285*, 633–659, doi:10.1023/A:1026144806831.

Collings, M. P., M. A. Anderson, R. Chen, J. W. Dever, S. Viti, D. A. Williams, and M. R. S. McCoustra (2004), A laboratory survey of the thermal desorption of astrophysically relevant molecules, *MNRAS*, *354*, 1133–1140, doi:10.1111/j.1365-2966.2004.08272.x.

Consolmagno, G. J., and J. R. Jokipii (1978), 26Al and the partial ionization of the solar nebula, *The moon and the planets*, *19*(2), 253–259, doi:10.1007/BF00896999.

Coutens, A., C. Vastel, E. Caux, C. Ceccarelli, S. Bottinelli, L. Wiesenfeld, A. Faure, Y. Scribano, and C. Kahane (2012), A study of deuterated water in the low-mass protostar IRAS 16293-2422, *A&A*, *539*, A132, doi:10.1051/0004-6361/201117627.

Crutcher, R. M. (2012), Magnetic Fields in Molecular Clouds, *ARA&A*, *50*, 29–63, doi:10.1146/annurev-astro-081811-125514.

Crutcher, R. M., B. Wandelt, C. Heiles, E. Falgarone, and T. H. Troland (2010), Magnetic Fields in Interstellar Clouds from Zeeman Observations: Inference of Total Field Strengths by Bayesian Analysis, *ApJ*, *725*, 466–479, doi:10.1088/0004-637X/725/1/466.

Cutri, R. M., et al. (2003), *2MASS All Sky Catalog of point sources.*

D'Alessio, P., J. Canto, N. Calvet, and S. Lizano (1998), Accretion Disks around Young Objects. I. The Detailed Vertical Structure, *ApJ*, *500*, 411–427, doi:10.1086/305702.

D'Alessio, P., N. Calvet, L. Hartmann, R. Franco-Hernández, and H. Servín (2006), Effects of Dust Growth and Settling in T Tauri Disks, *ApJ*, *638*, 314–335, doi:10.1086/498861.

Dalgarno, A. (2006), Interstellar Chemistry Special Feature: The galactic cosmic ray ionization rate, *Proceedings of the National Academy of Science*, *103*, 12,269–12,273, doi:10.1073/pnas.0602117103.

Dalgarno, A., M. Yan, and W. Liu (1999), Electron Energy Deposition in a Gas Mixture of Atomic and Molecular Hydrogen and Helium, *ApJS*, *125*, 237–256, doi:10.1086/313267.

Dartois, E., W.-F. Thi, T. R. Geballe, D. Deboffle, L. d'Hendecourt, and E. van Dishoeck (2003), Revisiting the solid HDO/H_2O abundances, *A&A*, *399*, 1009–1020, doi:10.1051/0004-6361:20021558.

Dauphas, N., and M. Chaussidon (2011), A Perspective from Extinct Radionuclides on a Young Stellar Object: The Sun and Its Accretion Disk, *Annual Review of Earth and Planetary Sciences*, *39*, 351–386, doi:10.1146/annurev-earth-040610-133428.

Davis, L. (1955), Interplanetary Magnetic Fields and Cosmic Rays, *Physical Review*, *100*, 1440–1444, doi:10.1103/PhysRev.100.1440.

Debes, J. H., H. Jang-Condell, A. J. Weinberger, A. Roberge, and G. Schneider (2013),

The 0.5-2.22 μm Scattered Light Spectrum of the Disk around TW Hya: Detection of a Partially Filled Disk Gap at 80 AU, *ApJ*, *771*, 45, doi:10.1088/0004-637X/771/1/45.

Decampli, W. M. (1981), T Tauri winds, *ApJ*, *244*, 124–146, doi:10.1086/158691.

Decker, R. B., S. M. Krimigis, E. C. Roelof, and M. E. Hill (2012), No meridional plasma flow in the heliosheath transition region, *Nature*, *489*, 124–127, doi:10.1038/nature11441.

Deloule, E., and F. Robert (1995), Interstellar water in meteorites?, *Geochim. Cosmochim. Acta*, *59*, 4695–4706, doi:10.1016/0016-7037(95)00313-4.

Desch, S. J., H. C. Connolly, Jr., and G. Srinivasan (2004), An Interstellar Origin for the Beryllium 10 in Calcium-rich, Aluminum-rich Inclusions, *ApJ*, *602*, 528–542, doi:10.1086/380831.

Diehl, R., et al. (2006), Radioactive ^{26}Al from massive stars in the Galaxy, *Nature*, *439*, 45–47, doi:10.1038/nature04364.

Dolginov, A. Z., and T. F. Stepinski (1994), Are cosmic rays effective for ionization of protoplanetary disks?, *ApJ*, *427*, 377–383, doi:10.1086/174146.

Donati, J.-F. (2003), ESPaDOnS: An Echelle SpectroPolarimetric Device for the Observation of Stars at CFHT, in *Solar Polarization*, *Astronomical Society of the Pacific Conference Series*, vol. 307, edited by J. Trujillo-Bueno and J. Sanchez Almeida, p. 41.

Donati, J.-F., S. G. Gregory, S. H. P. Alencar, G. Hussain, J. Bouvier, C. Dougados, M. M. Jardine, F. Ménard, and M. M. Romanova (2012), Magnetometry of the classical T Tauri star GQ Lup: non-stationary dynamos and spin evolution of young Suns, *MNRAS*, *425*, 2948–2963, doi:10.1111/j.1365-2966.2012.21482.x.

Donati, J.-F., et al. (2007), Magnetic fields and accretion flows on the classical T Tauri star V2129 Oph, *MNRAS*, *380*, 1297–1312, doi:10.1111/j.1365-2966.2007.12194.x.

Donati, J.-F., et al. (2011a), The large-scale magnetic field and poleward mass accretion of the classical T Tauri star TW Hya, *MNRAS*, *417*, 472–487, doi:10.1111/j.1365-2966.2011.19288.x.

Donati, J.-F., et al. (2011b), The close classical T Tauri binary V4046 Sgr: complex magnetic fields and distributed mass accretion, *MNRAS*, *417*, 1747–1759, doi:10.1111/j.1365-2966.2011.19366.x.

Draine, B. T. (1978), Photoelectric heating of interstellar gas, *ApJS*, *36*, 595–619, doi:10.1086/190513.

Draine, B. T., and H. M. Lee (1984), Optical properties of interstellar graphite and silicate grains, *ApJ*, *285*, 89–108, doi:10.1086/162480.

Du, F. (2012), Modeling Gas-Grain Chemistry in Dark Cloud Conditions, *Dissertation*, *Ch. 6*, 101–178.

Duchêne, G., H. Beust, F. Adjali, Q. M. Konopacky, and A. M. Ghez (2006), Accurate stellar masses in the multiple system T Tauri, *A&A*, *457*, L9–L12, doi:10.1051/0004-6361:20065917.

Dullemond, C. P., and C. Dominik (2004), The effect of dust settling on the appearance of protoplanetary disks, *A&A*, *421*, 1075–1086, doi:10.1051/0004-6361:20040284.

Dullemond, C. P., and C. Dominik (2005), Dust coagulation in protoplanetary disks: A rapid depletion of small grains, *Astronomy and Astrophysics*, *434*(3), 971–986.

Dullemond, C. P., C. Dominik, and A. Natta (2001), Passive Irradiated Circumstellar Disks with an Inner Hole, *ApJ*, *560*, 957–969, doi:10.1086/323057.

Dunham, M. M., et al. (2014), The Evolution of Protostars: Insights from Ten Years of Infrared Surveys with Spitzer and Herschel, *Protostars and Planets VI*, pp. 195–218, doi:10.2458/azuuapress9780816531240-ch009.

Dupree, A. K., et al. (2012), TW Hya: Spectral Variability, X-Rays, and Accretion Diagnostics, *ApJ*, *750*, 73, doi:10.1088/0004-637X/750/1/73.

Dutrey, A., S. Guilloteau, and M. Simon (1994), Images of the GG Tauri rotating ring, *A&A*, *286*, 149–159.

Dutrey, A., S. Guilloteau, and M. Guelin (1997), Chemistry of protosolar-like nebulae: The molecular content of the DM Tau and GG Tau disks., *A&A*, *317*, L55–L58.

Dutrey, A., et al. (2007), Chemistry in disks. I. Deep search for $N2H^+$ in the protoplanetary disks around LkCa 15, MWC 480, and DM Tauri, *A&A*, *464*, 615–623, doi:10.1051/0004-6361:20065385.

Dutrey, A., et al. (2014), Physical and Chemical Structure of Planet-Forming Disks Probed by Millimeter Observations and Modeling, *Protostars and Planets VI*, pp. 317–338.

Dyck, H. M., T. Simon, and B. Zuckerman (1982), Discovery of an infrared companion to T Tauri, *ApJ*, *255*, L103–L106, doi:10.1086/183778.

Eberhardt, P., M. Reber, D. Krankowsky, and R. R. Hodges (1995), The D/H and ˆ18ˆO/ˆ16ˆO ratios in water from comet P/Halley., *A&A*, *302*, 301.

Elmegreen, B. G., and C. J. Lada (1977), Sequential formation of subgroups in OB associations, *ApJ*, *214*, 725–741, doi:10.1086/155302.

Encrenaz, T. (2008), Water in the Solar System, *ARA&A*, *46*, 57–87, doi:10.1146/annurev.astro.46.060407.145229.

Ercolano, B., and A. E. Glassgold (2013), X-ray ionization rates in protoplanetary discs, *MNRAS*, *436*, 3446–3450, doi:10.1093/mnras/stt1826.

Espaillat, C. (2009), The Evolution of Dusty Disks Around Low-Mass Pre-Main Sequence Stars, Ph.D. thesis, University of Michigan.

Espaillat, C., P. D'Alessio, J. Hernández, E. Nagel, K. L. Luhman, D. M. Watson, N. Calvet, J. Muzerolle, and M. McClure (2010), Unveiling the Structure of Pre-transitional Disks, *ApJ*, *717*, 441–457, doi:10.1088/0004-637X/717/1/441.

Espaillat, C., et al. (2007), Probing the Dust and Gas in the Transitional Disk of CS Cha with Spitzer, *ApJ*, *664*, L111–L114, doi:10.1086/520879.

Falgarone, E., T. H. Troland, R. M. Crutcher, and G. Paubert (2008), CN Zeeman measurements in star formation regions, *A&A*, *487*, 247–252, doi:10.1051/0004-6361:200809577.

Fatuzzo, M., and F. C. Adams (2008), UV Radiation Fields Produced by Young Embedded Star Clusters, *ApJ*, *675*, 1361–1374, doi:10.1086/527469.

Fatuzzo, M., and F. C. Adams (2014), Effects of Turbulence on Cosmic Ray Propagation in Protostars and Young Star/Disk Systems, *ApJ*, *787*, 26, doi:10.1088/0004-637X/787/1/26.

Fatuzzo, M., F. C. Adams, and F. Melia (2006), Enhanced Cosmic-Ray Flux and Ionization for Star Formation in Molecular Clouds Interacting with Supernova Remnants, *ApJ*, *653*, L49–L52, doi:10.1086/510408.

Favata, F., and G. Micela (2003), Stellar Coronal Astronomy, *Space Sci. Rev.*, *108*, 577–708, doi:10.1023/B:SPAC.0000007491.80144.21.

Favre, C., L. I. Cleeves, E. A. Bergin, C. Qi, and G. A. Blake (2013), A Significantly Low CO Abundance toward the TW Hya Protoplanetary Disk: A Path to Active Carbon Chemistry?, *ApJ*, *776*, L38, doi:10.1088/2041-8205/776/2/L38.

Feigelson, E. D. (1996), Dispersed T Tauri Stars and Galactic Star Formation, *ApJ*, *468*, 306, doi:10.1086/177691.

Feigelson, E. D., and W. M. Decampli (1981a), Observations of X-ray emission from T Tauri stars, *ApJ*, *243*, L89–L93, doi:10.1086/183449.

Feigelson, E. D., and W. M. Decampli (1981b), Observations of X-ray emission from T Tauri stars, *ApJ*, *243*, L89–L93, doi:10.1086/183449.

Feigelson, E. D., and G. A. Kriss (1981), Discovery of three X-ray luminous pre-main-sequence stars, *ApJ*, *248*, L35–L38, doi:10.1086/183618.

Feigelson, E. D., and T. Montmerle (1999), High-Energy Processes in Young Stellar Objects, *ARA&A*, *37*, 363–408, doi:10.1146/annurev.astro.37.1.363.

Feigelson, E. D., S. Casanova, T. Montmerle, and J. Guibert (1993), ROSAT X-Ray Study of the Chamaeleon I Dark Cloud. I. The Stellar Population, *ApJ*, *416*, 623, doi:10.1086/173264.

Feigelson, E. D., P. Broos, J. A. Gaffney, III, G. Garmire, L. A. Hillenbrand, S. H. Pravdo, L. Townsley, and Y. Tsuboi (2002), X-Ray-emitting Young Stars in the Orion Nebula, *ApJ*, *574*, 258–292, doi:10.1086/340936.

Feuchtgruber, H., et al. (2013), The D/H ratio in the atmospheres of Uranus and Neptune from Herschel-PACS observations, *A&A*, *551*, A126, doi:10.1051/0004-6361/201220857.

Finocchi, F., and H.-P. Gail (1997), Chemical reactions in protoplanetary accretion disks. III. The role of ionisation processes., *A&A*, *327*, 825–844.

Flaccomio, E., G. Micela, and S. Sciortino (2012), X-ray variability of pre-main-sequence stars. Toward an explanation of the different X-ray properties of classical and weak-line T Tauri stars, *A&A*, *548*, A85, doi:10.1051/0004-6361/201219362.

Fleming, T., and J. M. Stone (2003), Local Magnetohydrodynamic Models of Layered Accretion Disks, *ApJ*, *585*, 908–920, doi:10.1086/345848.

Flock, M., T. Henning, and H. Klahr (2012), Turbulence in weakly-ionized proto-planetary disks, *ArXiv e-prints*.

Florinski, V., S. E. S. Ferreira, and N. V. Pogorelov (2011), Galactic Cosmic Rays in the Outer Heliosphere: Theory and Models, *Space Sci. Rev.*, p. 111, doi:10.1007/s11214-011-9756-1.

Flower, D. R. (1999), Rotational excitation of HCO^+ by H_2, *MNRAS*, *305*, 651–653, doi:10.1046/j.1365-8711.1999.02451.x.

Flower, D. R., G. Pineau Des Forêts, and C. M. Walmsley (2006), The importance of the ortho:para H_2 ratio for the deuteration of molecules during pre-protostellar collapse, *A&A*, *449*, 621–629, doi:10.1051/0004-6361:20054246.

Fogel, J. K. J. (2011), Chemical Evolution in Protoplanetary Disks, Ph.D. thesis, University of Michigan.

Fogel, J. K. J., T. J. Bethell, E. A. Bergin, N. Calvet, and D. Semenov (2011), Chemistry of a Protoplanetary Disk with Grain Settling and Lyα Radiation, *ApJ*, *726*, 29, doi:10.1088/0004-637X/726/1/29.

France, K., E. Schindhelm, E. A. Bergin, E. Roueff, and H. Abgrall (2014), High-resolution Ultraviolet Radiation Fields of Classical T Tauri Stars, *ApJ*, *784*, 127, doi:10.1088/0004-637X/784/2/127.

Fromang, S., C. Terquem, and S. A. Balbus (2002), The ionization fraction in α models of protoplanetary discs, *MNRAS*, *329*, 18–28, doi:10.1046/j.1365-8711.2002.04940.x.

Furlan, E., et al. (2006), A Survey and Analysis of Spitzer Infrared Spectrograph Spectra of T Tauri Stars in Taurus, *ApJS*, *165*, 568–605, doi:10.1086/505468.

Furuya, K., and Y. Aikawa (2014), Reprocessing of Ices in Turbulent Protoplanetary Disks: Carbon and Nitrogen Chemistry, *ApJ*, *790*, 97, doi:10.1088/0004-637X/790/2/97.

Furuya, K., Y. Aikawa, H. Nomura, F. Hersant, and V. Wakelam (2013), Water in Protoplanetary Disks: Deuteration and Turbulent Mixing, *ApJ*, *779*, 11, doi:10.1088/0004-637X/779/1/11.

Gaidos, E., A. N. Krot, J. P. Williams, and S. N. Raymond (2009), ^{26}Al and the Formation of the Solar System from a Molecular Cloud Contaminated by Wolf-Rayet Winds, *ApJ*, *696*, 1854–1863, doi:10.1088/0004-637X/696/2/1854.

Gammie, C. F. (1996), Layered Accretion in T Tauri Disks, *ApJ*, *457*, 355, doi:10.1086/176735.

Garrod, R. T., and E. Herbst (2006), Formation of methyl formate and other organic species in the warm-up phase of hot molecular cores, *A&A*, *457*, 927–936, doi:10.1051/0004-6361:20065560.

Garrod, R. T., and T. Pauly (2011), On the Formation of CO_2 and Other Interstellar Ices, *ApJ*, *735*, 15, doi:10.1088/0004-637X/735/1/15.

Garrod, R. T., V. Wakelam, and E. Herbst (2007), Non-thermal desorption from interstellar dust grains via exothermic surface reactions, *A&A*, *467*, 1103–1115, doi:10.1051/0004-6361:20066704.

Garrod, R. T., S. L. W. Weaver, and E. Herbst (2008), Complex Chemistry in Star-forming Regions: An Expanded Gas-Grain Warm-up Chemical Model, *ApJ*, *682*, 283–302, doi:10.1086/588035.

Geiss, J., and G. Gloeckler (2003), Isotopic Composition of H, HE and NE in the Protosolar Cloud, *Space Sci. Rev.*, *106*, 3–18, doi:10.1023/A:1024651232758.

Gerakines, P. A., W. A. Schutte, and P. Ehrenfreund (1996), Ultraviolet processing of interstellar ice analogs. I. Pure ices., *A&A*, *312*, 289–305.

Getman, K. V., E. D. Feigelson, P. S. Broos, G. Micela, and G. P. Garmire (2008), X-Ray Flares in Orion Young Stars. I. Flare Characteristics, *ApJ*, *688*, 418–436, doi:10.1086/592033.

Getman, K. V., et al. (2005), Chandra Orion Ultradeep Project: Observations and Source Lists, *ApJS*, *160*, 319–352, doi:10.1086/432092.

Girart, J. M., R. Rao, and D. P. Marrone (2006), Magnetic Fields in the Formation of Sun-Like Stars, *Science*, *313*, 812–814, doi:10.1126/science.1129093.

Glassgold, A. E. (1999), Circumstellar Chemistry of AGB Winds, in *Asymptotic Giant Branch Stars*, *IAU Symposium*, vol. 191, edited by T. Le Bertre, A. Lebre, and C. Waelkens, p. 337.

Glassgold, A. E., and W. D. Langer (1973), Heating of Molecular-Hydrogen Clouds by Cosmic Rays and X-Rays, *ApJ*, *186*, 859–888, doi:10.1086/152552.

Glassgold, A. E., and J. R. Najita (2001), The Effects of X-Rays on the Diffuse Gas in Protoplanetary Disks, in *Young Stars Near Earth: Progress and Prospects*, *Astronomical Society of the Pacific Conference Series*, vol. 244, edited by R. Jayawardhana and T. Greene, p. 251.

Glassgold, A. E., J. Najita, and J. Igea (1997), X-Ray Ionization of Protoplanetary Disks, *ApJ*, *480*, 344–+, doi:10.1086/303952.

Glassgold, A. E., J. Najita, and J. Igea (2004), Heating Protoplanetary Disk Atmospheres, *ApJ*, *615*, 972–990, doi:10.1086/424509.

Glassgold, A. E., D. Galli, and M. Padovani (2012), Cosmic-Ray and X-Ray Heating of Interstellar Clouds and Protoplanetary Disks, *ApJ*, *756*, 157, doi:10.1088/0004-637X/756/2/157.

Gleeson, L. J., and W. I. Axford (1967), Cosmic Rays in the Interplanetary Medium, *ApJ*, *149*, L115, doi:10.1086/180070.

Gleeson, L. J., and W. I. Axford (1968), Solar Modulation of Galactic Cosmic Rays, *ApJ*, *154*, 1011, doi:10.1086/149822.

Goldreich, P., and W. R. Ward (1973), The Formation of Planetesimals, *ApJ*, *183*, 1051–1062, doi:10.1086/152291.

Gombosi, T. I. (2004), *Physics of the Space Environment*.

Gorti, U., and D. Hollenbach (2008), Line Emission from Gas in Optically Thick Dust Disks around Young Stars, *ApJ*, *683*, 287–303, doi:10.1086/589616.

Gorti, U., and D. Hollenbach (2009), Photoevaporation of Circumstellar Disks By Far-Ultraviolet, Extreme-Ultraviolet and X-Ray Radiation from the Central Star, *ApJ*, *690*, 1539–1552, doi:10.1088/0004-637X/690/2/1539.

Gorti, U., D. Hollenbach, J. Najita, and I. Pascucci (2011), Emission Lines from the Gas Disk around TW Hydra and the Origin of the Inner Hole, *ApJ*, *735*, 90, doi:10.1088/0004-637X/735/2/90.

Gounelle, M., and G. Meynet (2012), Solar system genealogy revealed by extinct short-lived radionuclides in meteorites, *A&A*, *545*, A4, doi:10.1051/0004-6361/201219031.

Gounelle, M., F. H. Shu, H. Shang, A. E. Glassgold, K. E. Rehm, and T. Lee (2001), Extinct Radioactivities and Protosolar Cosmic Rays: Self-Shielding and Light Elements, *ApJ*, *548*, 1051–1070, doi:10.1086/319019.

Gounelle, M., A. Meibom, P. Hennebelle, and S.-i. Inutsuka (2009), Supernova Propagation and Cloud Enrichment: A New Model for the Origin of ^{60}Fe in the Early Solar System, *ApJ*, *694*, L1–L5, doi:10.1088/0004-637X/694/1/L1.

Gray, C. M. (1974), Excess ^{26}Mg in the Allende Meteorite, *Nature*, *251*, 495–497, doi:10.1038/251495a0.

Greenberg, J. M., and A. Li (1999), Morphological Structure and Chemical Composition of Cometary Nuclei and Dust, *Space Sci. Rev.*, *90*, 149–161, doi:10.1023/A:1005298014670.

Gressel, O., R. P. Nelson, and N. J. Turner (2012), Dead zones as safe havens for planetesimals: influence of disc mass and external magnetic field, *MNRAS*, *422*, 1140–1159, doi:10.1111/j.1365-2966.2012.20701.x.

Grim, R. J. A., and J. M. Greenberg (1987), Photoprocessing of H2S in interstellar grain mantles as an explanation for S2 in comets, *A&A*, *181*, 155–168.

Güdel, M., and A. Telleschi (2007), The X-ray soft excess in classical T Tauri stars, *A&A*, *474*, L25–L28, doi:10.1051/0004-6361:20078143.

Guelin, M. (1988), Organic and exotic molecules in space, in *Molecules in Physics, Chemistry, and Biology*, *Topics in Molecular Organization and Engineering*, vol. 2, edited by J. Maruani, pp. 175–187, Springer Netherlands, doi:10.1007/978-94-009-2851-0.

Guenther, E. W., and J. P. Emerson (1997), Spectrophotometry of flares and short time scale variations in weak line, and classical T Tauri stars in Chamaeleon., *A&A*, *321*, 803–810.

Guilloteau, S., V. Piétu, A. Dutrey, and M. Guélin (2006), Deuterated molecules in DM Tauri: DCO^+, but no HDO, *A&A*, *448*, L5–L8, doi:10.1051/0004-6361:200600005.

Guilloteau, S., A. Dutrey, V. Wakelam, F. Hersant, D. Semenov, E. Chapillon, T. Henning, and V. Piétu (2012), Chemistry in disks. VIII. The CS molecule as an analytic tracer of turbulence in disks, *A&A*, *548*, A70, doi:10.1051/0004-6361/201220331.

Gullbring, E., L. Hartmann, C. Briceño, and N. Calvet (1998), Disk Accretion Rates for T Tauri Stars, *ApJ*, *492*, 323–341, doi:10.1086/305032.

Günther, H. M., J. H. M. M. Schmitt, J. Robrade, and C. Liefke (2007), X-ray emission from classical T Tauri stars: accretion shocks and coronae?, *A&A*, *466*, 1111–1121, doi:10.1051/0004-6361:20065669.

Habing, H. J. (1968), The interstellar radiation density between 912 A and 2400 A, *Bull. Astron. Inst. Netherlands*, *19*, 421.

Harries, T. J. (2000), Synthetic line profiles of rotationally distorted hot-star winds, *MNRAS*, *315*, 722–734, doi:10.1046/j.1365-8711.2000.03505.x.

Harries, T. J., J. D. Monnier, N. H. Symington, and R. Kurosawa (2004), Three-dimensional dust radiative-transfer models: the Pinwheel Nebula of WR 104, *MNRAS*, *350*, 565–574, doi:10.1111/j.1365-2966.2004.07668.x.

Hartigan, P., S. Edwards, and L. Ghandour (1995), Disk Accretion and Mass Loss from Young Stars, *ApJ*, *452*, 736, doi:10.1086/176344.

Hartmann, J. (1904), Investigations on the spectrum and orbit of delta Orionis., *ApJ*, *19*, 268–286, doi:10.1086/141112.

Hartmann, L., and S. J. Kenyon (1985), On the nature of FU Orionis objects, *ApJ*, *299*, 462–478, doi:10.1086/163713.

Hartmann, L., N. Calvet, E. Gullbring, and P. D'alessio (1998), Accretion and the Evolution of T Tauri Disks, *The Astrophysical Journal*, *495*(1), 385–400.

Hartmann, L., S. T. Megeath, L. Allen, K. Luhman, N. Calvet, P. D'Alessio, R. Franco-Hernandez, and G. Fazio (2005), IRAC Observations of Taurus Pre-Main-Sequence Stars, *ApJ*, *629*, 881–896, doi:10.1086/431472.

Hartogh, P., et al. (2011), Ocean-like water in the Jupiter-family comet 103P/Hartley 2, *Nature*, *478*, 218–220, doi:10.1038/nature10519.

Hasegawa, T. I., and E. Herbst (1993), New gas-grain chemical models of quiescent dense interstellar clouds - The effects of H2 tunnelling reactions and cosmic ray induced desorption, *MNRAS*, *261*, 83–102.

Hasegawa, T. I., E. Herbst, and C. M. Leung (1992a), Models of gas-grain chemistry in dense interstellar clouds with complex organic molecules, *ApJS*, *82*, 167–195, doi:10.1086/191713.

Hasegawa, T. I., E. Herbst, and C. M. Leung (1992b), Models of gas-grain chemistry in dense interstellar clouds with complex organic molecules, *ApJS*, *82*, 167–195, doi:10.1086/191713.

Hatchell, J., M. A. Thompson, T. J. Millar, and G. H. MacDonald (1998), Sulphur chemistry and evolution in hot cores, *A&A*, *338*, 713–722.

Hawley, J. F., and J. M. Stone (1998), Nonlinear Evolution of the Magnetorotational Instability in Ion-Neutral Disks, *ApJ*, *501*, 758, doi:10.1086/305849.

Hayakawa, S., S. Nishimura, and T. Takayanagi (1961), Radiation from the Interstellar Hydrogen Atoms, *PASJ*, *13*, 184.

Heays, A. N., R. Visser, R. Gredel, W. Ubachs, B. R. Lewis, S. T. Gibson, and E. F. van Dishoeck (2014), Isotope selective photodissociation of N_2 by the interstellar radiation field and cosmic rays, *A&A*, *562*, A61, doi:10.1051/0004-6361/201322832.

Henkel, C., T. L. Wilson, N. Langer, Y.-N. Chin, and R. Mauersberger (1994), Interstellar CNO Isotope Ratios, in *The Structure and Content of Molecular Clouds*, *Lecture Notes in Physics, Berlin Springer Verlag*, vol. 439, edited by T. L. Wilson and K. J. Johnston, pp. 72–88, doi:10.1007/3540586210.

Henning, T., and D. Semenov (2013), Chemistry in protoplanetary disks, *Chemical Reviews*, *113*(12), 9016–9042, doi:10.1021/cr400128p.

Herbst, E., and W. Klemperer (1973), The Formation and Depletion of Molecules in Dense Interstellar Clouds, *ApJ*, *185*, 505–534, doi:10.1086/152436.

Herczeg, G. J., J. L. Linsky, J. A. Valenti, C. M. Johns-Krull, and B. E. Wood (2002), The Far-Ultraviolet Spectrum of TW Hydrae. I. Observations of H_2 Fluorescence, *ApJ*, *572*, 310–325, doi:10.1086/339731.

Herczeg, G. J., B. E. Wood, J. L. Linsky, J. A. Valenti, and C. M. Johns-Krull (2004), The Far-Ultraviolet Spectra of TW Hydrae. II. Models of H_2 Fluorescence in a Disk, *ApJ*, *607*, 369–383, doi:10.1086/383340.

Hernández, J., et al. (2007), A Spitzer Space Telescope Study of Disks in the Young σ Orionis Cluster, *ApJ*, *662*, 1067–1081, doi:10.1086/513735.

Hersant, F., D. Gautier, and J.-M. Huré (2001), A Two-dimensional Model for the Primordial Nebula Constrained by D/H Measurements in the Solar System: Implications for the Formation of Giant Planets, *ApJ*, *554*, 391–407, doi:10.1086/321355.

Ho, P. T. P., and C. H. Townes (1983), Interstellar Ammonia, *Annual Review of Astronomy and Astrophysics*, *21*(1), 239–270.

Ho, P. T. P., J. M. Moran, and K. Y. Lo (2004), The Submillimeter Array, *ApJ*, *616*, L1–L6, doi:10.1086/423245.

Hoff, W., T. Henning, and W. Pfau (1998), The nature of isolated T Tauri stars, *A&A*, *336*, 242–250.

Hogerheijde, M. R., et al. (2011), Detection of the Water Reservoir in a Forming Planetary System, *Science*, *334*, 338–, doi:10.1126/science.1208931.

Hollenbach, D. J., H. W. Yorke, and D. Johnstone (2000), Disk Dispersal around Young Stars, *Protostars and Planets IV*, p. 401.

Horimoto, N., H. S. Kato, and M. Kawai (2002), Stepwise morphological change of porous amorphous ice films observed through adsorption of methane, *J. Chem. Phys.*, *116*, 4375–4378, doi:10.1063/1.1458937.

Hughes, A. M., D. J. Wilner, C. Qi, and M. R. Hogerheijde (2008), Gas and Dust Emission at the Outer Edge of Protoplanetary Disks, *ApJ*, *678*, 1119–1126, doi:10.1086/586730.

Hughes, A. M., S. M. Andrews, C. Espaillat, D. J. Wilner, N. Calvet, P. D'Alessio, C. Qi, J. P. Williams, and M. R. Hogerheijde (2009), A Spatially Resolved Inner Hole in the Disk Around GM Aurigae, *ApJ*, *698*, 131–142, doi:10.1088/0004-637X/698/1/131.

Hughes, A. M., D. J. Wilner, S. M. Andrews, C. Qi, and M. R. Hogerheijde (2011), Empirical Constraints on Turbulence in Protoplanetary Accretion Disks, *ApJ*, *727*, 85, doi:10.1088/0004-637X/727/2/85.

Hugo, E., O. Asvany, and S. Schlemmer (2009), $H_3^+ + H_2$ isotopic system at low temperatures: Microcanonical model and experimental study, *J. Chem. Phys.*, *130*(16), 164,302, doi:10.1063/1.3089422.

Igea, J., and A. E. Glassgold (1999), X-Ray Ionization of the Disks of Young Stellar Objects, *ApJ*, *518*, 848–858, doi:10.1086/307302.

Imanishi, K., K. Koyama, and Y. Tsuboi (2001), Chandra Observation of the ρ Ophiuchi Cloud, *ApJ*, *557*, 747–760, doi:10.1086/321691.

Indriolo, N., and B. J. McCall (2012), Investigating the Cosmic-Ray Ionization Rate in the Galactic Diffuse Interstellar Medium through Observations of H^+_3, *ApJ*, *745*, 91, doi:10.1088/0004-637X/745/1/91.

Indriolo, N., T. R. Geballe, T. Oka, and B. J. McCall (2007), H^+_3 in Diffuse Interstellar Clouds: A Tracer for the Cosmic-Ray Ionization Rate, *ApJ*, *671*, 1736–1747, doi:10.1086/523036.

Ingleby, L., et al. (2013), Accretion Rates for T Tauri Stars Using Nearly Simultaneous Ultraviolet and Optical Spectra, *ApJ*, *767*, 112, doi:10.1088/0004-637X/767/2/112.

Insley, J. E., V. Moore, and R. A. Harrison (1997), First Observations of Coronal Hole Structure and Evolution Using Soho-Cds, *Sol. Phys.*, *175*, 437–456, doi:10.1023/A:1004930219222.

Isella, A., J. M. Carpenter, and A. I. Sargent (2009), Structure and Evolution of Pre-main-sequence Circumstellar Disks, *ApJ*, *701*, 260–282, doi:10.1088/0004-637X/701/1/260.

Jang-Condell, H. (2008), Planet Shadows in Protoplanetary Disks. I. Temperature Perturbations, *ApJ*, *679*, 797–812, doi:10.1086/533583.

Jang-Condell, H. (2009), Planet Shadows in Protoplanetary Disks. II. Observable Signatures, *ApJ*, *700*, 820–831, doi:10.1088/0004-637X/700/1/820.

Jang-Condell, H., and N. J. Turner (2012), Gaps in Protoplanetary Disks as Signatures of Planets. I. Methodology and Validation, *ApJ*, *749*, 153, doi:10.1088/0004-637X/749/2/153.

Jessop, N. E., and D. Ward-Thompson (2000), A far-infrared survey of molecular cloud cores, *MNRAS*, *311*, 63–74, doi:10.1046/j.1365-8711.2000.03011.x.

Johns-Krull, C. M. (2007), The Magnetic Fields of Classical T Tauri Stars, *ApJ*, *664*, 975–985, doi:10.1086/519017.

Johns-Krull, C. M., J. A. Valenti, and C. Koresko (1999), Measuring the Magnetic Field on the Classical T Tauri Star BP Tauri, *ApJ*, *516*, 900–915, doi:10.1086/307128.

Jonkheid, B., F. G. A. Faas, G.-J. van Zadelhoff, and E. F. van Dishoeck (2004), The gas temperature in flaring disks around pre-main sequence stars, *A&A*, *428*, 511–521, doi:10.1051/0004-6361:20048013.

Jonkheid, B., C. P. Dullemond, M. R. Hogerheijde, and E. F. van Dishoeck (2007), Chemistry and line emission from evolving Herbig Ae disks, *A&A*, *463*, 203–216, doi:10.1051/0004-6361:20065668.

Jørgensen, J. K., F. L. Schöier, and E. F. van Dishoeck (2004), Molecular inventories and chemical evolution of low-mass protostellar envelopes, *A&A*, *416*, 603–622, doi:10.1051/0004-6361:20034440.

Joseph, C. L., T. P. Snow, Jr., C. G. Seab, and R. M. Crutcher (1986), Interstellar abun-

dances in dense, moderately reddened lines of sight. I - Observational evidence for density-dependent depletion, *ApJ*, *309*, 771–782, doi:10.1086/164647.

Jura, M., S. Xu, and E. D. Young (2013), ^{26}Al in the Early Solar System: Not So Unusual after All, *ApJ*, *775*, L41, doi:10.1088/2041-8205/775/2/L41.

Kahane, C., J. Cernicharo, J. Gomez-Gonzalez, and M. Guelin (1992), Isotopic abundances in carbon-rich circumstellar envelopes - A further iteration on the oxygen isotope puzzle, *A&A*, *256*, 235–250.

Kamp, I., and C. P. Dullemond (2004), The Gas Temperature in the Surface Layers of Protoplanetary Disks, *ApJ*, *615*, 991–999, doi:10.1086/424703.

Kastner, J. H., B. Zuckerman, D. A. Weintraub, and T. Forveille (1997), X-ray and molecular emission from the nearest region of recent star formation., *Science*, *277*, 67–71, doi:10.1126/science.277.5322.67.

Kastner, J. H., D. P. Huenemoerder, N. S. Schulz, and D. A. Weintraub (1999), X-Ray Spectroscopy of the Nearby, Classical T Tauri Star TW Hydrae, *ApJ*, *525*, 837–844, doi:10.1086/307946.

Kastner, J. H., D. P. Huenemoerder, N. S. Schulz, C. R. Canizares, and D. A. Weintraub (2002), Evidence for Accretion: High-Resolution X-Ray Spectroscopy of the Classical T Tauri Star TW Hydrae, *ApJ*, *567*, 434–440, doi:10.1086/338419.

Keene, J., P. Schilke, J. Kooi, D. C. Lis, D. M. Mehringer, and T. G. Phillips (1998), Detection of the 3P 2 3P 1 Submillimeter Transition of 13C i in the Interstellar Medium: Implication for Chemical Fractionation, *ApJ*, *494*, L107, doi:10.1086/311164.

Kley, W., and R. P. Nelson (2012), Planet-Disk Interaction and Orbital Evolution, *ARA&A*, *50*, 211–249, doi:10.1146/annurev-astro-081811-125523.

Koerner, D. W., and A. I. Sargent (1995), Imaging the Small-Scale Circumstellar Gas Around T Tauri Stars, *AJ*, *109*, 2138, doi:10.1086/117439.

Koresko, C. D. (2000), A Third Star in the T Tauri System, *ApJ*, *531*, L147–L149, doi:10.1086/312543.

Kratter, K. M., C. D. Matzner, M. R. Krumholz, and R. I. Klein (2010), On the Role of Disks in the Formation of Stellar Systems: A Numerical Parameter Study of Rapid Accretion, *ApJ*, *708*, 1585–1597, doi:10.1088/0004-637X/708/2/1585.

Kraus, A. L., and M. J. Ireland (2012), LkCa 15: A Young Exoplanet Caught at Formation?, *ApJ*, *745*, 5, doi:10.1088/0004-637X/745/1/5.

Kretke, K. A., H. F. Levison, M. W. Buie, and A. Morbidelli (2012), A Method to Constrain the Size of the Protosolar Nebula, *AJ*, *143*, 91, doi:10.1088/0004-6256/143/4/91.

Krimigis, S. M., E. C. Roelof, R. B. Decker, and M. E. Hill (2011), Zero outward

flow velocity for plasma in a heliosheath transition layer, *Nature*, *474*, 359–361, doi: 10.1038/nature10115.

Krist, J. E., K. R. Stapelfeldt, F. Ménard, D. L. Padgett, and C. J. Burrows (2000), WFPC2 Images of a Face-on Disk Surrounding TW Hydrae, *ApJ*, *538*, 793–800, doi: 10.1086/309170.

Ku, W. H.-M., and G. A. Chanan (1979), Einstein observations of the Orion Nebula, *ApJ*, *234*, L59–L63, doi:10.1086/183109.

Kurosawa, R., T. J. Harries, M. R. Bate, and N. H. Symington (2004), Synthetic infrared images and spectral energy distributions of a young low-mass stellar cluster, *MNRAS*, *351*, 1134–1150, doi:10.1111/j.1365-2966.2004.07869.x.

Kutschera, W., et al. (1984), Half-life of ^{60}Fe, *Nuclear Instruments and Methods in Physics Research B*, *5*, 430–435, doi:10.1016/0168-583X(84)90555-X.

Lamzin, S. A. (1999), X-ray emission from T Tauri stars attributable to an accretion shock wave, *Astronomy Letters*, *25*, 430–436.

Langer, W. D., A. Castets, and B. Lefloch (1996), The IRAS 2 and IRAS 4 Outflows and Star Formation in NGC 1333, *ApJ*, *471*, L111, doi:10.1086/310337.

Langner, U. W., and M. S. Potgieter (2005), Modulation of Galactic Protons in an Asymmetrical Heliosphere, *ApJ*, *630*, 1114–1124, doi:10.1086/431547.

Lawrence, D. J., et al. (2013), Evidence for Water Ice Near Mercury's North Pole from MESSENGER Neutron Spectrometer Measurements, *Science*, *339*, 292–, doi: 10.1126/science.1229953.

Lecar, M., M. Podolak, D. Sasselov, and E. Chiang (2006), On the Location of the Snow Line in a Protoplanetary Disk, *ApJ*, *640*, 1115–1118, doi:10.1086/500287.

Lee, C. W., and P. C. Myers (1999), A Catalog of Optically Selected Cores, *ApJS*, *123*, 233–250, doi:10.1086/313234.

Lee, H.-H., E. Herbst, G. Pineau des Forêts, E. Roueff, and J. Le Bourlot (1996), Photodissociation of H_2 and CO and time dependent chemistry in inhomogeneous interstellar clouds., *Astronomy and Astrophysics*, *311*, 690–707.

Lee, J., and E. A. Bergin (2014), The D/H Ratio of Water Ice at Low Temperatures, *ApJ*.

Lee, T., F. H. Shu, H. Shang, A. E. Glassgold, and K. E. Rehm (1998), Protostellar Cosmic Rays and Extinct Radioactivities in Meteorites, *ApJ*, *506*, 898–912, doi:10.1086/306284.

Leger, A., M. Jura, and A. Omont (1985), Desorption from interstellar grains, *Astronomy and Astrophysics*, *144*, 147–160.

Lesur, G., M. W. Kunz, and S. Fromang (2014), Thanatology in protoplanetary discs. The

combined influence of Ohmic, Hall, and ambipolar diffusion on dead zones, *A&A*, *566*, A56, doi:10.1051/0004-6361/201423660.

Li, X., A. N. Heays, R. Visser, W. Ubachs, B. R. Lewis, S. T. Gibson, and E. F. van Dishoeck (2013), Photodissociation of interstellar N_2, *A&A*, *555*, A14, doi:10.1051/0004-6361/201220625.

Li, Z.-Y., and F. H. Shu (1996), Magnetized Singular Isothermal Toroids, *ApJ*, *472*, 211, doi:10.1086/178056.

Liedahl, D. A., A. L. Osterheld, and W. H. Goldstein (1995), New calculations of Fe L-shell X-ray spectra in high-temperature plasmas, *ApJ*, *438*, L115–L118, doi:10.1086/187729.

Lin, D. N. C., and J. Papaloizou (1986), On the tidal interaction between protoplanets and the primordial solar nebula. II - Self-consistent nonlinear interaction, *ApJ*, *307*, 395–409, doi:10.1086/164426.

Lin, D. N. C., and J. C. B. Papaloizou (1993), On the tidal interaction between protostellar disks and companions, in *Protostars and Planets III*, edited by E. H. Levy and J. I. Lunine, pp. 749–835.

Linsky, J. L. (1998), Deuterium Abundance in the Local ISM and Possible Spatial Variations, *Space Sci. Rev.*, *84*, 285.

Low, F. J., P. S. Smith, M. Werner, C. Chen, V. Krause, M. Jura, and D. C. Hines (2005), Exploring Terrestrial Planet Formation in the TW Hydrae Association, *ApJ*, *631*, 1170–1179, doi:10.1086/432640.

Lubow, S. H., and R. G. Martin (2012), Accretion Outbursts in Circumplanetary Disks, *ApJ*, *749*, L37, doi:10.1088/2041-8205/749/2/L37.

Lubow, S. H., M. Seibert, and P. Artymowicz (1999), Disk Accretion onto High-Mass Planets, *ApJ*, *526*, 1001–1012, doi:10.1086/308045.

Lucy, L. B. (1999), Computing radiative equilibria with Monte Carlo techniques, *A&A*, *344*, 282–288.

Lyons, J. R., and E. D. Young (2005), CO self-shielding as the origin of oxygen isotope anomalies in the early solar nebula, *Nature*, *435*, 317–320, doi:10.1038/nature03557.

MacPherson, G. J., A. M. Davis, and E. K. Zinner (1995), The distribution of aluminum-26 in the early Solar System - A reappraisal, *Meteoritics*, *30*, 365.

Madhusudhan, N. (2012), C/O Ratio as a Dimension for Characterizing Exoplanetary Atmospheres, *ApJ*, *758*, 36, doi:10.1088/0004-637X/758/1/36.

Mahaffy, P. R., T. M. Donahue, S. K. Atreya, T. C. Owen, and H. B. Niemann (1998), Galileo Probe Measurements of D/H and 3He/4He in Jupiter's Atmosphere, *Space Sci. Rev.*, *84*, 251–263.

Makide, K., K. Nagashima, A. N. Krot, G. R. Huss, F. J. Ciesla, E. Hellebrand, E. Gaidos, and L. Yang (2011), Heterogeneous Distribution of ^{26}Al at the Birth of the Solar System, *ApJ*, *733*, L31, doi:10.1088/2041-8205/733/2/L31.

Mamajek, E. E. (2009), Initial Conditions of Planet Formation: Lifetimes of Primordial Disks, in *American Institute of Physics Conference Series*, *American Institute of Physics Conference Series*, vol. 1158, edited by T. Usuda, M. Tamura, and M. Ishii, pp. 3–10, doi:10.1063/1.3215910.

Manuel, R. (2011), Long-term galactic cosmic ray modulation in the heliosphere, in *International Cosmic Ray Conference*, *International Cosmic Ray Conference*, vol. 11, p. 23.

Manuel, R., S. E. S. Ferreira, and M. S. Potgieter (2011), Cosmic ray modulation in the outer heliosphere: Predictions for cosmic ray intensities up to the heliopause along Voyager 1 and 2 trajectories, *Advances in Space Research*, *48*, 874–883, doi:10.1016/j.asr.2011.04.015.

Maret, S., and E. A. Bergin (2007), The Ionization Fraction of Barnard 68: Implications for Star and Planet Formation, *ApJ*, *664*, 956–963, doi:10.1086/519152.

Mathis, J. S., W. Rumpl, and K. H. Nordsieck (1977), The size distribution of interstellar grains, *ApJ*, *217*, 425–433, doi:10.1086/155591.

Matsumura, S., and R. E. Pudritz (2003), The Origin of Jovian Planets in Protostellar Disks: The Role of Dead Zones, *ApJ*, *598*, 645–656, doi:10.1086/378846.

Matsumura, S., and R. E. Pudritz (2005), Dead Zones and the Origin of Planetary Masses, *ApJ*, *618*, L137–L140, doi:10.1086/427920.

Matsumura, S., and R. E. Pudritz (2006), Dead zones and extrasolar planetary properties, *MNRAS*, *365*, 572–584, doi:10.1111/j.1365-2966.2005.09737.x.

Matsumura, S., R. E. Pudritz, and E. W. Thommes (2007), Saving Planetary Systems: Dead Zones and Planetary Migration, *ApJ*, *660*, 1609–1623, doi:10.1086/513175.

McCall, B. J., et al. (2003), An enhanced cosmic-ray flux towards ζ Persei inferred from a laboratory study of the H_3^+-e^- recombination rate, *Nature*, *422*, 500–502, doi:10.1038/nature01498.

McCaughrean, M. J., and C. R. O'Dell (1996), Direct Imaging of Circumstellar Disks in the Orion Nebula, *AJ*, *111*, 1977, doi:10.1086/117934.

Meier, R., T. C. Owen, H. E. Matthews, D. C. Jewitt, D. Bockelee-Morvan, N. Biver, J. Crovisier, and D. Gautier (1998), A Determination of the HDO/H2O Ratio in Comet C/1995 O1 (Hale-Bopp), *Science*, *279*, 842, doi:10.1126/science.279.5352.842.

Mekkaden, M. V. (1998), Photometric and polarimetric variability of the isolated T Tauri star TW Hydrae, *A&A*, *340*, 135–142.

Mendoza V., E. E. (1966), Infrared Photometry of T Tauri Stars and Related Objects, *ApJ*, *143*, 1010, doi:10.1086/148584.

Mendoza V., E. E. (1968), Infrared Excesses in T Tauri Stars and Related Objects, *ApJ*, *151*, 977, doi:10.1086/149497.

Mentuch, E., A. Brandeker, M. H. van Kerkwijk, R. Jayawardhana, and P. H. Hauschildt (2008), Lithium Depletion of Nearby Young Stellar Associations, *ApJ*, *689*, 1127–1140, doi:10.1086/592764.

Menu, J., et al. (2014), On the structure of the transition disk around TW Hydrae, *A&A*, *564*, A93, doi:10.1051/0004-6361/201322961.

Millar, T. J., A. Bennett, and E. Herbst (1989), Deuterium fractionation in dense interstellar clouds, *ApJ*, *340*, 906–920, doi:10.1086/167444.

Minamidani, T., et al. (2011), Dense Clumps in Giant Molecular Clouds in the Large Magellanic Cloud: Density and Temperature Derived from ^{13}CO(J = 3-2) Observations, *AJ*, *141*, 73, doi:10.1088/0004-6256/141/3/73.

Miotello, A., S. Bruderer, and E. F. van Dishoeck (2014), Protoplanetary disk masses from CO isotopologue line emission, *A&A*, *572*, A96, doi:10.1051/0004-6361/201424712.

Montmerle, T., L. Koch-Miramond, E. Falgarone, and J. E. Grindlay (1983), Einstein observations of the Rho Ophiuchi dark cloud - an X-ray Christmas tree, *ApJ*, *269*, 182–201, doi:10.1086/161029.

Morbidelli, A., J. I. Lunine, D. P. O'Brien, S. N. Raymond, and K. J. Walsh (2012), Building Terrestrial Planets, *Annual Review of Earth and Planetary Sciences*, *40*, 251–275.

Moskalenko, I. V., A. W. Strong, J. F. Ormes, and M. S. Potgieter (2002), Secondary Antiprotons and Propagation of Cosmic Rays in the Galaxy and Heliosphere, *ApJ*, *565*, 280–296, doi:10.1086/324402.

Moynier, F., J. Blichert-Toft, K. Wang, G. F. Herzog, and F. Albarede (2011), The Elusive ^{60}Fe in the Solar Nebula, *ApJ*, *741*, 71, doi:10.1088/0004-637X/741/2/71.

Müller, H. S. P., S. Thorwirth, D. A. Roth, and G. Winnewisser (2001), The Cologne Database for Molecular Spectroscopy, CDMS, *A&A*, *370*, L49–L52, doi:10.1051/0004-6361:20010367.

Müller, H. S. P., F. Schlöder, S. Stutzki, and G. Winnewisser (2005), The cologne database for molecular spectroscopy, cdms: a useful tool for astronomers and spectroscopists, *Journal of Molecular Structure*, *742*, 215 – 227, doi:http://dx.doi.org/10.1016/j.molstruc.2005.01.027.

Myers, P. C. (2009), Filamentary Structure of Star-forming Complexes, *ApJ*, *700*, 1609–1625, doi:10.1088/0004-637X/700/2/1609.

Najita, J., E. A. Bergin, and J. N. Ullom (2001), X-Ray Desorption of Molecules from Grains in Protoplanetary Disks, *ApJ*, *561*, 880–889, doi:10.1086/323320.

Nakagawa, Y., M. Sekiya, and C. Hayashi (1986), Settling and growth of dust particles

in a laminar phase of a low-mass solar nebula, *Icarus*, *67*, 375–390, doi:10.1016/0019-1035(86)90121-1.

Nath, B. B., N. Gupta, and P. L. Biermann (2012), Spectrum and ionization rate of low-energy Galactic cosmic rays, *MNRAS*, *425*, L86–L90, doi:10.1111/j.1745-3933.2012.01307.x.

Nelson, R. P., and W. D. Langer (1997), The Dynamics of Low-Mass Molecular Clouds in External Radiation Fields, *ApJ*, *482*, 796, doi:10.1086/304167.

Neufeld, D. A., et al. (2010), Herschel/HIFI observations of interstellar OH^+ and H_2O^+ towards W49N: a probe of diffuse clouds with a small molecular fraction, *A&A*, *521*, L10, doi:10.1051/0004-6361/201015077.

Neuhaeuser, R., M. F. Sterzik, J. H. M. M. Schmitt, R. Wichmann, and J. Krautter (1995), ROSAT survey observation of T Tauri stars in Taurus., *A&A*, *297*, 391.

Nomura, H., Y. Aikawa, M. Tsujimoto, Y. Nakagawa, and T. J. Millar (2007), Molecular Hydrogen Emission from Protoplanetary Disks. II. Effects of X-Ray Irradiation and Dust Evolution, *ApJ*, *661*, 334–353, doi:10.1086/513419.

Öberg, K. I., F. van Broekhuizen, H. J. Fraser, S. E. Bisschop, E. F. van Dishoeck, and S. Schlemmer (2005), Competition between CO and N_2 Desorption from Interstellar Ices, *ApJ*, *621*, L33–L36, doi:10.1086/428901.

Öberg, K. I., C. Qi, J. K. J. Fogel, E. A. Bergin, S. M. Andrews, C. Espaillat, T. A. van Kempen, D. J. Wilner, and I. Pascucci (2010), The Disk Imaging Survey of Chemistry with SMA. I. Taurus Protoplanetary Disk Data, *ApJ*, *720*, 480–493, doi:10.1088/0004-637X/720/1/480.

Öberg, K. I., A. C. A. Boogert, K. M. Pontoppidan, S. van den Broek, E. F. van Dishoeck, S. Bottinelli, G. A. Blake, and N. J. Evans, II (2011a), The Spitzer Ice Legacy: Ice Evolution from Cores to Protostars, *ApJ*, *740*, 109, doi:10.1088/0004-637X/740/2/109.

Öberg, K. I., R. Murray-Clay, and E. A. Bergin (2011b), The Effects of Snowlines on C/O in Planetary Atmospheres, *ApJ*, *743*, L16, doi:10.1088/2041-8205/743/1/L16.

Öberg, K. I., C. Qi, J. K. J. Fogel, E. A. Bergin, S. M. Andrews, C. Espaillat, D. J. Wilner, I. Pascucci, and J. H. Kastner (2011c), Disk Imaging Survey of Chemistry with SMA. II. Southern Sky Protoplanetary Disk Data and Full Sample Statistics, *ApJ*, *734*, 98, doi:10.1088/0004-637X/734/2/98.

Öberg, K. I., C. Qi, D. J. Wilner, and S. M. Andrews (2011d), The Ionization Fraction in the DM Tau Protoplanetary Disk, *ApJ*, *743*, 152, doi:10.1088/0004-637X/743/2/152.

Öberg, K. I., C. Qi, D. J. Wilner, and M. R. Hogerheijde (2012), Evidence for Multiple Pathways to Deuterium Enhancements in Protoplanetary Disks, *ApJ*, *749*, 162, doi:10.1088/0004-637X/749/2/162.

O'Loughlin, K. F. (1997), Spidr on the web: Space physics interactive data resource on-line analysis tool, *Radio Science*, *32*(5), 2021–2026, doi:10.1029/97RS00662.

Opher, M., J. F. Drake, M. Swisdak, K. M. Schoeffler, J. D. Richardson, R. B. Decker, and G. Toth (2011), Is the Magnetic Field in the Heliosheath Laminar or a Turbulent Sea of Bubbles?, *ApJ*, *734*, 71, doi:10.1088/0004-637X/734/1/71.

Ouellette, N., S. J. Desch, and J. J. Hester (2007), Interaction of Supernova Ejecta with Nearby Protoplanetary Disks, *ApJ*, *662*, 1268–1281, doi:10.1086/518102.

Ouellette, N., S. J. Desch, and J. J. Hester (2010), Injection of Supernova Dust in Nearby Protoplanetary Disks, *ApJ*, *711*, 597–612, doi:10.1088/0004-637X/711/2/597.

Padovani, M., and D. Galli (2011), Effects of magnetic fields on the cosmic-ray ionization of molecular cloud cores, *A&A*, *530*, A109, doi:10.1051/0004-6361/201116853.

Padovani, M., D. Galli, and A. E. Glassgold (2009), Cosmic-ray ionization of molecular clouds, *A&A*, *501*, 619–631, doi:10.1051/0004-6361/200911794.

Padovani, M., P. Hennebelle, and D. Galli (2013), Cosmic-ray ionisation in collapsing clouds, *A&A*, *560*, A114, doi:10.1051/0004-6361/201322407.

Pagani, L., et al. (2009), Chemical modeling of L183 (L134N): an estimate of the ortho/para H_2 ratio, *A&A*, *494*, 623–636, doi:10.1051/0004-6361:200810587.

Parise, B., T. Simon, E. Caux, E. Dartois, C. Ceccarelli, J. Rayner, and A. G. G. M. Tielens (2003), Search for solid HDO in low-mass protostars, *A&A*, *410*, 897–904, doi:10.1051/0004-6361:20031277.

Penzias, A. A., K. B. Jefferts, and R. W. Wilson (1971), Interstellar $^{12}C^{16}O$, $^{13}C^{16}O$, and $^{12}C^{18}O$, *ApJ*, *165*, 229, doi:10.1086/150893.

Penzias, A. A., P. M. Solomon, K. B. Jefferts, and R. W. Wilson (1972), Carbon Monoxide Observations of Dense Interstellar Clouds, *ApJ*, *174*, L43, doi:10.1086/180945.

Perez-Becker, D., and E. Chiang (2011a), Surface Layer Accretion in Transitional and Conventional Disks: From Polycyclic Aromatic Hydrocarbons to Planets, *ApJ*, *727*, 2, doi:10.1088/0004-637X/727/1/2.

Perez-Becker, D., and E. Chiang (2011b), Surface Layer Accretion in Conventional and Transitional Disks Driven by Far-ultraviolet Ionization, *ApJ*, *735*, 8, doi:10.1088/0004-637X/735/1/8.

Perryman, M. A. C., et al. (1997), The HIPPARCOS Catalogue, *A&A*, *323*, L49–L52.

Persson, M. V., J. K. Jørgensen, and E. F. van Dishoeck (2012), Subarcsecond resolution observations of warm water toward three deeply embedded low-mass protostars, *A&A*, *541*, A39, doi:10.1051/0004-6361/201117917.

Persson, M. V., J. K. Jørgensen, E. F. van Dishoeck, and D. Harsono (2014), The deuterium fractionation of water on solar-system scales in deeply-embedded low-mass protostars, *ArXiv e-prints*.

Pickett, H. M., R. L. Poynter, E. A. Cohen, M. L. Delitsky, J. C. Pearson, and H. S. P. Müller (1998), Submillimeter, millimeter and microwave spectral line catalog., *J. Quant. Spec. Radiat. Transf.*, *60*, 883–890, doi:10.1016/S0022-4073(98)00091-0.

Piétu, V., A. Dutrey, S. Guilloteau, E. Chapillon, and J. Pety (2006), Resolving the inner dust disks surrounding LkCa 15 and MWC 480 at mm wavelengths, *A&A*, *460*, L43–L47, doi:10.1051/0004-6361:20065968.

Pinte, C., T. J. Harries, M. Min, A. M. Watson, C. P. Dullemond, P. Woitke, F. Ménard, and M. C. Durán-Rojas (2009), Benchmark problems for continuum radiative transfer. High optical depths, anisotropic scattering, and polarisation, *A&A*, *498*, 967–980, doi:10.1051/0004-6361/200811555.

Prantzos, N., O. Aubert, and J. Audouze (1996), Evolution of the carbon and oxygen isotopes in the Galaxy., *A&A*, *309*, 760–774.

Preibisch, T., et al. (2005), The Origin of T Tauri X-Ray Emission: New Insights from the Chandra Orion Ultradeep Project, *ApJS*, *160*, 401–422, doi:10.1086/432891.

Pringle, J. E. (1981), Accretion discs in astrophysics, *ARA&A*, *19*, 137–162, doi:10.1146/annurev.aa.19.090181.001033.

Qi, C., J. E. Kessler, D. W. Koerner, A. I. Sargent, and G. A. Blake (2003), Continuum and CO/HCO^+ Emission from the Disk Around the T Tauri Star LkCa 15, *ApJ*, *597*, 986–997, doi:10.1086/378494.

Qi, C., D. J. Wilner, N. Calvet, T. L. Bourke, G. A. Blake, M. R. Hogerheijde, P. T. P. Ho, and E. Bergin (2006), CO J = 6-5 Observations of TW Hydrae with the Submillimeter Array, *ApJ*, *636*, L157–L160, doi:10.1086/500241.

Qi, C., D. J. Wilner, Y. Aikawa, G. A. Blake, and M. R. Hogerheijde (2008), Resolving the Chemistry in the Disk of TW Hydrae. I. Deuterated Species, *ApJ*, *681*, 1396–1407, doi:10.1086/588516.

Qi, C., K. I. Öberg, and D. J. Wilner (2013a), H_2CO and N_2H^+ in Protoplanetary Disks: Evidence for a CO-ice Regulated Chemistry, *ApJ*, *765*, 34, doi:10.1088/0004-637X/765/1/34.

Qi, C., K. I. Öberg, D. J. Wilner, P. D'Alessio, E. Bergin, S. M. Andrews, G. A. Blake, M. R. Hogerheijde, and E. F. van Dishoeck (2013b), Imaging of the CO Snow Line in a Solar Nebula Analog, *Science*, *341*, 630–632, doi:10.1126/science.1239560.

Qi, C., et al. (2004), Imaging the Disk around TW Hydrae with the Submillimeter Array, *ApJ*, *616*, L11–L14, doi:10.1086/421063.

Raassen, A. J. J. (2009), The X-ray spectrum of the classical TTauri star TW Hy-

drae observed by LETGS aboard Chandra, *A&A*, *505*, 755–762, doi:10.1051/0004-6361/200811374.

Rice, W. K. M., K. Wood, P. J. Armitage, B. A. Whitney, and J. E. Bjorkman (2003), Constraints on a planetary origin for the gap in the protoplanetary disc of GM Aurigae, *MNRAS*, *342*, 79–85, doi:10.1046/j.1365-8711.2003.06515.x.

Rimmer, P. B., E. Herbst, O. Morata, and E. Roueff (2012), Observing a column-dependent ζ in dense interstellar sources: the case of the Horsehead nebula, *A&A*, *537*, A7, doi:10.1051/0004-6361/201117048.

Roberge, A., A. J. Weinberger, and E. M. Malumuth (2005), Spatially Resolved Spectroscopy and Coronagraphic Imaging of the TW Hydrae Circumstellar Disk, *ApJ*, *622*, 1171–1181, doi:10.1086/427974.

Robert, F., D. Gautier, and B. Dubrulle (2000), The Solar System d/h Ratio: Observations and Theories, *Space Sci. Rev.*, *92*, 201–224, doi:10.1023/A:1005291127595.

Roberts, H., and T. J. Millar (2000), Modelling of deuterium chemistry and its application to molecular clouds, *A&A*, *361*, 388–398.

Roberts, H., E. Herbst, and T. J. Millar (2004), The chemistry of multiply deuterated species in cold, dense interstellar cores, *A&A*, *424*, 905–917, doi:10.1051/0004-6361:20040441.

Rosenfeld, K. A., S. M. Andrews, A. M. Hughes, D. J. Wilner, and C. Qi (2013), A SPATIALLY RESOLVED VERTICAL TEMPERATURE GRADIENT IN THE HD 163296 DISK, *ApJ*, *774*(1), 16.

Rosenfeld, K. A., et al. (2012), Kinematics of the CO Gas in the Inner Regions of the TW Hya Disk, *ApJ*, *757*, 129, doi:10.1088/0004-637X/757/2/129.

Roueff, E., M. Gerin, D. C. Lis, A. Wootten, N. Marcelino, J. Cernicharo, and B. Tercero (2013), CH2D+, the Search for the Holy Grail, *Journal of Physical Chemistry A*, *117*, 9959–9967, doi:10.1021/jp400119a.

Rucinski, S. M. (1985), IRAS observations of T Tauri and post-T Tauri stars, *AJ*, *90*, 2321–2330, doi:10.1086/113937.

Rucinski, S. M., and J. Krautter (1983), TW Hya - A T Tauri star far from any dark cloud, *A&A*, *121*, 217–225.

Rugel, G., et al. (2009), New Measurement of the Fe60 Half-Life, *Physical Review Letters*, *103*(7), 072502, doi:10.1103/PhysRevLett.103.072502.

Rybicki, G. B., and A. P. Lightman (1979), *Radiative processes in astrophysics*.

Rydbeck, O. E. H., A. Hjalmarson, G. Rydbeck, J. Ellder, E. Kollberg, and W. M. Irvine (1980), Observations of SO in dark and molecular clouds, *ApJ*, *235*, L171–L175, doi:10.1086/183184.

Rydgren, A. E., S. E. Strom, and K. M. Strom (1976), The nature of the objects of Joy - A study of the T Tauri phenomenon, *ApJS*, *30*, 307–336, doi:10.1086/190364.

Saff, E., and A. Kuijlaars (1997), Distributing many points on a sphere, *The Mathematical Intelligencer*, *19*, 5–11, doi:10.1007/BF03024331.

Safronov, V. S., and E. V. Zvjagina (1969), Relative Sizes of the Largest Bodies during the Accumulation of Planets, *Icarus*, *10*, 109–115, doi:10.1016/0019-1035(69)90013-X.

Saito, S., K. Kawaguchi, and E. Hirota (1985), The microwave spectrum of the H_2D^+ ion: The $2_{20} - 2_{21}$ transition, *J. Chem. Phys.*, *82*, 45–47, doi:10.1063/1.448767.

Sandford, S. A., and L. J. Allamandola (1990), The volume- and surface-binding energies of ice systems containing CO, CO2 and H2O, *Icarus*, *87*(1), 188–192.

Sandford, S. A., and L. J. Allamandola (1993), Condensation and vaporization studies of CH3OH and NH3 ices: Major implications for astrochemistry, *The Astrophysical Journal*, *417*, 815.

Sano, T., and J. M. Stone (2002), The Effect of the Hall Term on the Nonlinear Evolution of the Magnetorotational Instability. II. Saturation Level and Critical Magnetic Reynolds Number, *ApJ*, *577*, 534–553, doi:10.1086/342172.

Sano, T., S. M. Miyama, T. Umebayashi, and T. Nakano (2000), Magnetorotational Instability in Protoplanetary Disks. II. Ionization State and Unstable Regions, *ApJ*, *543*, 486–501, doi:10.1086/317075.

Sastry, K. V. L. N., P. Helminger, E. Herbst, and F. C. De Lucia (1981), Millimeter and submillimeter spectra of HN $^+{}_2$and DN $^+{}_2$, *Chemical Physics Letters*, *84*, 286–287, doi: 10.1016/0009-2614(81)80346-6.

Sauter, J., et al. (2009), The circumstellar disc in the Bok globule CB 26. Multi-wavelength observations and modelling of the dust disc and envelope, *A&A*, *505*, 1167–1182, doi: 10.1051/0004-6361/200912397.

Schindhelm, E., K. France, G. J. Herczeg, E. Bergin, H. Yang, A. Brown, J. M. Brown, J. L. Linsky, and J. Valenti (2012), Lyα Dominance of the Classical T Tauri Far-ultraviolet Radiation Field, *ApJ*, *756*, L23, doi:10.1088/2041-8205/756/1/L23.

Schneider, S., and B. G. Elmegreen (1979), A catalog of dark globular filaments, *ApJS*, *41*, 87–95, doi:10.1086/190609.

Schöier, F. L., F. F. S. van der Tak, E. F. van Dishoeck, and J. H. Black (2005), An atomic and molecular database for analysis of submillimetre line observations, *A&A*, *432*, 369–379, doi:10.1051/0004-6361:20041729.

Schramm, D. N. (1971), Nucleosynthesis of ^{26}A1 in the Early Solar System and in Cosmic Rays, *Ap&SS*, *13*, 249–266, doi:10.1007/BF00656331.

Schwarz, K. R., and E. A. Bergin (2014), The Effects of Initial Abundances on Nitrogen in Protoplanetary Disks, *ArXiv e-prints*.

Semenov, D. (2010), Chemistry in Protoplanetary Disks, *ArXiv e-prints*.

Semenov, D., and D. Wiebe (2011), Chemical Evolution of Turbulent Protoplanetary Disks and the Solar Nebula, *ApJS*, *196*, 25, doi:10.1088/0067-0049/196/2/25.

Semenov, D., D. Wiebe, and T. Henning (2004), Reduction of chemical networks. II. Analysis of the fractional ionisation in protoplanetary discs, *A&A*, *417*, 93–106, doi:10.1051/0004-6361:20034128.

Shang, H., F. H. Shu, T. Lee, and A. E. Glassgold (2000), Protostellar Winds and Chondritic Meteorites, *Space Sci. Rev.*, *92*, 153–176, doi:10.1023/A:1005234909848.

Shaw, G., G. J. Ferland, R. Srianand, N. P. Abel, P. A. M. van Hoof, and P. C. Stancil (2008), On the Enhanced Cosmic-Ray Ionization Rate in the Diffuse Cloud toward ζ Persei, *ApJ*, *675*, 405–412, doi:10.1086/526395.

Shu, F., J. Najita, E. Ostriker, F. Wilkin, S. Ruden, and S. Lizano (1994), Magnetocentrifugally driven flows from young stars and disks. 1: A generalized model, *ApJ*, *429*, 781–796, doi:10.1086/174363.

Shu, F. H., H. Shang, M. Gounelle, A. E. Glassgold, and T. Lee (2001), The Origin of Chondrules and Refractory Inclusions in Chondritic Meteorites, *ApJ*, *548*, 1029–1050, doi:10.1086/319018.

Shull, J. M., and M. E. van Steenberg (1985), X-ray secondary heating and ionization in quasar emission-line clouds, *ApJ*, *298*, 268–274, doi:10.1086/163605.

Skinner, S. L., M. Guedel, K. Koyama, and S. Yamauchi (1997), ASCA Observations of the Barnard 209 Dark Cloud and an Intense X-Ray Flare on V773 Tauri, *ApJ*, *486*, 886, doi:10.1086/304561.

Skrutskie, M. F., D. Dutkevitch, S. E. Strom, S. Edwards, K. M. Strom, and M. A. Shure (1990), A sensitive 10-micron search for emission arising from circumstellar dust associated with solar-type pre-main-sequence stars, *AJ*, *99*, 1187–1195, doi:10.1086/115407.

Smith, I. W. M., E. Herbst, and Q. Chang (2004), Rapid neutral-neutral reactions at low temperatures: a new network and first results for TMC-1, *MNRAS*, *350*, 323–330, doi:10.1111/j.1365-2966.2004.07656.x.

Solomon, P. M., A. A. Penzias, K. B. Jefferts, and R. W. Wilson (1973), Millimeter Emission Lines of Polyatomic Molecules in Sagittarius B2, *The Astrophysical Journal*, *185*, L63.

Spaans, M., and D. A. Neufeld (1997), Molecular Hydrogen in Diffuse Interstellar Clouds of Arbitrary Three-dimensional Geometry, *ApJ*, *484*, 785, doi:10.1086/304366.

Stelzer, B., and J. H. M. M. Schmitt (2004), X-ray emission from a metal depleted accretion

shock onto the classical T Tauri star TW Hya, *A&A*, *418*, 687–697, doi:10.1051/0004-6361:20040041.

Stephens, I. W., L. W. Looney, W. Kwon, M. Fernández-López, A. M. Hughes, L. G. Mundy, R. M. Crutcher, Z.-Y. Li, and R. Rao (2014), Spatially resolved magnetic field structure in the disk of a T Tauri star, *Nature*, *514*, 597–599, doi:10.1038/nature13850.

Sterenborg, M. G., O. Cohen, J. J. Drake, and T. I. Gombosi (2011), Modeling the young Sun's solar wind and its interaction with Earth's paleomagnetosphere, *Journal of Geophysical Research (Space Physics)*, *116*(15), A01217, doi:10.1029/2010JA016036.

Stevenson, D. J., and J. I. Lunine (1988), Rapid formation of Jupiter by diffuse redistribution of water vapor in the solar nebula, *Icarus*, *75*, 146–155, doi:10.1016/0019-1035(88)90133-9.

Stone, J. M., J. F. Hawley, C. F. Gammie, and S. A. Balbus (1996), Three-dimensional Magnetohydrodynamical Simulations of Vertically Stratified Accretion Disks, *ApJ*, *463*, 656, doi:10.1086/177280.

Strom, K. M., S. E. Strom, S. Edwards, S. Cabrit, and M. F. Skrutskie (1989), Circumstellar material associated with solar-type pre-main-sequence stars - A possible constraint on the timescale for planet building, *AJ*, *97*, 1451–1470, doi:10.1086/115085.

Svensmark, H. (2006), Cosmic rays and the biosphere over 4 billion years, *Astronomische Nachrichten*, *327*, 871, doi:10.1002/asna.200610651.

Tachibana, S., G. R. Huss, N. T. Kita, G. Shimoda, and Y. Morishita (2006), ^{60}Fe in Chondrites: Debris from a Nearby Supernova in the Early Solar System?, *ApJ*, *639*, L87–L90, doi:10.1086/503201.

Tachihara, K., R. Neuhäuser, and Y. Fukui (2009), Search for Remnant Clouds Associated with the TW Hya Association, *PASJ*, *61*, 585–, doi:10.1093/pasj/61.3.585.

Tang, H., and N. Dauphas (2012), Abundance, distribution, and origin of ^{60}Fe in the solar protoplanetary disk, *Earth and Planetary Science Letters*, *359*, 248–263, doi:10.1016/j.epsl.2012.10.011.

Tange, O. (2011), Gnu parallel - the command-line power tool, *;login: The USENIX Magazine*, *36*(1), 42–47.

Telleschi, A., M. Güdel, K. R. Briggs, M. Audard, and L. Scelsi (2007), High-resolution X-ray spectroscopy of T Tauri stars in the Taurus-Auriga complex, *A&A*, *468*, 443–462, doi:10.1051/0004-6361:20066193.

Teske, J. K., K. Cunha, S. C. Schuler, C. A. Griffith, and V. V. Smith (2013), Carbon and Oxygen Abundances in Cool Metal-rich Exoplanet Hosts: A Case Study of the C/O Ratio of 55 Cancri, *ApJ*, *778*, 132, doi:10.1088/0004-637X/778/2/132.

Testi, L., et al. (2014), Dust Evolution in Protoplanetary Disks, *Protostars and Planets VI*, pp. 339–361, doi:10.2458/azu:uapress:9780816531240-ch015.

The ALMA Partnership, et al. (2015), First Results from High Angular Resolution ALMA Observations Toward the HL Tau Region, *ArXiv e-prints*.

Thi, W.-F., G.-J. van Zadelhoff, and E. F. van Dishoeck (2004), Organic molecules in protoplanetary disks around T Tauri and Herbig Ae stars, *A&A*, *425*, 955–972, doi: 10.1051/0004-6361:200400026.

Thi, W.-F., P. Woitke, and I. Kamp (2010a), Warm non-equilibrium gas phase chemistry as a possible origin of high HDO/H_2O ratios in hot and dense gases: application to inner protoplanetary discs, *MNRAS*, *407*, 232–246, doi:10.1111/j.1365-2966.2009.16162.x.

Thi, W.-F., et al. (2001), H 2and CO Emission from Disks around T Tauri and Herbig Ae Pre–Main-Sequence Stars and from Debris Disks around Young Stars: Warm and Cold Circumstellar Gas, *The Astrophysical Journal*, *561*(2), 1074–1094.

Thi, W.-F., et al. (2010b), Herschel-PACS observation of the 10 Myr old T Tauri disk TW Hya. Constraining the disk gas mass, *A&A*, *518*, L125, doi:10.1051/0004-6361/201014578.

Tieftrunk, A., G. Pineau des Forets, P. Schilke, and C. M. Walmsley (1994), SO and H2S in low density molecular clouds, *A&A*, *289*, 579–596.

Tielens, A. G. G. M. (1983), Surface chemistry of deuterated molecules, *A&A*, *119*, 177–184.

Tielens, A. G. G. M., and W. Hagen (1982), Model calculations of the molecular composition of interstellar grain mantles, *A&A*, *114*, 245–260.

Tielens, A. G. G. M., and D. Hollenbach (1985), Photodissociation regions. I - Basic model. II - A model for the Orion photodissociation region, *ApJ*, *291*, 722–754, doi:10.1086/163111.

Trilling, D. E., D. W. Koerner, J. W. Barnes, C. Ftaclas, and R. H. Brown (2001), Near-Infrared Coronagraphic Imaging of the Circumstellar Disk around TW Hydrae, *ApJ*, *552*, L151–L154, doi:10.1086/320332.

Turner, N. J., and J. F. Drake (2009), Energetic Protons, Radionuclides, and Magnetic Activity in Protostellar Disks, *ApJ*, *703*, 2152–2159, doi:10.1088/0004-637X/703/2/2152.

Turner, N. J., and T. Sano (2008), Dead Zone Accretion Flows in Protostellar Disks, *ApJ*, *679*, L131–L134, doi:10.1086/589540.

Turner, N. J., M. Benisty, C. P. Dullemond, and S. Hirose (2014a), Herbig Stars' Near-infrared Excess: An Origin in the Protostellar Disk's Magnetically Supported Atmosphere, *ApJ*, *780*, 42, doi:10.1088/0004-637X/780/1/42.

Turner, N. J., S. Fromang, C. Gammie, H. Klahr, G. Lesur, M. Wardle, and X.-N. Bai (2014b), Transport and Accretion in Planet-Forming Disks, *ArXiv e-prints*.

Uchida, K. I., et al. (2004), The State of Protoplanetary Material 10 Million years after Stellar Formation: Circumstellar Disks in the TW Hydrae Association, *ApJS*, *154*, 439–442, doi:10.1086/422888.

Uchida, Y., and K. Shibata (1985), Magnetodynamical acceleration of CO and optical bipolar flows from the region of star formation, *PASJ*, *37*, 515–535.

Umebayashi, T., and T. Nakano (1981), Fluxes of Energetic Particles and the Ionization Rate in Very Dense Interstellar Clouds, *PASJ*, *33*, 617–+.

Umebayashi, T., and T. Nakano (2009), Effects of Radionuclides on the Ionization State of Protoplanetary Disks and Dense Cloud Cores, *ApJ*, *690*, 69–81, doi:10.1088/0004-637X/690/1/69.

Umebayashi, T., N. Katsuma, and H. Nomura (2013), Effects of Dust Growth and Settling on the Ionization by Radionuclides. I. Formulation and Results in a Quiescent State of Protoplanetary Disks, *ApJ*, *764*, 104, doi:10.1088/0004-637X/764/1/104.

Usoskin, I. G., K. Alanko-Huotari, G. A. Kovaltsov, and K. Mursula (2005), Heliospheric modulation of cosmic rays: Monthly reconstruction for 1951-2004, *Journal of Geophysical Research (Space Physics)*, *110*(9), A12108, doi:10.1029/2005JA011250.

Usui, T., C. M. O. Alexander, J. Wang, J. I. Simon, and J. H. Jones (2012), Origin of water and mantle–crust interactions on mars inferred from hydrogen isotopes and volatile element abundances of olivine-hosted melt inclusions of primitive shergottites, *Earth and Planetary Science Letters*, *357-358*(0), 119 – 129, doi:http://dx.doi.org/10.1016/j.epsl.2012.09.008.

Vacca, W. D., and G. Sandell (2011), Near-infrared Spectroscopy of TW Hya: A Revised Spectral Type and Comparison with Magnetospheric Accretion Models, *ApJ*, *732*, 8, doi:10.1088/0004-637X/732/1/8.

van der Marel, N., E. F. van Dishoeck, S. Bruderer, and T. A. van Kempen (2014), Warm formaldehyde in the Ophiuchus IRS 48 transitional disk, *A&A*, *563*, A113, doi:10.1051/0004-6361/201322960.

van der Marel, N., et al. (2013), A Major Asymmetric Dust Trap in a Transition Disk, *Science*, *340*, 1199–1202, doi:10.1126/science.1236770.

van der Tak, F. F. S., J. H. Black, F. L. Schöier, D. J. Jansen, and E. F. van Dishoeck (2007), A computer program for fast non-LTE analysis of interstellar line spectra. With diagnostic plots to interpret observed line intensity ratios, *A&A*, *468*, 627–635, doi:10.1051/0004-6361:20066820.

van Dishoeck, E. F., and J. H. Black (1988), The photodissociation and chemistry of interstellar CO, *The Astrophysical Journal*, *334*, 771–802.

van Dishoeck, E. F., W.-F. Thi, and G.-J. van Zadelhoff (2003), Detection of DCO^+ in a circumstellar disk, *A&A*, *400*, L1–L4, doi:10.1051/0004-6361:20030091.

van Dishoeck, E. F., E. A. Bergin, D. C. Lis, and J. I. Lunine (2014), Water: from clouds to planets, *Protostars and Planets VI*.

van Leeuwen, F. (2007), Validation of the new Hipparcos reduction, *A&A*, *474*, 653–664,

doi:10.1051/0004-6361:20078357.

van Zadelhoff, G.-J., E. F. van Dishoeck, W.-F. Thi, and G. A. Blake (2001), Submillimeter lines from circumstellar disks around pre-main sequence stars, *A&A*, *377*, 566–580, doi:10.1051/0004-6361:20011137.

van Zadelhoff, G.-J., Y. Aikawa, M. R. Hogerheijde, and E. F. van Dishoeck (2003), Axisymmetric models of ultraviolet radiative transfer with applications to circumstellar disk chemistry, *A&A*, *397*, 789–802, doi:10.1051/0004-6361:20021592.

Vasileiadis, A., Å. Nordlund, and M. Bizzarro (2013), Abundance of ^{26}Al and ^{60}Fe in Evolving Giant Molecular Clouds, *ApJ*, *769*, L8, doi:10.1088/2041-8205/769/1/L8.

Velikhov, E. P. (1959), Stability of an Ideally Conducting Liquid Flowing Between Cylinders Rotating in a Magnetic Field, *JETP*, *36*, 995.

Vidotto, A. A., M. Opher, V. Jatenco-Pereira, and T. I. Gombosi (2009), Simulations of Winds of Weak-Lined T Tauri Stars: The Magnetic Field Geometry and the Influence of the Wind on Giant Planet Migration, *ApJ*, *703*, 1734–1742, doi:10.1088/0004-637X/703/2/1734.

Visser, R., E. F. van Dishoeck, and J. H. Black (2009a), The photodissociation and chemistry of CO isotopologues: applications to interstellar clouds and circumstellar disks, *A&A*, *503*, 323–343, doi:10.1051/0004-6361/200912129.

Visser, R., E. F. van Dishoeck, S. D. Doty, and C. P. Dullemond (2009b), The chemical history of molecules in circumstellar disks. I. Ices, *A&A*, *495*, 881–897, doi:10.1051/0004-6361/200810846.

Voit, G. M. (1991), Energy deposition by X-ray photoelectrons into interstellar molecular clouds, *ApJ*, *377*, 158–170, doi:10.1086/170344.

Wakelam, V., P. Caselli, C. Ceccarelli, E. Herbst, and A. Castets (2004), Resetting chemical clocks of hot cores based on S-bearing molecules, *A&A*, *422*, 159–169, doi:10.1051/0004-6361:20047186.

Wakelam, V., F. Hersant, and F. Herpin (2011), Sulfur chemistry: 1D modeling in massive dense cores, *A&A*, *529*, A112, doi:10.1051/0004-6361/201016164.

Walmsley, C. M., D. R. Flower, and G. Pineau des Forêts (2004), Complete depletion in prestellar cores, *A&A*, *418*, 1035–1043, doi:10.1051/0004-6361:20035718.

Walsh, C., H. Nomura, T. J. Millar, and Y. Aikawa (2012), Chemical Processes in Protoplanetary Disks. II. On the Importance of Photochemistry and X-Ray Ionization, *ApJ*, *747*, 114, doi:10.1088/0004-637X/747/2/114.

Ward-Thompson, D., et al. (2010), A Herschel study of the properties of starless cores in the Polaris Flare dark cloud region using PACS and SPIRE, *A&A*, *518*, L92, doi:10.1051/0004-6361/201014618.

Wardle, M. (1999), The Balbus-Hawley instability in weakly ionized discs, *MNRAS*, *307*, 849–856, doi:10.1046/j.1365-8711.1999.02670.x.

Wasserburg, G. J., M. Busso, R. Gallino, and K. M. Nollett (2006), Short-lived nuclei in the early Solar System: Possible AGB sources, *Nuclear Physics A*, *777*, 5–69, doi:10.1016/j.nuclphysa.2005.07.015.

Watson, W. D. (1976), Interstellar molecule reactions, *Reviews of Modern Physics*, *48*, 513–552, doi:10.1103/RevModPhys.48.513.

Webb, R. A., B. Zuckerman, I. Platais, J. Patience, R. J. White, M. J. Schwartz, and C. McCarthy (1999), Discovery of Seven T Tauri Stars and a Brown Dwarf Candidatein the Nearby TW Hydrae Association, *ApJ*, *512*, L63–L67, doi:10.1086/311856.

Webber, W., and F. McDonald (2013), Recent voyager 1 data indicate that on august 25, 2012 at a distance of 121.7 au from the sun, sudden and unprecedented intensity changes were observed in anomalous and galactic cosmic rays, *Geophysical Research Letters*, pp. n/a–n/a, doi:10.1002/grl.50383.

Webber, W. R. (1998), A New Estimate of the Local Interstellar Energy Density and Ionization Rate of Galactic Cosmic Cosmic Rays, *ApJ*, *506*, 329–334, doi:10.1086/306222.

Webber, W. R., and J. A. Lezniak (1974), The comparative spectra of cosmic-ray protons and helium nuclei, *Ap&SS*, *30*, 361–380, doi:10.1007/BF00648282.

Weidenschilling, S. J. (1977), Aerodynamics of solid bodies in the solar nebula, *MNRAS*, *180*, 57–70.

Weidenschilling, S. J., and J. N. Cuzzi (1993), Formation of planetesimals in the solar nebula, in *Protostars and Planets III*, edited by E. H. Levy and J. I. Lunine, pp. 1031–1060.

Weinberger, A. J., E. E. Becklin, G. Schneider, E. I. Chiang, P. J. Lowrance, M. Silverstone, B. Zuckerman, D. C. Hines, and B. A. Smith (2002), Infrared Views of the TW Hydra Disk, *ApJ*, *566*, 409–418, doi:10.1086/338076.

Weinberger, A. J., G. Anglada-Escudé, and A. P. Boss (2013), Distance and Kinematics of the TW Hydrae Association from Parallaxes, *ApJ*, *762*, 118, doi:10.1088/0004-637X/762/2/118.

Weingartner, J. C., and B. T. Draine (2001), Dust Grain-Size Distributions and Extinction in the Milky Way, Large Magellanic Cloud, and Small Magellanic Cloud, *ApJ*, *548*, 296–309, doi:10.1086/318651.

Weintraub, D. A., B. Zuckerman, and C. R. Masson (1987), Structure of a possible circumbinary disk around T Tauri, *ApJ*, *320*, 336–343, doi:10.1086/165547.

Weintraub, D. A., G. Sandell, and W. D. Duncan (1989a), Submillimeter measurements of T Tauri and FU Orionis stars, *ApJ*, *340*, L69–L72, doi:10.1086/185441.

Weintraub, D. A., B. Zuckerman, and C. R. Masson (1989b), Measurements of Keplerian rotation of the gas in the circumbinary disk around T Tauri, *ApJ*, *344*, 915–924, doi: 10.1086/167859.

Weintraub, D. A., D. Saumon, J. H. Kastner, and T. Forveille (2000), NICMOS Narrow-band Infrared Photometry of TW Hydrae Association Stars, *ApJ*, *530*, 867–874, doi: 10.1086/308402.

Weymann, R. (1960), Coronal Evaporation as a Possible Mechanism for Mass Loss in Red Giants., *ApJ*, *132*, 380, doi:10.1086/146937.

Willacy, K., and W. D. Langer (2000), The Importance of Photoprocessing in Protoplanetary Disks, *ApJ*, *544*, 903–920, doi:10.1086/317236.

Willacy, K., and P. M. Woods (2009), Deuterium Chemistry in Protoplanetary Disks. II. The Inner 30 AU, *ApJ*, *703*, 479–499, doi:10.1088/0004-637X/703/1/479.

Williams, J. P., and W. M. J. Best (2014), A Parametric Modeling Approach to Measuring the Gas Masses of Circumstellar Disks, *ApJ*, *788*, 59, doi:10.1088/0004-637X/788/1/59.

Williams, J. P., and L. A. Cieza (2011a), Protoplanetary Disks and Their Evolution, *ARA&A*, *49*, 67–117, doi:10.1146/annurev-astro-081710-102548.

Williams, J. P., and L. A. Cieza (2011b), Protoplanetary Disks and Their Evolution, *ARA&A*, *49*, 67–117, doi:10.1146/annurev-astro-081710-102548.

Williams, J. P., L. Blitz, and C. F. McKee (2000), The Structure and Evolution of Molecular Clouds: from Clumps to Cores to the IMF, *Protostars and Planets IV*, p. 97.

Wilner, D. J., P. T. P. Ho, J. H. Kastner, and L. F. Rodríguez (2000), VLA Imaging of the Disk Surrounding the Nearby Young Star TW Hydrae, *ApJ*, *534*, L101–L104, doi: 10.1086/312642.

Wilner, D. J., T. L. Bourke, C. M. Wright, J. K. Jørgensen, E. F. van Dishoeck, and T. Wong (2003), Disks around the Young Stars TW Hydrae and HD 100546 Imaged at 3.4 Millimeters with the Australia Telescope Compact Array, *ApJ*, *596*, 597–602, doi: 10.1086/377627.

Wilner, D. J., P. D'Alessio, N. Calvet, M. J. Claussen, and L. Hartmann (2005), Toward Planetesimals in the Disk around TW Hydrae: 3.5 Centimeter Dust Emission, *ApJ*, *626*, L109–L112, doi:10.1086/431757.

Woitke, P. (1999), Dust formation in Radioactive Environments, in *Astronomy with Radioactivities*, edited by R. Diehl and D. Hartmann, p. 163.

Woitke, P., I. Kamp, and W.-F. Thi (2009), Radiation thermo-chemical models of protoplanetary disks. I. Hydrostatic disk structure and inner rim, *A&A*, *501*, 383–406, doi: 10.1051/0004-6361/200911821.

Wolcott-Green, J., and Z. Haiman (2011), Suppression of HD cooling in protogalactic gas clouds by Lyman-Werner radiation, *MNRAS*, *412*, 2603–2616, doi:10.1111/j.1365-2966.2010.18080.x.

Wolf, S., and G. D'Angelo (2005), On the Observability of Giant Protoplanets in Circumstellar Disks, *ApJ*, *619*, 1114–1122, doi:10.1086/426662.

Wolf, S., T. Henning, and B. Stecklum (1999), Multidimensional self-consistent radiative transfer simulations based on the Monte-Carlo method, *A&A*, *349*, 839–850.

Wolf, S., F. Gueth, T. Henning, and W. Kley (2002), Detecting Planets in Protoplanetary Disks: A Prospective Study, *ApJ*, *566*, L97–L99, doi:10.1086/339544.

Wolk, S. J., F. R. Harnden, Jr., E. Flaccomio, G. Micela, F. Favata, H. Shang, and E. D. Feigelson (2005), Stellar Activity on the Young Suns of Orion: COUP Observations of K5-7 Pre-Main-Sequence Stars, *ApJS*, *160*, 423–449, doi:10.1086/432099.

Yan, M., H. R. Sadeghpour, and A. Dalgarno (1998), Photoionization Cross Sections of He and H_2, *ApJ*, *496*, 1044–1050, doi:10.1086/305420.

Yang, H., C. M. Johns-Krull, and J. A. Valenti (2005), Measuring the Magnetic Field of the Classical T Tauri Star TW Hydrae, *ApJ*, *635*, 466–475, doi:10.1086/497070.

Yang, H., G. J. Herczeg, J. L. Linsky, A. Brown, C. M. Johns-Krull, L. Ingleby, N. Calvet, E. Bergin, and J. A. Valenti (2012), A Far-ultraviolet Atlas of Low-resolution Hubble Space Telescope Spectra of T Tauri Stars, *ApJ*, *744*, 121, doi:10.1088/0004-637X/744/2/121.

Yang, L., F. J. Ciesla, and C. M. O. Alexander (2013), The D/H ratio of water in the solar nebula during its formation and evolution, *Icarus*, *226*, 256–267, doi:10.1016/j.icarus.2013.05.027.

Yonezu, T., F. Matsushima, Y. Moriwaki, K. Takagi, and T. Amano (2009), THz spectroscopy of H_2D^+, *Journal of Molecular Spectroscopy*, *256*, 238–241, doi:10.1016/j.jms.2009.04.006.

Zhu, Z. (2015), Accreting Circumplanetary Disks: Observational Signatures, *ApJ*, *799*, 16, doi:10.1088/0004-637X/799/1/16.

Zhu, Z., L. Hartmann, C. Gammie, and J. C. McKinney (2009), Two-dimensional Simulations of FU Orionis Disk Outbursts, *ApJ*, *701*, 620–634, doi:10.1088/0004-637X/701/1/620.

Zhu, Z., L. Hartmann, and C. Gammie (2010), Long-term Evolution of Protostellar and Protoplanetary Disks. II. Layered Accretion with Infall, *ApJ*, *713*, 1143–1158, doi:10.1088/0004-637X/713/2/1143.